Airfoil-Vortex Interaction and the Wake of an Oscillating Airfoil

by

Michael C. Wilder

Dissertation submitted to the Faculty of the

Virginia Polytechnic Institute and State University

in partial fulfillment of the requirements for the degree of

Doctor of Philosophy

in

Engineering Mechanics

APPROVED:

D. P. Telionis, Chairman

S. L. Hendricks

D. T. Mook

D. H. Morris

W. H. Mason

February, 1992

Blacksburg, Virginia

Airfoil-Vortex Interaction and the Wake of an Oscillating Airfoil

by

Michael C. Wilder

D. P. Telionis, Chairman

Engineering Mechanics

(ABSTRACT)

Laser Doppler velocimetry, a non-intrusive flow measurement technique, was employed to experimentally investigate two-dimensional airfoil-vortex interaction. Vortices were generated by sinusoidally oscillating a NACA 0012 airfoil about its quarter-chord at a reduced frequency of $k = 2.05$ and an amplitude of $\pm 10°$ angle of attack. The target airfoil, a NACA 63_2A015, was immersed in the wake, two chord lengths downstream of the vortex generator's trailing edge. Phase-averaged velocity measurements of the flow around the target airfoil were made with the airfoil at angles of attack of $\alpha = 0°$ and $\alpha = 10°$. A close encounter with a counterclockwise rotating vortex was observed for both angles of attack, and a head-on collision, which split the counterclockwise rotating vortex in two, was observed for $\alpha = 10°$. Vorticity fields were constructed from the velocity measurements and the circulation of the vortex was evaluated throughout the interaction. The surface pressure fluctuations on the airfoil were determined by substituting the measured velocities into the Navier-Stokes equations and numerically integrating the resulting pressure gradients. Furthermore, an extensive investigation of the undisturbed wake of the oscillating airfoil was performed in order to determine the effect of oscillation frequency and amplitude on the wake development.

dedicated to Zola and Martin
my parents

Acknowledgements

To professor Demetri Telionis, I offer my most heartfelt thanks for the advise and knowledge imparted to me and the opportunities extended to me these past years.

I also acknowledge the members of my committee: Drs. Hendricks, Mason, Mook, and Morris, for their useful criticism while reviewing this work, and all the other educators who have shaped my academic life, including: Dr. Ragab and Dr. Cramer, Dr. Ianna and Dr. Goldstein (as an undergraduate), and Mrs. Massart, Dr. Tartar and Mr. Wood.

My appreciation is extended to NASA Langley Research Center and Boeing Helicopter Company for their interest in, and financial support of, this work and my education. Particular thanks are given to Mr. Earl Booth (principal contact at NASA), Dr. Paul Pao and Dr. J. Preisser (NASA project monitors, grant number NGT-50123), Dr. David Poling (project monitor at Boeing, contract number TT127270) and Dr. Leo Dadone (project monitor at Boeing, contract number TT957811).

Thanks and gratatude are also extended to Nasrin Lotfi, who managed to keep our laboratory computer operating just a little while longer, and Lucinda Willis for her clerical help and friendship.

Finally, I would like to thank my friends and colleagues, who gave meaning to it all: Sarah Whitlock, Ngoc Hoang, Norman Scheaffler, Erik Panzer, Othon Rediniotis, Sandie Klute, Deborah Furey, and the Collegate Times photo staff.

Table of Contents

List of Illustrations

Chapter 1

Introduction

Vorticity generated at the tip of helicopter rotor blades rolls up into concentrated vortices which sustain their character for considerable distances downstream of the rotor. When these vortices interact with following rotor blades, the unsteady pressure fluctuations induced on the blade lead to dynamic structural loading of the blade and noise production. The blade-vortex interaction, or BVI, is the source of the familiar "blade slap" sound of helicopters.

This interaction is an example of a broad class of unsteady fluid dynamics problems which can be generalized as body-turbulence interaction (Bushnell, 1984). The turbulence field can take any form, from full three-dimensional, uncorrelated turbulence (wind gusts against structures), to highly coherent, uniform vortices (such as the helicopter BVI). Any wing-like surface, however, will shed vorticity at the tip, which can encounter trailing surfaces. Examples include; rotor wake-stator interacaction; propeller wake-wing or fuselage interaction; canard-wing interaction, to name a few.

Research into the airfoil-vortex interaction phenomenon may be placed into two broad categories. In the first, the emphasis is placed upon the influence that a vortex has on an airfoil (or any body, in general), whereas, research in the second category ex-

amines the effect of the interaction on the vortex. The scale and circulation of the vorticity affect the nature of the interaction, therefore, a detailed investigation of the flow field in the leading edge region of the airfoil is required to better understand the fluid mechanics involved in the interaction. Research yielding qualitative measurements of an airfoil-vortex interaction predominately fall within the first category (one exception known to the author is Gursul and Rockwell, 1990). These measurements are typically in the form of unsteady surface pressures. Research focusing on the details of the flow field have been primarily flow visualization in nature.

In some cases, research into helicopter BVI has closely approximated the actual flow around the rotor blade. Caradonna et al. (1988) reported unsteady pressure measurements made on a non-lifting rotor model during blade-vortex interaction (BVI). A leading-edge pressure pulse was the dominant feature of the BVI. Detailed velocity measurements in the tip vortex core of a single-bladed model rotor in hover were made by Thompson et al. (1987), however, due to the downwash of the rotor, no blade-vortex interaction occured in this study.

Blade-vortex interactions within a helicopter rotor system are shown schematically in Fig. 1.1. We see in this figure a site at which the vortex core is nearly perpendicular to the blade span and another site at which the core is nearly parallel. By considering the extreme case of a parallel interaction, the helicopter rotor blade-vortex interaction can be modeled in two dimensions, while retaining many of the physical characteristics of the actual interaction. Analytical predictions by Widnall (1971) indicate that the parallel interaction produces the largest amplitude radiated noise pulse. Noise directivity studies (Martin et al., 1987) and noise source indentification (Splettstoesser et al., 1987) bear out this conclusion. Therefore, the helicopter BVI problem has quite often been studied in the form of a two-dimensional parallel interaction.

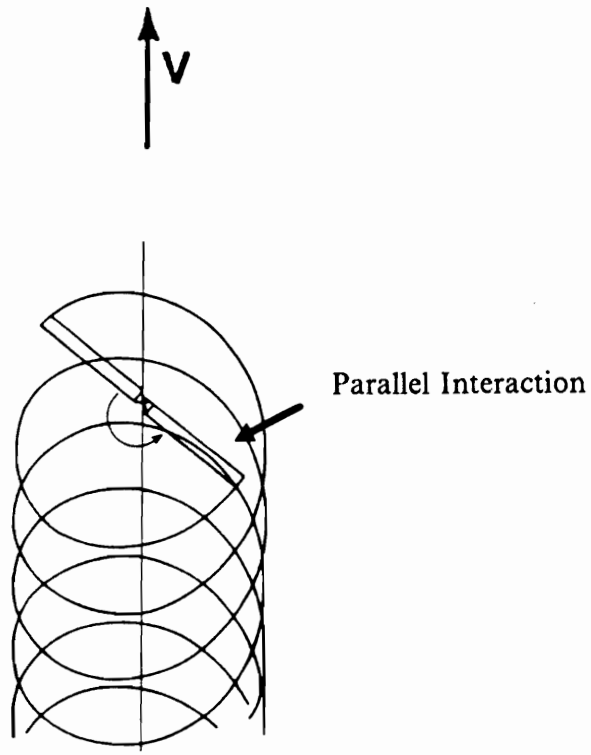

Figure 1.1. Blade-vortex interaction in a helicopter rotor.

Two-dimensional vortex disturbances can be generated by a variety of methods. Rockwell and Knisely (1979) and Graf and Durgin (1990) made use of the natural intstabilities inherent in a free shear layer to investigate vortex impingment upon a corner. Kaykayoglu and Rockwell (1985) and Sohn and Rockwell (1987) have also employed mixing-layers in the examination of vortex impingement with sharp and elliptical leading edges at zero angle of incidence. Rockwell (1984) provides an overview of earlier work of this type. Unsteady surface pressure measurements, and streakline and timeline flow visualizations were employed in these studies.

The vortices naturally formed in the wake of a bluff body have also been used in the study of vortex interaction with a body. The obvious disadvantages of using the von Karman vortex street are the relatively close vortex spacings and the elavated turbulence due to the dead-air region behind the bluff body. Meier and Timm (1985) employed Mach-Zehnder interferometry (a precise method of determining density variations within a flow) to study the interaction with an airfoil of vortices generated by different shedding cylinders. Gursul and Rockwell (1990) too, studied body-vortex interaction by immersing the body in the wake of a shedding cylinder. Unsteady surface pressures and streakline flow visualization results of the interaction of the vortices with an elliptical leading edge were presented. Gursul and Rockwell also provided detailed two-dimensional LDV velocity measurements in the leading-edge region. The velocity measurements were used to calculate vorticity and pressure fields, and to simulate streakline and timeline flow visualizations.

Meier and Timm (1985) also employed vortices generated by an airfoil placed in the starting flow. In a shock-tube, a second airfoil was placed upstream of the test airfoil. The starting vortex shed by the second airfoil had a very small core radius and velocity distribution close to a potential vortex. The experimental results were compared with inviscid calculations using conformal mapping.

A popular method — and the one employed by the author — of generating a two-dimensional vortex disturbance is by oscillating an airfoil in pitch. Free shear layers, shed from the airfoil's trailing edge as it undergoes rapid changes in angle of attack, quickly roll up into large scale coherent vortical structures. For sinusoidal oscillations, these structures arrange themselves as a street of vortices of alternating rotational sense. This wake is similar in appearance to the Karman vortex street of bluff bodies, but the rotational sense of the vortices is opposite to that of the bluff body wake.

Booth and Yu presented smoke flow visualization for a symmetric airfoil in the wake of a sinusoidally oscillating airfoil (September, 1986), and a nonsinusoidally oscillating airfoil (March, 1986). The nonsinusoidal oscillation waveform consisted of a rapid upstroke (in the first 20% of the period) followed by a gradual return. In this way only one strong vortex was formed per oscillation period, increasing the separation between vortices by about five times, and isolating each encounter from the effects of the previous and successive ones. Booth (1986) recorded unsteady pressures on the first 20 percent of the blade surface and later (1987, 1990) computed the far field noise from the measured surface pressures.

Steady and unsteady pressures were measured by Straus et al. (1990) for the interaction of a counterclockwise rotating vortex with a symmetric airfoil at zero angle of incidence. The vortices were formed by pitching a symmetric airfoil about its center of mass. Measured pressures were compared with pressures computed by discrete vortex methods. Lift and moment coefficients were compared with those derived by discrete vortex method and linear theory of Sears.

Swirydczuk (1990) also employed a non-sinusoidal pitching schedule in order to lengthen the separation between vortices. Smoke-wire visualization was used to examine the interaction of a single vortex with a thin symmetrical airfoil and its wake. The emphasis of this investigation was placed of the vortex-wake interaction.

A variety of numerical simulations of parallel blade-vortex interaction have been reported as well. Experiments must be performed to establish the validity of the various models employed. Methods range from inviscid discrete-vortex modeling to numerical solutions of the Euler and Navier-Stokes equations to exact analytical solutions.

Poling et al. (1989) used a single discrete vortex and confomal mapping analysis with an unsteady Kutta condition to model the airfoil-vortex interaction. The vortex was replaced with a cloud of vortices to represent an extended vortex core (Poling et al. 1988). Unsteady pressures using the vortex cloud were compared with experimental results (Poling et al. 1991). Panaras (1987), and Lee and Smith (1987), also employed a cloud of discrete vortices in modeling the vortex core.

Inviscid calculations were made by Swirydczuk (1990), Straus et al. (1990), and Meier and Timm (1985) to compare with there experimental results.

Hardin and Lamkin (1987) developed an Euler code for predicting the radiated noise due to the interaction of a distributed vortex with a Joukowski airfoil. Wu et al. (1985) used the Euler equations in calculations of compressible inviscid transonic flow, and Lee et al. (1990) used an Euler-Lagrangian method.

The problem of vortex-wing interaction was treated analytically and exact solutions were obtained by Jones (1972). Farassat and Succi (1983) developed analytical fomulations for predicting radiated helicopter noise. These fomulations were employed by Booth (1990) to calculate radiated noise from experimentally obtained surface pressures. Lee and Roberts (1985) computed the impulsive noise due to blade-vortex interaction using an analytical turbulent vortex core model. Hardin and Lamkin (1986) identified the critical parameters controling noise generation by an analysis of a simplified physical model.

The vortex disturbance for the experimental work reported here was generated by oscillating a symmetrical airfoil about its quarter-chord point. A careful survey of the

velocity distribution of the vortices and of the repeatability of producing the disturbance was conducted. Beyond this, a more extensive investigation of the wake of an oscillating airfoil was performed. Unsteady velocity measurements were made in the mid- and far-wake regions to examine the developement of the wake and the effects of oscillation frequency and amplitude were investigated. These results are reported in chapter 3.

Like the airfoil-vortex interaction problem, there exists little quantitative experimental data on the unsteady flow in the wake of an oscillating airfoil. Other vortex dominated flows and free shear flows are also lacking in experimental detail while much effort has gone into modeling such unsteady flows (Aref and Siggia (1980), Wygnanski and Petersen (1987), Mook et al. (1987), and Sundaram et al. (1991)).

Much of the experimental effort in unsteady aerodynamics of airfoils has concentrated on the unsteady loading associated with the dynamic stall phenomenon. Such research efforts were reviewed by McCroskey (1977, 1981). The applicability of an unsteady Kutta-Joukowski trailing-edge condition has also received considerable attention (Satyanarayana and Davis (1978), Poling and Telionis (1986), and Liu et al. (1990)).

Two non-dimensional parameters, namely, the reduced frequency and the reduced amplitude, determine the nature of the ocsillating airfoil wake. These parameters are defined as,

$$k = \frac{\omega c}{2U_\infty}$$
$$H = \frac{a}{c},$$

respectively, where ω is the angular frequency of oscillation, c is the chordlength of the airfoil, U_∞ is the magnitude of the mean freestream velocity, and a is the amplitude of oscillation (the linear distance traveled by the trailing edge). Inviscid calculations by Katz and Weihs (1978) suggest that the wake of a sinusoidally pitching airfoil rolls up

into discrete concentrations of vorticity for reduced frequencies greater than 2. Experimental results (flow visualization) show that roll up is dependent on amplitude as well as frequency.

Flow visualization studies, such as performed by Bratt (1953), provide insight into the structure of unsteady wakes and the nature of vortex roll-up, but do not offer quantitative data on the flow. Extensive streakline flow visualization results were presented by Oshima and Oshima (1980) and compared with inviscid calculations using discrete vortices. Experiments for a NACA 0012 airfoil oscillating in pitch were performed for reduced frequencies ranging from $k = 0.99$ to 4.90, reduced amplitudes from $H = 0.2$ to 0.74 and at low Reynolds numbers ($Re < 20{,}000$). LDV and hot-film measurements were also made, though only a single sample of the LDV measurements were presented.

Koochesfahani (1989) has also employed streakline flow visualization in the study of an oscillating airfoil wake, only here the emphasis was placed on controlling the wake structure by controlling the frequency, amplitude and the shape of the oscillation waveform. Pitching amplitudes of $\pm 2°$ and $\pm 4°$, reduced frequencies between 0.8 and 10.0 at a Reynolds number of 12,000 for both sinusoidal and non-sinusoidal pitching waveforms, or pitching schedules, were studied. Mean velocity profiles obtained with LDV at a station 1 chordlength from the trailing edge were also presented.

Caution must be used in interpreting streakline visualizations in unsteady flows. Williams and Hama (1980) have shown that streaklines can give the erroneous impression of growth and the presence of discrete vortices in a shear layer. Kurosaka and Sundaram (1986) calculated straklines for a single vortex and for a Karman vortex street and found the streaklines gave the impression of growth and flow reversal which did not exist. Moreover, associating the dye of the streakline with vorticity is erroneous since the diffusivity of the vorticity is different than that of the dye.

Until resently, the majority of the studies reported in the literature which do provide unsteady velocity and/or turdulence measurements have been predominately concerened with the near-field wake and typically involve low reduced frequencies ($k \leq 1$). Ho and Chin (1981) reported that the upper and lower parts of the wake of a plunging airfoil have different turbulent structures. Ensemble averaged velocity measurements were carried out between 0.08 and 1.0 chordlengths downstream of the airfoil trailing edge using a rake of five x-wire hot-wire probes.

De Ruyck and Hirsch (1983) made instantaneous velocity and turbulence profile measurements by hot-wire at five locations in the near-wake of a sinusoidally pitching NACA 0012 airfoil. The furthest downstream measurement was only 0.2 chordlengths from the trailing edge. For a reduced frequency of $k = 1$ (the highest frequency employed) a small recirculation area was observed up to 2% chord downstream of the trailing edge. Also, the wake did not appear to be stalled during osillation even when the static stall angle ($\alpha = 14°$) was slightly exceeded (by 1°).

Hot-wire velocity and turbulence measurements combined with smoke-wire flow visualizations were made as far as 1.5 chordlengths into the wake by Park and Kim (1987). A NACA 0012 airfoil was pitched siusoidally about the ¼-chord at low reduced frequencies ($k = 0.09$, 0.13, and 0.2) and at Reynolds numbers of $Re = 47{,}000$, 40,000, and 27,000, respectively. The airfoil was oscillated about zero mean angle of attack with an amplitude of 7.4°. The authors reported a sudden increase in wake thickness as a result of dynamic trailing edge stall, and that wake thickness increases with reduced frequency. From work done at similar experimental parameters, Park et al. (1988) established the convection velocity of the trailing edge stall to be 0.6 times the free-stream velocity. In comparison, Carr et al. (1977) found the convection speed of the vortex generated over an airfoil during deep dynamic stall to be from 0.35 to 0.4 times the free-stream velocity.

Extending to higher reduced frequencies, Mathioulakis et al. (1985), made one-component laser Doppler velocimetry measuremenst in the wake of a NACA 0012 pitching sinusoidally at a reduced frequency of $k = 2.77$. These experiments were performed in the same facilities as the present author's research. Instantaneous velocity profiles were obtained along eight columns between 0.6 and 1.3 chordlengths downstream of the trailing edge. The streamwise velocity component (u) was measured and the cross-stream component (v) was computed by integrating the continuity equation and assuming that $v = 0$ along the top row of the measurement grid. Results were compared with the velocity field produced by the complex velocity potential for an infinite double row of ideal vortices, and with the results of descrete vortex computations by Kim and Mook (1985).

Velocity and vorticity measurements were made at one chordlength into the wake of a pitching NACA 0012 airfoil by Booth (1987). The measurements were performed in a low-speed, low-turbulence wind tunnel at a chord Reynolds number of about 46,000, a reduced frequency of $k = 3.14.$, a 10° amplitude about a zero mean angle of attack. Hot-wire velocity measurements as well as vorticity measurements via a prototype vorticity probe were made along a survey line for both sinusoidal and non-sinusoidal pitching schedules. The non-sinusoidal (or tailored) schedule was sawtooth-like, with the airfoil going from minimum incidence to maximum incidence in a sinusoidal sweep in the first 20 percent of the pitching period, followed by a linear return sweep over the remaining 80 percent of the cycle. The vortex produced by the tailored pitching schedule was weaker than one formed by sinusoidal pitching at the same reduced frequency and appeared as two distinct vorticity accumulations. The tailored pitching schedule increased the spacing between vortices of like sign, from the order of one chordlength for the sinusoidal wake to about 5.1c for the tailored wake, and although prominent vortices of one sign were produced there were no strong vortices of the op-

posite sense evident. For a similar tailared pitching schedule (Koochesfahani (1989)), flow visualization in water clearly showed several weaker vortices of this opposite sense.

In the next chapter a discussion of the experimental facilities and techniques is offered. Included is an examination of the two-dimensionality and repeatability of the flow in the wake of the oscillating airfoil.

An airfoil oscillating about its quarter chord was employed to create the vortex disturbance used for the airfoil-vortex interaction experiments. A careful study of the wake of the sinusoidally pitching airfoil was performed, and the results compose chapter 3. Laser Doppler velocimetry, a non-intrusive flow measurement technique, was employed to provide detailed, unsteady velocity measurements as far as four chordlengths into the wake for a range of reduced frequencies and two pitching amplitudes. These measurements were made in order to determine how the wake structure depends on reduced frequency and amplitude, and to establish the qualities of the vortex disturbance utilized in the airfoil-vortex interaction study.

The results of a detailed investigation of the airfoil-vortex interaction are presented in chapter 4. LDV measurements were made around the leading edge of the airfoil during the interaction. Three cases were studied; a close encounter with the airfoil at a zero degree angle of attack, and both a close encounter and a direct encounter with the airfoil at ten degrees. In the direct encounter the vortex was split in two, while in the close encounter the vortex skimmed across the upper surface of the airfoil. With the velocity measurements, instantaneous vorticity fields, the instantaneous circulation of the vortex, and the unsteady surface pressure coefficients on the airfoil were calculated. A complete sequence of vorticity contour maps for each case is presented as appendices.

Chapter 2

Experimental Facilities and Techniques

2.1 Introduction

Velocity measurements were performed with a two-component laser-Doppler velocimeter (LDV) in the VPI & SU water tunnel. Laser Doppler velocimetry is an optical measurement technique employing laser light to measure the velocity of small tracer particles suspended in the fluid. As an optical measurement technique, LDV is non-intrusive; a feature of particular importance here, where a mechanical measurement probe would upset the vortical structures that we wish to observe. This chapter offers a description of the experimental facilities, including the water tunnel, the vortex generator, and the laser velocimetry systems used, and an analysis of the expected experimental errors and the methods employed for data reduction.

2.2 The Water Tunnel

Built in 1976 by the Engineering Science and Mechanics Department with the support of the Army Research Office, the water tunnel is a 570-gallon closed-circuit tunnel

constructed of plexiglass and poly-vinyl chloride (PVC) pipe, Fig. 2.1. The settling chamber has a 6:1 two-dimensional contraction and features screens, honeycombs, accurately positioned flow straighteners and a set of guide vanes in the divergence to the settling chamber for improving flow quality within the test section. The basic design is described by Koromilas (1978) and by Mezaris (1979), while a detailed calibration of the tunnel can be found in Telionis et al. (1986). A centrifugal pump powered by a 2 h.p. variable speed dc motor provided free-stream velocities in the test section from about 45 cm/sec up to 1.5 m/sec. Lower speeds, down to 10 cm/sec could be reached by closing a butterfly valve located immediately after the pump. Free-stream turbulence levels at the upstream end of the test section were consistently 1% for velocities from 12 cm/sec to 25 cm/sec. These measurements were made 12.7 cm (5 in.) into the test section immediately following the contraction, and roughly in the center of the tunnel cross section. At locations further downstream, the turbulence levels ranged from 1.5% to 5%. The magnitude of the turbulence was heavily influenced by the cleanliness of the water tunnel. A typical span-wise turbulence intensity profile is presented in section 2.6(iii) (see Figure 2.10 on page 40).

Recently a new test section was designed and installed (Telionis and Wilder, 1988) Built of clear plexiglass, the inside cross section of the test section is 25 cm (span) x 30 cm, (9.8 in. x 11.8 in.) and the length is 244 cm (8 ft.) measured from the end of the settling chamber contraction. The test section proper; i.e., the segment of the 244 cm-long test section in which measurements were performed (hereafter refered to simply as the test section), is a removable plexiglass box. The top and bottom of this box serve as the roof and inner floor of the water tunnel when in place, while the box's walls serve as side (or false) walls to our models. The inside dimensions of the test-section box are 21.5 cm (span) x 30 cm (8.46 in. x 11.8 in.), leaving a 0.9525 cm (6/16 in.) gap between the false walls and the tunnel walls. The false walls are bevelled at the leading-edge and

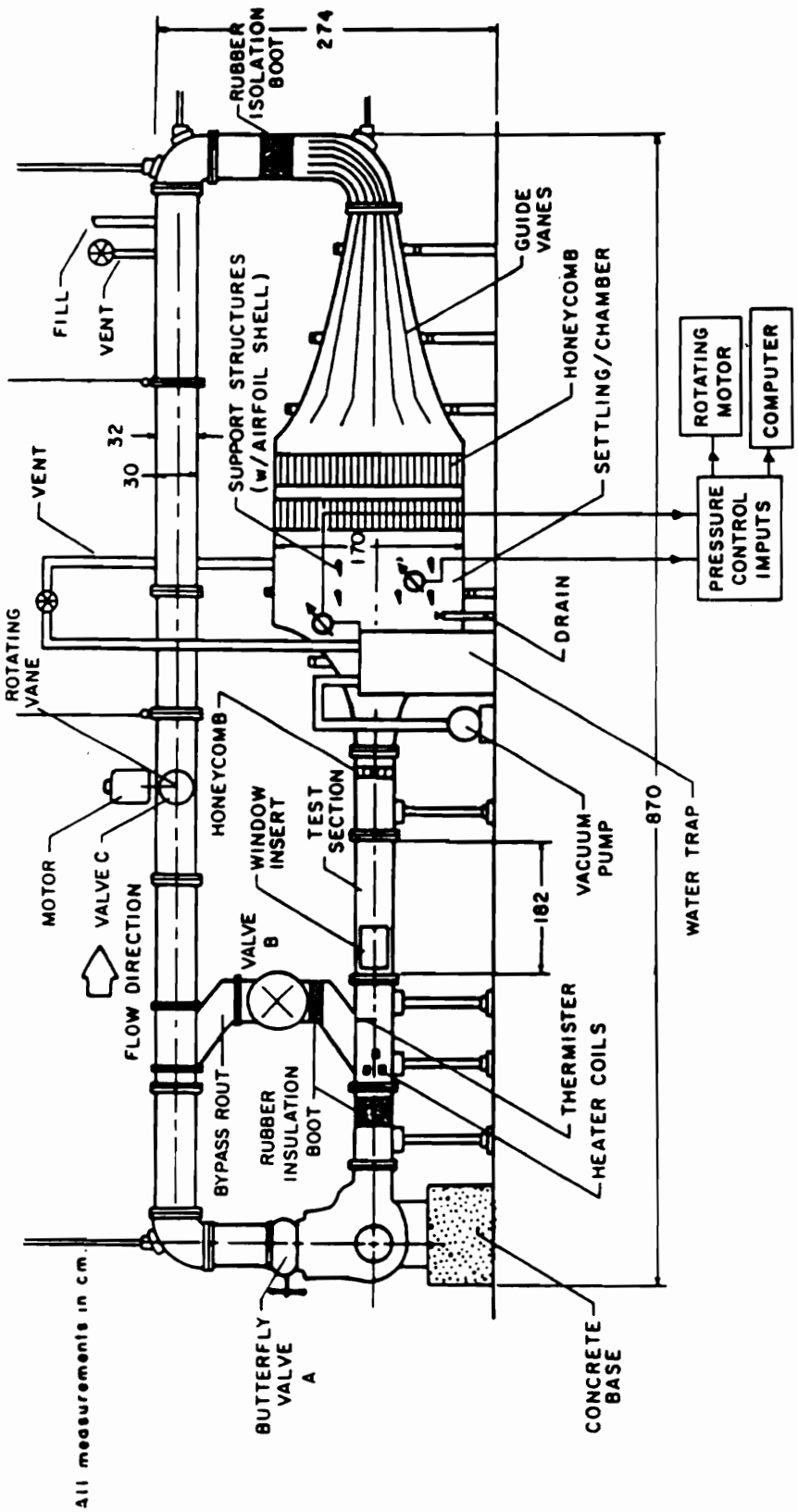

Figure 2.1. ESM water tunnel.

act as end plates for the airfoil models. The test-section box is 48.26 cm (19 in.) long, while the false walls are extended by another 22.86 cm (9 in.) by segments permanently mounted inside the tunnel. Finally, 10.16 cm (4 in.) long flaps are located at the trailing-edge of the fixed wall segments. The position of the flaps can be varied from fully open to fully closed and are used to control the flow rate through the gaps between false walls and tunnel walls. The flap position has a negligible effect on turbulence levels over the central 70% of the test-section span, and little effect on mean velocity over this same span untill the flaps are fully closed, (Poling, 1986). A flap angle of 10° was used in this work. This new design allows simpler, quicker access to the models in comparison with the older design, and greatly facilitates making adjustments to model position and cleaning. A second access to the test section interior (the first being the test-section box) is located at the upstream end of the test section and opens onto a removable honeycomb and three fine-mesh screens.

An adjustable mounting bracket is attached to one false wall of the test-section box. The bracket can slide up or down along slots in the false wall. A slotted hub supports our airfoil models (which are equipped with a tab to match this slot). The hub can be fixed in place with the model at a 0°, $\pm$ 5°, or $\pm$ 10° angle of attack. With all adjustments fixed, a set screw located within the hub is used to press the model firmly against the opposite false wall. At present, the model position cannot be adjusted in the streamwise direction.

2.3 The Vortex Generator

Vortices were generated by oscillating an airfoil in pitch. The free shear layers shed from the airfoil during rapid changes in the angle of incidence quickly roll up into coherent vortical structures with sizes on the order of the airfoil chord. The airfoil, a

NACA 0012 with a 10.16 cm (4 in.) chord length, was pitched about its ¼-chord by a ¾-horsepower dc motor. The rotational motion of the motor was translated to a pitching motion of the airfoil via a four-bar linkage system. A 16:1 speed-reducing gear box and flywheel connected the motor to the linkage system (see Fig. 2.2). The four-bar linkage provided structural rigidity to the drive and allowed the pitching motion to be smooth and cotinuous. Running the motor at a constant speed resulted in a sinusoidal variation in the angle of attack, which can be written as,

$$\begin{aligned} \alpha(t) &= \alpha_0 + \alpha_1 \sin(\omega t) \\ &= \alpha_0 + \alpha_1 \sin\left(\frac{2\pi}{\tau} t\right), \end{aligned} \qquad [2.1]$$

where α_0 is the mean angle of attack, α_1 is the amplitude of oscillation, τ is the period of oscillation, $\omega = \frac{2\pi}{\tau}$ is the angular frequency of oscillation, and t is time. In the present case we kept $\alpha_0 = 0°$. Motor speed, and therefore pitching frequency, was set by a Morse MDC-II controller. In manual operation, speed was selected by a potentiometer. Oscillation frequencies from 0 to 11 Hz were possible. We also experimented with non-sinusoidal pitching waveforms, which required a periodic variation of the motor speed. This variation was achieved with an automatic potentiometer/tachometer. The speed of the motor was proportional to a dc-voltage input to the potentiometer/tachometer, the voltage being sent from a laboratory computer. With this computer-controlled system a wide range of oscillation waveforms could be produced.

Data acquisition was coordinated with the oscillating airfoil via an optical trigger (a side-by-side LED - phototransistor pair) mounted beside the flywheel of the pitching mechanism. Infrared light emitted by the LED would reflect off a mirrored tab attached to the flywheel, and be detected by the phototransisitor. A current produced by the phototransistor caused a pulse to be sent to the laboratory computer. This pulse initi-

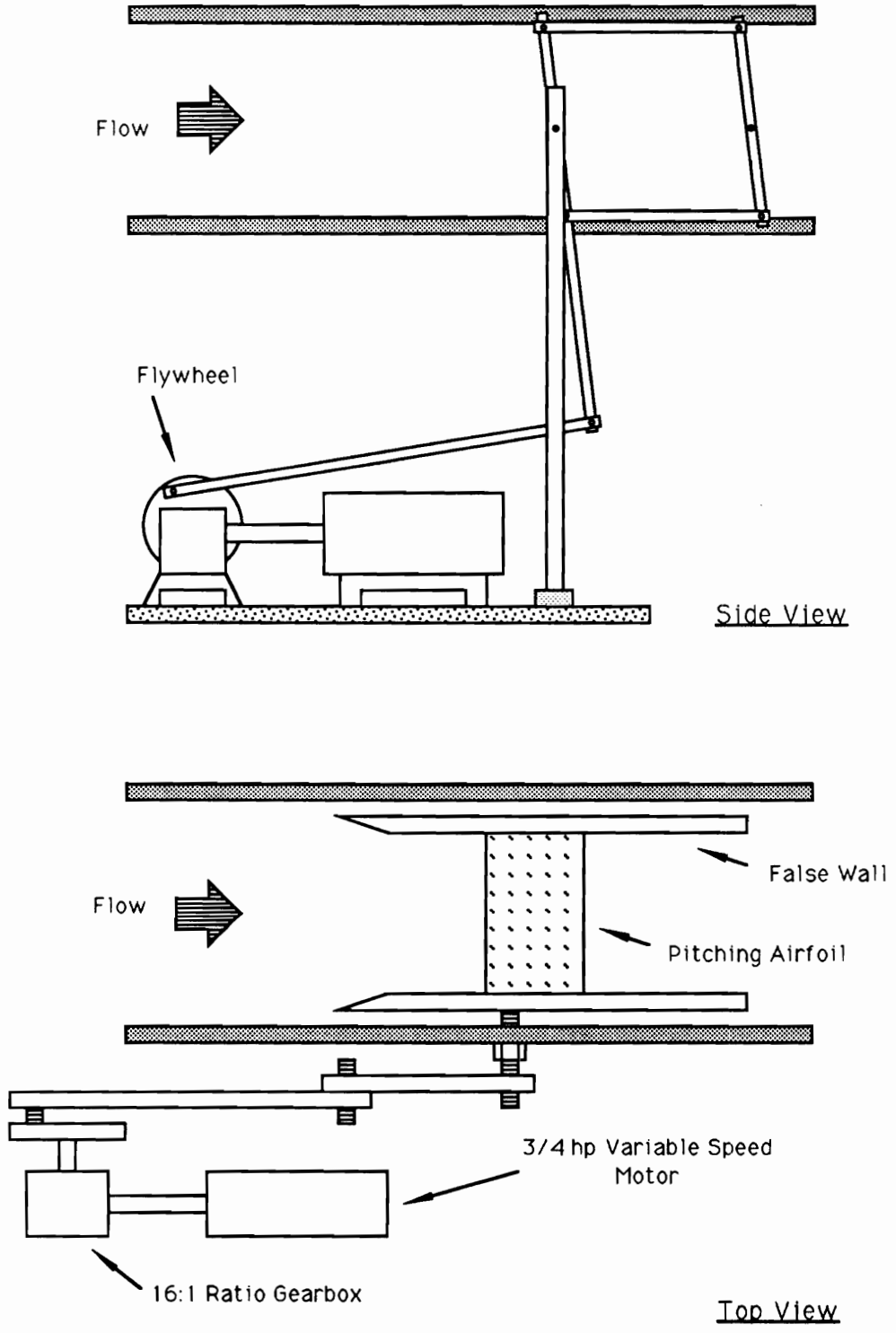

Figure 2.2. The Vortex Generator.

ated data acquisition by activating the computer's clock. The reflective tab was positioned so that the triggering pulse occured as the airfoil begins its upstroke; i.e., the airfoil is at -10° angle of attack and is beginning to pitch up.

Physical characteristics of vortices produced by the oscillating airfoil are described in chapter 3.

2.4 Laser Doppler Velocimetry

Laser Doppler velocimetry (LDV) is a non-intrusive flow measurement technique which allows the measurement of the instantaneous velocity (magnitude and direction) of tracer particles suspended in the fluid. The technique provides high spacial resolution, high frequency response, and measurements which are independent of the fluid properties. However, LDV systems are often expensive and complex, requiring for proper operation a working knowledge of optics and electronics. Since light beams serve as the probe, optical access to the test section (a window) is necessary. In addition, the tracer particles must accurately follow the flow. *Seeding* the flow with particles is a demanding task when air is the working fluid, but water often contains enough natural impurities to make seeding unnecessary. For best results the particles should be neutrally buoyant and quite small ($\sim 1\mu m$ in diameter).

Laser Doppler velocimetry makes use of the Doppler effect —the frequency shift in light due to the relative motion of source and observer— to detect the velocity of the seeding particles. Light scattered from the moving particles is Doppler shifted in frequency. An interference pattern forms when the scattered light is mixed with unshifted laser light. The resulting interference patteren varies in intensity with a frequency equal to the Doppler frequency, and this variation is detectable with a photodetector.

The Doppler frequency is directly proportional to the speed of the particle. For the dual-beam, or differential-Doppler, type velocimeters employed in this work, the relationship between Doppler frequency, f_D, and velocity is;

$$f_D = \frac{V}{d_f} = \frac{1}{\lambda} V(2 \sin K), \qquad [2.2]$$

where, d_f is fringe spacing (the distance between fringes in the interference patteren formed by mixing the light scattered from the two beams), V is the component of the velocity to which the LDV is sensitive, λ is the wavelength of the unshifted laser light, and κ is half the angle with which the beams cross. Figure 2.3 schematically illustrates the velocimeter. A probe volume, or measuring volume, is formed where the two laser beams cross. Typically, the probe volume is less than one millimeter in diameter and a few millimeters long; the size of the probe volume defines the spacial resolution of the velocimeter. A fringe pattern forms in the probe volume, with a fring spacing of d_f. The LDV is sensitive to the component of velocity in the plane of the beams, and normal to the bisector of the two beams. For an indepth discussion of the principles of laser velocimetry the interested reader is refered to Durst, Melling and Whitelaw (1976).

Basic components of a laser velocimeter include a laser light source, beam splitting prisms or mirrors, a focusing lens, a photodetector for receiving information, signal processing equipment for analyzing this information, and a computer for storing the information. Lasers are used for their power, small beam diameter, and most importantly, the special nature of laser light. Laser light is highly coherent and monochromatic, two qualities which are necessary for interference to occur. The small diameter of laser beams relates directly to the spacial resolution of the velocimeter, and the laser power to the strength and quality of the signal.

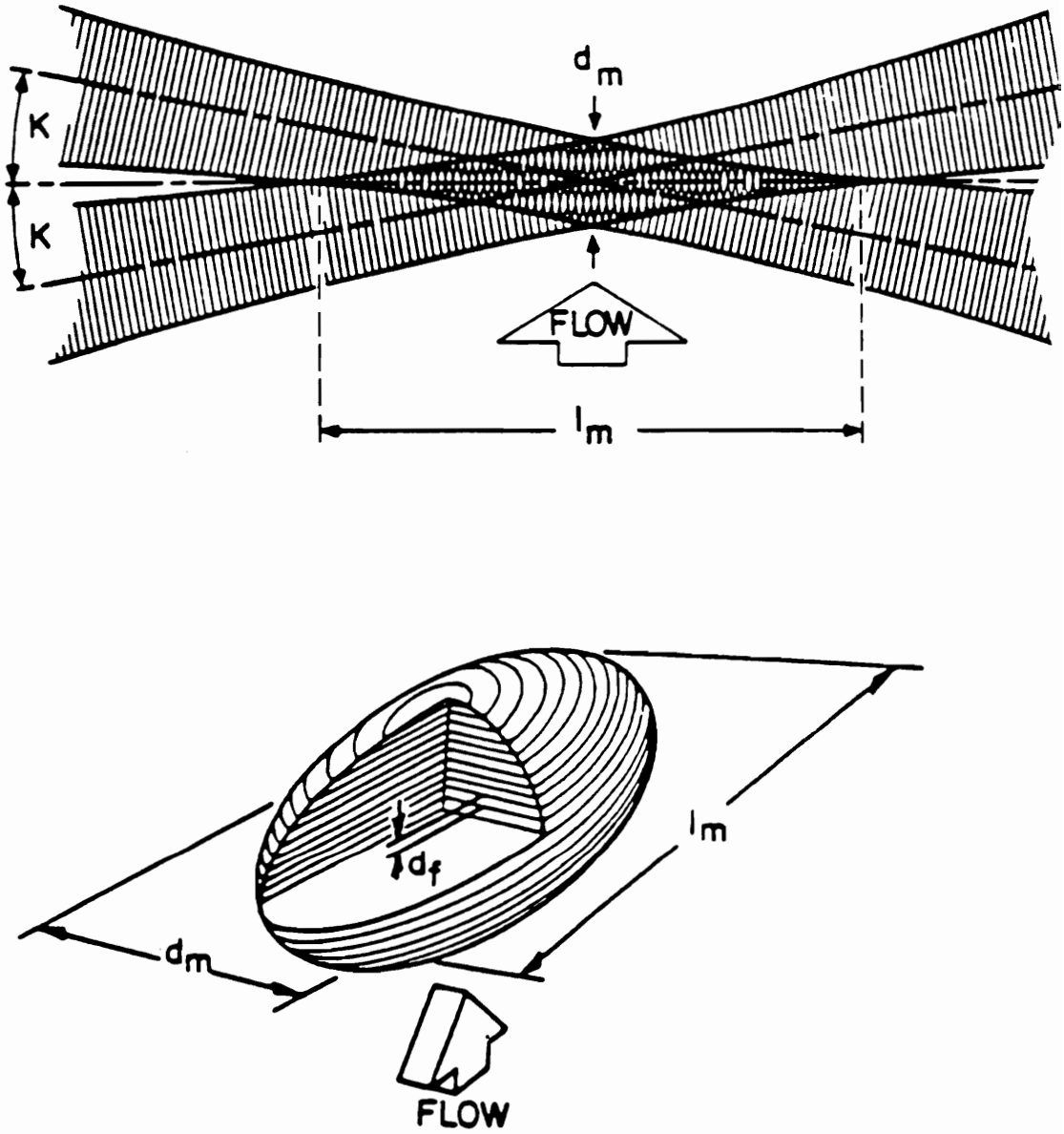

Figure 2.3. Dual-beam laser-Doppler velocimeter.

Two laser Doppler velocimeters were used in this work. A single-component system monitered the free-stream velocity of the water tunnel and a more complex two-component system was employed in making velocity measurements in the test section. The two-component system was capable of detecting flow reversals and could automatically traverse the measurement volume over a predefined grid. Both systems had one element in common; the laboratory computer.

A Digital Equipment Corporation MINC-11 (Modular INstrument Computer) controlled the laboratory equipment and recorded the data on 8″ floppy disks. The MINC featured a 12-channel analog-to-digital (A/D) board for converting the analog output of the signal processors to digital information for manipulation and storage, a digital-to-analog (D/A) converter and a digital output for controlling the stepping motors which traverse the probe volume, and a Schmitt trigger activated clock which synchronized data acquisition with the pitching airfoil. Other than the MINC, the two LDV systems were separate and distinct.

The free-stream monitor was a single-component DISA type 55L laser Doppler velocimeter which will be referred to here as the DISA LDV or DISA system. A 5-mW Helium-Neon Spectra Physics laser served as the light source. The beam was split by a prism into two equal-intensity beams which were focused by a 300 mm focal length, f/4.5 focal ratio lens. The measurement volume was 3.23 mm long and 0.24 mm in diameter, with a fringe spacing of 4.2 μm. The probe volume was positioned 14 cm downstream of the tunnel contraction and as near to the center of the tunnel cross section as possible. A photomultiplier tube (PMT), located on the opposite side of the tunnel, received the scattered light. This arrangement is known as forward-scatter mode. The components of the DISA system were mounted on a stationary optical bench. A DISA model 55L20 frequency tracker Doppler signal analyzer processed the signal from the PMT. Frequency trackers "follow" the Doppler frequency by forming a phase-locked loop be-

tween the Doppler frequency and the output of a voltage controlled oscillator (VCO). If the Doppler signal is lost for a sufficiently long time (high drop-out) or if fluctuations in the Doppler frequency (high turbulence) are too great, the phase-locked loop will be broken. Then, the frequency tracker needs to be manually re-tuned. For this reason we employed a tracker only in the free-stream velocity monitor.

The other system, a two-component He-Ne LDV from TSI Inc. was the principle instrument in this investigation. The system layout is shown in Fig. 2.4. Optical components (collectively referred to as the optics train) included a beam collimator, two polarization axis rotators, a pair of beam splitters (prism type), two Bragg cells, beam steering wedges (for fine tuning the alignment), a single photodetector, and a beam expansion unit with a 2.27 expansion ratio. The beam expander reduces the measuring volume length by five times and the diameter by 2.27 times and improves the signal-to-noise ratio by five times. Following the optics train a pair of mirrors project the laser beams through a 250 mm f/4 lens. This gives a measuring volume with a length of 1.26 mm, a diameter of only 0.089 mm, and a fringe spacing of 4.5 μm. Signals are collected in backscatter mode, with the transmission optics also serving as the receiving optics. This greatly simplifies traversing the measuring probe volume since the trasmission and reception optics necessarilly move in unison. However, because backscattered light is nearly 100 times weaker than forward scattered light, seeding the flow (even water) was necessary. A small amount of silicon carbide powder was added to the water. Silicon carbide particles have an irregular shape with a mean diameter of 1.5 μm, a density of 3.2 gm/cm^3 and a refractive index of 2.65. Re-seeding in necessary roughly every 12 hours (whenever the data rate drops below 200 particles/second) as the particles gradually sink to the bottom of the setteling chamber.

Features of the TSI velocimeter taht are not common to the DISA system include,

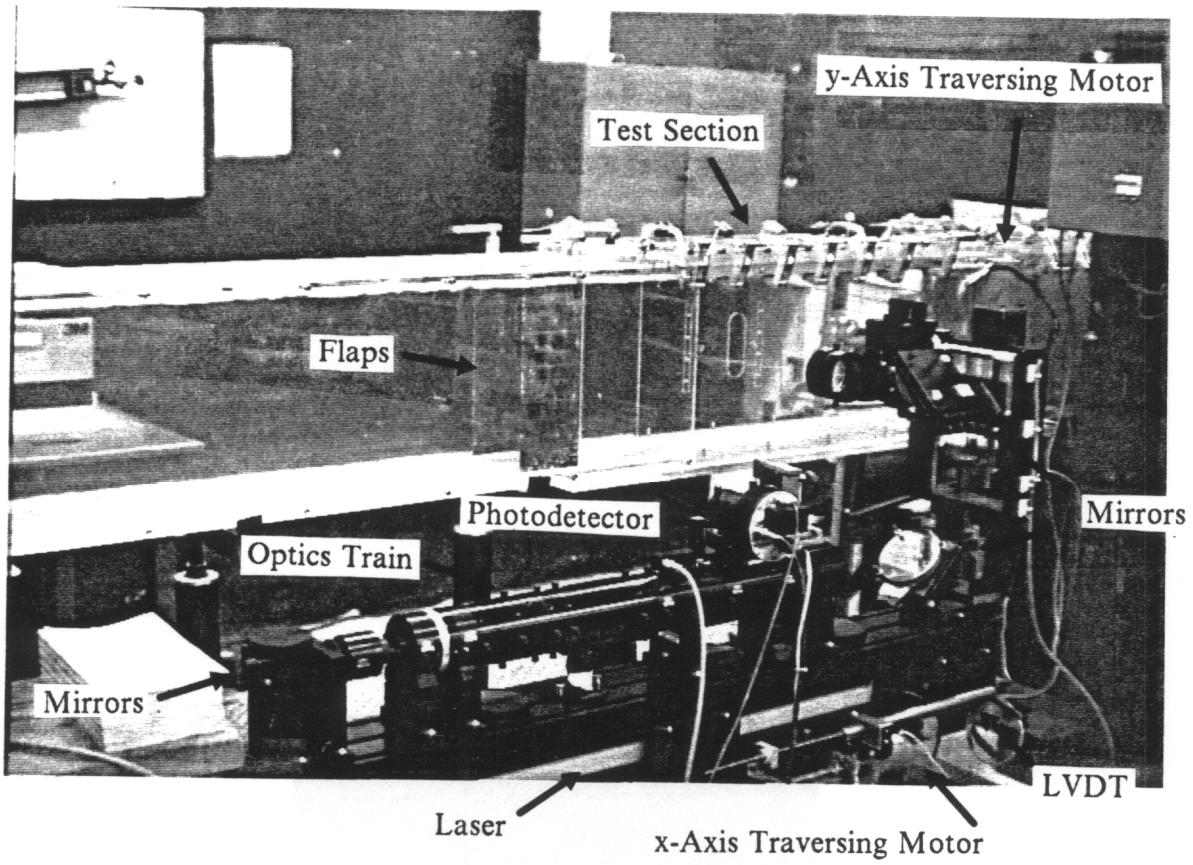

Figure 2.4. The TSI laser Doppler velocimeter.

1. The TSI system measures two mutually orthogonal velocity components,
2. Bragg cells are included to allow the measure of flow reversals,
3. The measurement volume can be automatically traversed over a predefined grid,
4. The optical components can rotate in unison,
5. Counter type signal processors are used, and
6. The scattered light is received in backscatter mode.

The significance of each item is discussed below.

Items 1. and 2. must be combined because the Bragg cells make two-component measurements possible with this particular velocimeter. Usually, multi-colored beams are used in multi-component LDV work. Individual signals then are separated with color (optical) filters. The system used here employs a single color laser and frequency shifting linked with *electronic* filtering to separate the scattered light signals. The laser beam from a 15 mW He-Ne Spectra Physics laser is split into three equal intensity beams. Two of the beams are frequency shifted by the Bragg cells; one beam is shifted by 40 MHz and the other by 60 MHz. The three beams are arranged to form the vertices of a 45°, 45°, 90° triangle as is shown in Fig. 2.5. Each beam pair is sensitive to a component of the velocity, however, only two are linearly independent. The two components measured are orthogonal to one another and inclined by $\pm$ 45°, respectively, to the direction of the free-stream. One velocity component is measured with the 40 MHz - 60 MHz beam pair and has a measured frequency of $f_D + 20$ MHz. The other component uses the 40 MHz - unshifted beam pair. It's frequency is $f_D + 40$ MHz. Both signals are received with the same photodetector and are electronically separated with band-pass filters. After separating the signals, the Bragg cell frequencies are subtracted by electronic down-mixing. Flow revesals are made detectable by adding an additional frequency shift to the laser beams. This additional frequency is typically selected to be

approximately twice the mean Doppler frequency of the flow, and is not down-mixed from the signals. The signal sent to the signal processors, then, has a frequency equal to f_D + shift frequency. A particle with zero velocity will produce a signal frequency equal to the shift frequency.

3. Automatic displacement of the measurement volume within a vertical plane is made possible with a pair of stepping motors. Stepping is controlled by the MINC-11 laboratory computer and each motor is equipped with a linear variable-differential transformer (LVDT) which acts in a feedback loop with the MINC to insure accurate positioning of the measurement volume to within 0.05 mm, (nearly half the measurement volume diameter).

Vertical displacement is done with mirrors. A fixed mirror reflects the beams vertically up a tower where they are turned through another 90° by a second mirror. The latter mirror projects the beams through the focusing lens and into the test section. The second mirror and the focusing lens are moved together in the vertical direction by the stepping motor. For horizontal displacement the entire optical train is displaced. The laser, optics, and vertical traversing tower are all mounted on a sliding table which moves parallel to the test section.

4. The train of optics is suspended between rotatable mounts. This feature becomes necessary when making measurements near a curved surface. Figure 2.6a illustrates how measurements near the leading edge of an airfoil model are facilitated by rotating the measurement volume. The beams are also slightly tilted towards the model surface (tilt angles are between 4° and 6°). Tilting the probe volume allows measurements to be made closer to the model surface (see Fig. 2.6b).

Lastly, item 5. Counting signal processors measure the time between cycles of the Doppler signal; inverse of this time is the Doppler frequency. Both a TSI model 1980 and a TSI model 1990 counter are employed; one for each velocity component. The two

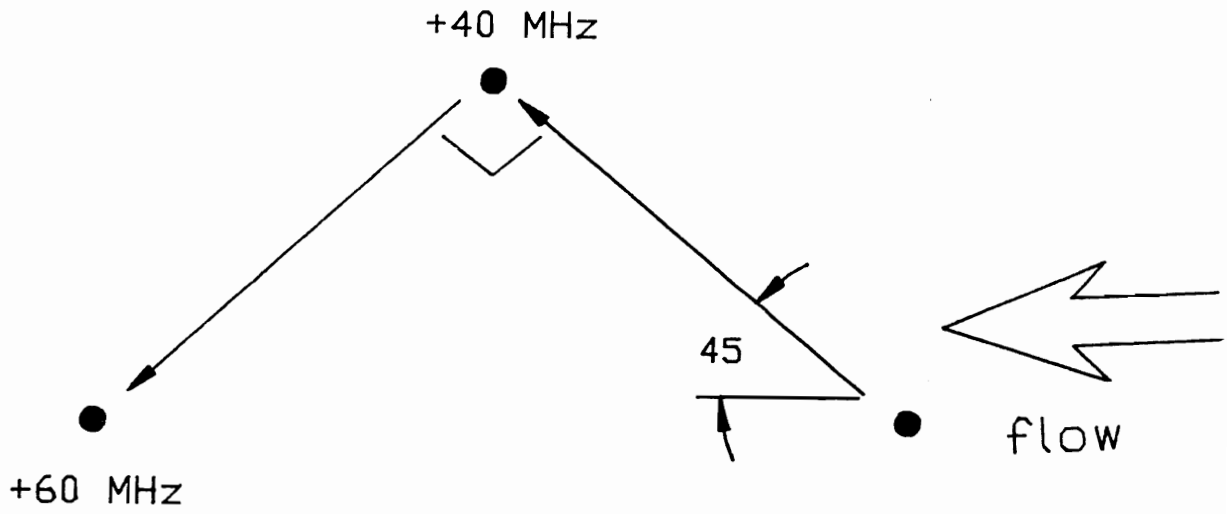

Figure 2.5. Beam arrangement for the TSI LDV.

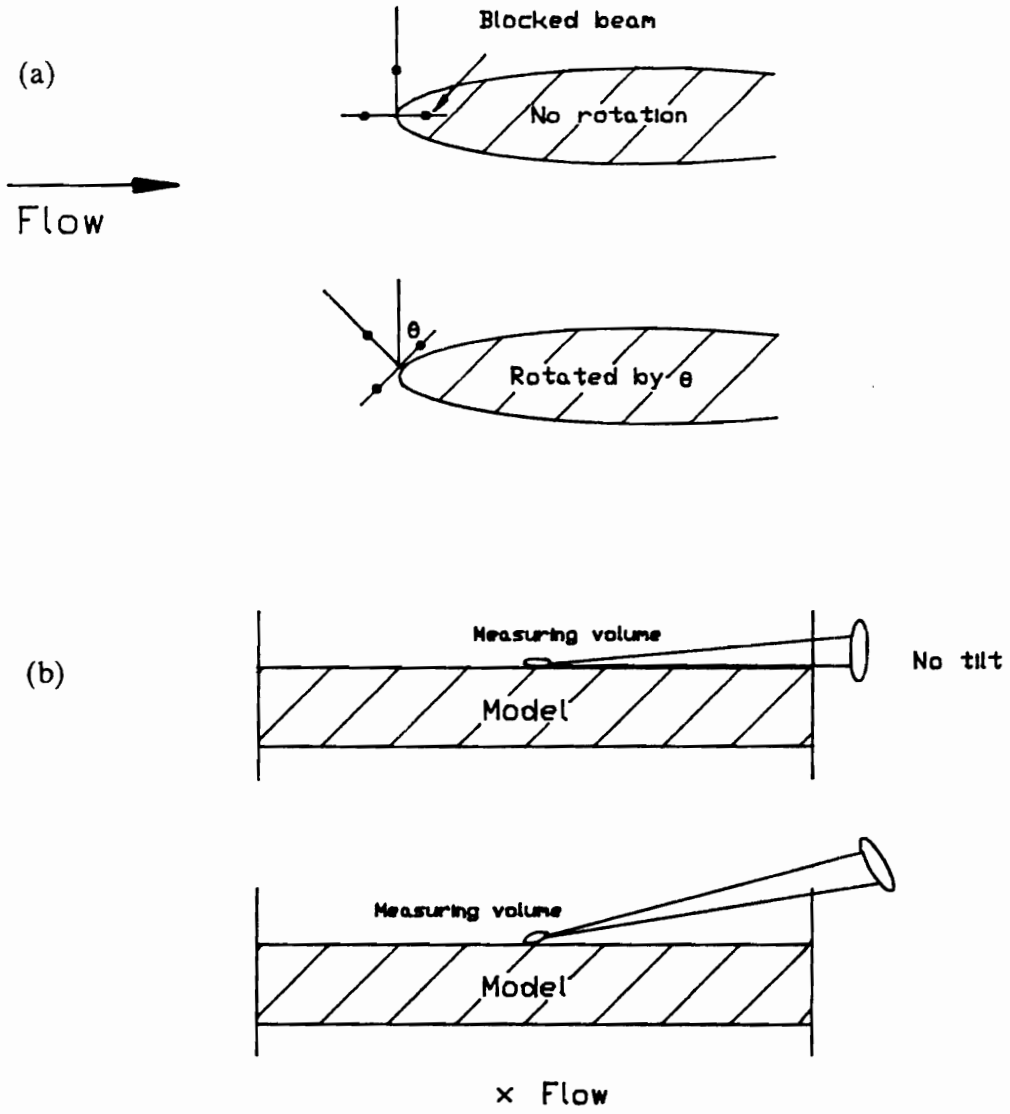

Figure 2.6. Effect of rotating and tilting the probe volume: (a) rotation (b) tilt

counters are essentially alike and are operated in the *N cycle* mode with N = 8. This means that the counter times eight cycles of the Doppler signal. To help eliminate spurious signals the counter also measures the time for four cycles and compares twice the four cycle time with the eight cycle time. If the two are within a certain percentage of one another (the comparison percentage is 7% here) then the signal is considered valid. Also, each cycle must exceed a preset amplitude limit. Counting begins with the first cycle to exceed this limit. A hysteresis limit is used in conjunction with the amplitude limit to avoid timing turbulent fluctuations rather than cycles of the signal.

The TSI counters have two analog outputs: one outputs a voltage which is proportional to the measured time. The other output is proportional to the Doppler frequency, and is simply the inverse of the time output. The MINC laboratory computer records the frequency output; the proportionality factor being determined by the front pannel settings of the counters.

2.5 Data Reduction

i) Velocity Reductions

The voltage output of the LDV signal processors is proportional to the Doppler frequency. A tabulated conversion factor is provided with the TSI counters. The factor is determined by front pannel adjustments on the counter and has units Hz/volt. The DISA frequency tracker associated with the free-stream velocity monitor, however, must be directly calibrated. Calibration was performed prior to each experimental run by processing the free-stream measurement with both the DISA tracker and a TSI counter. A calibration constant relating the DISA output voltage to the TSI output frequency for the same signal was defined as

$$DISA\ factor\ (Hz/volt) = \frac{TSI\ f_D}{DISA\ voltage} \quad .$$

The free-stream Doppler frequency, then, is defined as,

$$(f_D)_\infty = [DISA\ factor\ (Hz/volt)]\ [DISA\ voltage\ (volt)].$$

Velocity follows from Doppler frequency according to eqn. 2.2 (rearranged here);

$$V = (f_D - f_{shift})\ \frac{\lambda}{2 \sin K} \quad , \qquad [2.3]$$

where f_{shift} is the optional frequency shift for flow reversal detection; the DISA free-stream monitor has no frequency shift capabilities, therefore $f_{shift} = 0$. The velocity measurements at each instant were non-dimensionalized with the free-stream velocity measurement made at that same instant. The ratio of the fringe spacing, $d_f = \frac{\lambda}{2 \sin K}$, for the two systems was a constant equal to 1.06, therefore, the non-dimensional velocity was 1.06 times the ratio of the Doppler signal frequencies.

For purposes of calculating the vorticity, the velocity data are smoothed. The IMSL routine DCSSMH, which fits a natural cubic spline approximation to the data, is used for smoothing the velocity profiles. The unsmoothed velocity data are used in circulation and pressure calculations since the numerical integration involved in these calculations acts to smooth the results.

ii) Calculation of Vorticity and Circulation

By plotting isolevel contours of vorticity, we can track the path and evolution of vorticies in the wake of the pitching airfoil and their interaction with the fixed airfoil. Vorticity is defined as the curl of the velocity vector;

$$\vec{\Omega} = \nabla \times \vec{V}.$$

For a two-dimensional flow only one component of the vorticity is non-zero, namely,

$$\Omega_z = \frac{\partial v}{\partial x} - \frac{\partial u}{\partial y} \quad ;$$

(henceforth, refered to simply as Ω). The two-dimensionality of the flow is discussed below in section 2.6(v).

Vorticity was calculated from the measurements by using finite-difference formulas to evaluate the velocity derivatives. Two and three point difference formulas were employed, depending on the step size between measurement stations. For example, if the x-step size of the measurements was twice the y-step size ($\Delta x = 2\Delta y$), a two point formula was used for the x-derivative and a three point formula for the y-derivative;

$$\Omega(x,y,t) = \frac{v(x+\Delta x, y, t) - v(x,y,t)}{\Delta x} - \frac{u(x, y+\Delta y, t) - u(x, y-\Delta y, t)}{2\Delta y}. \qquad [2.4]$$

This ratio of step sizes is typical for much of the data presented in this text.

Some of the measurements in the wake of the oscillating airfoil were made along single columns in space. Velocity time records made along a single column (or survey line) can be utilized to construct an instantaneous spacial velocity or vorticity field by assuming that the vortices convect downstream with a constant velocity, U_d, in a "frozen" pattern. In this situation, an observation made at time t_2 and a distance $U_d \Delta t$ downstream of the measurement station would be equivalent to an observation made at the measurement station and time $t_1 = t_2 - \Delta t$ A velocity vector field constructed by this method is displayed in Fig. 2.7. This field is essentially the time record in reverse

order with the spacing between columns equal to $U_d \Delta t$. When calculating vorticity for this type of measurements the x-derivative is evaluated as

$$\frac{\partial v}{\partial x} \cong \frac{v(y,t) - v(y,t+\Delta t)}{U_d \Delta t}$$

where again, U_d is the drift velocity of the vortices.

An extention of the frozen vorticity assumption, which allows for local distortions of the vortices, is introduced here. Velocity measurements are made along a closely spaced pair of survey lines, and the vorticity time record is evaluated according to eqn. 2.4. The vorticity field is then constructed from the time record by assuming that, over short distances, the vorticity propagates with the local velocity. The pair of survey lines is used to "open a window" in the flow. A whole region of the flow can be defined with relatively few measurements by using several windows. The validity of the method is demonstraited in Fig. 2.8; an instantaneous vorticity field calculated from measurements on a 27x41 grid is compared with the vorticity field constructed via the window method using only 8 of the 27 survey lines. The location and strength of the vortex is in good agreement.

Circulation is calculated either

by the line integral

$$\Gamma = \oint \vec{V} \cdot \vec{dl} \ , \qquad [2.5]$$

or by the area integral of the vorticity,

$$\Gamma = \int_A \Omega \, dA \ .$$

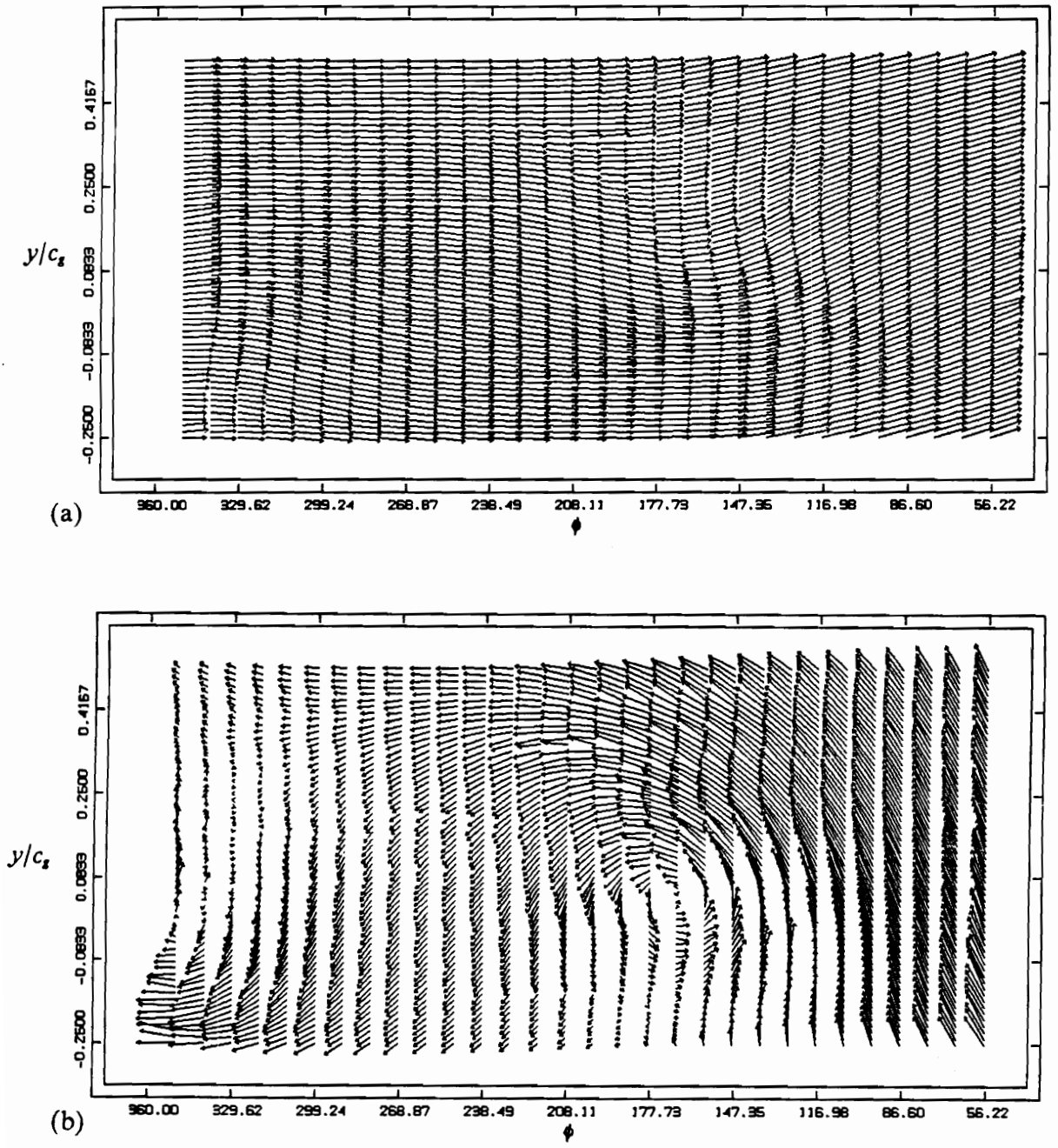

Figure 2.7. A 2-D velocity vector field constructed from a 1-D time record: (a) Total velocity, $\vec{V}$ (b) $\vec{V} - U_d$

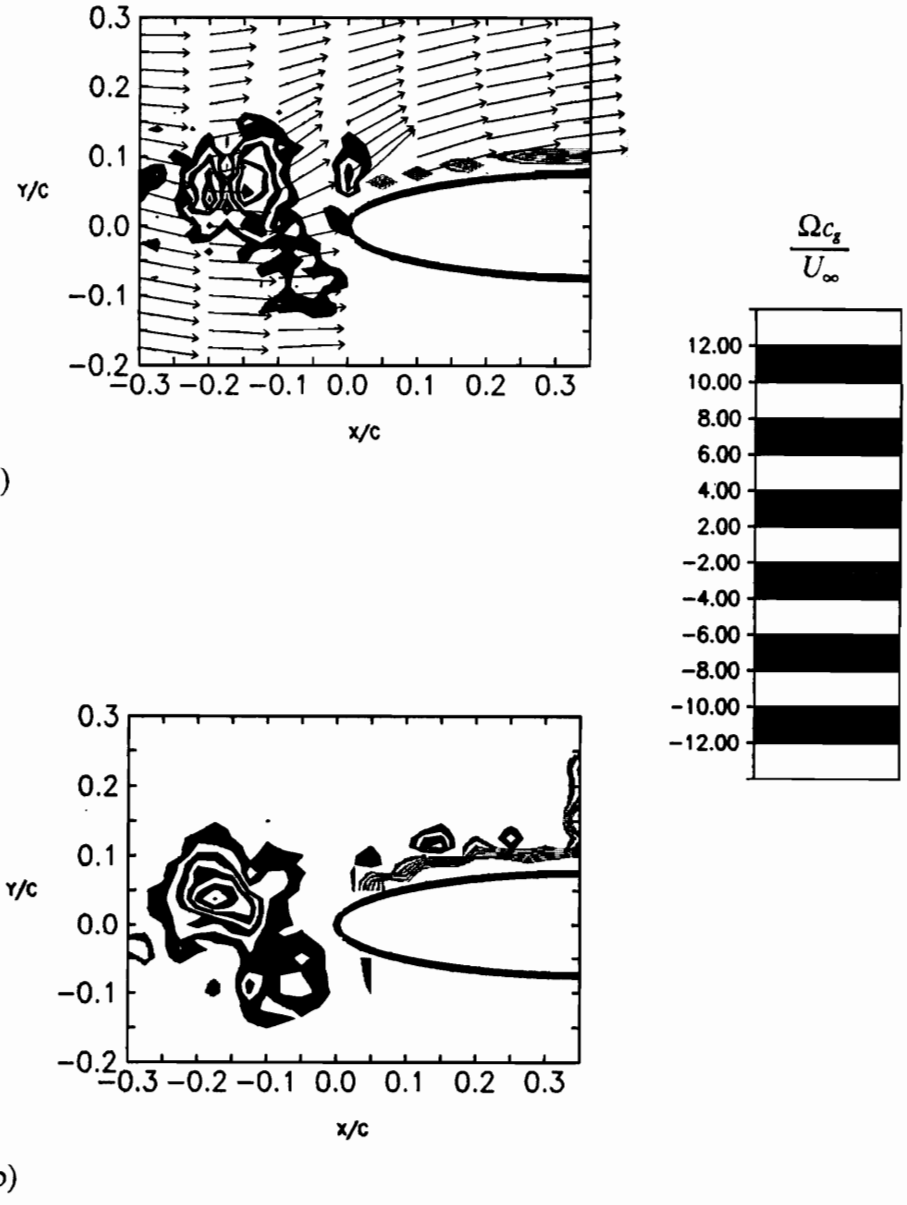

Figure 2.8. Illustration of the validity of the window method: (a) Vorticity contours from a 27x41 grid of measurements
(b) Window method vorticity field constructed from 8 of the columns.

The line integral is evaluated by repeated application of the trapazoid rule, and is performed on either circular paths or paths of constant vorticity. Integration proceedes in the counter-clockwise direction, so that a vortex with counter-clockwise rotation has positive circulation. The area integral is evaluated by summing the vorticity multiplied with the incremental area of the measurement grid.

iii) Calculation of Pressure

A major concern in the study of the airfoil-vortex interaction is the effect of the vortex on the loads experenced by the airfoil. Unsteady surface pressures on the model are evaluated by integrating the Navier-Stokes equations;

$$\begin{aligned} \frac{\partial p}{\partial x} &= \mu \nabla^2 u - \rho \left(\frac{\partial u}{\partial t} + u \frac{\partial u}{\partial x} + v \frac{\partial u}{\partial y} \right) \\ \frac{\partial p}{\partial y} &= \mu \nabla^2 v - \rho \left(\frac{\partial v}{\partial t} + u \frac{\partial v}{\partial x} + v \frac{\partial v}{\partial y} \right) . \end{aligned} \qquad [2.6]$$

The density and viscosity of the fluid are μ and ρ, respectively. The right-hand-side of each equation is evaluated using the measured velocities and the resulting pressure gradients are integrated along x- and y-coordinate lines;

$$p(x,y,t) = p_\infty + \int \left(\frac{\partial p}{\partial x} \, dx + \frac{\partial p}{\partial y} \, dy \right) . \qquad [2.7]$$

The assumption is made that the pressure equals p_∞ at the measurement location farthest upstream and above the airfoil. The pressures are presented in terms of a non-dimensional coefficient of pressure;

$$C_p = \frac{(p - p_\infty)}{\frac{1}{2}\rho U_\infty^2} \quad .$$

2.6 Uncertainty Analysis

i) Introduction

Any experimentally obtained quantity must necessarily be qualified by an estimation of its uncertainty. An experimental uncertainty can be classified as one of two types: systematic or random. Systematic uncertainties are predictable biases introduced by the experimental apparatus. Random uncertainties, on the other hand, are due to spurious signals in the system (electronic noise, vibrations, etc.), and the natural randomness, or turbulence, of the quantity being measured. A precision limit (standard deviation, for example) can be placed on a measured quantity to indicate the degree of random uncertainty in the measurement. The uncertainty of a value calculated from measured quantities must also be considered. Let the result R be a function of the n measured quantities $x_1, x_2, \ldots, x_n$, with associated uncertainties $w_1, w_2, \ldots, w_n$. Thus, R = R($x_1, x_2, \ldots, x_n$). The uncertainty of the result is given as (Holman, 1984)

$$w_R = \left[\left(\frac{\partial R}{\partial x_1} w_1 \right)^2 + \left(\frac{\partial R}{\partial x_2} w_2 \right)^2 + \cdots + \left(\frac{\partial R}{\partial x_n} w_n \right)^2 \right]^{1/2} . \qquad [2.8]$$

The remainder of this chapter is a discussion of the uncertainties on the measurements and on the quantities calculated from the measurements.

ii) Systematic Uncertainties

As was discussed in the preceeding sections, the laser-Doppler velocimeter is sensitive to the velocity component given by,

$$V = f_D \frac{\lambda}{2 \sin \kappa} \quad , \qquad [2.9]$$

where f_D is the Doppler frequency, λ is the wavelength of the laser light, and κ is half the beam crossing angle (refer to Figure 2.3 on page 20). Since the wavelength of the light emitted by a laser is precisely known, the influence of its uncertainty can be ignored. Therefore, the systematic uncertainty inherent in a velocity measurement is due to inaccurate beam alignment and the systematic uncertainty of the measured Doppler frequency.

First, let us consider the beam alignment. The beam crossing angle was determined by measuring the focal length of the lens and the distance between the laser beams at the plane of the focusing lens. An alignment mask (provided by TSI) was employed to measure the beam separation. These distances were measured with an estimated accuracy of half a beam diameter, or 0.5 mm. Thus the crossing angle κ was determined to within 0.1°, or 2.5% of κ. The beam rotation and tilt angles, θ and ϕ (refer to Figure 2.6 on page 27), were measured with similar accuracy. The accuracy of the tilt angle is of less concern though, because ϕ was a small angle (between +4° and -6°) and entered the velocity calculations through a cosine term.

Next, the systematic uncertainty of the Doppler frequency, introduced through the signal processors and computer analog-to-digital converter, was estimated by sampling a signal of known frequency. A sine wave signal was produced with a function generator (Hewlett Packard HP 3311A) and input to the TSI counters. As a check on the signal generator, the signal was also examined with a frequency counter (HP 5381A) and a

dynamic signal analyzer (HP 3562A). The frequency measured by these two devices was within 0.5% of one another. A signal frequency of 130 kHz, equivalent to the mean Doppler frequency typical of the experiments, was selected and the adjustments of the TSI counters were set as in the experiments. Adjusments included the input signal filter bandwidths, the timer range and the timer comparison. The analog frequency output of the counters was sent to the MINC a/d board, which was sampled for three seconds at a rate of 100 Hz; a typical sampling rate in the experiments. From these samples, the mean frequency and its standard deviation were computed as follows;

$$\bar{f} = \frac{1}{N} \sum_{n=1}^{N} f_n$$

$$\sigma = \sqrt{\frac{1}{1-N} \sum_{n=1}^{N} (f_n - \bar{f})^2} \quad ,$$

where N = 300 was the number of samples. The mean frequency for each signal processor differed by less than 0.1% of the source frequency as determined by the HP counter, and the sample standard deviation was consistantly around 0.05% of the mean. This test was repeated with a source signal of 30 kHz and 100 kHz. Sample standard deviation was again around 0.05% of the mean, but the mean differed by 0.8% of the source frequency for the lower frequencies. Using $w_f = 0.01\bar{f}_D$ as a worst case for the uncertainty on the frequency, $w_\kappa = 0.025\kappa$ for the beam alignment uncertainty and eqn. 2.9 for the velocity gives, from eqn. 2.8, an uncertainty of $w_r = 0.027U_\infty$, where we have taken $\bar{f}_D \frac{\lambda}{2 \sin \kappa} = U_\infty$.

With the instrumentation available, the analysis described above could not be performed on the DISA frequency tracker. Instead, a comparison was made between the DISA tracker and the TSI counter by processing the photomultiplier signal from the

free-stream monitor LDV with both instruments. Figure 2.9 shows the normalized velocity probability histogram for each processor along with the Gaussian distribution having the same mean velocity and standard deviation as the DISA tracker data. A sample velocity time record is also shown. These data were taken for a steady mean free-stream velocity of 12.56 cm/s ($f_D = 30$kHz). The two signal processors give nearly identical results, and the velocity histograms are Gaussian, indicating a statistically normal random variation in the free-stream velocity.

iii) Random Uncertainties

The only random errors in the data which can be estimated are attributable to turbulence present in the flow and to any lack of repeatability of the flow in the wake of the oscillating airfoil. Figure 2.10 shows the turbulence intensity profiles across the test section span for steady flow with a mean free-stream velocity of 12.5 cm/s. The measurements were made 127 mm downstream from the leading edge of the false wall and mid-way between the tunnel floor and ceiling. The profiles extend from the false wall to nearly one quarter of the span of the test section. Turbulence levels in the center of the test section were typically 2% of the mean free-stream velocity for steady flow at 12.5 cm/s, and increased to nearly 3% for a free-stream velocity of 25 cm/s. Turbulence levels were, however, dependent upon the cleanliness of the water tunnel. After a thorough cleaning of the settling chamber and honeycombs, turbulence levels in the test section dropped to 1.9% for $U_\infty = 25$cm/s.

Flow quality was better at the free-stream velocity monitoring location, 14 cm after the contraction. Here, turbulence intensities ranged from 0.5% to 1.3% of the mean free-stream velocity for all velocities tested. To verify that blockage due to the motion of the vortex generator did not affect the free-stream velocity, measurements were made

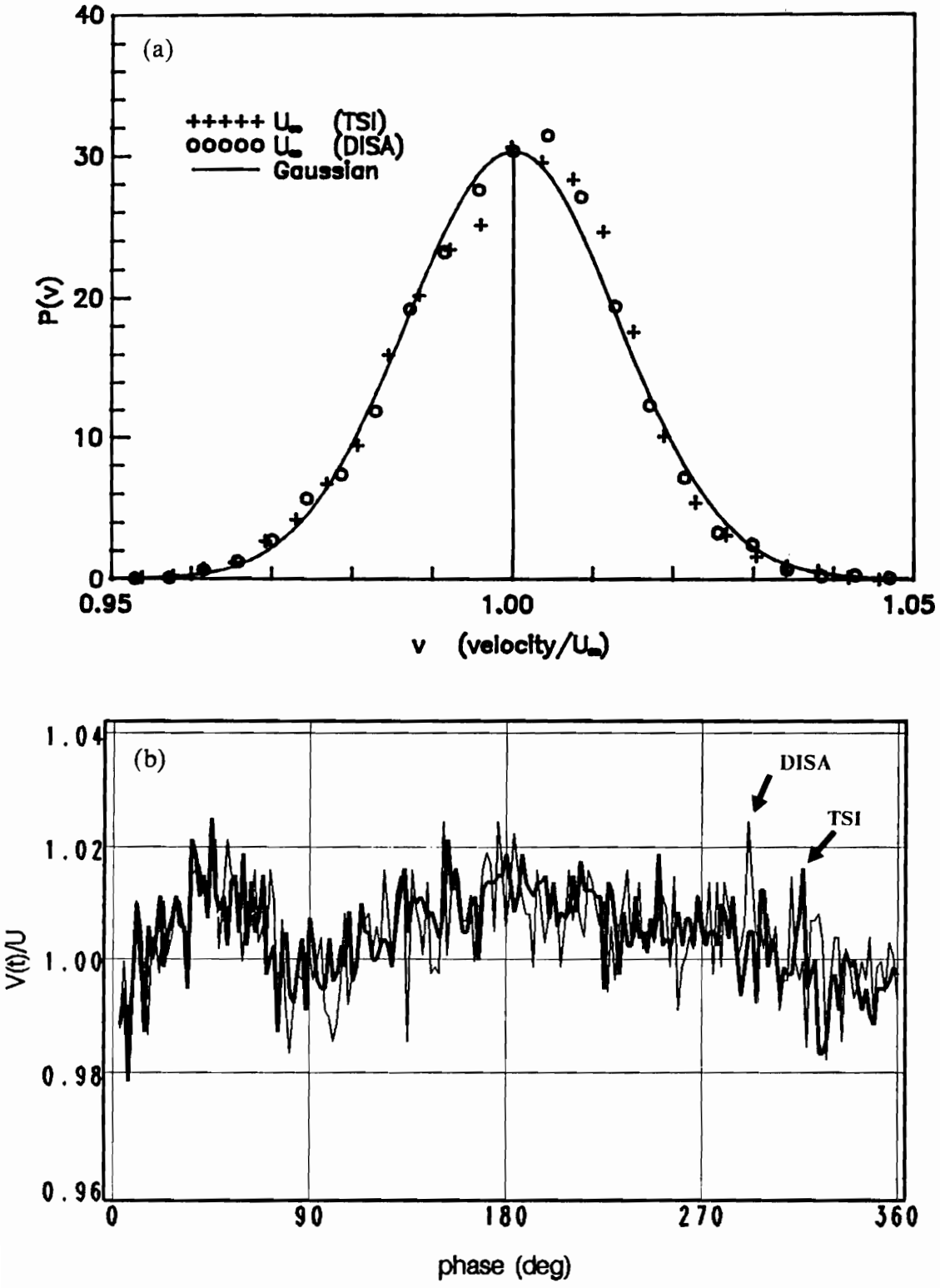

Figure 2.9. A comparison between the DISA and TSI signal processors for steady flow: (a) Normalized velocity probability histogram (b) Velocity time record.

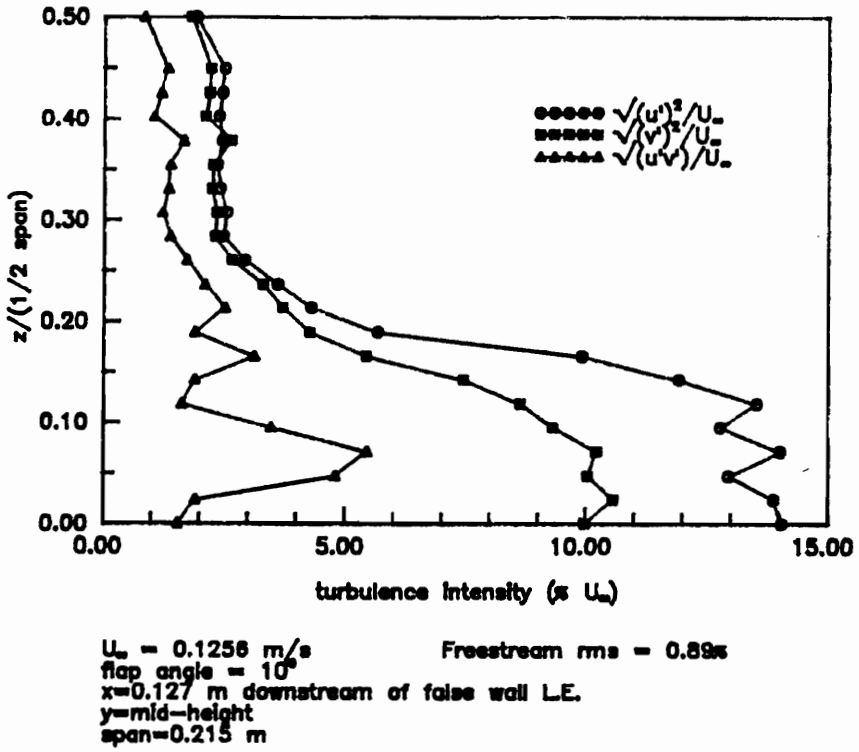

Figure 2.10. ESM water tunnel turbulence intensity profiles: Steady flow, U_∞ = 12.5 cm/s, x = 127 mm downstream from false wall leading edge, y = mid-height of test section.

with the vortex generator switched off, as well as in operation with an oscillation period of 1.24 seconds (reduced frequency k = 2.05). In both cases 30 consecutive velocity time records, each 1.24 seconds long and consisting of 200 samples, were recorded. The velocity probability histograms and time records proved to be nearly identical (well within the range of variability expected form the quality of the flow).

Velocity measurements performed in the unsteady wake of the oscillating airfoil were *ensemble averaged* over many oscillations. Ensemble averaging is discussed in the next section. The effectiveness of ensemble averaging in reducing the influence of random fluctuations on the freestream measurements is demonstrated in Fig. 2.11. The normalized velocity histogram for the ensemble averaged data is compared with that of the same data with no averaging (also shown in -- Figure id 'stun' unknown --). The standard deviation of the free-stream velocity measurements dropped from 1.3% to 0.3% as a result of the ensemble averaging.

iv) Ensemble Averaging and Flow Repeatability

Ensemble averaging is a method for removing random fluctuations from periodic data. In a periodic flow, each sample corresponds to a particular phase in the period. The average value of a measurement repeatedly made at a given phase is called the ensemble average. The ensemble average is sometimes called the phase-average or the conditional-average. The oscillating airfoil provides the periodicity to the flow. Velocity measurements were made during M periods of the pitching motion. Each period contained N samples separated in time by the sample interval $\Delta t = T/N$, where T is the period of oscillation. The sample interval is the time between analog-to-digital convertions performed by the laboratory computer. Every Δt seconds, the computer converts the voltage output of the signal processor to a digital value. The seeding particles,

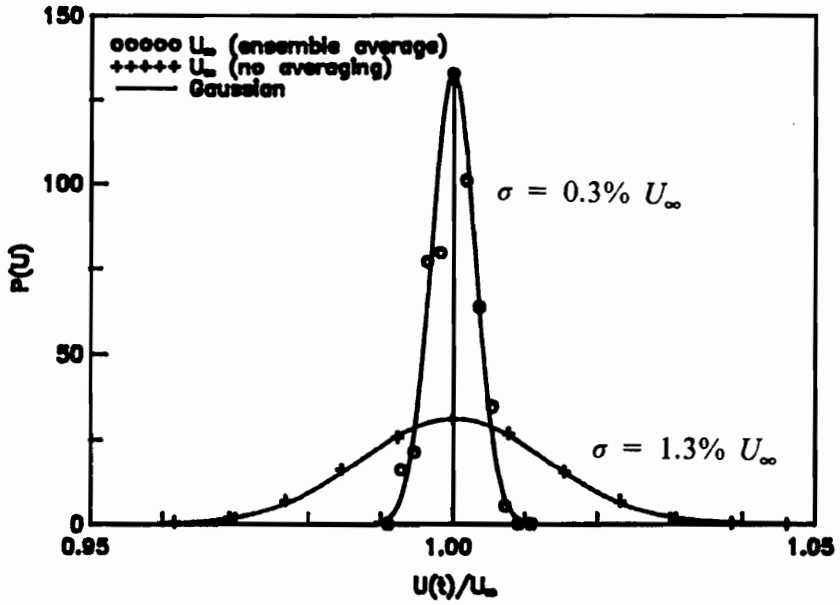

Figure 2.11. **The effect of ensemble averaging on the velocity statistics:** Normalized velocity histograms before and after averaging.

however, pass through the LDV measuring volume at random intervals. The laboratory computer employes a sample-and-hold technique in which, if no new signal is output by the LDV signal processor, the last signal is repeatedly sampled every Δt seconds. For low data rates (or high sample rates), this process results in a choppy representation of the periodic fluctuation. By repeating the measurements over several periods and ensemble averaging, the time record is filled in and random fluctuation are averaged out. This is illustrated in Fig. 2.12, which compares a single velocity time record with the ensemble averaged time record constructed with thirty individual time records.

Ideally, for each cycle of the vortex gererator's motion, an identical velocity field is created, however, experiments are rarely ideal. There are variations in the velocity from cycle to cycle. To estimate the repeatability of the flow in the wake of the oscillating airfoil the standard deviation of the measured veloctiy components was evaluated for each phase of the pitching motion. This phase-standard-deviation or phase-rms is defined as,

$$\sigma(\phi) = \sqrt{\frac{1}{1-M}\sum_{m=1}^{M}(U_m(\phi) - \overline{U}(\phi))^2} \quad ,$$

where the phase $\phi = \frac{t}{T}\ 360°$ is a non-dimensional time with 360° equal to one period of oscillation, M is the total number of time records, and $\overline{U}(\phi)$ is the velocity for a given phase averaged over all M time records. The ensemble-averaged velocity components are presented along with their respective phase-rms in Fig. 2.13. Shown are the results obtained using five, fifteen and thirty time records (also compare with the single velocity time record shown in Figure 2.12 on page 45). The thirty records were consecutively recorded at the point $x/c_z = 2$, $y/c_z = 0.1$, which lay on the center line of the upper row of vortices (refer to Figure 3.3 on page 60 for the definition of the coordinate system).

The reduced frequency of the oscillating airfoil was equal to 2.05 and the average free-stream velocity was $U_\infty = 12.5$cm/s.

We see that as few as five records are sufficient to produce a reasonably smooth ensemble average and that, with the exception of certain phase angles, the phase-rms for five and thirty averages are quite similar. This means that with thirty time records we can accurately estimate the phase-wise velocity statistics; namely the ensemble-average velocity and phase-rms. The phase-rms is maximum around 90° and 270° of phase, when the change in the velocity gradient is maximum (i.e., when a vortex passes the measuring station), and averages 7% for the first component and 8.5% for the second component.

Typically, twenty to thirty velocity time records were measured. Time was a constraint in selecting the number of ensembles to employ. A survey line consisting of forty measurement stations required about two hours for completion when thirty time records were recorded. An order of magnitude increase in the number of records was required to improve the velocity statistics.

In addition to the period-to-period flow repeatability represented by the phase-rms in Fig. 2.13, the repeatability from moment-to-moment, and even from day-to-day, of the ensemble average must also be considered. Measurement survey lines, as stated above, required several hours to complete, while data sets consisting of tens of survey lines required days, or even weeks, to complete. To check the repeatability of the ensemble average, one ensemble average was evaluated using the first fifteen time records and another using the second fifteen out of the thirty represented in Fig. 2.13. This is equivelent to two ensemble averages made at the same point in space, with the second beginning immediately after the first ends. These are compared with one another in Fig. 2.14. The two averages differ from one another by as much as 10% at a phase of 90°

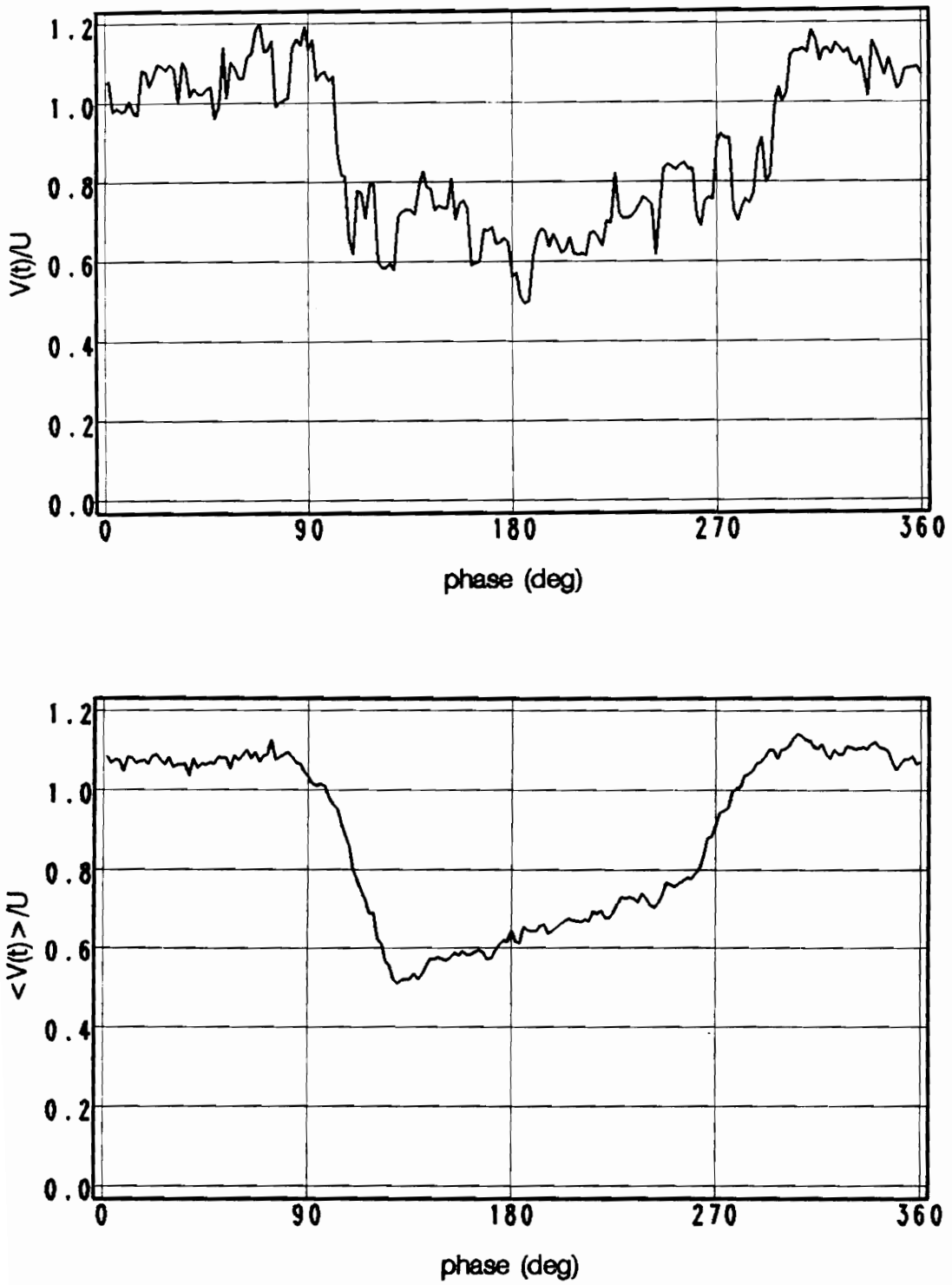

Figure 2.12. **Ensemble averaging:** (a) A single time record (b) Ensemble average of 30 time records $U_\infty = 12.5cm/s$, k = 2.05, $x/c_g = 2.0$, $y/c_g = 0.1$

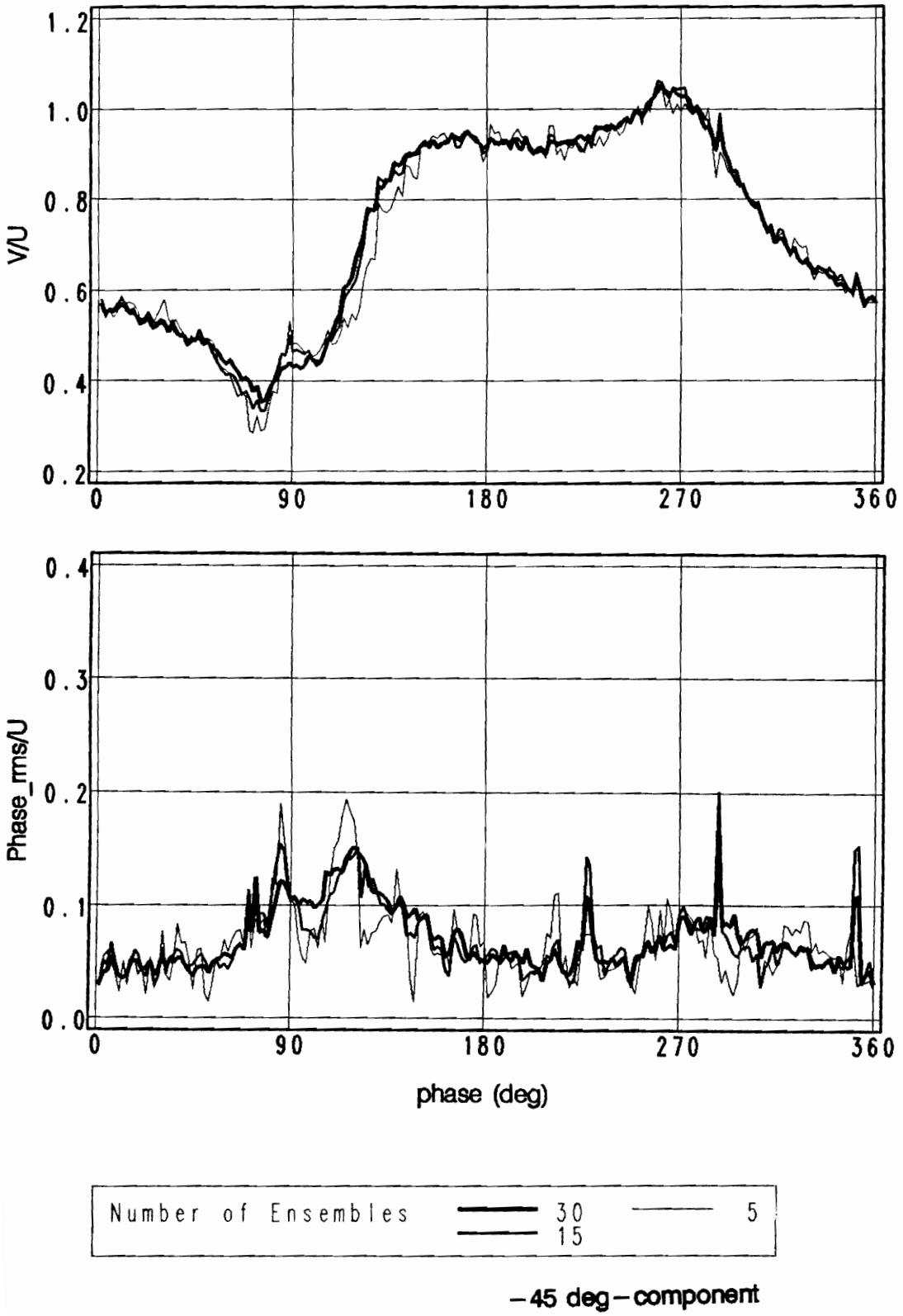

Figure 2.13. Ensemble averaged velocity and phase-rms for 5, 15 and 30 ensembles : $U_\infty = 12.5cm/s$, k = 2.05, $x/c_g = 2.0$, $y/c_g = 0.1$

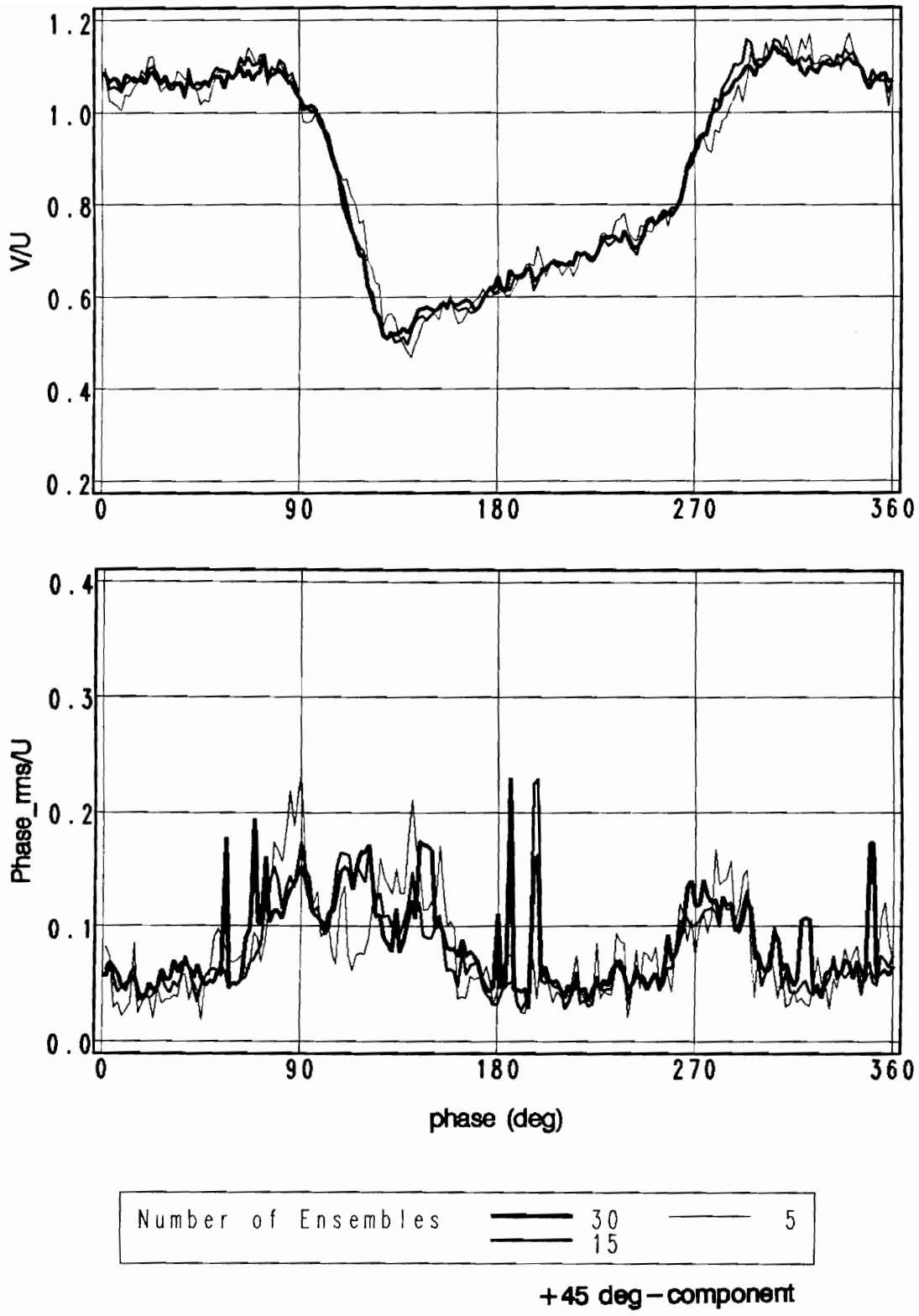

Figure 2.13 continued: $U_\infty = 12.5cm/s$, k = 2.05, $x/c_g = 2.0$, $y/c_g = 0.1$

and 270° (the points of maximum phase-rms). The average difference over the entire period is only -0.2% for the -45° velocity component and 0.6% for the +45° component.

The daily flow repeatability is next assessed. Velocity measurements were made on two consecutive days and at the same point in space, again, the point $x/c_s = 2.0$, $y/c_s = 0.1$, $z/c_s = 0.0$. The ensemble average of the +45° velocity component for each day is compared in Fig. 2.15. The maximum velocity difference is around 10% of the free-stream velocity, and the mean difference over the period is 2.1%. Since the water tunnel and data acquisition equipment were shut down for more than twelve hours between these measurements, Fig. 2.15 demonstrates the ability to reacquire the test parameters (Re and k) from day-to-day.

v) Flow Two-Dimensionality

A basic premise of this work is that the wake of the oscillating airfoil is two-dimensional. Since it was not possible to directly measure the third velocity component with the equipment available, a less direct method was employed to determine the two-dimensionality of the flow. Because a two-dimensional flow must be invarient in the third dimension (the span-wise or z-direction), a comparison of the velocity components measured at several span-wise locations provides a sufficient measure of the two-dimensionality. Measurements were made in the upper row of vortices ($x/c_s = 2.0$, $y/c_s = 0.1$) and at five different z-locations across the water tunnel span. The measurements cover a span of 5.08 cm, or $0.5c_s$ (or ¼ of the test-section span) and are centered about the tunnel center line. The ensemble averaged velocity time records (with M = 30) for the five locations are given in Fig. 2.16. With the exception of the $z/c_s = -0.25$ measurement, the velocity profiles are agreeably similar to one another, and even this disparate profile is within the expected daily variation of the ensemble average

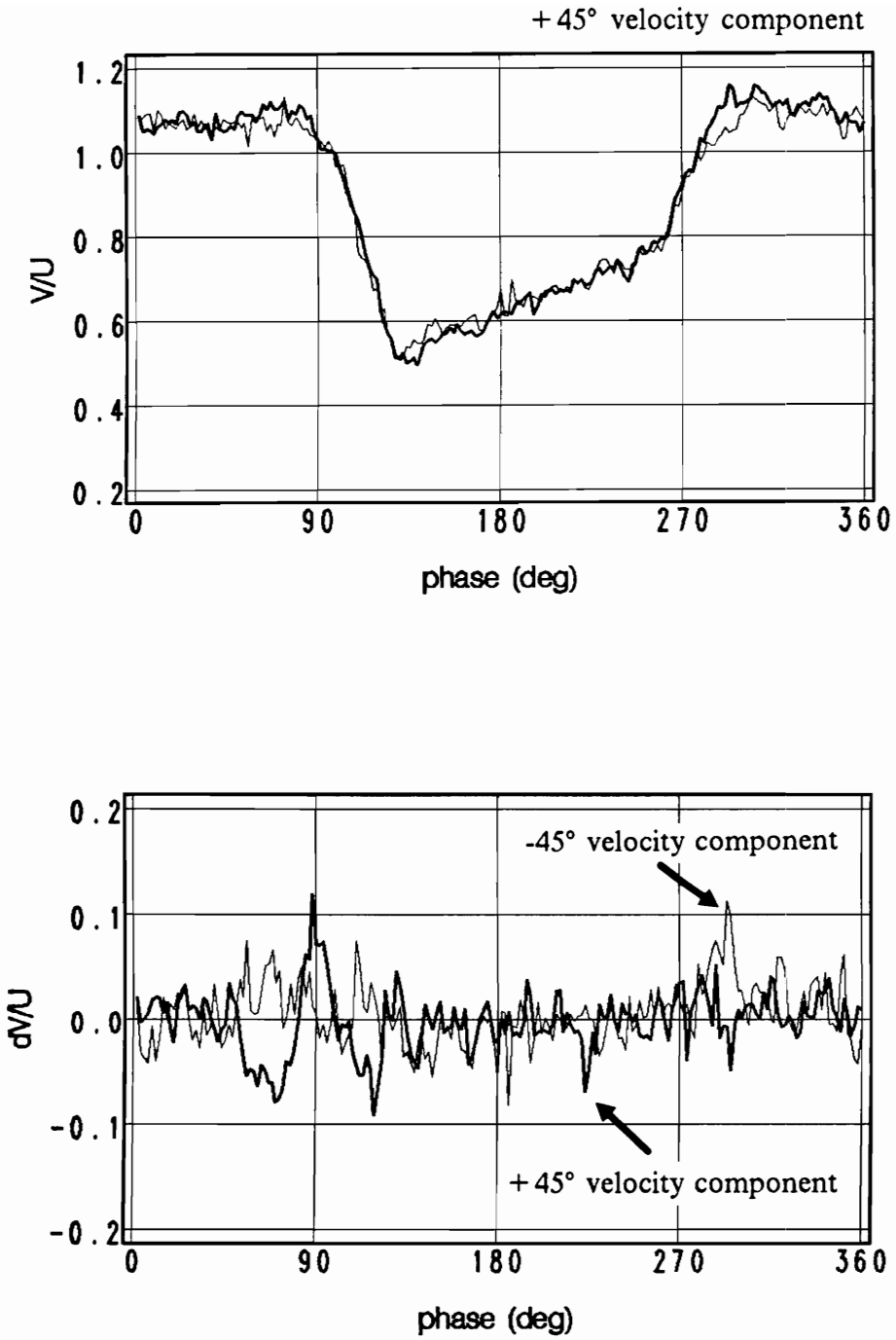

Figure 2.14. Repeatability of the ensemble averaged velocity : $U_\infty = 12.5cm/s$, k = 2.05, $x/c_g = 2.0$, $y/c_g = 0.1$

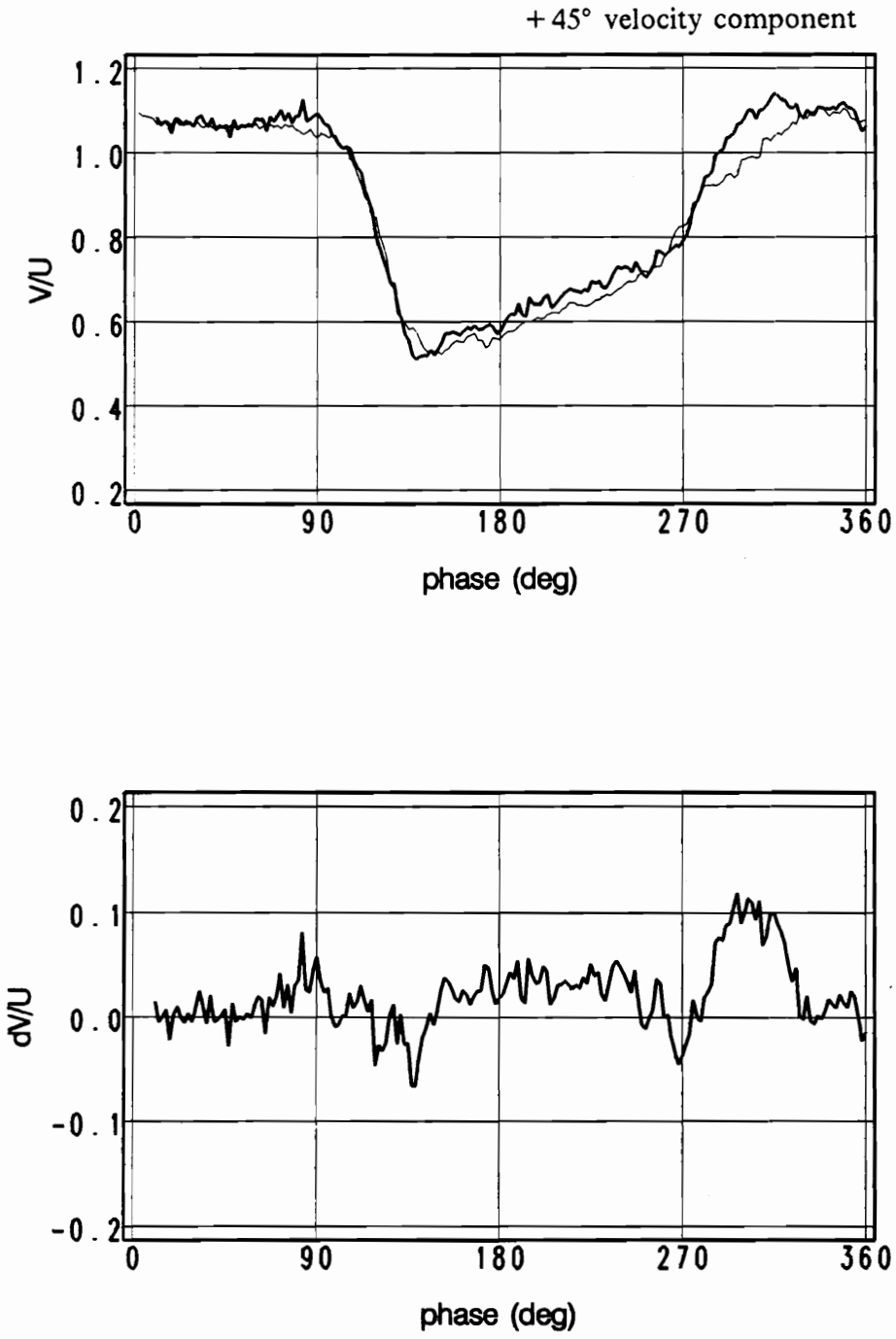

Figure 2.15. Day-to-day flow repeatability (ensemble averaged velocity): $U_\infty = 12.5cm/s$, k = 2.05, $x/c_g = 2.0$, $y/c_g = 0.1$

(refer to Figure 2.14 on page 49 and Figure 2.15 on page 50). The velocity difference between the center line (z/c = 0) and each measurement plane is shown in Fig. 2.17.

vi) Calculation Errors

Naturally, the use of finite-difference formulas in estimating derivatives introduces errors into the calculated results. These errors depend on the measurement grid size and the degree of "turbulence" present in the data. Here, tubulence indicates fluctuations of any kind. An estimation of this error was determined by evaluating the sufficiency of the continuity equation on a grid element (Imaichi and Ohmi, 1983). The error for the grid element at (i,j) is,

$$\varepsilon_{ij} = \left| \frac{(\partial u/\partial x)_{ij}\Delta x\,\Delta y + (\partial v/\partial y)_{ij}\Delta y\,\Delta x}{U_\infty \Delta y} \right| ,$$

where the grid step sizes are Δx and Δy. The error is given as a percentage of the inflow to the grid cell ($U_\infty \Delta y$). The distribution of the error for measurements in the wake of the oscillating airfoil is shown as a histogram in Fig. 2.18. The figure shows the distribution of error for measurements made two, three and four chordlengths downstream of the oscillating airfoil. We see in Fig. 2.18a that the error is less than 1% of $U_\infty \Delta y$ for over 45% of the grid cells. Figure 2.18b involves measurements made at twice the Reynolds number as those of Fig. 2.18a. The inability of the data to satisfy the continuity equation can be thought of as the error introduced when differentiating the velocity, and can be taken as the error introduced for any first order derivative of the velocity.

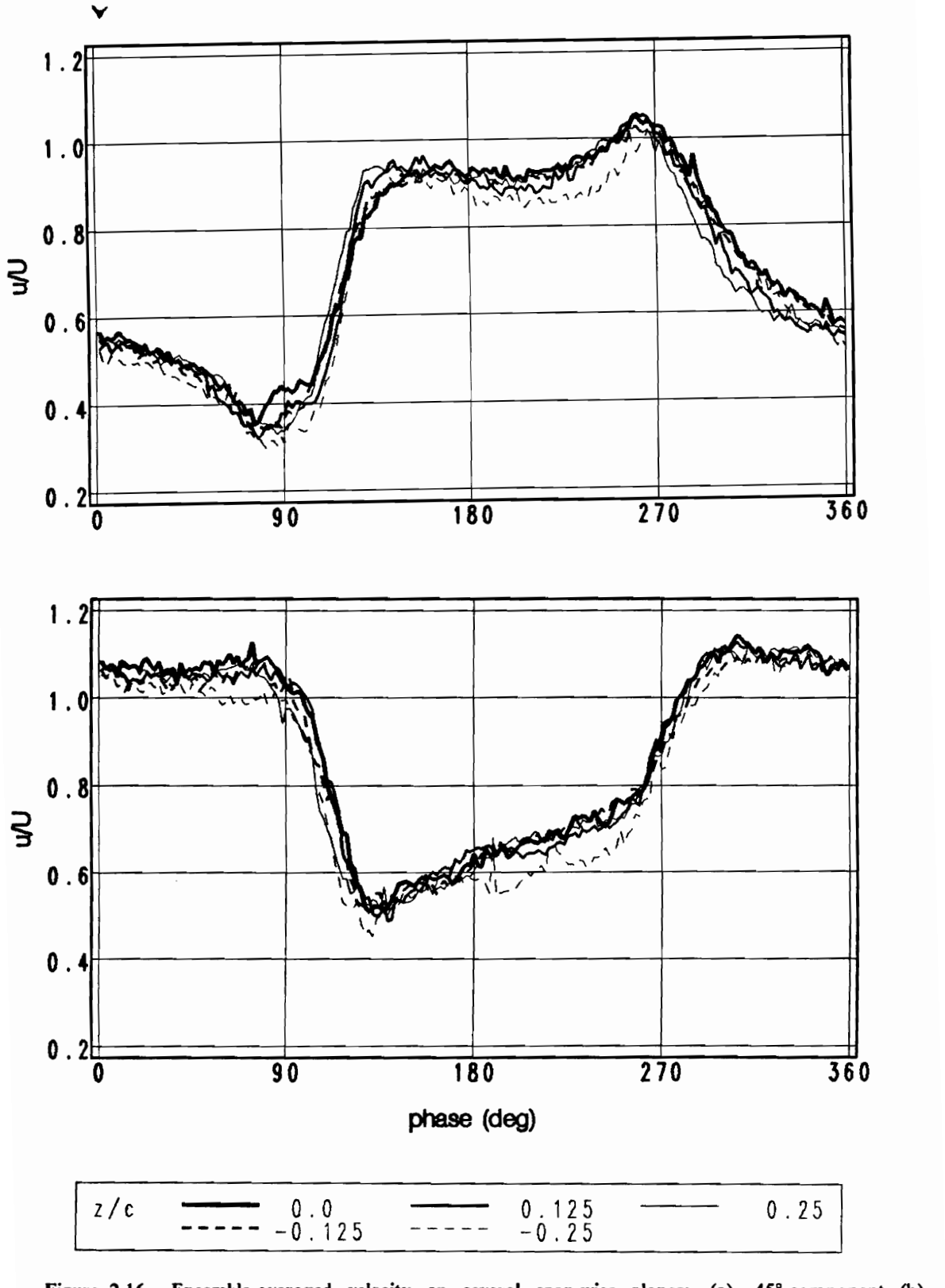

Figure 2.16. **Ensemble-averaged velocity on several span-wise planes:** (a) -45°-component (b) +45°-component : $x/c_g = 2, y/c_g = 0$

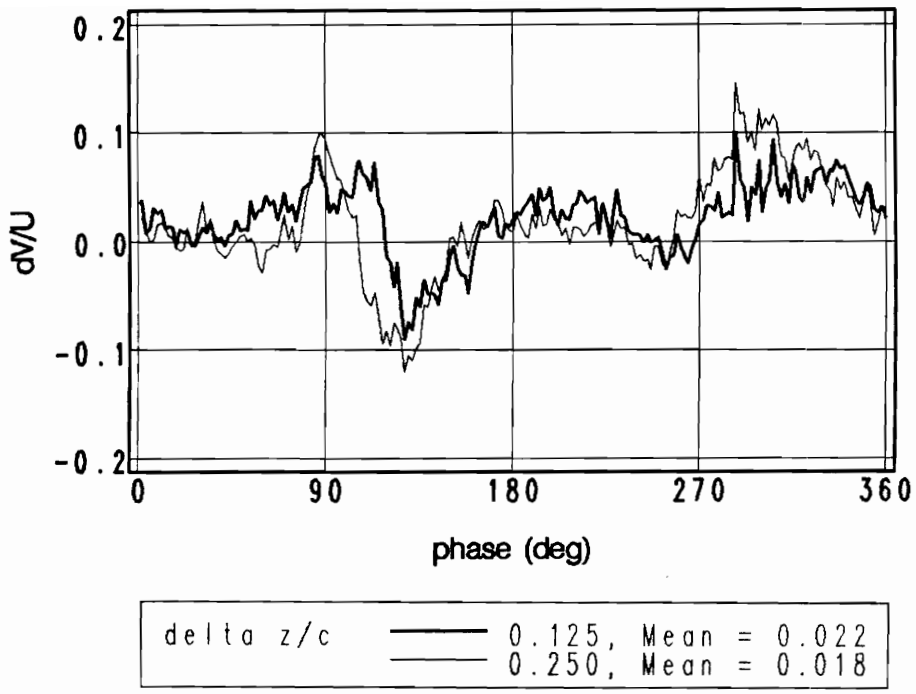

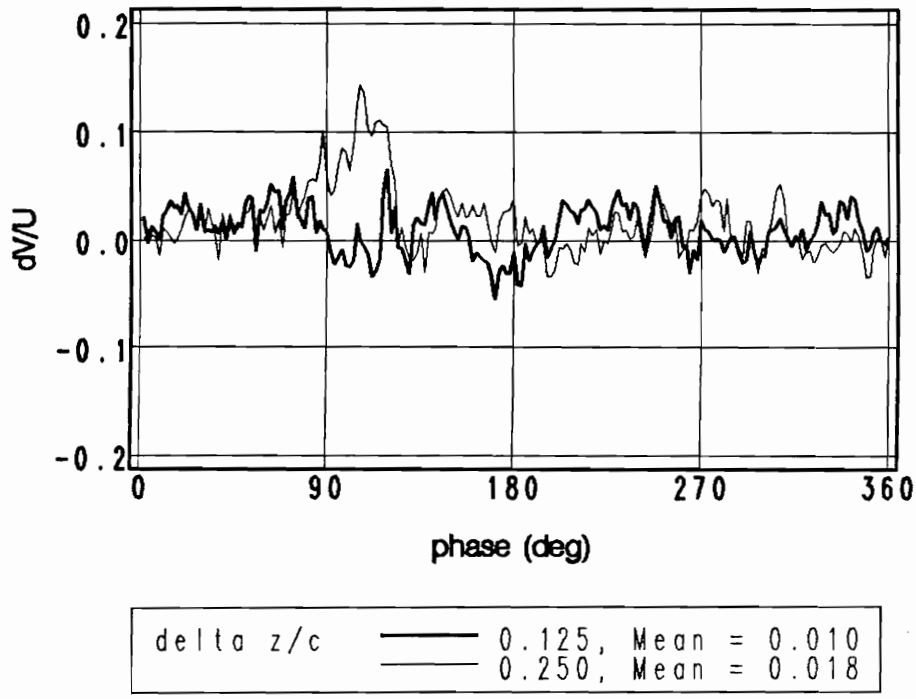

Figure 2.17. **Span-wise velocity variation in the wake of the oscillating airfoil:** (a) -45°-component (b) +45°-component : $x/c_g = 2, y/c_g = 0$

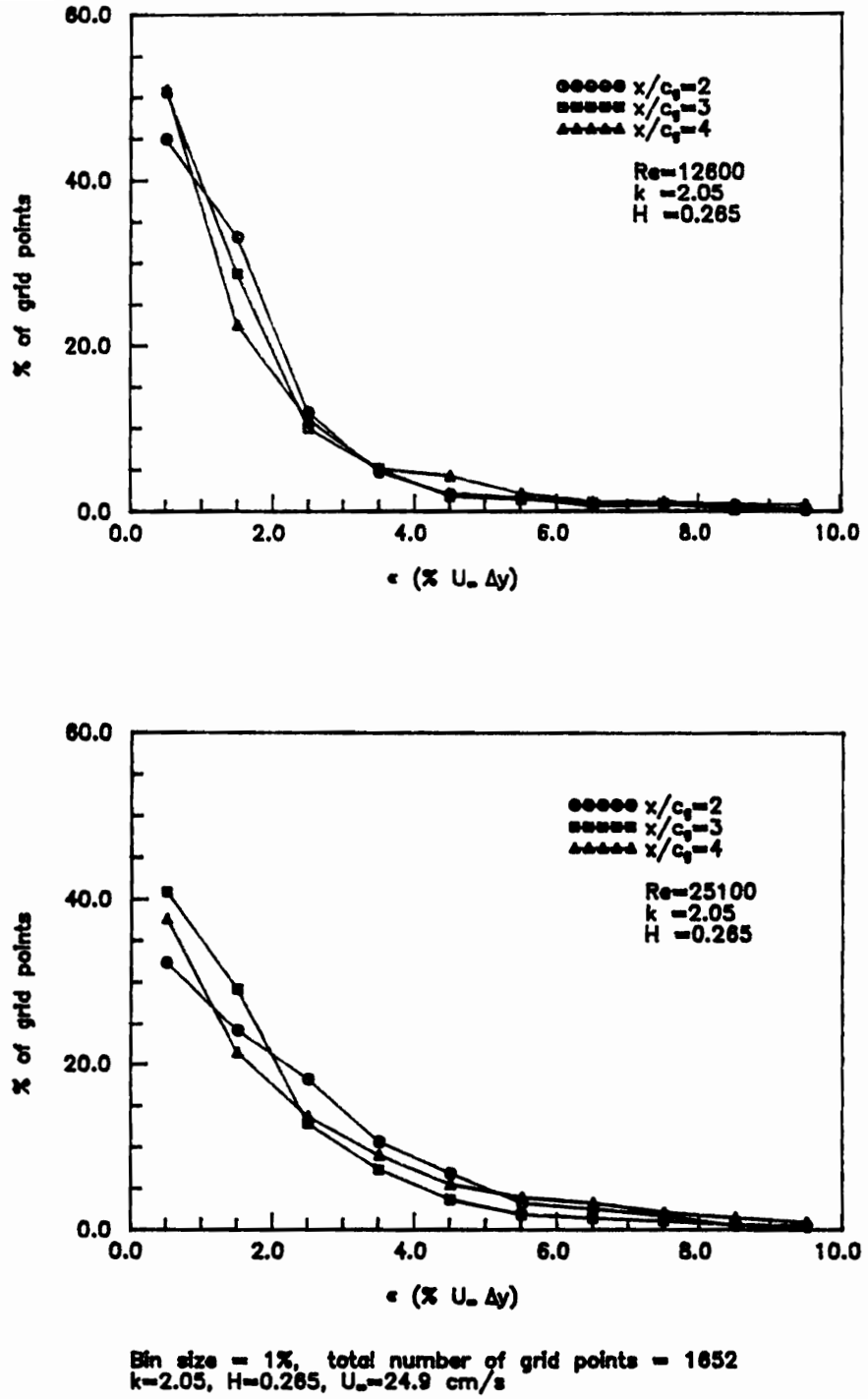

Figure 2.18. Distribution of estimated computational error (sufficiency of continuity)

Chapter 3

The Wake of an Oscillating Airfoil

3.1 Introduction

This and following chapters will present and discuss experimental results. Before investigating airfoil-vortex interaction, a thorough study of the vortical disturbance is warranted. To create the desired vortex disturbance, advantage is taken of the natural instability of free shear layers. Free shear layers are regions of high concentrations of vorticity which tend to "roll up" into large scale coherent vortical structures. A coherent structure is " ... a connected turbulent fluid mass with instantaneous phase-correlated vorticity over its spatial extent " (Hussain, 1986). The coherent structures formed in the wake of an oscillating airfoil are essentially two-dimensional vortices for which the axis of rotation is perpendicular to the direction of propagation.

Recall that the vortex generator is a NACA 0012 airfoil oscillating in pitch about its ¼-chord point. For moderate amplitudes, the boundary layers remain attached throughout the oscillating motion. Vorticity in the boundary layers is transfered, or *shed* , to the free shear layer from the airfoil's trailing edge. As the airfoil's trailing edge moves downward (α increasing), vorticity is shed from the lower surface of the trailing

edge. For a free-stream moving left to right, this vorticity has a counter-clockwise (positive) sense of rotation. Conversely, as α decreases, clockwise (negative) vorticity is shed from the upper surface. The free shear layer in the wake of an oscillating airfoil consists of alternating streaks of positive and negative vorticity. These streaks interact and quickly roll up to form a double row of coherent vortices with alternating rotational senses, (see Fig. 3.1). For sinusoidal oscillations, these vortices are equally spaced and have the same magnitude of vorticity.

Two non-dimensional parameters, the reduced frequency ($k = \omega c/2U_\infty$) and the reduced amplitude ($H = a/c$), determine the nature of this wake. Here, ω is the angular frequency of oscillation, c is the chordlength of the airfoil, U_∞ is the magnitude of the mean freestream velocity, and a is the amplitude of oscillation (the linear distance traveled by the trailing edge). Inviscid calculations by Katz and Weihs (1978) suggest that the wake of a sinusoidally pitching airfoil rolls up into discrete concentrations of vorticity for reduced frequencies greater than 2. Flow visualization results, however, show that roll up is dependent on amplitude as well as frequency (Oshima and Oshima, 1980; Koochesfahani, 1989). Figure 3.2, after Oshima and Oshima (1980) illustrates how the wake structure depends on these two parameters. Also indicated in this figure is the combination of parameters for the measurement presented in this chapter.

The work presented in this chapter has a twofold purpose: to fully determine the physical properties of the vortices employed in the airfoil-vortex interaction experiments, and to determine how these properties are controlled by the method of vortex generation. To these ends, instantaneous velocity measurements were made in the mid- and far-field wake of the pitching airfoil, for a wide range of reduced frequencies, two amplitudes, and a range of Reynolds numbers. Vorticity and circulation were computed and compared for the different cases.

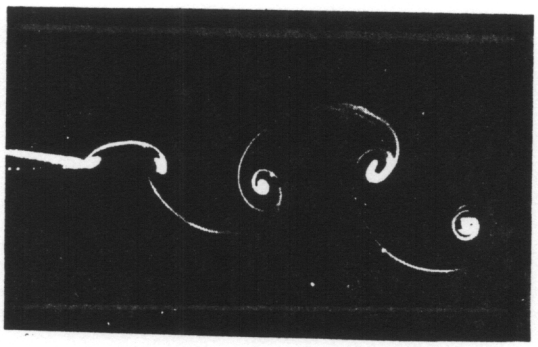

Figure 3.1. Oscillating airfoil wake structure (from Oshima and Oshima, 1980).

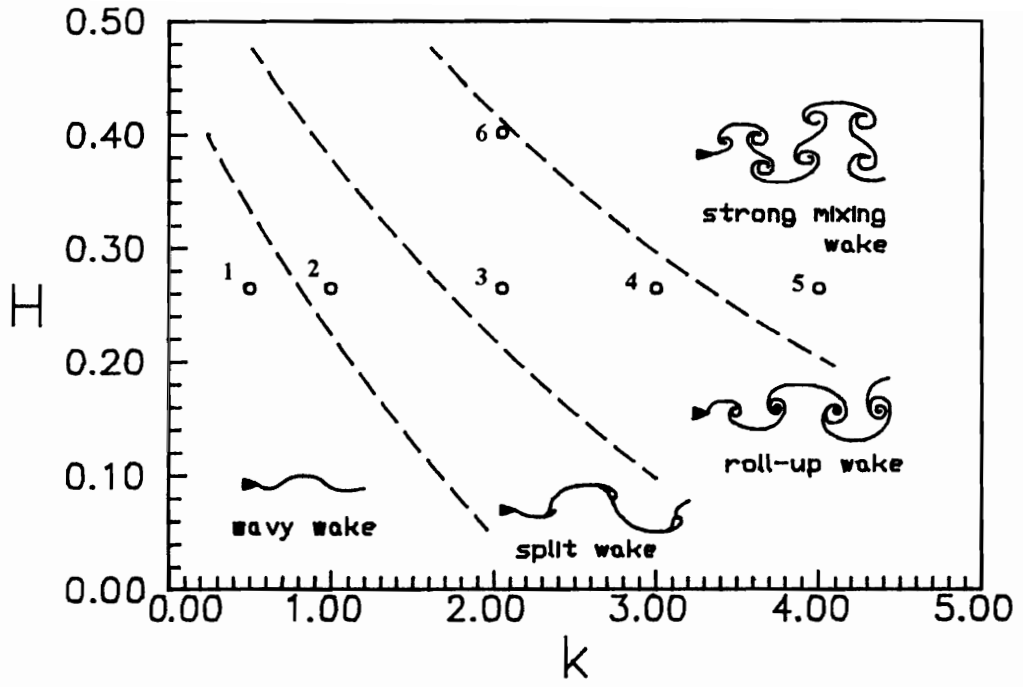

1. k = 0.5, H = 0.265
   x/c_g = 4.0; Re = 26000
2. k = 1, H = 0.265
   x/c_g = 2.0, 4.0; Re = 12600
3. k = 2, H = 0.265
   x/c_g = 1.75 to 3.0 by 0.125, 4.0; Re = 12600
   x/c_g = 2.0, 3.0 and 4.0; Re = 26000
4. k = 3, H = 0.265
   x/c_g = 4.0; Re = 17200
5. k = 4, H = 0.265
   x/c_g = 2.0; Re = 12600
6. k = 2, H = 0.402
   x/c_g = 3.0; Re = 12600, 26000

Figure 3.2. **Classification of wake types and combination of measurement parameters:** (after Oshima and Oshima, 1980).

3.2 Experimental Conditions

A thorough survey of the velocity field in the mid- and far-wake of an airfoil oscillating in pitch was preformed using a two-component laser-Doppler velocimeter. The measurements were executed in the ESM water tunnel, (described in chapter 2). A NACA 0012 airfoil having a chordlength of $c_s = 10.16$ cm and a span of 21 cm was mounted between end walls in the test section and connected through the water tunnel wall to the pitching mechanism; see Figure 2.2 on page 17. The airfoil was pitched sinusoidally about its ¼-chord point with zero mean angle of attack and with an amplitude of $\pm$ 10° (H = 0.265). Thus, the static stall angle of attack was not exceeded. The airfoil was also pitched with an amplitude of $\pm$ 15° (H = 0.402). At this amplitude of oscillation, light dynamic stall likely occured (McCroskey, 1981).

Velocity measurements were conducted for reduced frequencies of k = 0.5, 1.0, 2.05, 3.0, and 4.0 and at chord Reynolds numbers ranging from 12,600 to 25,100. Figure 3.2 on page 58 indicates the combinations of reduced frequency and reduced amplitude for which data were obtained. Parameters were chosen to cover each class of wake structure. Ensemble averaged velocities were obtained along survey lines (columns) lying between 1.75 and 4.0 chordlengths downstream of the pitching airfoil's trailing edge. Figure 3.3 defines the coordinate system. Measurements were ensemble averaged over 20 to 30 cycles of the pitching motion, with sampling intervals ranging from 1/300 to 1/200 of the pitching period. The combination of all parameters (pitching frequency and amplitude, free-stream velocity and measuring station) for the data presented in the following section is displayed in Figure 3.2 on page 58. Vorticity and circulation were computed according to the methods described in chapter 2.

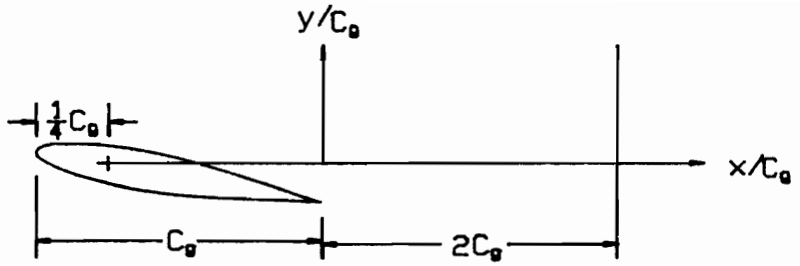

Figure 3.3. Coordinate system.

3.3 Results

i) A Comparison of Grid, Column and Window Data

In this section, results obtained from three "classes" of data (grid, column and window data) are compared. Grid data are measurements made on an $n_x x n_y$ rectangular measurement grid. Column data are the measurements along a single survey line consisting of n_y points. Window data are a pair of survey lines separated by a small distance, $\Delta x = \Delta y$. The methods for constructing velocity and vorticity fields from each class of data was discussed in chapter 2, section 2.5ii. Vorticity and circulation are compared for a positive (counter-clockwise rotating) vortex, at the instant it passes $x/c_s = 2.0$. Only the roll-up wake is considered here; $k = 2.05$ ($\omega = 5.07$ Hz), $H = 0.265$ ($\alpha = \pm 10°$), $Re = 12600$ ($U_\infty = 12.5$ cm/s).

The grid data are a set of velocity measurements made on a rectangular grid consisting of 11 columns and 61 rows covering the region

$$1.75 \leq x/c_g \leq 3.0,$$
$$-0.25 \leq y/c_g \leq 0.5.$$

The step sizes between rows and columns are

$$\Delta x = 0.125 c_g = 12.7mm$$
$$\Delta y = 0.0125 c_g = 1.27mm,$$

respectively. The ensemble averaged velocities were recorded every $\Delta t = 0.03$ seconds, giving thirty samples throughout a cycle of the oscillation.

Any single column of measurements can be classified as column data. A two-dimensional velocity field is formed from column data by assuming that the vortices drift downstream, with the velocity U_d, in a frozen pattern. This assumption is known as

Tayler's hypothesis. A column of time records is employed to form an instantaneous spacial velocity field with an x-step size equivalent to $\Delta x = U_d \Delta t$. Measurement columns consist of 61 measurement stations ($\Delta y = 0.0125 c_g$). The vortex drift velocity was determined by measuring the phase lag in velocity measurements made at different downstream locations in the wake (see Fig. 3.4). The drift velocity for these parameters (k = 2.05, H = 0.265) was found to be $U_d = 1.15 U_\infty \pm 0.05 U_\infty$. Columns taken from the grid data measurements have a temporal resolution of $\Delta t = 0.03$seconds, so that

$$\begin{aligned} \Delta x &= U_d \Delta t \\ &= 0.0424 c_g \\ &= 4.31 mm, \\ &\simeq 3.5 \Delta y. \end{aligned}$$

A two-dimensional velocity field constructed from measurements made along a single column at $x/c_g = 2.0$ is displayed in Fig. 3.5. To more clearly bring out the vortical character of the flow, the drift velocity was subtracted. The resulting vector field is shown in Fig. 3.6. Figure 3.7 offers a comparison of this vector field with the grid data described above. Every third column of Fig. 3.6 was plotted, to give a column spacing similar to the grid data. Circulation integals were calculated around concentric circular paths centered on the vortical cores. The integral represents the net vorticity associated with the vortex, and the extent of the vortex core. The circulation for the grid data and the column data is shown in Fig. 3.8, and the agreement is acceptable.

The third class of data, window data, consists of pairs of columns separated by the small distance $\Delta x = \Delta y = 0.0125 c_g$. Vorticity can be evaluated with column data without making the assumption of a frozen vorticity pattern. However, such an assumption must be made to produce a two-dimensional vorticity field. The vorticity along the column pair is calculated according to eqn. 2.4, and a vorticity field is constructed by assuming

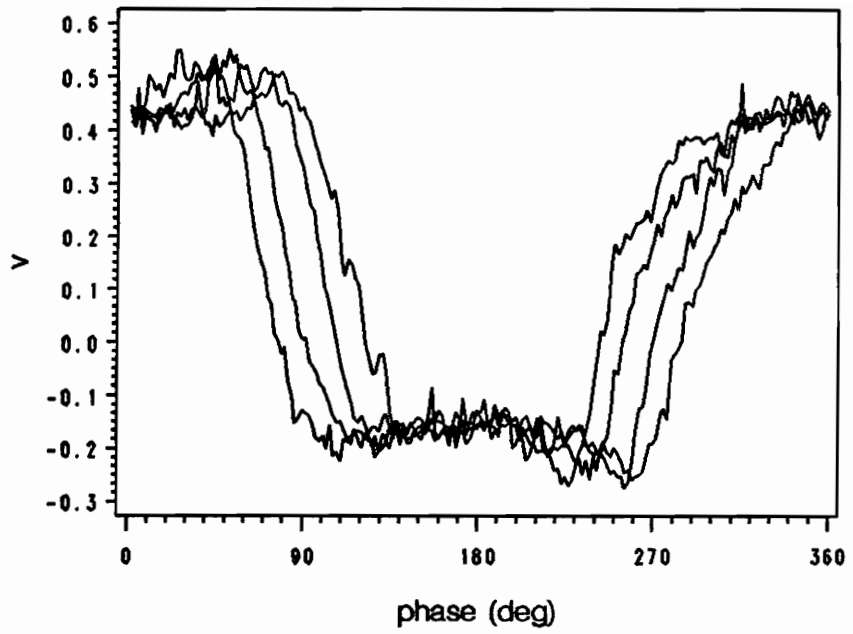

Figure 3.4. Velocity waveforms at four downstream locations in the wake: x/c_g = 1.85, 1.925, 2.0, 2.075; y/c_g = 0.1; k = 2.0

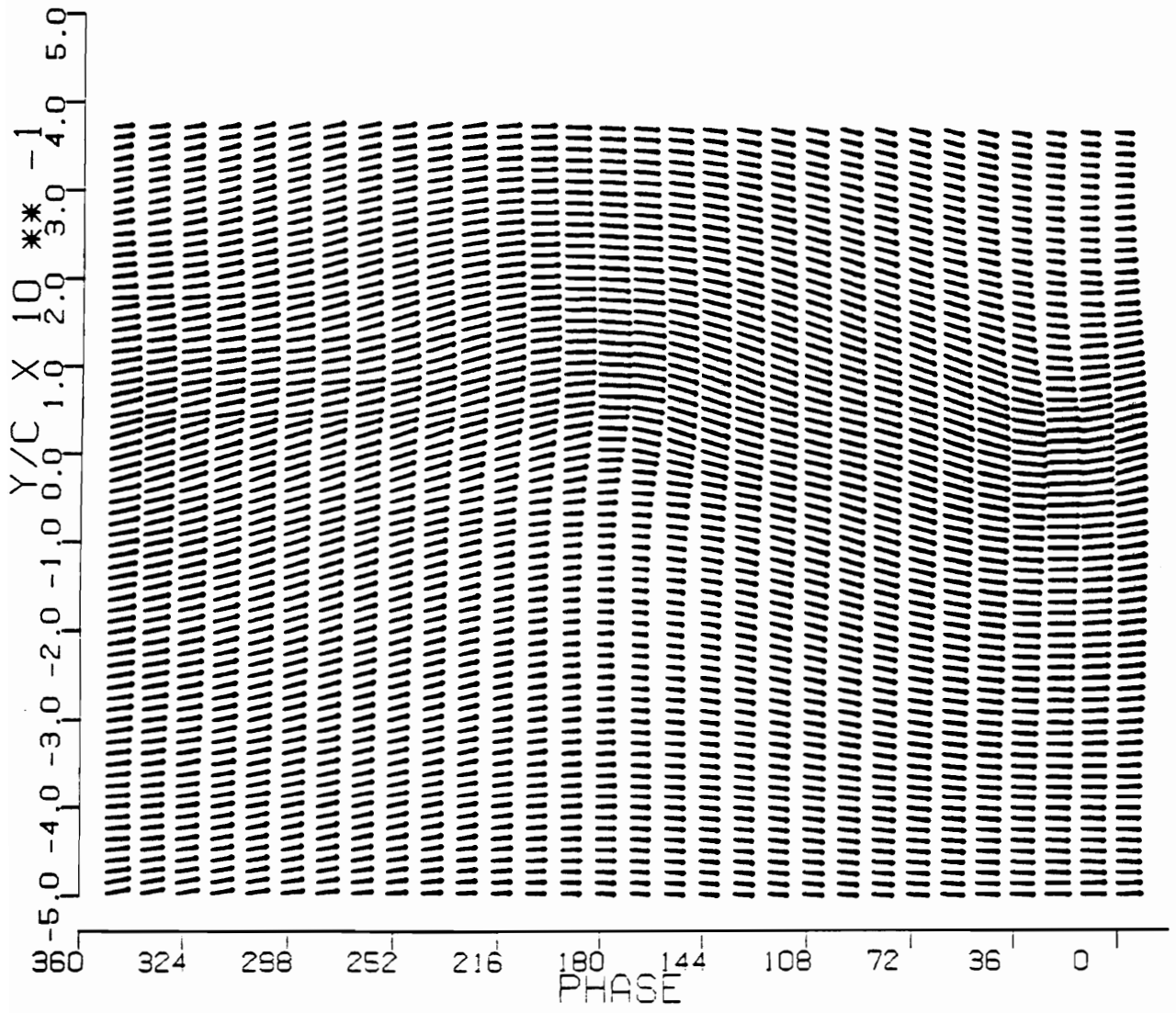

Figure 3.5. Velocity vector field constructed from a single column of measurements: x/c_g = 2.0, k = 2.05, Re = 14000

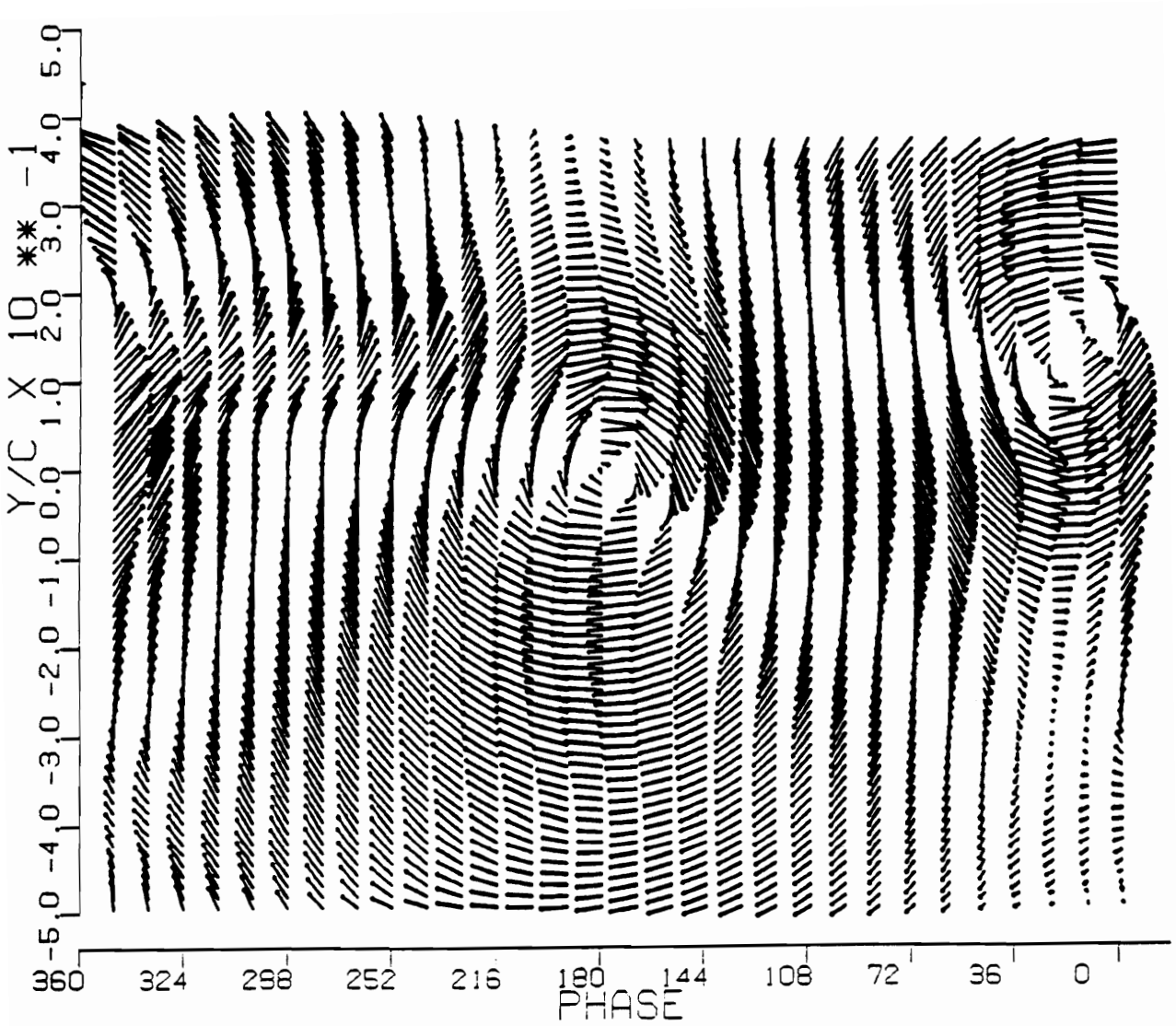

Figure 3.6. Velocity vector field in reference frame of vortex (from Fig. 3.6): x/c_g = 2.0, k = 2.05, Re = 14000

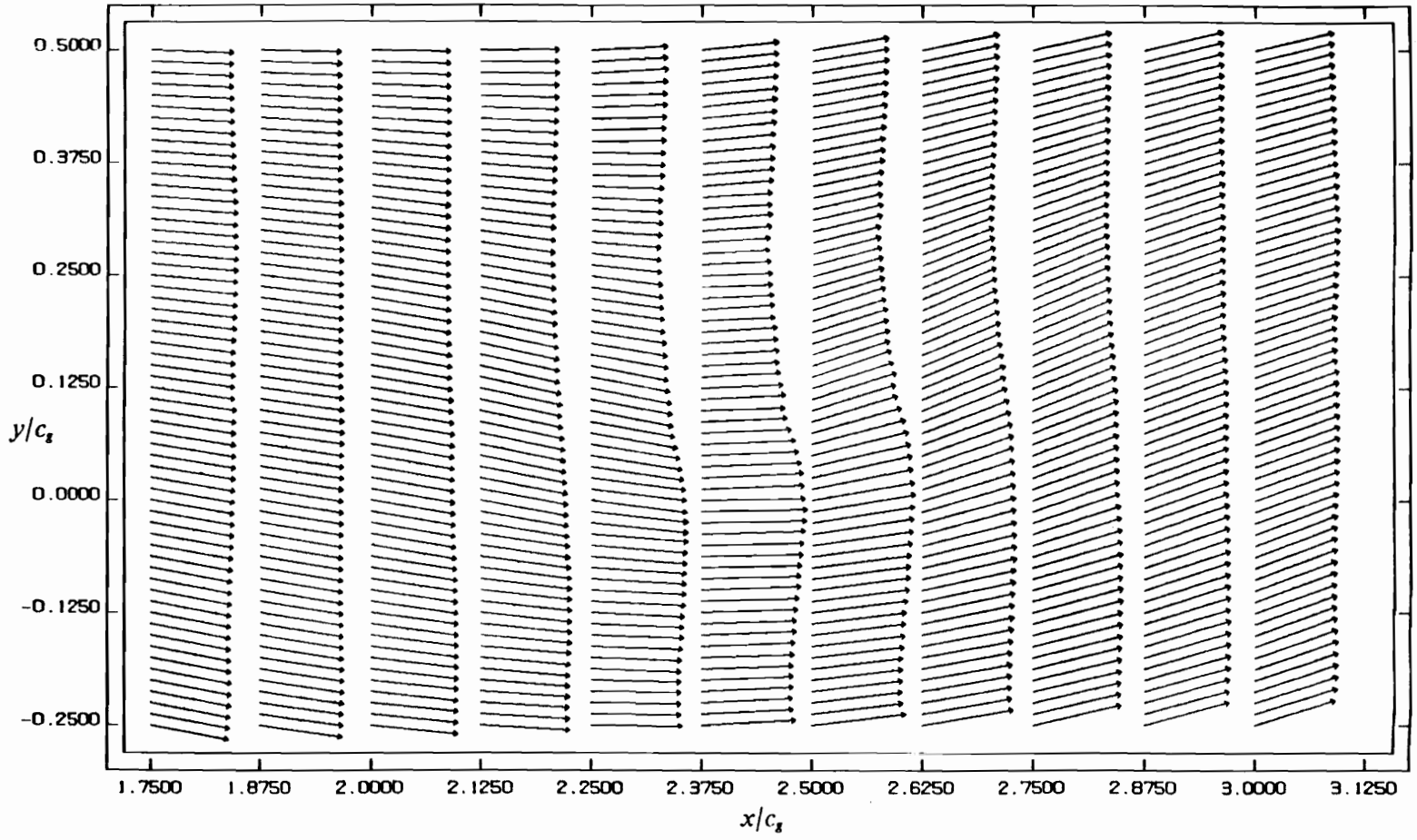

Figure 3.7. **A comparison of grid and column data: Velocity vector fields**
: Instantaneous vector field from 11x61 measurement grid. x/c_g = 2.0, k = 2.05, Re = 14000.

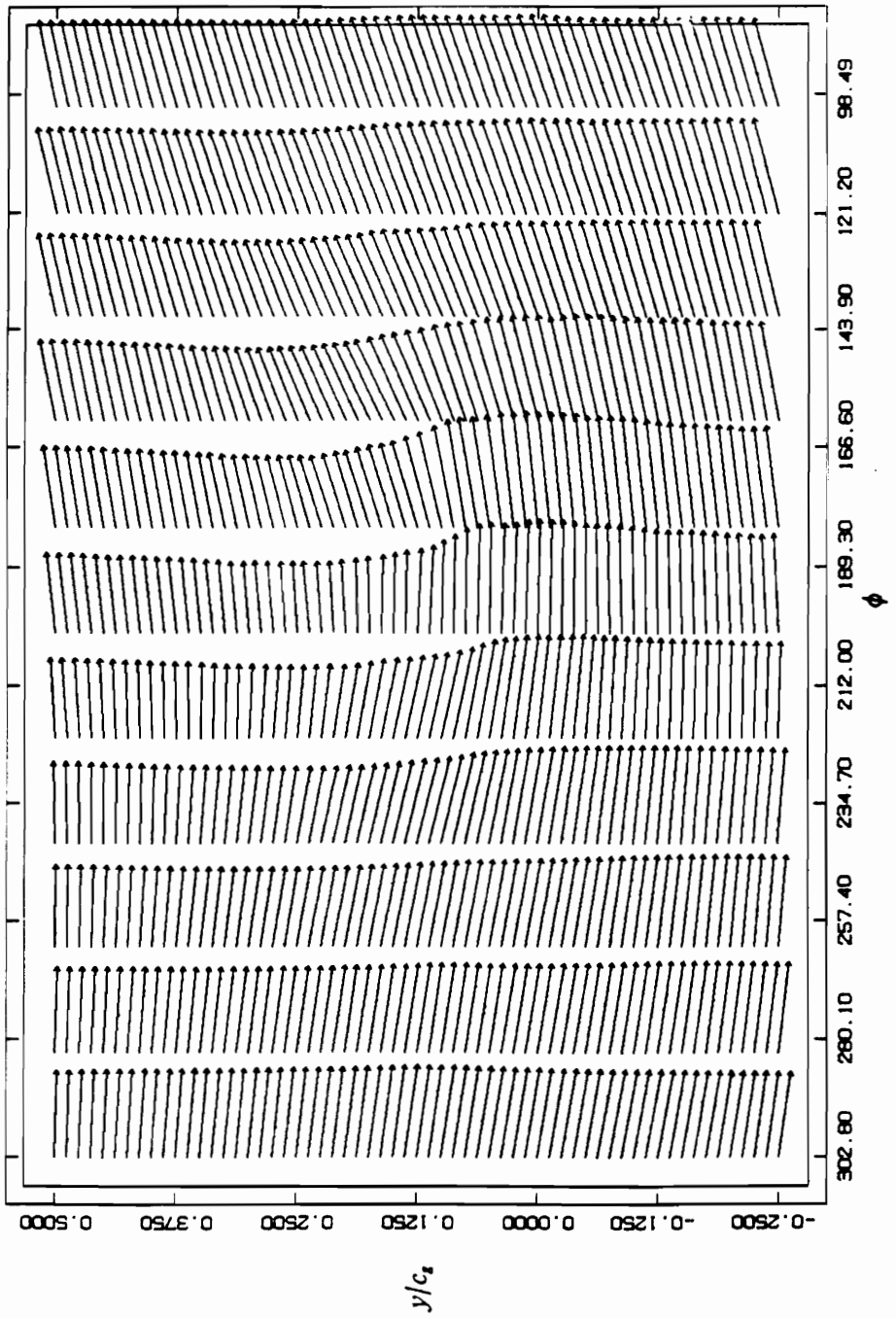

Figure 3.7 continued: Velocity vector field from column data using Taylor's hypothesis. x/c_g = 2.0, k = 2.05, Re = 14000.

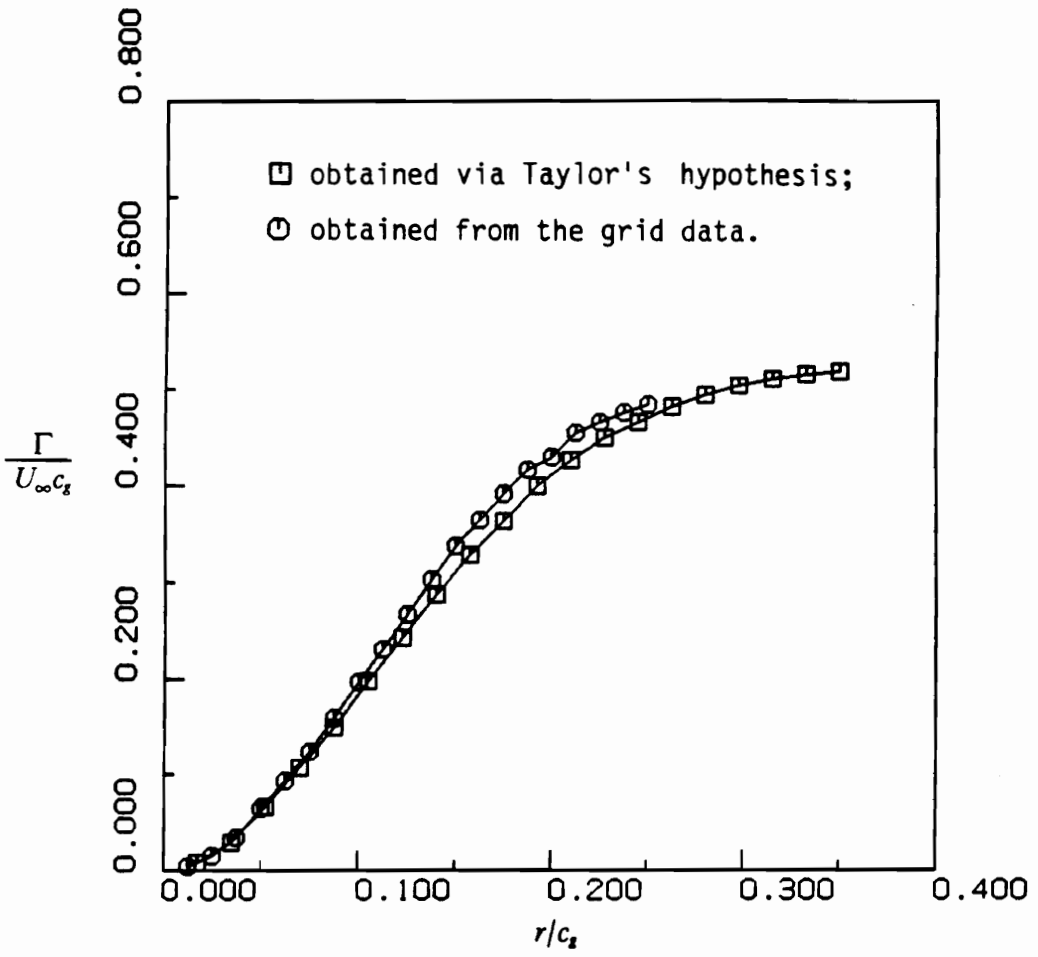

Figure 3.8. A comparison of grid and column data: Total circulation : x/c_g = 2.0, k = 2.05, Re = 14000

that the vorticity propagates with the local partical velocity. This assumption can be stated for an inviscid fluid as,

$$\frac{D\Gamma}{Dt} = 0,$$

which means that the circulation around any surface element moving with the fluid remains constant for all times (Karamcheti, 1980). The temporal resolution of the window data is upgraded over that of the column data. For each period of oscillation 200 velocity samples were recorded, giving a time step of $\Delta t = 0.0062$ seconds.

In an extension of the window method, a set of paired-column measurements is made. Each pair is used to open a small window. The complete set of consecutive windows cover the entire vorticity field. Such a set of measurements, consisting of six column pairs, was made for k = 2.05 and H = 0.265. The column pairs were centered at

$$x/c_g = 1.7$$
$$x/c_g = 2.0$$
$$x/c_g = 2.3375$$
$$x/c_g = 2.525$$
$$x/c_g = 2.7125 \text{ and}$$
$$x/c_g = 2.9.$$

Each column consisted of 41 measuring stations ranging from $-0.2 \leq y/c_g \leq 0.3$, with step sizes $\Delta x = \Delta y = 0.01875 c_g = 1.905mm, and\Delta t = 0.0062$ seconds.

The vorticity field was constructed from a single column pair and from the complete set. Vorticity contour maps for all four cases of data (grid, column, window and six windows) are compared in Fig. 3.9. We see that the vortex appears considerably weaker for the grid data (Fig. 3.9a) than for the other cases. This is due to the lack of resolution

in the x-direction. The circulation integrals (Fig. 3.8) more accurately indicate the strength of the vortex.

ii) Downstream Development of the Roll-up Wake

The method described in the preceeding section are utilized to study the development of the roll-up wake between $x/c_z = 2.0$ and 4.0. The wake development has been investigated extensively in the past using flow visualization techniques (Oshima and Oshima, 1980; Poling, 1985; Koochesfahani, 1989). However, such visualizations cannot give a clear indication of vortex strength, and, unless the transport properties of the visualization medium are equivalent to those of vorticity, the visualization will not correctly indicate the extent of the vortices.

The circulation versus integration path size for the positive vortex at different downstream locations is shown in Fig. 3.10. Column data measurements at $x/c_z = 2.0$, 3.0, and 4.0 are the sorce for this figure. Vorticity tends to spread form the center of the vortex as it moves downstream. This effect cannot be attributed to viscous diffusion. A solution to the vorticity transport equation (given in a reference frame with circular motion only) yields the following expression for the viscous diffusion of circulation (Milne-Thomson, 1968).

$$\Gamma = \Gamma_0\left[1 - \exp\left(\frac{-r^2}{4\nu t}\right)\right], \qquad [3.1]$$

where Γ_0 is the circulation at time $t=0$, r is the distance from the vortex center, and ν is the kinematic viscosity of the fluid. The time required for eqn. 3.1 to account for the diffusion represented in Fig. 3.10, the vortex would have traveled several tens of chordlengths rather than only two. The diffusion is attributable in a small part to the

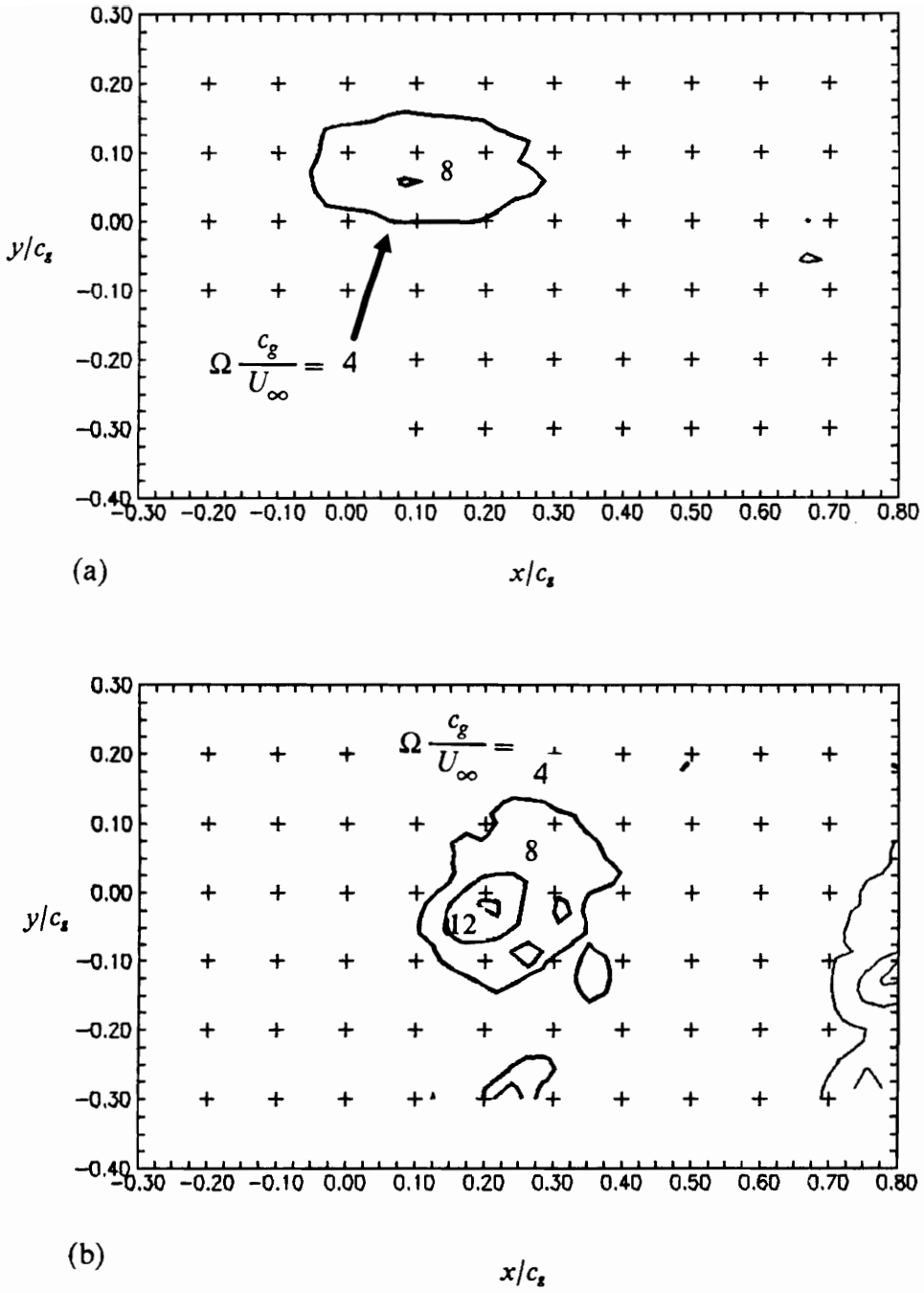

Figure 3.9. A comparison of grid, column and window data: vorticity contours: (a) grid (b) column: k = 2.05, H = 0.265, Re = 12600, $x/c_g = 2.0$

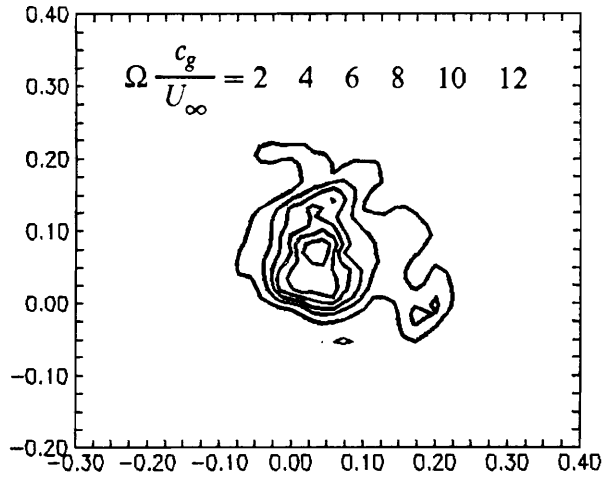

(c)

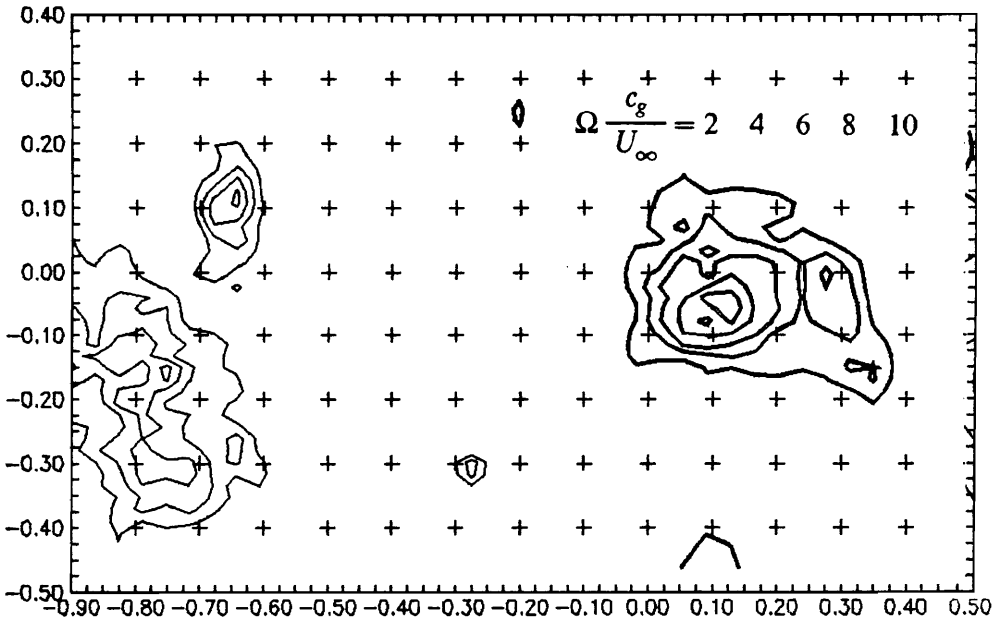

(d)

Figure 3.9 continued: (c) single window (d) multiple windows, $x/c_g = 2.0$, k = 2.05, H = 0.265, Re = 12600.

widening of the wake; a small amount of the vorticity moves beyond the range covered in the measurements. Three-dimensional effects become more pronounced at locations deeper into the wake. Koochesfahani (1989) has shown that the no-slip boundary condition at the bounding wall is sufficient to induce an axial velocity component in the core of the vortices. This, in combination with the growing boundary layers on the water tunnel walls, causes the vortices to become less two-dimensional and less repeatable with downstream travel. The ensemble averaged measurements tend to "smear out", causing the vortices to appear weaker and dimensionally larger.

The column data measurements at $x/c_s = 2$, 3and 4 were repeated with a Reynolds number of 25000 (twice the value for the preceeding data), but with the aifoil oscillating at the same reduced frequency (twice the pitching frequency in Hz as the preceeding data). The change in Reynolds number had little affect on the circulation of the vortices (Fig. 3.11), however, the turbulent intensity increased, causing a corresponding increase in the calculation errors for derivatives (refer to Figure 2.18 on page 54).

iii) Wake Structure Dependency on Frequency and Amplitude

For the airfoil-vortex interaction (chapter 4), strong, widely spaced vortices were desired. A measure of control over the distribution of vorticity and the separation distance between concentrations of vorticity can be obtained simply by varying the reduced frequency and/or the reduced amplitude of sinusoidal oscillation. Greater control over the vortex spacing can be achieved by pitching the airfoil in a nonsinusoidal fashion (Booth 1987, Koochesfahani 1989), however, this is beyond the scope of this work.

Window data velocity measurements were made two chordlengths into the wake of the sinusoidally oscillating airfoil. The pair of survey lines were separated by $\Delta x = 0.01875c_s = 1.905$ mm and each column consisted of 42 measurement stations sep-

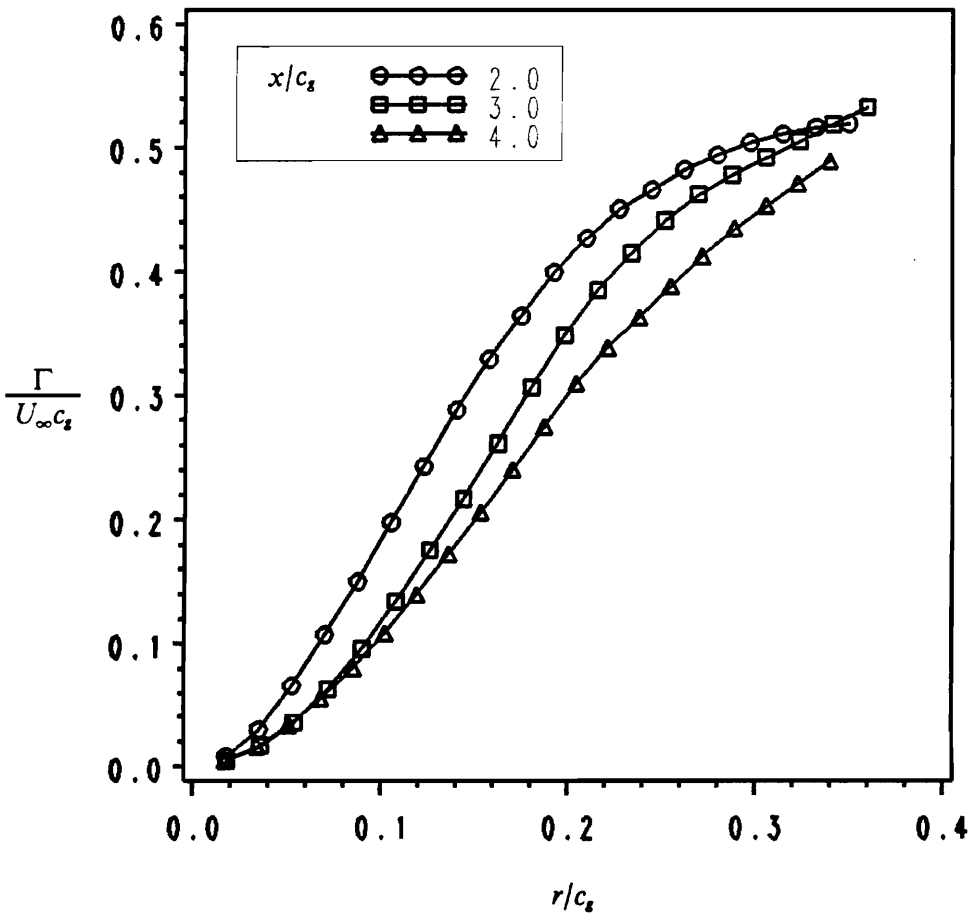

Figure 3.10. Roll-up wake development (1): Total circulation at $x/c_g = 2,3,4$: k = 2.05, Re = 12600

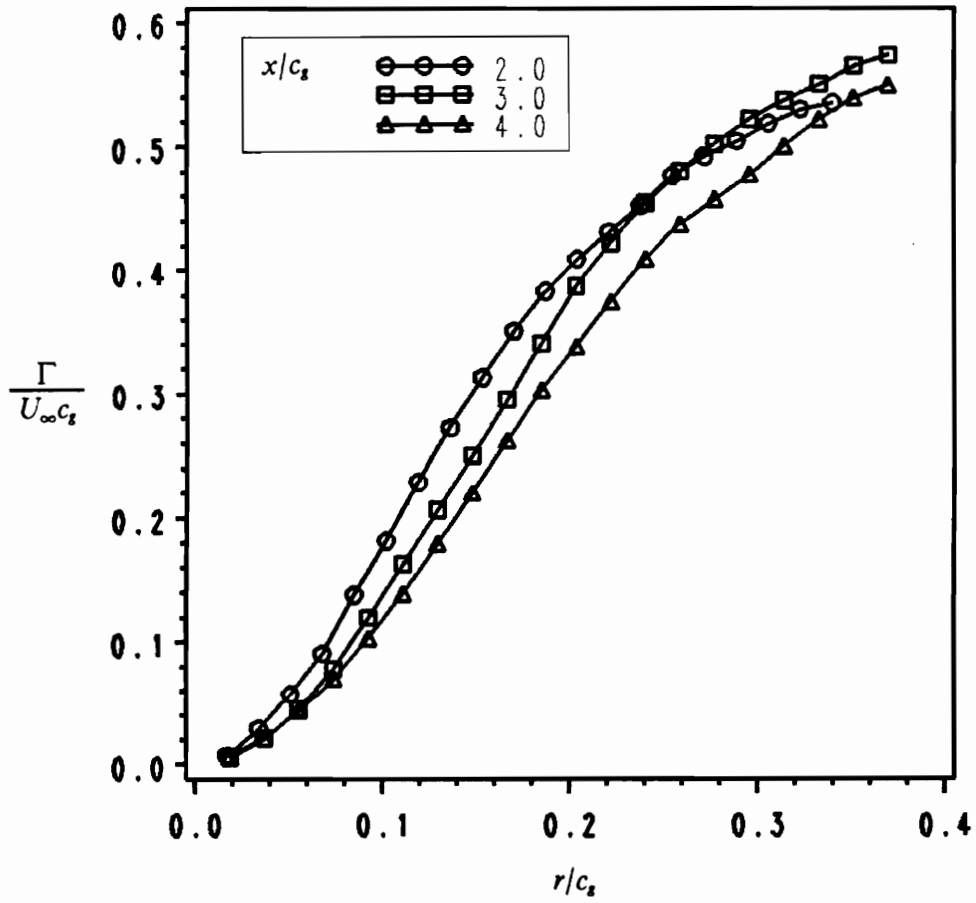

Figure 3.11. Roll-up wake development (2): Total circulation at $x/c_g = 2,3,4$: k = 2.05, Re = 25000

arated by the distance $\Delta y = \Delta x$. During each period of oscillation (0.62 sec. $\leq$ T $\leq$ 1.24 sec.) the velocity was sampled 200 times. Thirty time records were used for the ensemble average. Measurements were made for the reduced frequencies of k = 1, k = 2 and k = 4, and a reduced amplitude of H = 0.265 ($\alpha = \pm 10°$).

Additional measurements (column data) were made along survey lines at $x/c_s = 4.0$ for reduced frequencies of k = 0.5, 1.0, 2.05, and 3.0 (H = 0.265).

When oscillating at a higher reduced frequency, the acceleration of the airfoil's trailing edge, relative to the free stream, is greater. For this reason the shed vorticity is more intense. Moreover, the stronger shear layers roll up into larger structures. Vorticity contours for each reduced frequency are displayed in Fig. 3.12. The flow appears highly turbulent for the highest reduced frequency. The parameters place these measurements within the strong-mixing wake classification. For the reduced frequency of k = 1 (split wake) the vorticity of like sign does not roll up into a single concentration. Instead, the vorticity in the free shear layer remains spread out, and forms several small concentrations.

In addition to the total circulation of the vortices (the circulation in a reference frame fixed with respect to the vortices), we can also examine the circulation in a space-fixed reference frame. This quantity, called the circulation flux here, is the time variation of the circulation around a cross section of the flow. Vorticity is calculated, for all times, using two adjacent columns of velocity measurements (such as the window data). The circulation is evaluated by integrating the vorticity;

$$\begin{aligned} \Gamma(t) &= \int_A \Omega(t)\, dA \\ &\cong \sum_j \Omega_j^n \Delta x \Delta y, \end{aligned} \qquad [3.2]$$

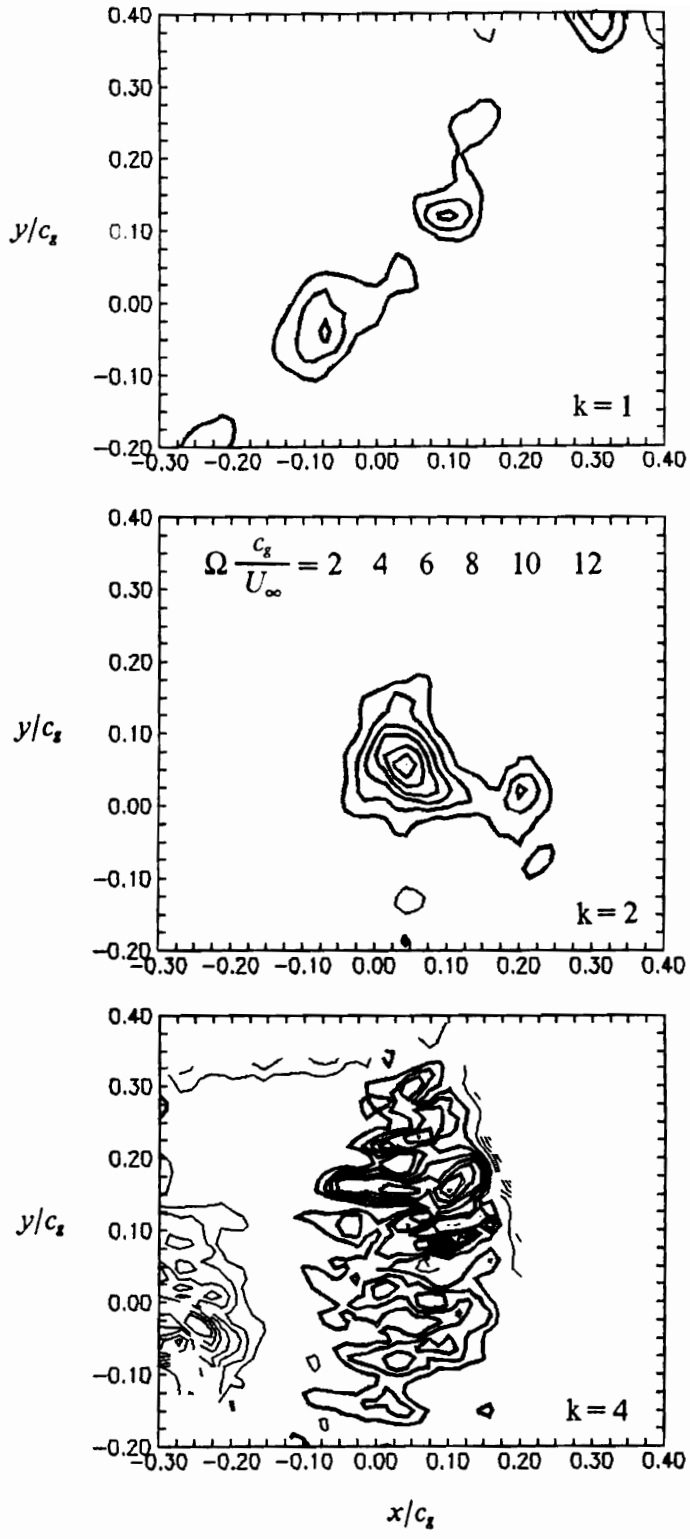

Figure 3.12. Vorticity contours for k = 1, 2, and 4: H = 0.265 ($\alpha = \pm 10°$), $x/c_g = 2.0$.

where n is the time index, and Δx and Δy are the measurement step sizes. The area of integration is the area spanned by the two columns; $A = (N_y - 1)\Delta y \Delta x$, where N_y is the number of points in a column of data. The summation is performed using only positive values of Ω_j to determine the circulation due to the counter-clockwise rotating vortex, and with negative values of vorticity for the clockwise vortex.

Circulation flux for the three reduced frequencies is shown in Fig. 3.13. From the circulation flux we see that there is a reduced frequency dependent phase difference in the arrival time of the vortices at the measurement station. The vortex spacing decreases with increasing reduced frequency since the freestream fluid travels a shorter distance in the time to complete one oscillation. The vortex drift velocity increases slightly with reduced frequency due to an increase in mean velocity across the wake. This velocity increase is induced by the rotation of the vortices.

The total amount of vorticity and the size of the vortex core depend on the amplitude of the pitching as well as on the frequency. The circulation distribution for pitching with a reduced amplitude of $H = 0.402$ ($\alpha = \pm 15°$) is compared with the distribution obtained for $H = 0.265$ ($\alpha = \pm 10°$) in Fig. 3.14. The reduced frequency was $k = 2.05$ and the Reynolds number was $Re = 12600$ for both measurements. As might be expected, the higher amplitude creates a stronger, larger vortical structure. However, the vortex spacing, which is influenced most by the reduced frequency, is not effected.

The combination of parameters chosen for the airfoil-vortex interaction investigation were $k = 2.05$ and $H = 0.265$. This selection resulted in good vortex roll-up and provided a reasonable vortex spacing.

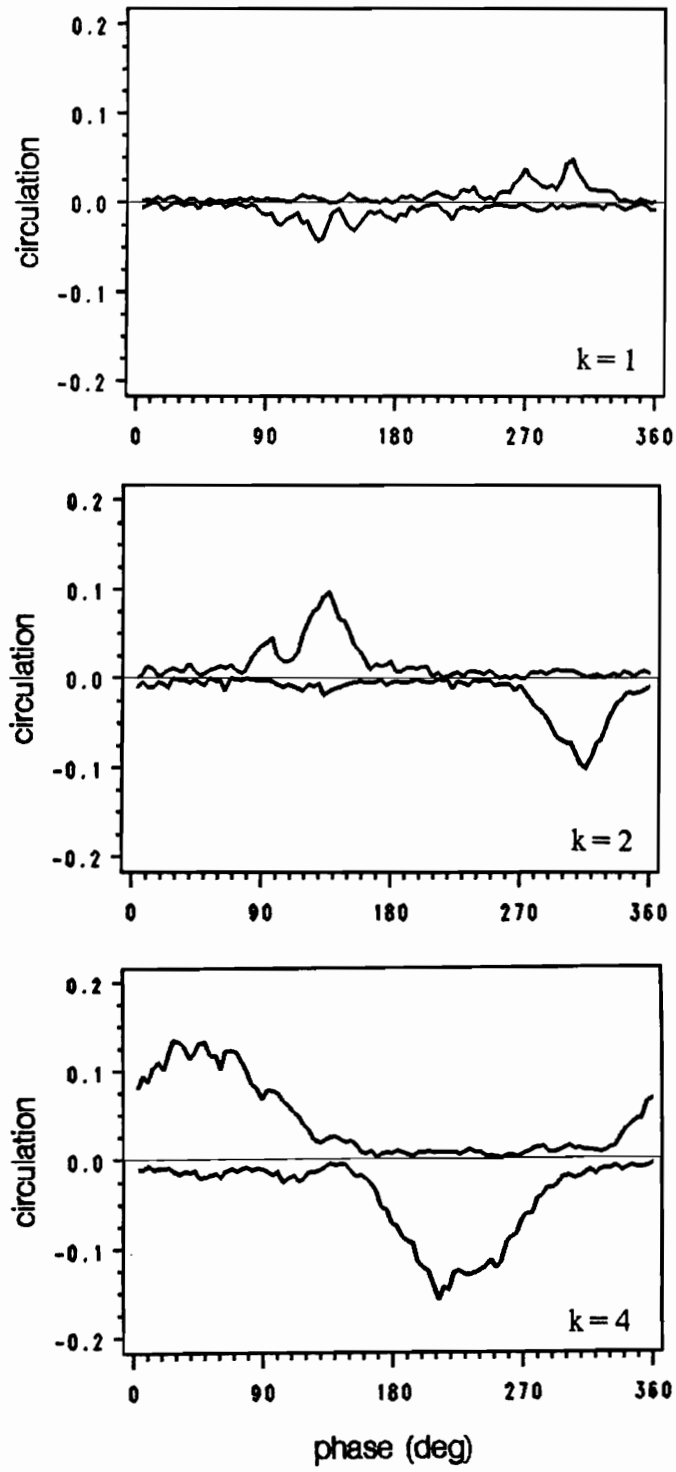

Figure 3.13. Circulation flux for k = 1, 2, and 4: H = 0.265 ($\alpha = \pm 10°$), $x/c_g = 2.0$.

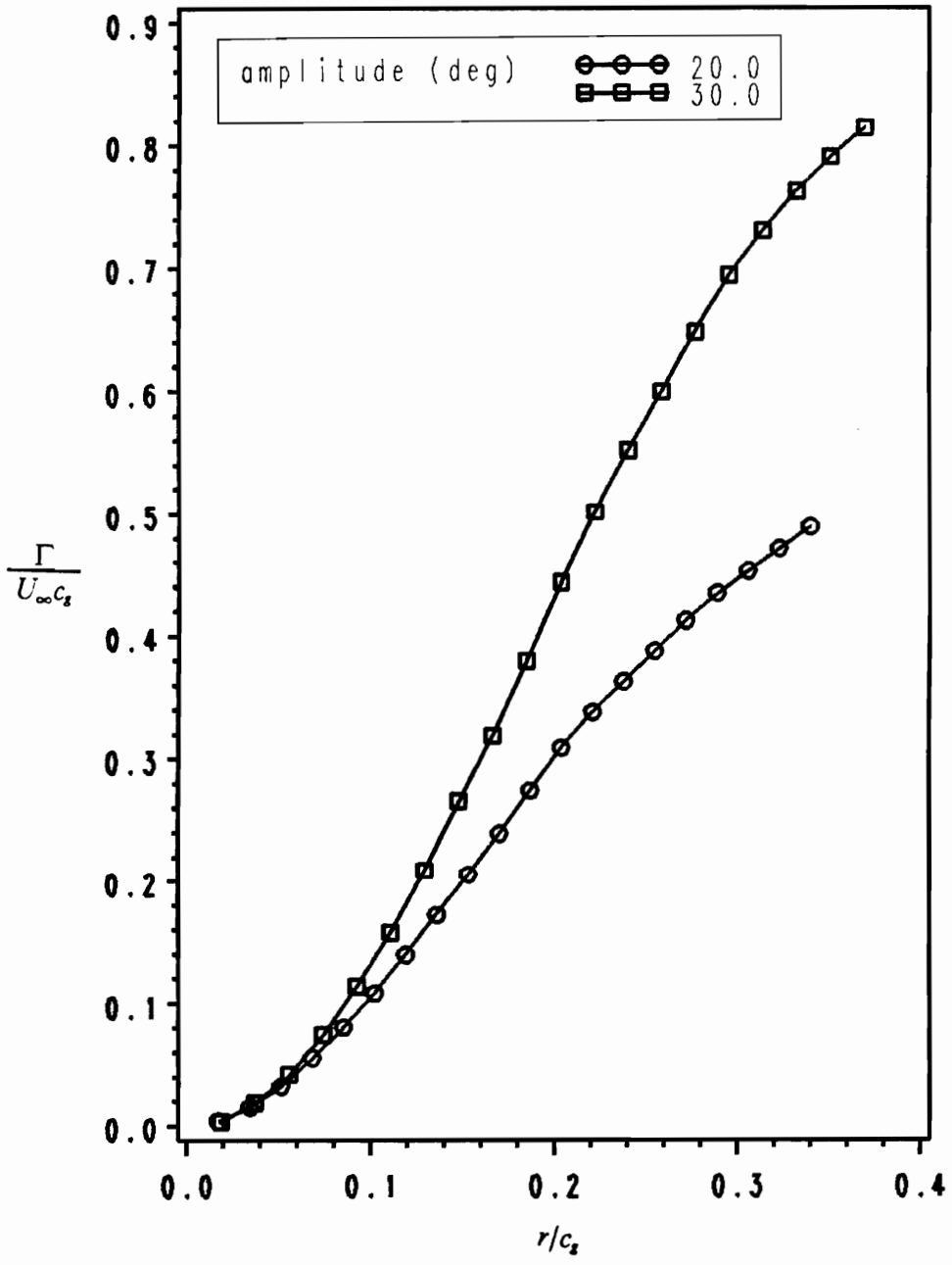

Figure 3.14. Total circulation for reduced amplitudes of 0.265 and 0.402: k = 2.05, Re = 12600, $x/c_g = 4.0$

Chapter 4

The Interaction of Vortices with an Airfoil

4.1 Introduction

In this chapter the airfoil-vortex interaction results are discussed. The data are presented in two parts; (1) steady velocity measurements around the target airfoil, and (2) unsteady measurements during the airfoil-vortex interaction. The steady measurements were used to provide a base-line case to determine the reliability of the calculated pressure distributions. Three cases of unsteady results are presented; (i) a counterclockwise rotating vortex passing over the target airfoil at a zero-degree angle of attack; (ii) a similar interaction with the airfoil at a ten-degree angle of attack, and (iii) a direct encounter (head-on collision) with the counterclockwise vortex (which includes a near miss below the airfoil with the clockwise vortex), $\alpha = 10°$. Case (iii) data employs the window method, demonstrated in chapter 3, to determine the instantaneous vorticity fields. In each case, the reduced frequency and the reduced amplitude of the vortex generator were $k = \frac{\omega c_g}{2U_\infty} = 2.05$ and $H = 0.265$ ($\alpha = \pm 10°$), respectively, and the Reynolds number based on the target-airfoil chordlength was $Re = 19000$ ($c = 15.24$ cm, $U_\infty = 12.6$ cm/s).

The target airfoil, also called the blade, was a NACA 63_2A015 symmetrical airfoil. The chordlength was 15.24 cm and the airfoil spanned the water tunnel test section. The leading edge was placed two vortex-generator-chordlengths ($2c_z = 20.32$ cm) downstream of the neutral position ($\alpha = 0°$) of the vortex generator's trailing edge, and displaced by a distance Δh in the y-direction. The origin of the coordinate system was located at the leading edge of the target airfoil and aligned with the stream. Figure 4.1 defines the coordinate system.

Vorticity, circulation, and surface pressure coefficients were calculated from the measured velocities and used to analyze the interaction between the vortex and the airfoil boundary layer. Vorticity and circulation calculation methods were detailed above (chapters 2 and 3). The measured velocities were utilized to calculate the unsteady pressure distribution from the Navier-Stokes equations;

$$\begin{aligned} \frac{\partial p}{\partial x} &= \mu \nabla^2 u - \rho \left(\frac{\partial u}{\partial t} + u \frac{\partial u}{\partial x} + v \frac{\partial u}{\partial y} \right) \\ \frac{\partial p}{\partial y} &= \mu \nabla^2 v - \rho \left(\frac{\partial v}{\partial t} + u \frac{\partial v}{\partial x} + v \frac{\partial v}{\partial y} \right) . \end{aligned} \qquad [4.1]$$

The right-hand-side terms were evaluated with the velocity measurements and the resulting pressure gradients were integrated along measurement grid lines to yield the pressure;

$$p(x,y) = p_\infty + \int \left(\frac{\partial p}{\partial x}\, dx + \frac{\partial p}{\partial y}\, dy \right), \qquad [4.2]$$

which may be expressed as a nondimensional coefficient of pressure,

$$C_p = \frac{(p - p_\infty)}{\frac{1}{2}\rho U_\infty^2} .$$

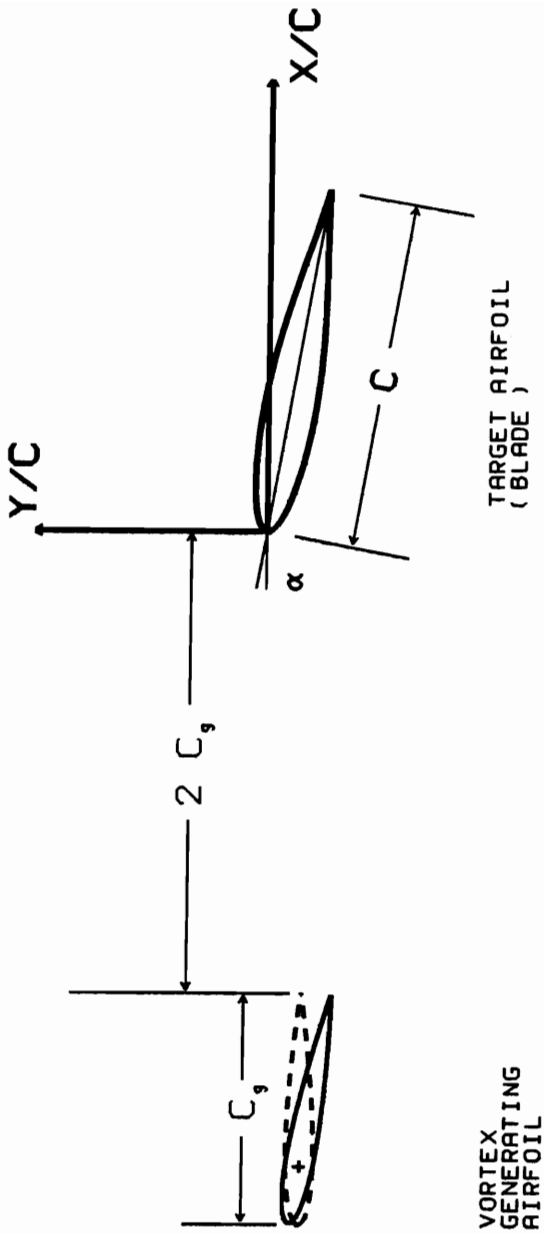

Figure 4.1. Coordinate system for the airfoil-vortex interaction experiments.

The integral path began at the measurement station furthest upstream and above the airfoil. It was assumed that the pressure at this location was steady and equal to the freestream pressure, P_∞. In related work, Pesce (1990) and Gursul and Rockwell (1990) demonstrated that the resultant pressure was dependent upon the path of integration. Therefore, to better compare the results, the same integration path was used for each case of data presented below.

4.2 Steady State Measurements

A complete mapping of the steady-state flow field around the blade model was obtained for the 10° angle-of-attack case. The vortex generator was removed from the water tunnel for these measurements. The velocity was measured on 112 columns on the grid,

$$-0.3 \leq x/c \leq 1.2$$
$$-0.4 \leq y/c \leq 0.25,$$

with, $\Delta x = 0.0125c = 1.905$ mm and $\Delta y = 0.025c = 3.81$ mm. A finner step size, $\Delta y = 0.0025c = 0.381$ mm was used over the airfoil surface in order to resolve the boundary layer. Figure 4.2 is a vector plot of the steady velocities. For clarity, only evey 7th column is shown. The velocity measurements were integrated over 10 seconds to ensure a stable mean.

The steady surface pressure distribution was determined from eqns. 4.1 and 4.2, with the acceleration terms in eqns. 4.1 set to zero. The velocity was set to zero at the surface of the airfoil, and this value was used in a three point up-wind finite-difference formulation to determine the gradients at the boundary. The pressure gradients were integrated by repeated application of the trapazoid rule. Pesce (1990) showed that

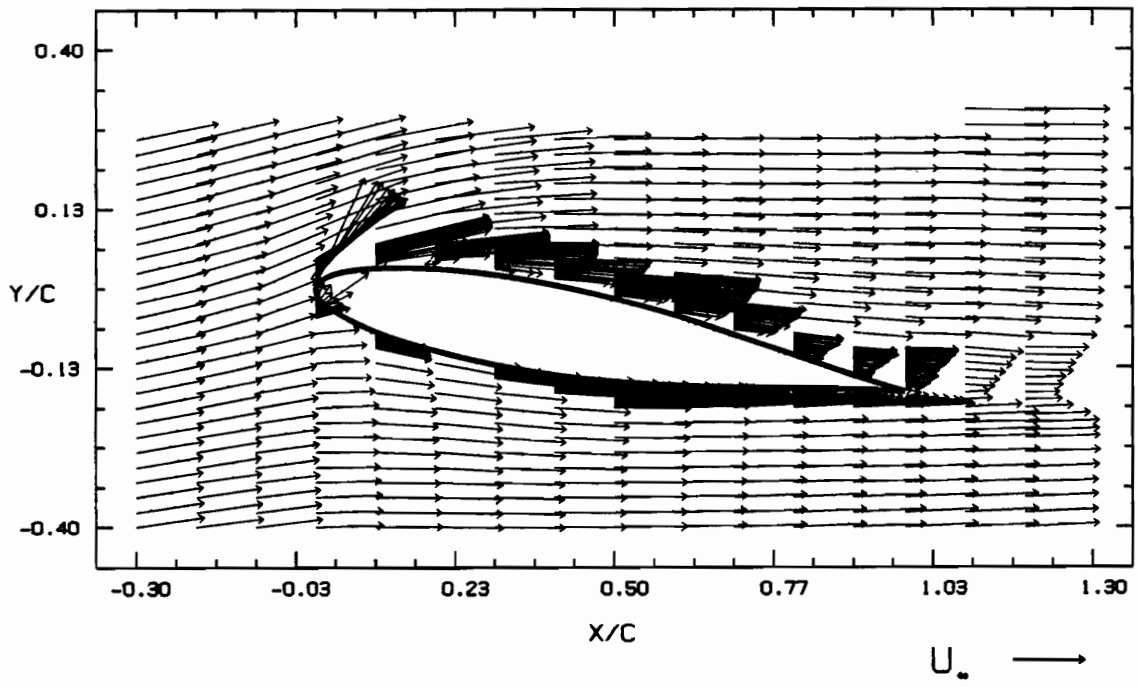

Figure 4.2. Steady velocity vectors around a NACA 63_2A015 at $\alpha = 10°$: Every seventh column of data is shown.

higher order integration schemes produced similar results. The pressure coefficient distribution is shown in Fig. 4.3 and is compared with the pressure distribution computed by inviscid theory (conformal mapping). The calculated pressures agree quite well with theory, except on the first 20% of the upper surface. The pressure coefficients were integrated to find a lift coefficient of $C_l = 0.8$, in comparison with the ideal lift coefficient of $C_l = 1.07$. The lift can also be determined from the circulation about the airfoil. The circulation, evaluated with the data presented in Fig. 4.2, is

$$\frac{\Gamma}{U_\infty c_g} = \oint \frac{\vec{V}}{U_\infty} \cdot \frac{\vec{dl}}{c_g} = 0.544 \ ,$$

and is clockwise around the airfoil. The ideal flow solution from conformal mapping is $\frac{\Gamma}{U_\infty c_g} = 0.5455$, which differs by less than 0.3% from the experimentally determined value.

4.3 Conditions for the Unsteady Measurements

(i) Target airfoil at $\alpha = 0°$: close encounter

The target airfoil was aligned to interact with the upper row of vortices (the counterclockwise rotating vortices) in the wake of the ocillating airfoil. The airfoil was displaced from the symmetry line of the wake by a distance of $\Delta h = 0.09c$, however, due to the influence of the airfoil, the trajectories of the vortices were deflected above the airfoil surface. Ensemble-averaged velocities were obtained along 27 survey lines from x/c = -0.3 to 0.35 in increments of $\Delta x/c$ = 0.025, on 41 stations per column from y/c = -0.2 to 0.3 in increments of $\Delta y/c$ = 0.0125, and at 50 time instances per period of oscillation, Δt = 0.0248 seconds. Ensemble averaged velocities were recorded for two

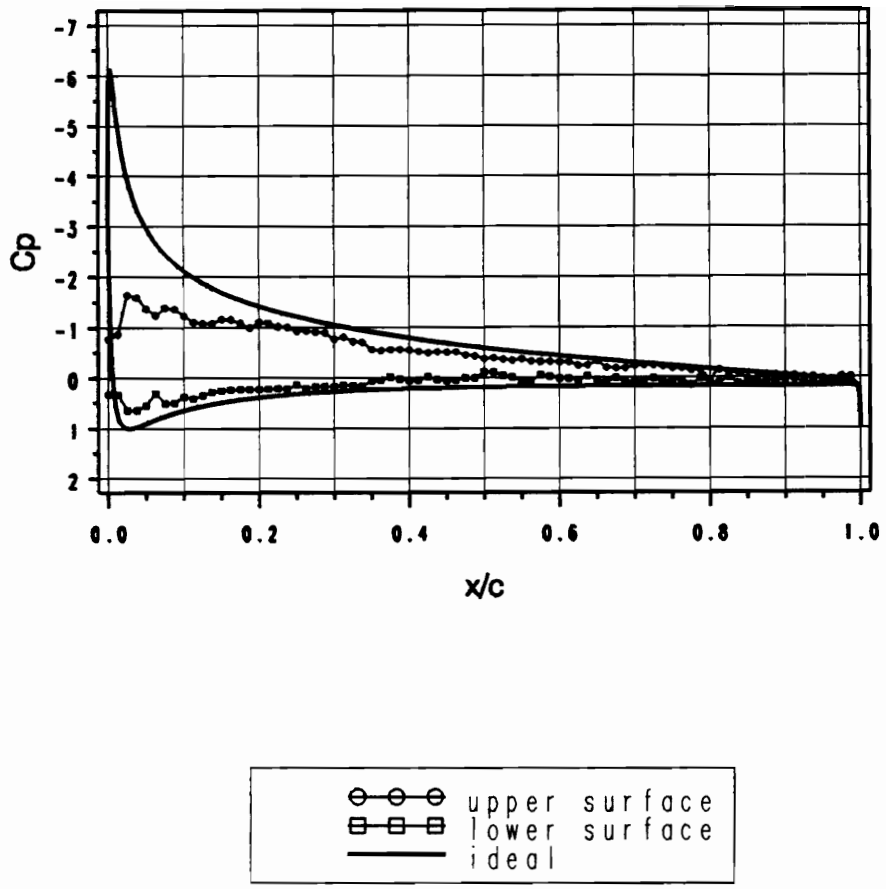

Figure 4.3. Steady pressure distribution calculated from measured velocities.

complete oscillations of the vortex generator, the two separate cycles being used to assess the repeatability of the process. Figure 4.4 is an example instantaneous velocity vector field illustrating the density of the measurement grid. In Fig. 4.5, the cross-sectional circulation flux is shown at a station 0.2c upstream of the airfoil's leading edge, illustrating the repeatability of the disturbance, and at a station 0.15c downstream of the leading edge, which illustrates the repeatability of the interaction. At the upstream location we see the passage of the primary vortices in the street. At the next position, the positive circulation curve represents the positive primary vortices passing over the blade surface. Associated with the primary positive vortices is a secondary concentration of negative vorticity generated at the airfoil's surface. A small piece of the negative primary vortex also passed over the airfoil, and is the source of the peak in negative circulation seen 180 degrees ahead of the positive circulation.

No measurements were made beneath the airfoil ($x/c \geq 0$, $y/c \leq 0$), and at several stations near the leading edge, measurement was impossible since one of the laser beams was blocked by the airfoil. Twenty to thirty time records were used in each ensemble average; thirty in the boundary layer regions where the velocity, and therefore, the data rates, were lower.

Results derived from these data are compared with results of the other two cases in section iv, below. Representative examples of the velocity vector fields and vorticity contours are also presented in section iv, while contour maps for the complete cycle of measurements are given in Appendix A.

(ii) Target airfoil at $\alpha = 10°$: close encounter

The target airfoil was displaced further from the wake symmetry line for this case ($\Delta h = 0.1c$), but again, the vortex core passed above the airfoil surface. The airfoil in this

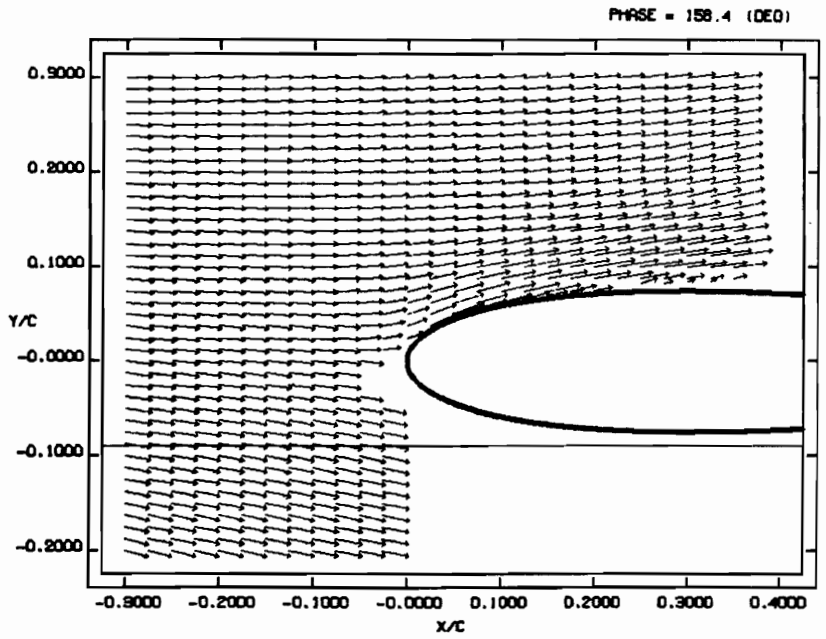

Figure 4.4. Instantaneous velocity vector field, $\alpha = 0°$.

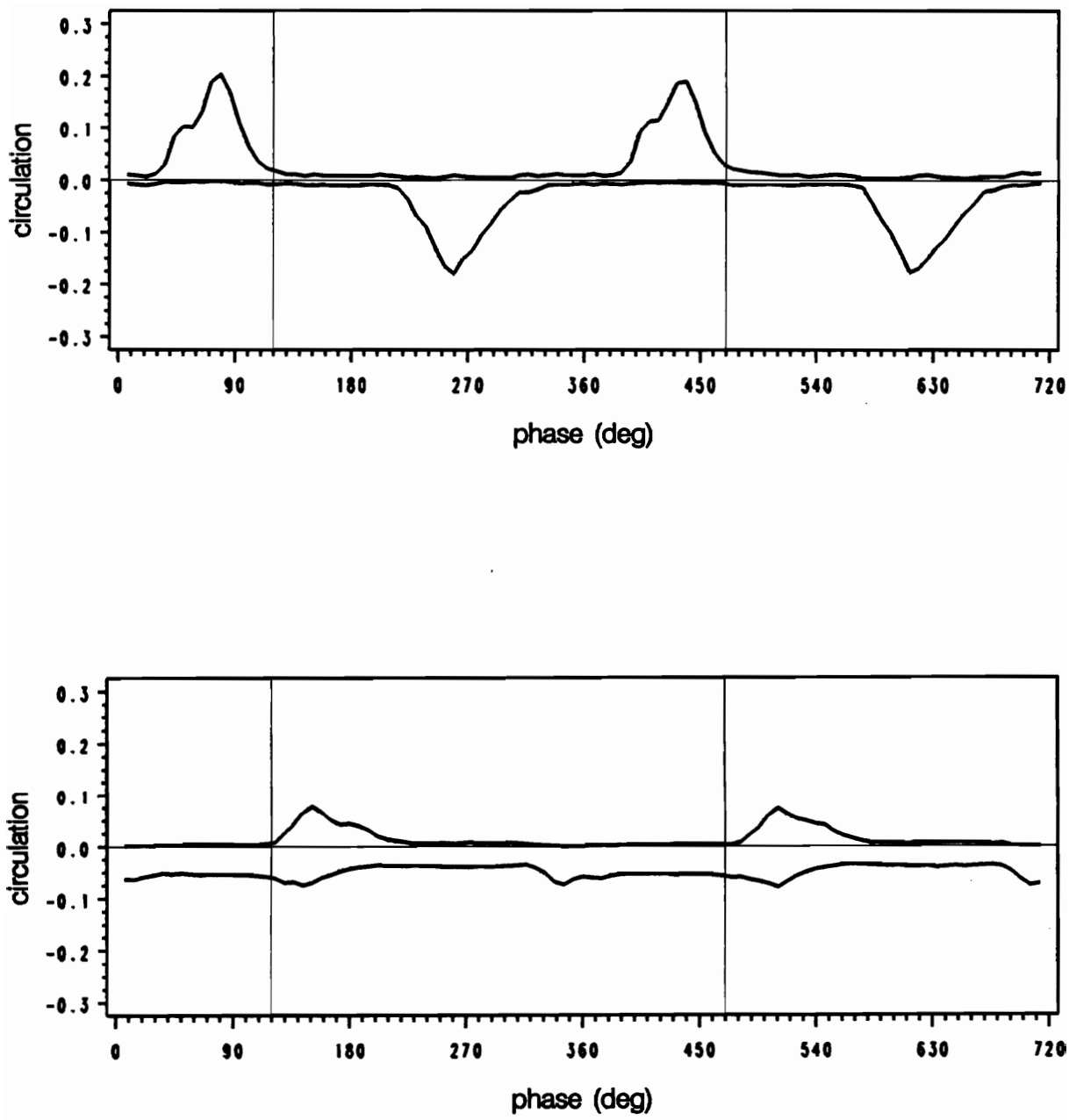

Figure 4.5. Repeatability of the airfoil-vortex interaction (circulation flux)

case had a greater influence upon the vortex trajectory. Measurements were made on two more survey lines, extending the grid to x/c = 0.4, and the range of the columns was shifted to include more of the region above the airfoil: y/c = -0.15 to 0.35. The time resolution was doubled, Δt = 0.0124 seconds, and only one cycle was saved. Figure 4.6 is a representative velocity vector field for this case. The complete cycle of vorticity contours can be found in Appendix B.

(iii) Target airfoil at $\alpha = 10°$: collision

One goal of this research was to study the direct encounter of the vortex and airfoil. But the interaction is a nonlinear process, so small adjustments in the position of the target airfoil sometimes yielded disproportionate changes in the vortex trajectories. Adjusting the airfoil's position involved draining the water tunnel (570 gallons), opening the test section, moving the airfoil, closing the test section, refilling the tunnel, and seeding the flow. Preliminary measurements could be made immediately upon seeding the flow, however, air bubbles trapped in the system drastically increased turbulence levels in the test section. At least twelve hours were required to bleed the tunnel of trapped air.

At this stage, the window method was first applied to airfoil-vortex interaction measurements. In order to facilitate the alignment process, velocity measurements were made along only two survey lines, separated by a small distance, and located just upstream of the airfoil's leading edge. Vorticity, as a function of time, was calculated along the column, and vorticity fields were constructed by assuming that, over short distances, the vorticity propagates with the local velocity. Determining the location of the vortex from so few measurements greatly accelerated the alignment process. Moreover, this

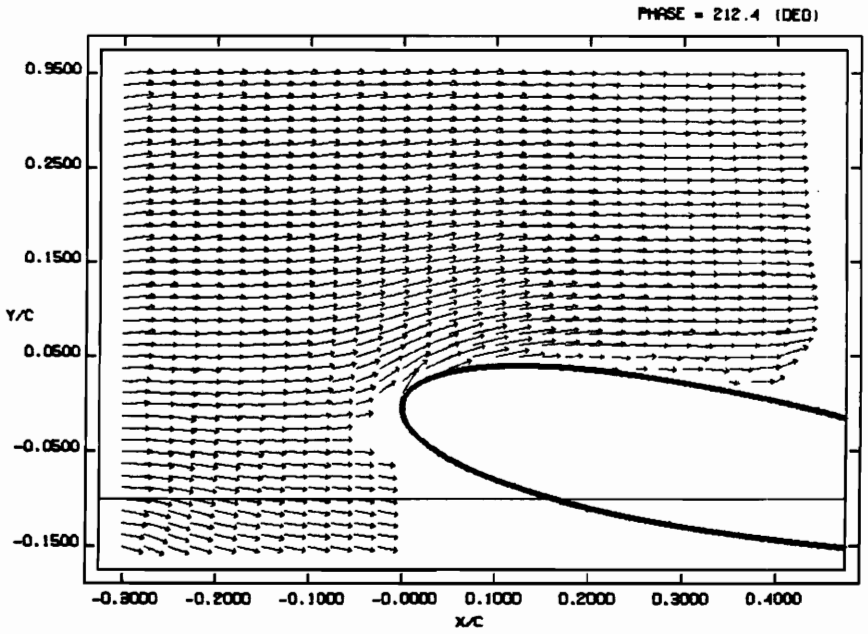

Figure 4.6. Instantaneous velocity vector field, $\alpha = 10°$.

preliminary study indicated that the window method could be used to study the interaction.

With the airfoil positioned for a direct encounter, a complete series of measurements was made. Each measurement window consisted of a pair of survey lines separated by the distance $\Delta x/c = 0.0125$. The survey lines covered the range $-0.4 \leq y/c \leq 0.4$, with a step size of $\Delta y/c = 0.005$ in the boundary region of the target airfoil and $\Delta y/c = 0.0125$ elsewhere. The windows were centered at,

$$
\begin{aligned}
x/c &= -0.20 \\
&= -0.06 \\
&= 0.05 \\
&= 0.15 \\
&= 0.30 \\
&= 0.45 \\
&= 0.575 \\
&= 0.725 \\
&= 0.85 \\
&= 0.978 \quad \text{(trailing edge at 2nd column in window)} \\
&= 1.05 \\
&= 1.20.
\end{aligned}
$$

The time resolution was doubled over the previous case, giving $\Delta t = 0.0062$ seconds, and measurements were recorded for 200 instances over the period of the vortex generator ($T = 1.24$ seconds). Appendix C contains a complete sequence of the velocity and vorticity fields, and a representative velocity vector field in given in Fig. 4.7.

4.4 Results for the Unsteady Measurements

Streamlines in the wake of the vortex generator take on a wavy pattern due to the street of alternating vortices. Hence, at any point in the wake, the angle that the velocity vector makes with respect to the streamwise direction varies periodically, as shown in

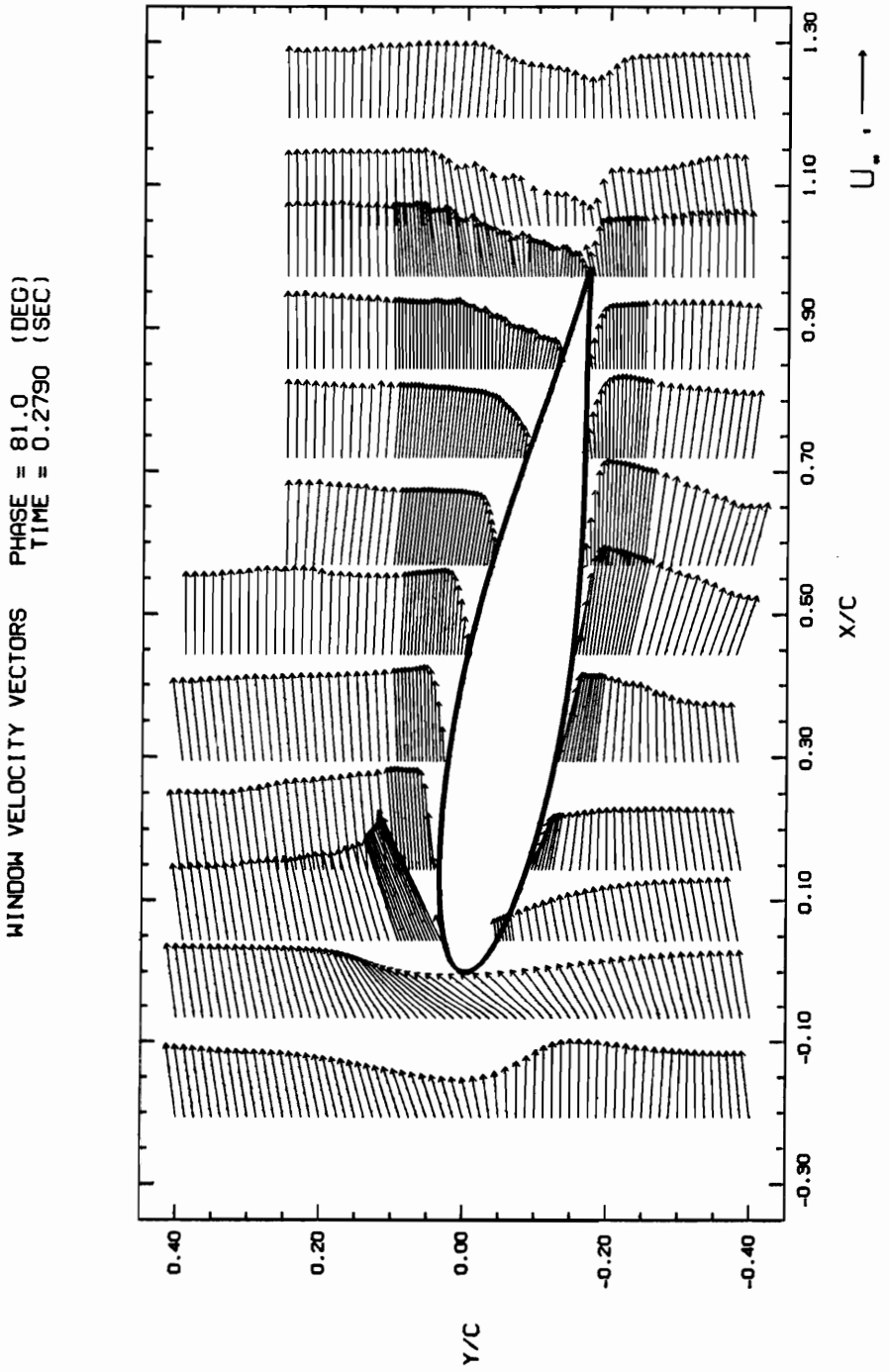

Figure 4.7. Instantaneous velocity vector field, $\alpha = 10°$ (direct encounter).

Fig. 4.8. As a result of the velocity induced by the interaction of the vortices with the solid surface of the airfoil, the flow angle is noticeably higher with the blade is immersed in the wake. A second notable feature of Fig. 4.8 is that the curves are not symmetrical, even along the symmetry line of the undisturbed wake. The positive rise in flow angle after $\phi = 180°$ is attributable to the small concentration of vorticity associated with the primary negative vortex.

The vortices periodically induce a high apparent angle of attack to the flow at the airfoil's leading edge. Based on the velocity vector fields (Fig. 4.11 and appendices A, B and C), the angle of the stagnation streamline during the approach of the positive vortex is roughly that of the flow angle at $y/c = -0.05$, shown in Fig. 4.8. Therefore, in the leading edge region of the airfoil, the flow is similar to that of an airfoil oscillating in pitch. The flow angle periodically exceedes the static stall angle of approximately 14°, and the flow exibits some features of dynamic stall. Since the high flow angles are localized to the neighborhood of the vortices, however, the stall is localized to the leading edge. As the positive vortex approaches the airfoil in the $\alpha = 10°$ cases, a secondary vortex forms at the leading edge, and extends over the first 20% of the upper surface. The secondary vortex is subsequently washed downstream with the primary vortex. In the $\alpha = 0°$ case, the strong secondary vroticity is not present. The trajectory of the primary and secondary vortices is illustrated in Fig. 4.9. The symbols indicate the location of the vortex core, which was determined from the vorticity contour maps found in the Appendices.

The circulation of the primary vortex and of the secondary vorticity at the boundary of the airfoil was calculated at each measured time instant, and the results are presented in Fig. 4.10. The circulation was determined by summing the vorticity, calculated from the measured velocities, over the area containing the vorticity; i.e.,

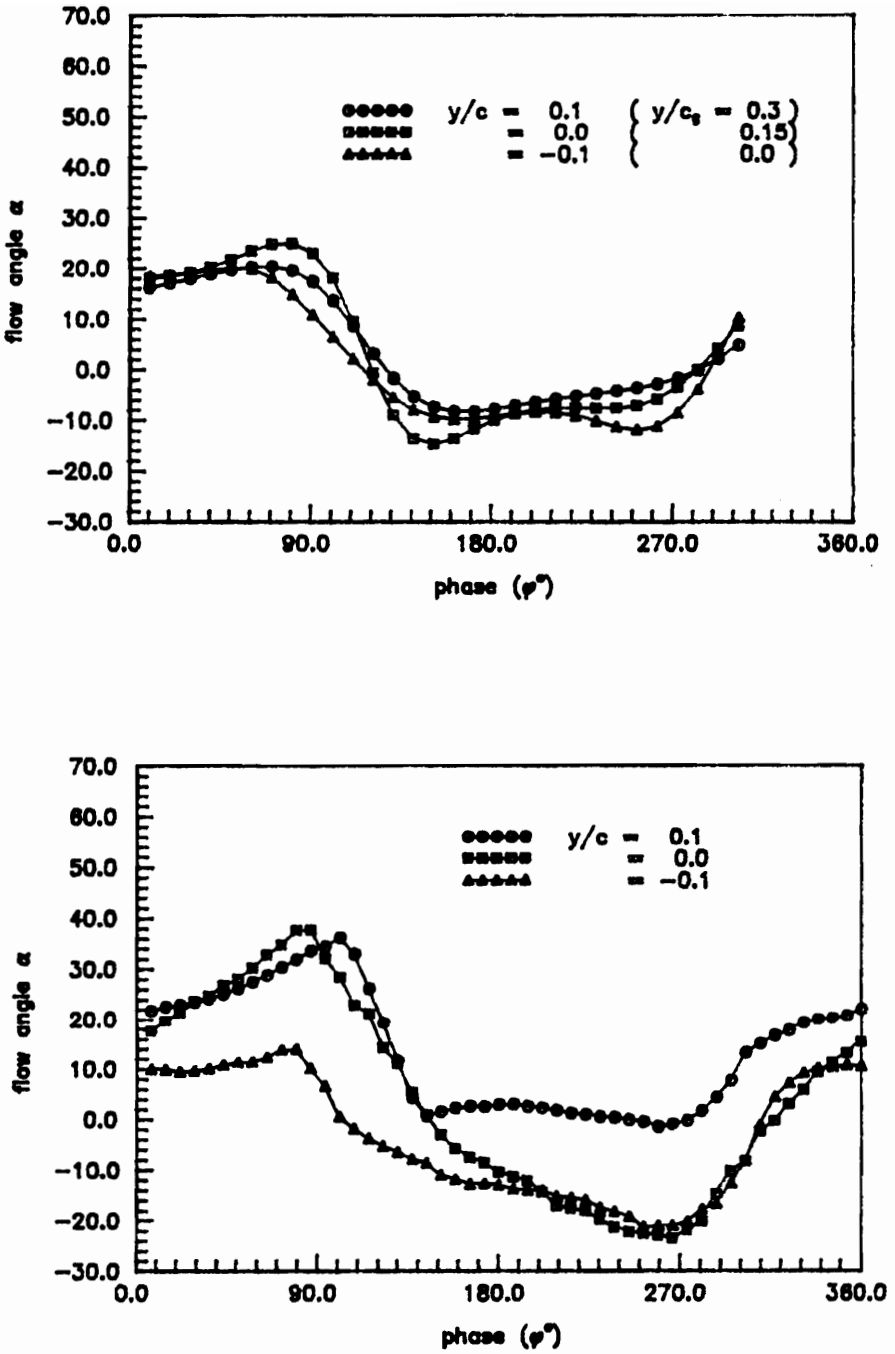

Figure 4.8. Periodic variation of the flow angle of incidence: (a) undisturbed wake, x/c = 0 (b) blade model in wake, x/c = -0.05, $\alpha = 0°$, $\Delta h = 0.09c$

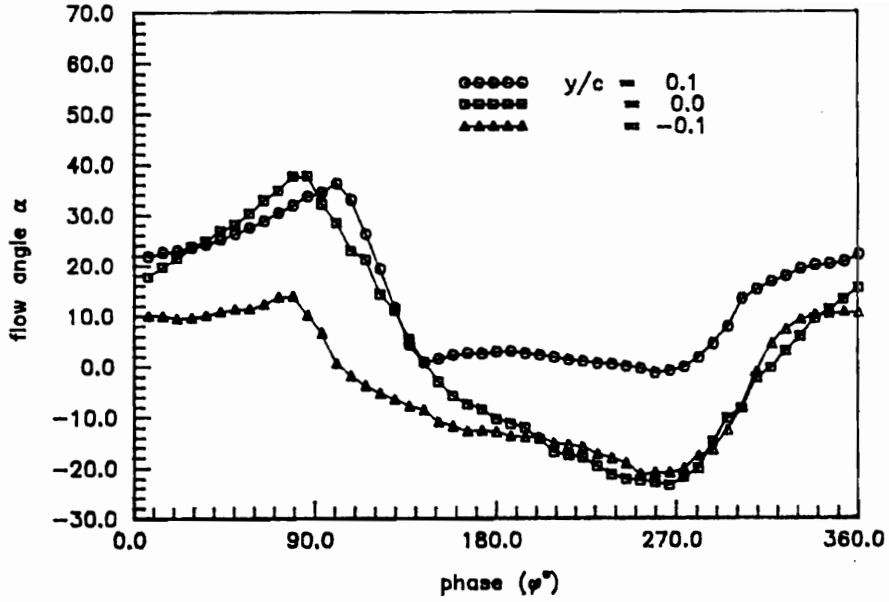

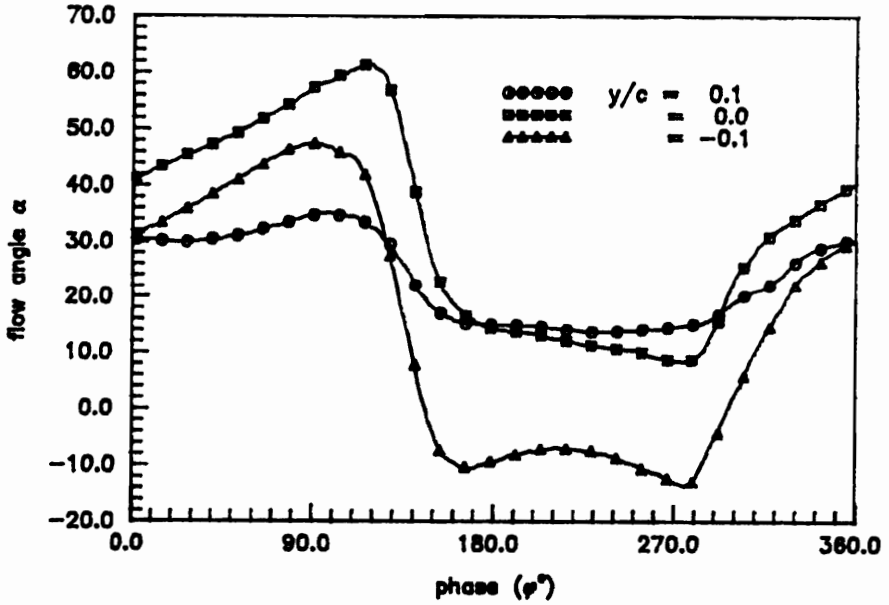

Figure 4.8. continued: blade model in wake (c) x/c = -0.05, $\alpha = 10°$, $\Delta h = 0.1c$ (d) x/c = -0.05375, $\alpha = 10°$, $\Delta h = 0.125c$

$$\Gamma = \sum_{i,j} \Omega_{i,j} \Delta x \Delta y \,, \qquad [4.3]$$

where Δx and Δy are the step sizes used in the finite-difference calculations of the vorticity. With the airfoil at $\alpha = 0°$, the strength of the vortex decreased by 30% of its upstream value while passing along the airfoil surface. The vorticity associated with the airfoil's boundary layer varied little throughout the encounter, increasing slightly (8% of the upstream circulation of the positive primary vortex) until the vortex passed the leading edge, then decreasing 14% as the vortex traveled from the leading edge to x/c = 0.25 (phase, $\phi = 158.4°$). At all times, the boundary layer circulation was less than half the strength of the primary vortex. We see from the vortex trajectory (Fig. 4.9a) that the vortex is in close proximity to the airfoil's surface. Friction between the fluid and the surface of the airfoil retarded the vortical motion of the flow, resulting in the net decrease in the total circulation of the vortex.

It was observed that the vortex had a considerably stronger influence on the boundary layer when the airfoil was at an angle of attack. With the vortex still 0.2 chordlengths upstream of the airfoil at $\alpha = 10°$, the circulation in the boundary layer was equivalent in magnitude to that of the vortex. The circulation grew 23% during the approach of the vortex and another 19% as the vortex traveled from the leading edge to x/c = 0.25 ($\phi = 158.4°$). This growing circulation is associated with the secondary vorticity generated at the airfoil's leading edge. Unlike the $\alpha = 0°$ case, the primary vortex suffered little during this encounter; only a 9% decrease in circulation was observed. The strong secondary vorticity isolated the primary vortex from the airfoil's surface (and the frictional losses experienced in the $\alpha = 0°$ case.) The secondary and primary vortices were arranged such that a jet-like flow, in the streamwise direction, was

produced between them (observable in the velocity vector profiles of Fig. 4.11). The primary vortex was cut in two in the head-on collision case and the circulation of each peice was only a fraction of the upstream vortex strength.

Vorticity fields for each of the three interaction cases are compared with one another in Fig. 4.11. The vorticity maps illustrate the trajectory and distortion of the vortices. On each page, the primary positive vortex is shown at the same x/c-location for the three cases of data. Notice that, as the vortex moves downstream, the three cases become out of phase with one another. The mutually induced velocity, between airfoil and vortex, is highly dependent not only on angle of attack of the airfoil, but also on the closeness of approach of the vortex. The maps are level contours of non-dimensional vorticity, $\Omega \frac{c_g}{U_\infty}$, shown in alternating bands of black and white, each band being two units wide, and the lowest band beginning with a magnitude of $\Omega \frac{c_g}{U_\infty} = 2$. Positive vorticity (counterclockwise rotation) is denoted by black contour bands, and negative vorticity by gray bands. Some velocity vectors are included in the figures.

Fig. 4.12 depicts the non-dimensional cross-sectional circulation $\frac{\Gamma}{U_\infty c_g}$ as a function of time at several locations in the flow. The vertical reference line on each plot indicates the phase at which the vortex core passed that particular location, and cooresponds with the phase of the contour maps in Fig. 4.11. The circulation associated with primary vortices is designated as Pp and Pn for the positive and negative vortices, respectively, and Sn designates the secondary negative vorticity (the stall vortex).

With the exception of the $\alpha = 0°$ case (i), we see evidence that a stall vortex begins forming at the leading edge when the primary positive vortex is still more than 0.2 chordlengths upstream ($\phi = 45$&deg), and the primary negative vortex is beneath the airfoil at approximately x/c = 0.35. There is a growing bulge in the vorticity (negative vorticity) at the leading edge which extends over nearly 20% of the chord. This growing stall vortex is more evident in the circulation time records of Fig. 4.12. At the x/c lo-

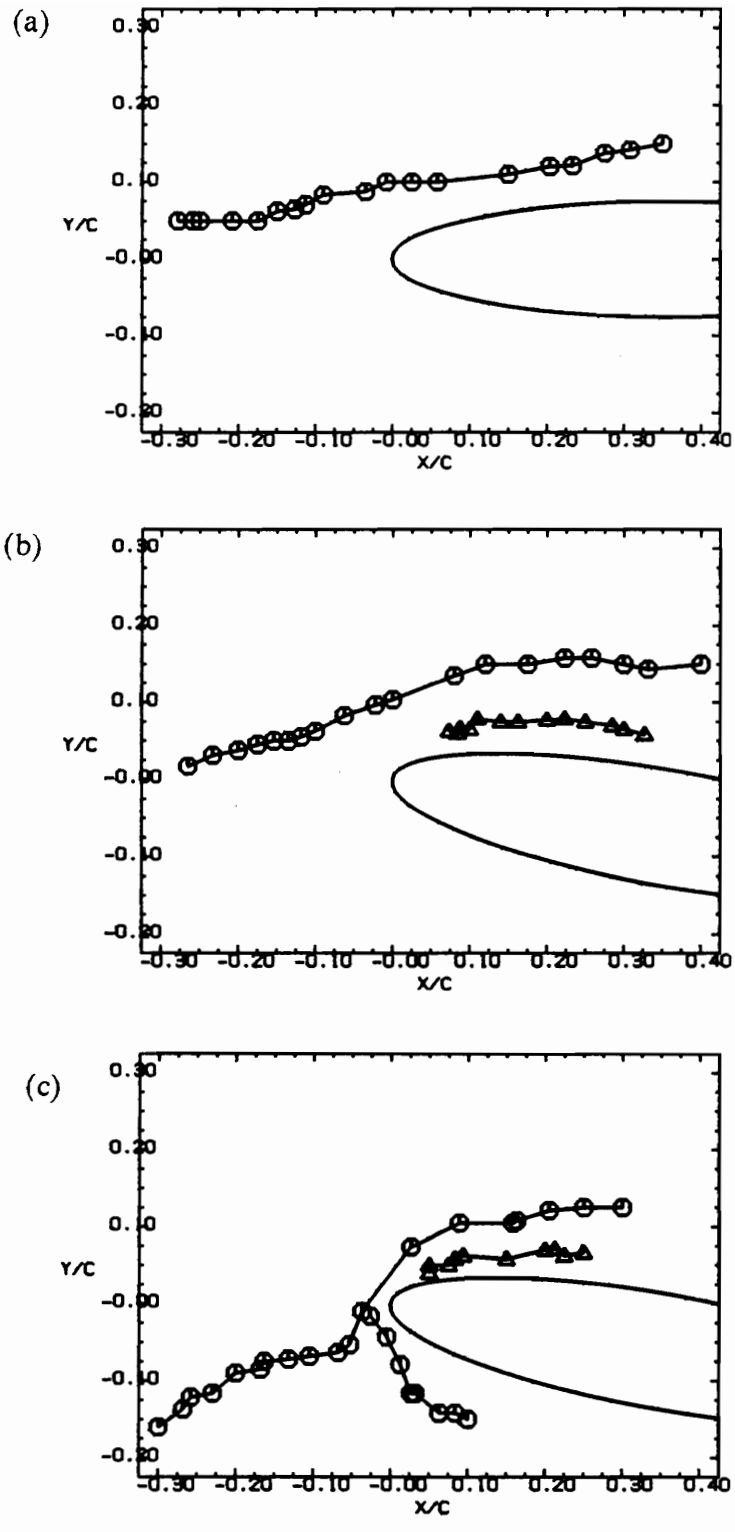

Figure 4.9. Trajectory of primary and secondary vortices for each case: (a) $\alpha = 0°$, $\Delta h = 0.09c$ (b) $\alpha = 10°$, $\Delta h = 0.1c$ (c) $\alpha = 10°$, $\Delta h = 0.125c$

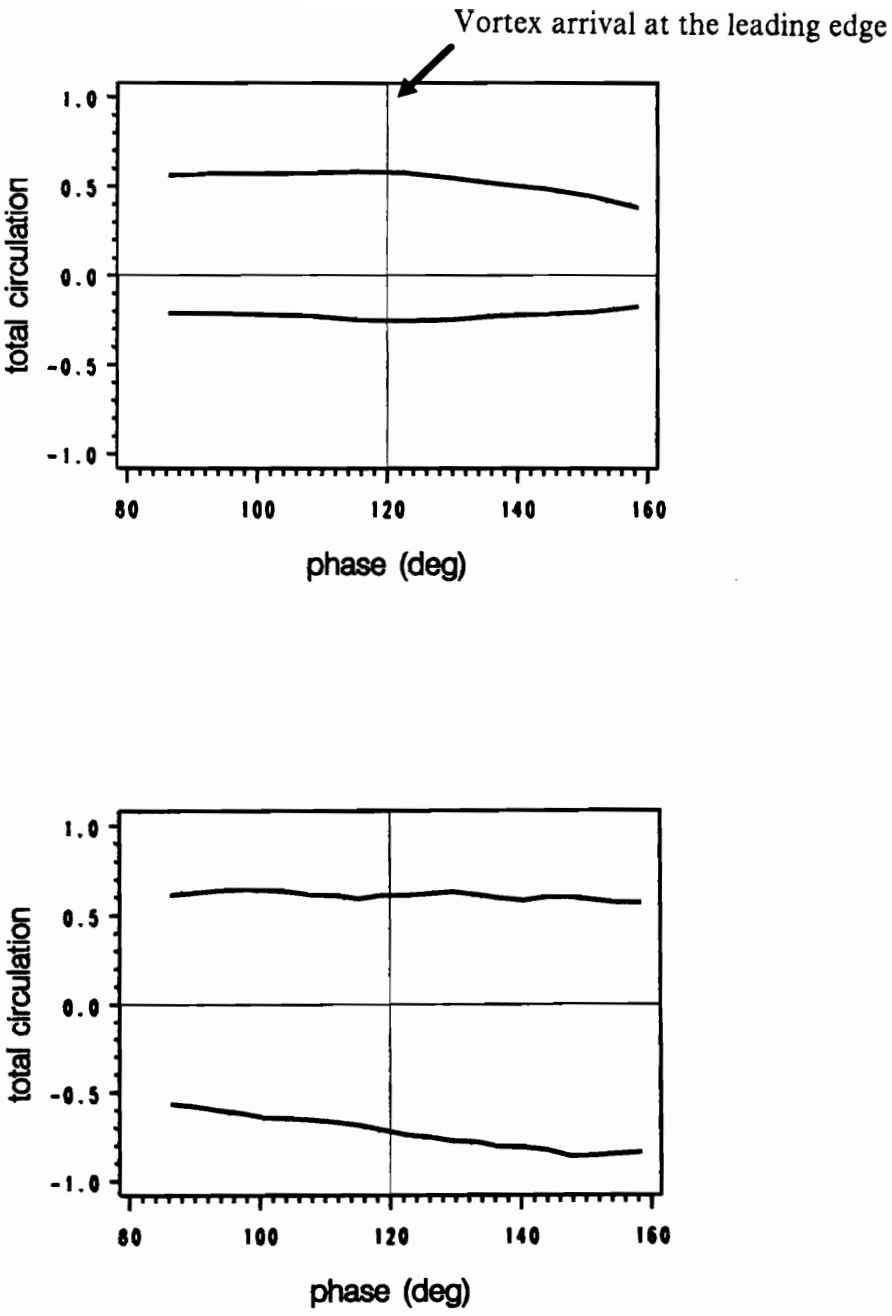

Figure 4.10. Variation of primary and secondary circulation during the interaction: (a) $\alpha = 0°$, $\Delta h = 0.09c$ (b) $\alpha = 10°$, $\Delta h = 0.1c$

cation of 0.05 we see that the negative circulation begins to grow at $\phi \simeq 45°$. It achieves its maximum when the primary vortex reaches the same station, and then propagates downstream with the primary vortex. At successive x/c stations, the primary and secondary circulations have similar temporal extents and peak at appoximately the same phase, indicating that the two vortices move together, which is observable in the vorticity contour maps. Refering to Figure 4.8 on page 96, we see that the growth of the leading edge stall vortex corresponds with the period of increasing flow angle. When the primary positive vortex reaches the leading edge a rapid decrease in flow angle occurs and the stall vortex begins to move downstream.

Care must be taken in interpreting the circulation flux information. Taking case ii as an example, as the primary vortex passes over the leading edge it accelerates and is elongated into an oval shape. The elongation has the effect of locally decreasing the vorticity, as the vorticity is spread out over a larger area. Comparing the circulation flux at x/c = -0.2125 and at x/c = 0.0625, there is a 30% decrease in the maximum circulation while both peaks have the same width ($\Delta\phi \simeq 90°$). This gives the impression that the strength of the vortex has decreased by 30% while traveling between these two stations, when in reality, at the second station we are seeing a more diffuse vortex pass by at a higher speed then at the first station. This is confirmed by evaluating the total circulation of the vortex at any particular phase, as was presented in Figure 4.10 on page 101.

Unsteady surface pressure coefficients were calculated with the measured velocities and eqns. 4.1 and 4.2. Like the steady pressures, the integration paths began at the measurement station furthest upstream and above the airfoil. The variation of C_p at x/c = 0.05, 0.15 and 0.3 is displayed in Fig. 4.13. Vertical reference lines indicate the phase at which the vortex core passed the leading edge and the measurement station in question. Horizontal reference lines represent the steady pressure coefficient. For the

$\alpha = 0°$ case, the values were taken from Abbott and von Doenhoff (1959). For the $\alpha = 10°$ cases the calculated steady pressure coefficients presented in Figure 4.3 on page 87 are indicated.

In all three cases, the pressure at $x/c = 0.05$ increased as the vortex approached and became a maximum as the "edge" of the vortex reached the leading edge. This occured at a phase of 90° for cases i and ii, but not until $\phi \simeq 130°$ in the head-on collision case. By the time the vortex core passed the leading edge ($\phi \simeq 120°$ for cases i and ii) the pressure had reached a minimum. This minimum pressure did not occure in case iii where the vortex is split, indicating that the minimum pressure may depend on the strength of the vortex. A second maximal value, which occured around a phase of 130° in the first two cases, can be associated with vortex core moving beyond $x/c = 0.05$. After the vortex has moved beyond $x/c = 0.3$, the pressure settled down to a relatively constant value at $x/c = 0.05$. This constant value was very near the steady value of pressure for cases i and ii, but lower for case iii.

On the next two stations, $x/c = 0.15$ and 0.3, case ii more closely resembles case iii (the other $\alpha = 10°$ case) than case i (the other close-encounter case). The peak in the pressure time record of cases ii and iii is associated with the edge of the primary/secondary vortex pair arriving at each station. The pressure becomes steady after the vortices have passed. This indicates that the effects at the leading edge are strongly influenced by the closeness of the encounter, while the effects felt along the airfoil's length are influenced more by the airfoil's angle of attack (no secondary vortex formed in case i, the $\alpha = 0°$ case). It is generally agreed that the airfoil-vortex interaction is a leading edge phenomenon (Booth, 1986; Rockwell, 1984). A positive spike in the lower surface pressures of case iii was observed at all stations along the airfoil chord at a phase of 60 degrees. This spike does not move and cannot be associated with any structure visible in the vorticity contour maps.

The two-dimensional airfoil-vortex interaction has been numerically modeled by Poling. The extended vortex of the experiments was simulated with a cloud of discrete vortices and conformal mapping methods were utilized in computing the flow. An encounter with the airfoil at a zero-degree angle of attack was presented in Poling et al., 1988. A comparison of the computed chordwise pressure distributions with the experimental results of case i is given in Fig. 4.14. The model is of an isolated encounter with a single vortex cloud, rather than the street of vortices present in the experiments. Nevertheless, agreement between theory and experimental results is good. The direct encounter (case iii) was similarly modeled, (Poling et al., 1991). The upper-surface pressures derived from the experiental results are compared with the model in Fig. 4.15. Agreement in this case is good only until the secondary vorticity begins to form at the leading edge. There was no strong secondary vorticity generated in the $\alpha = 0°$ case of the experiments.

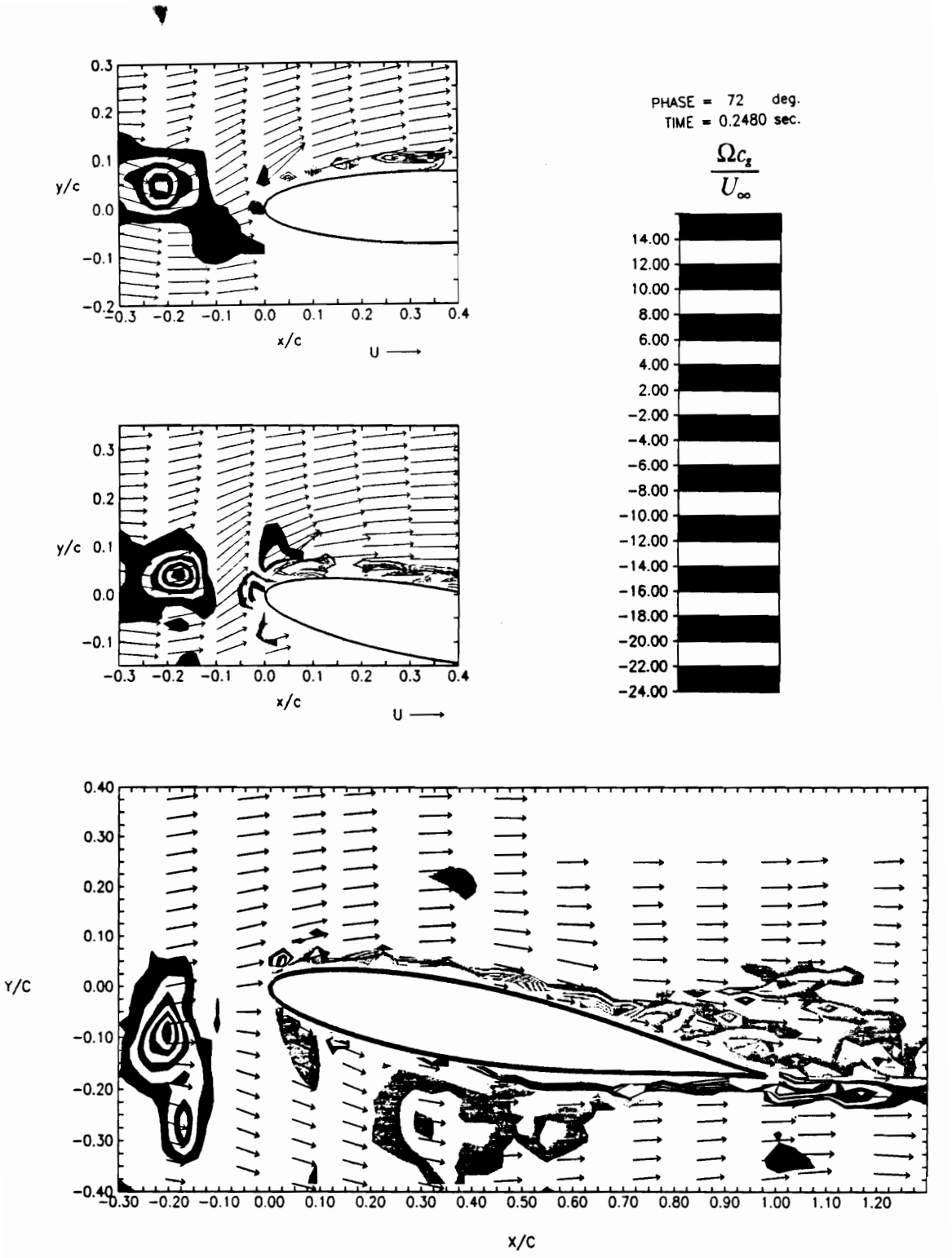

Figure 4.11. Vorticity contour maps: (a) $\alpha = 0°$, $\Delta h = 0.09c$ (b) $\alpha = 10°$, $\Delta h = 0.1c$ (c) $\alpha = 10°$, $\Delta h = 0.125c$

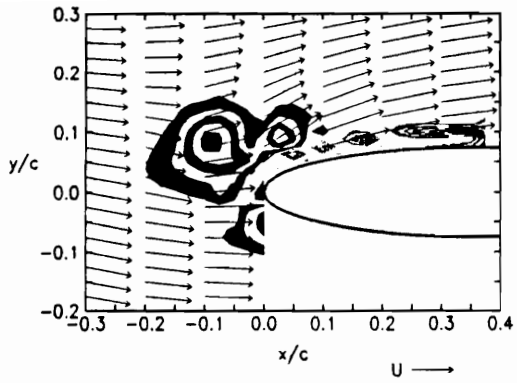

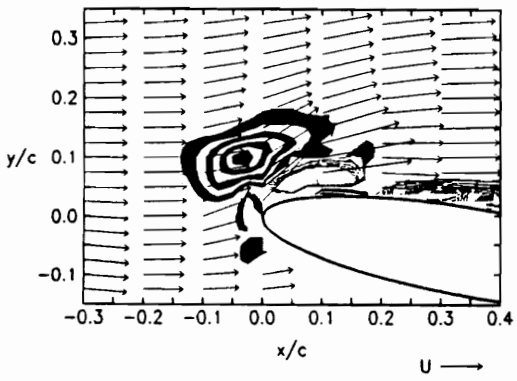

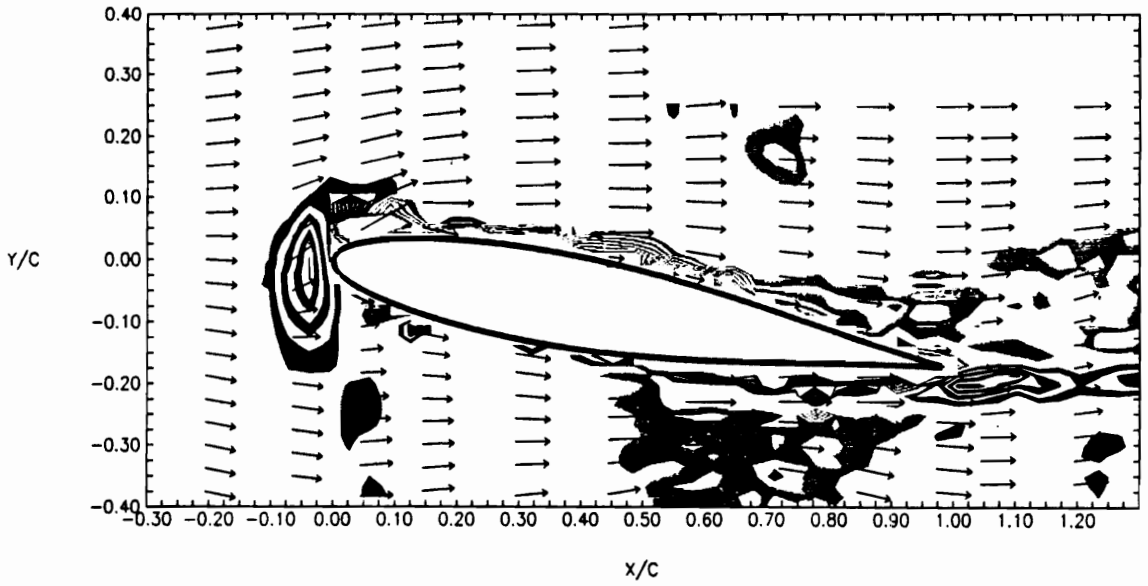

Figure 4.11. continued: (a) $\alpha = 0°$, $\Delta h = 0.09c$ (b) $\alpha = 10°$, $\Delta h = 0.1c$ (c) $\alpha = 10°$, $\Delta h = 0.125c$

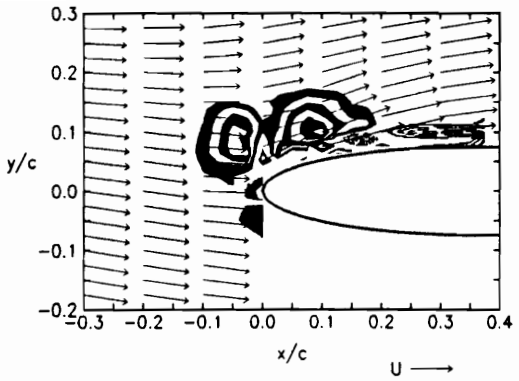

PHASE = 129.6 deg.
TIME = 0.4464 sec.

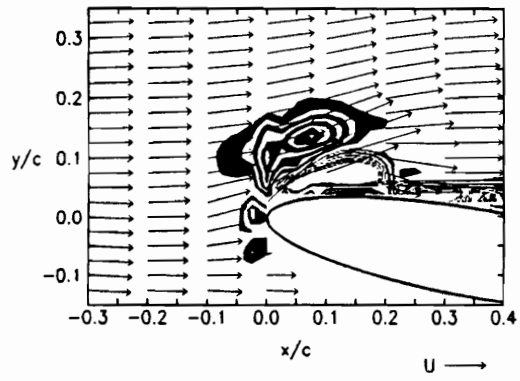

PHASE = 129.6 deg.
TIME = 0.4464 sec.

PHASE = 153 deg.
TIME = 0.5270 sec.

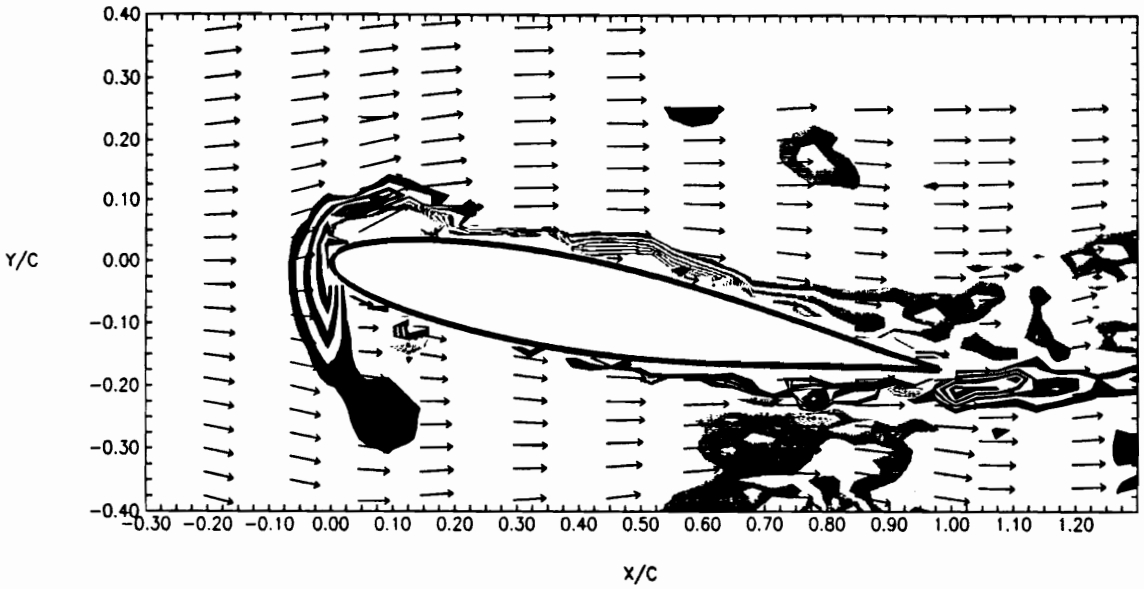

Figure 4.11. continued: (a) $\alpha = 0°$, $\Delta h = 0.09c$ (b) $\alpha = 10°$, $\Delta h = 0.1c$ (c) $\alpha = 10°$, $\Delta h = 0.125c$

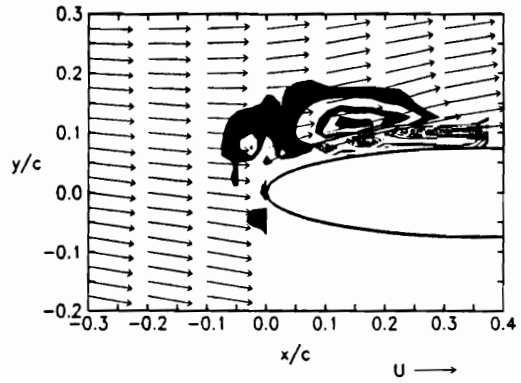

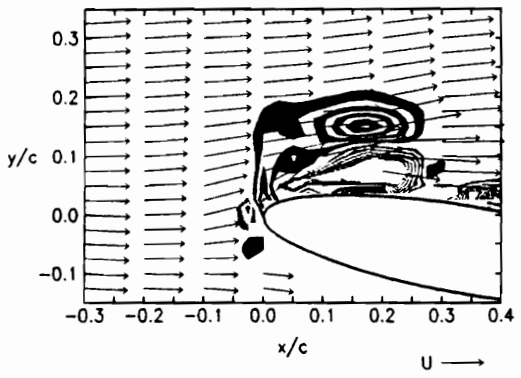

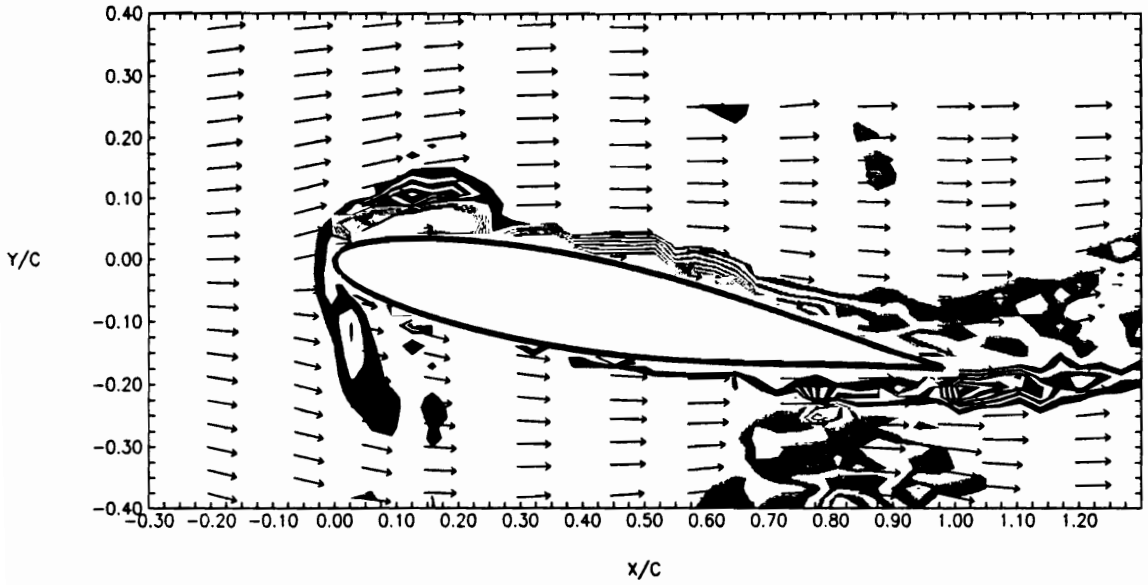

Figure 4.11. continued: (a) $\alpha = 0°$, $\Delta h = 0.09c$ (b) $\alpha = 10°$, $\Delta h = 0.1c$ (c) $\alpha = 10°$, $\Delta h = 0.125c$

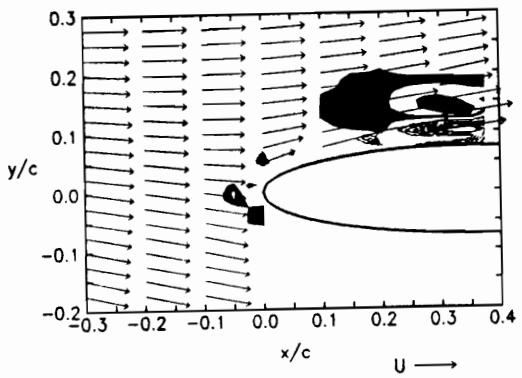

PHASE = 172.8 deg.
TIME = 0.5952 sec.

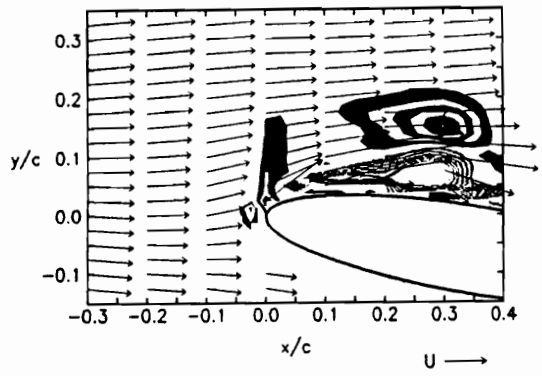

PHASE = 165.6 deg.
TIME = 0.5704 sec.

PHASE = 198 deg.
TIME = 0.6820 sec.

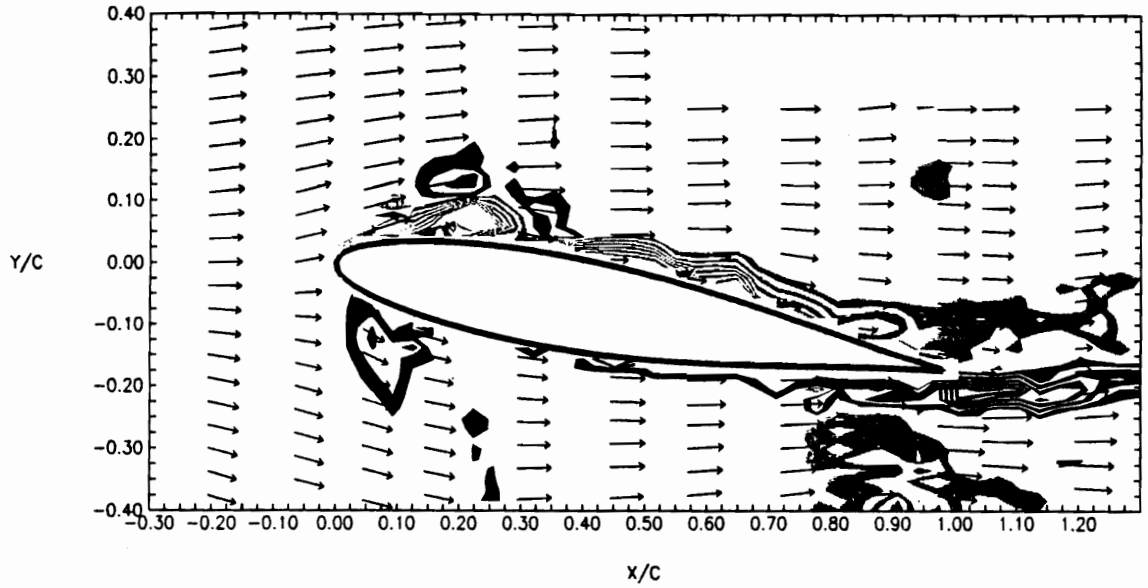

Figure 4.11. continued: (a) $\alpha = 0°$, $\Delta h = 0.09c$ (b) $\alpha = 10°$, $\Delta h = 0.1c$ (c) $\alpha = 10°$, $\Delta h = 0.125c$

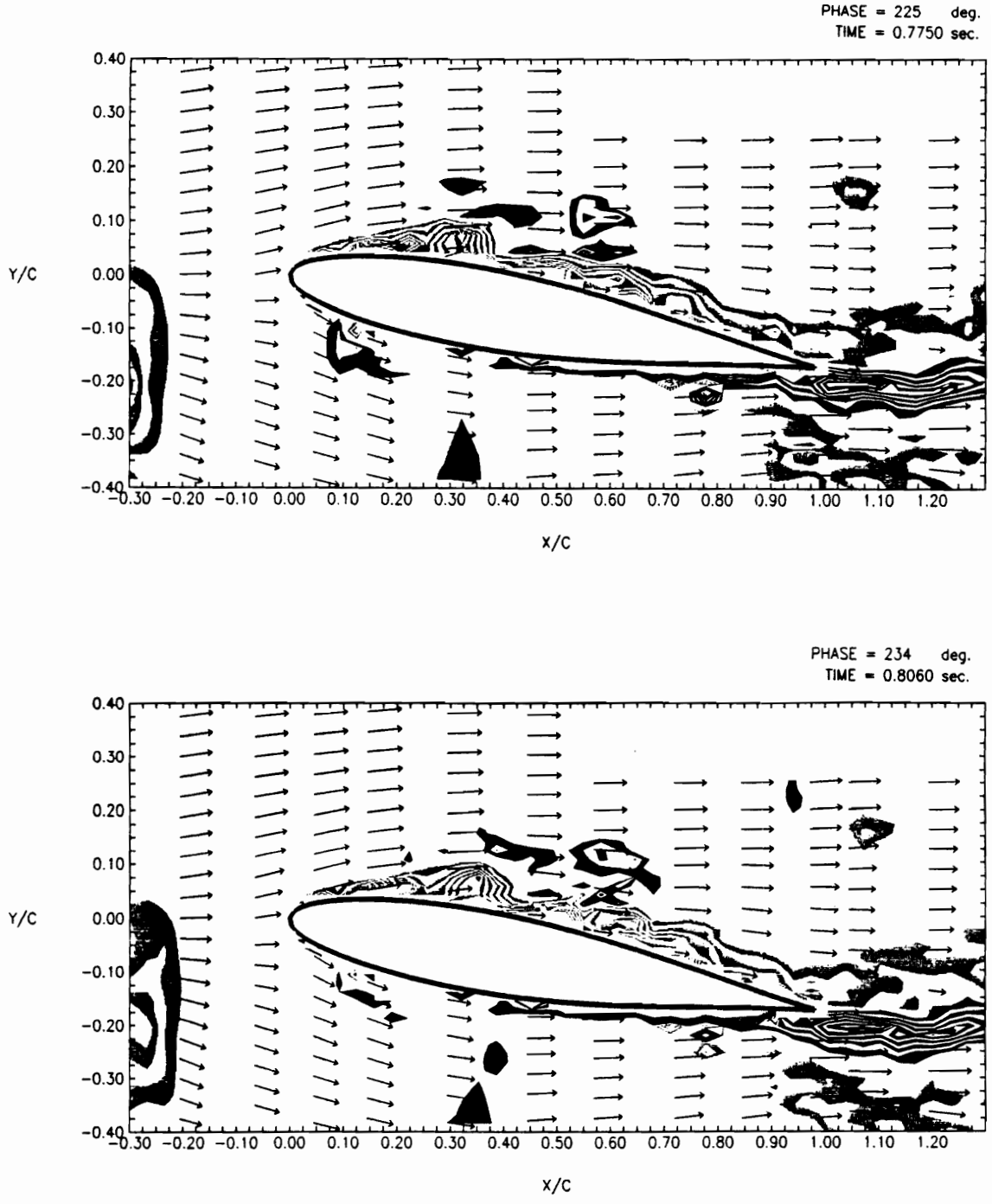

Figure 4.11. continued: (case iii only) $\alpha = 10°$, $\Delta h = 0.125c$

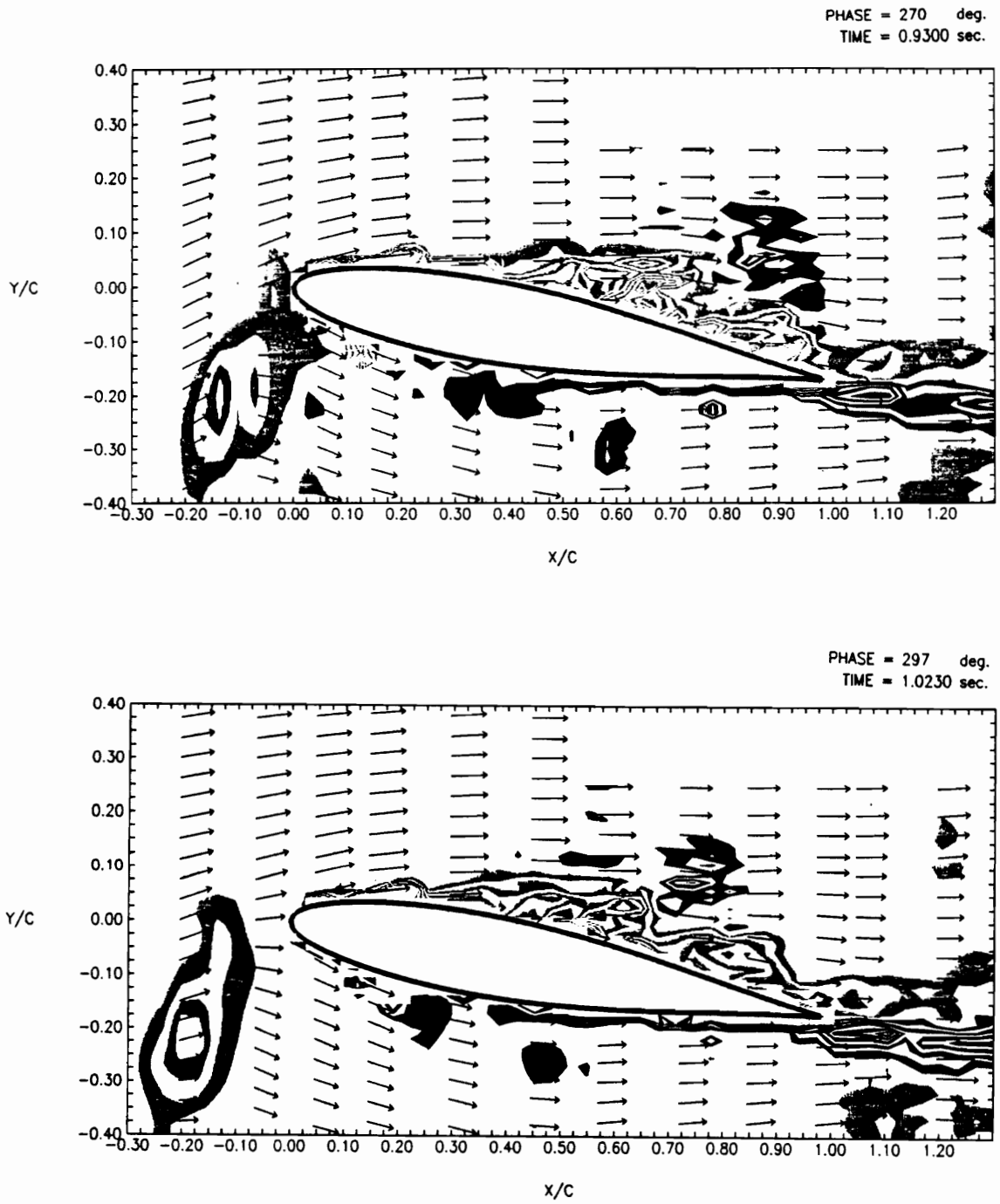

Figure 4.11. continued: (case iii only) $\alpha = 10°$, $\Delta h = 0.125c$

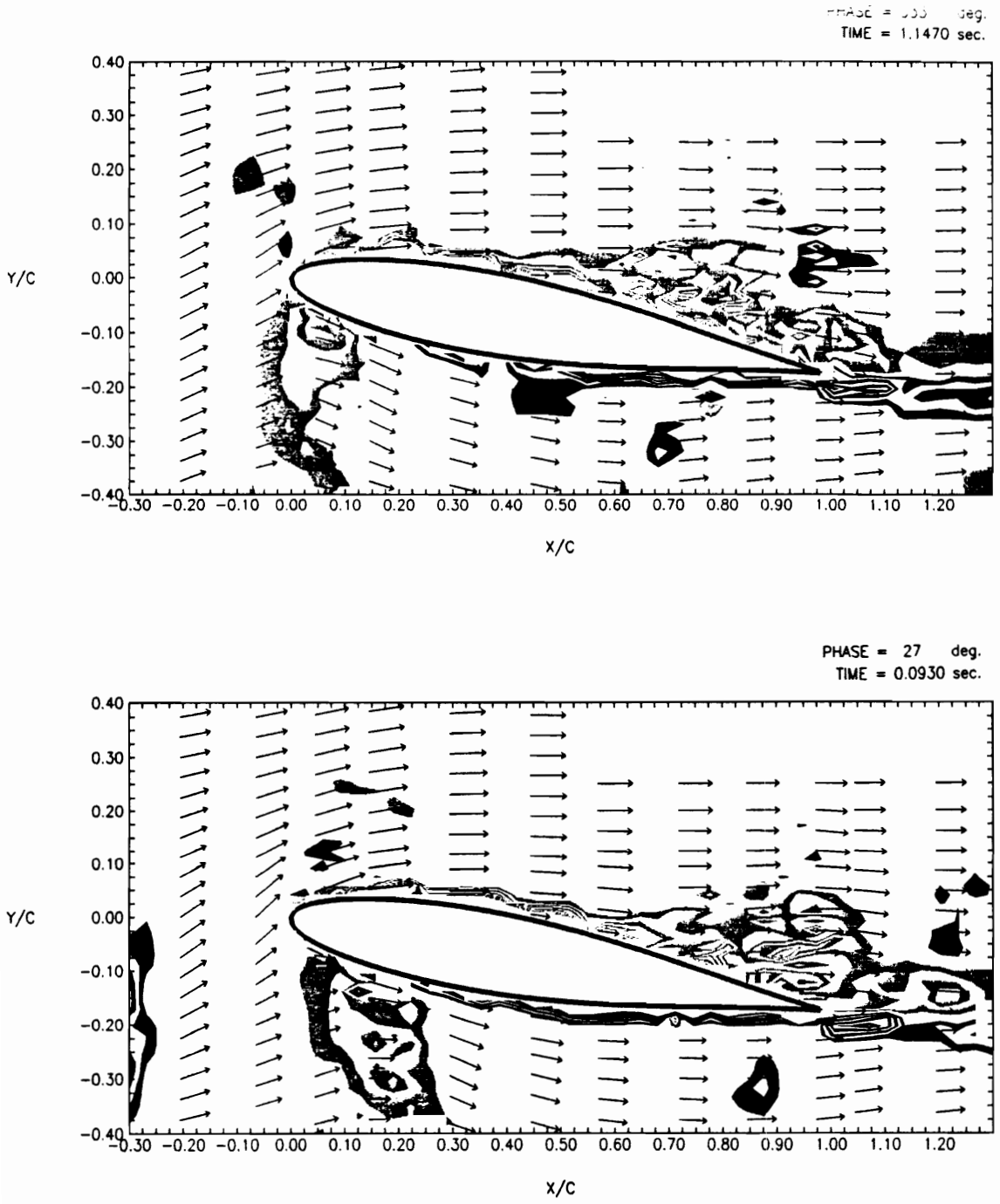

Figure 4.11. continued: (case iii only) $\alpha = 10°$, $\Delta h = 0.125c$

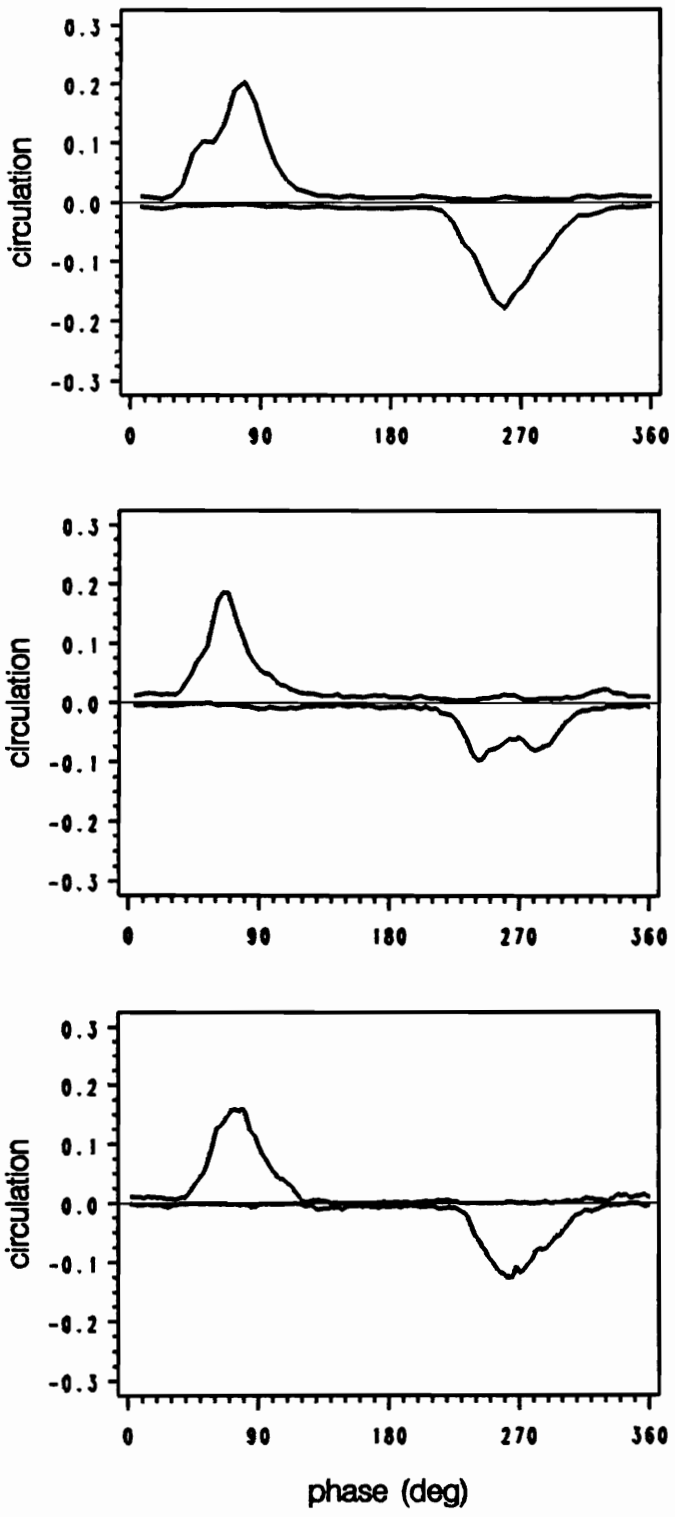

Figure 4.12. Cross-sectional circulation flux: x/c = -0.2: (a) $\alpha = 0°$, $\Delta h = 0.09c$ (b) $\alpha = 10°$, $\Delta h = 0.1c$ (c) $\alpha = 10°$, $\Delta h = 0.125c$

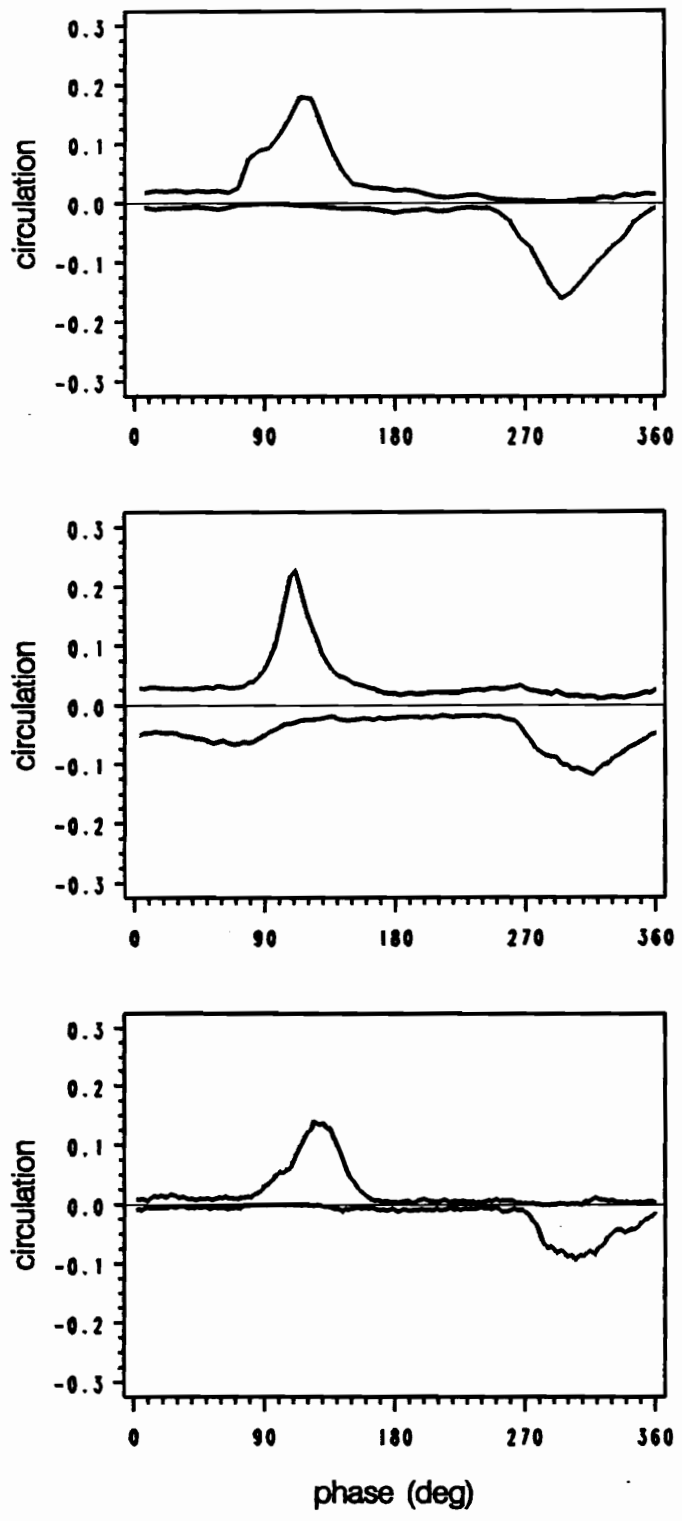

Figure 4.12. continued: x/c = -0.05: (a) $\alpha = 0°$, $\Delta h = 0.09c$ (b) $\alpha = 10°$, $\Delta h = 0.1c$ (c) $\alpha = 10°$, $\Delta h = 0.125c$

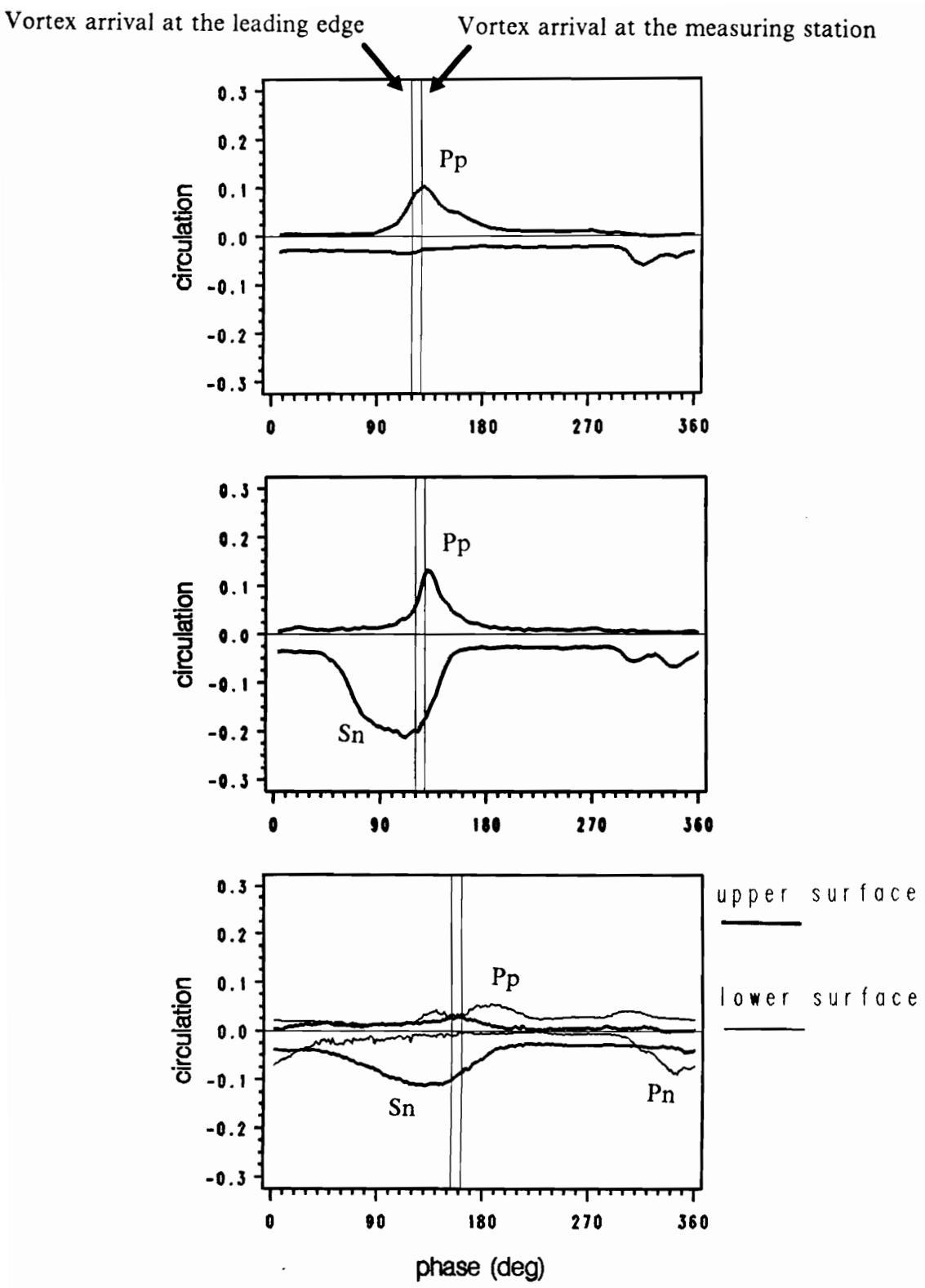

Figure 4.12. continued: x/c = 0.05: (a) $\alpha = 0°$, $\Delta h = 0.09c$ (b) $\alpha = 10°$, $\Delta h = 0.1c$ (c) $\alpha = 10°$, $\Delta h = 0.125c$

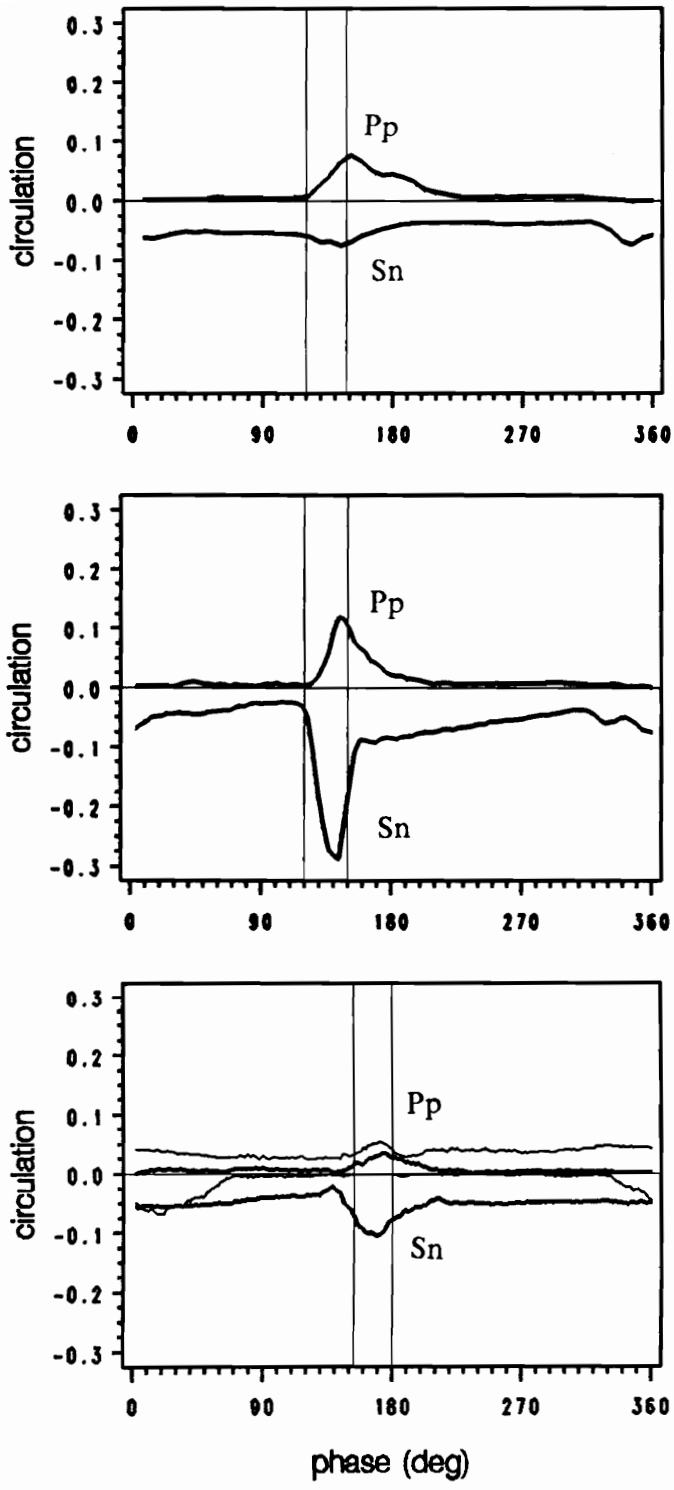

Figure 4.12. continued: x/c = 0.15: (a) $\alpha = 0°$, $\Delta h = 0.09c$ (b) $\alpha = 10°$, $\Delta h = 0.1c$ (c) $\alpha = 10°$, $\Delta h = 0.125c$

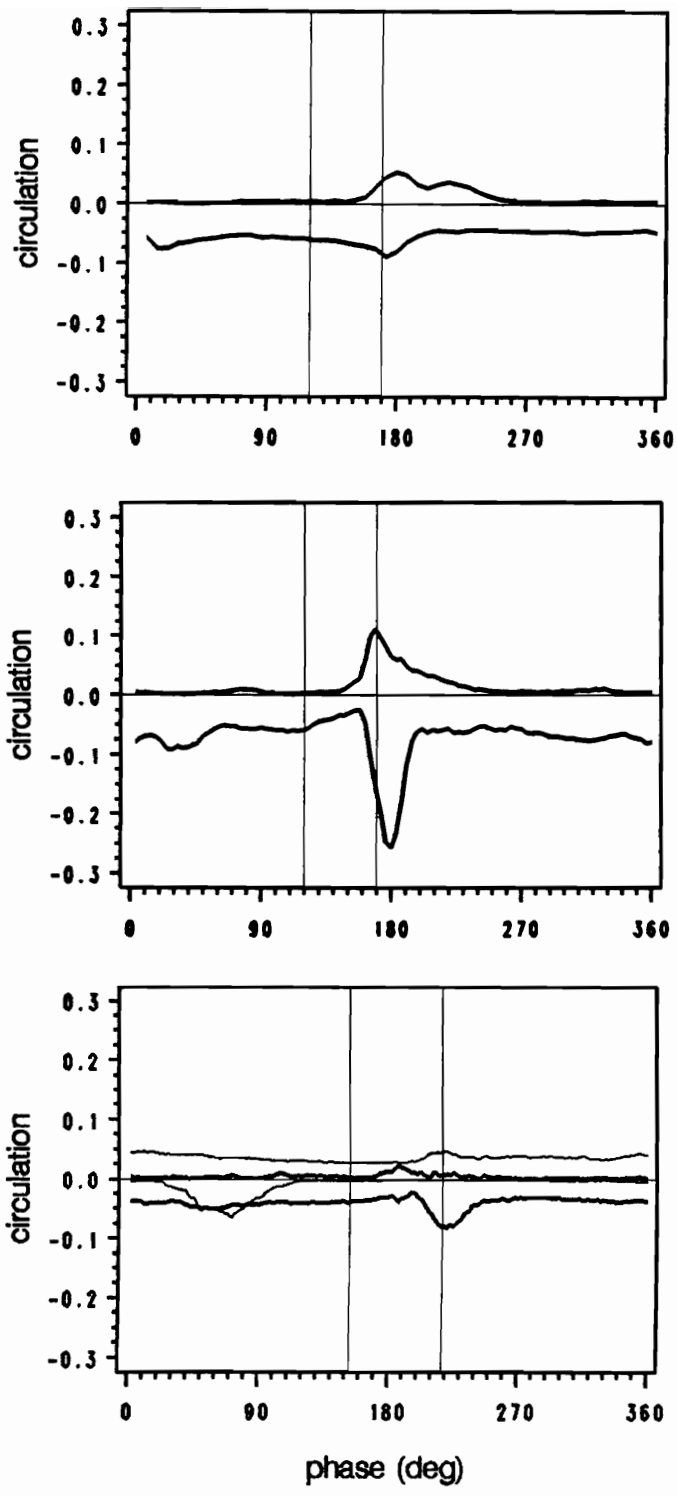

Figure 4.12. continued: x/c = 0.3: (a) $\alpha = 0°$, $\Delta h = 0.09c$ (b) $\alpha = 10°$, $\Delta h = 0.1c$ (c) $\alpha = 10°$, $\Delta h = 0.125c$

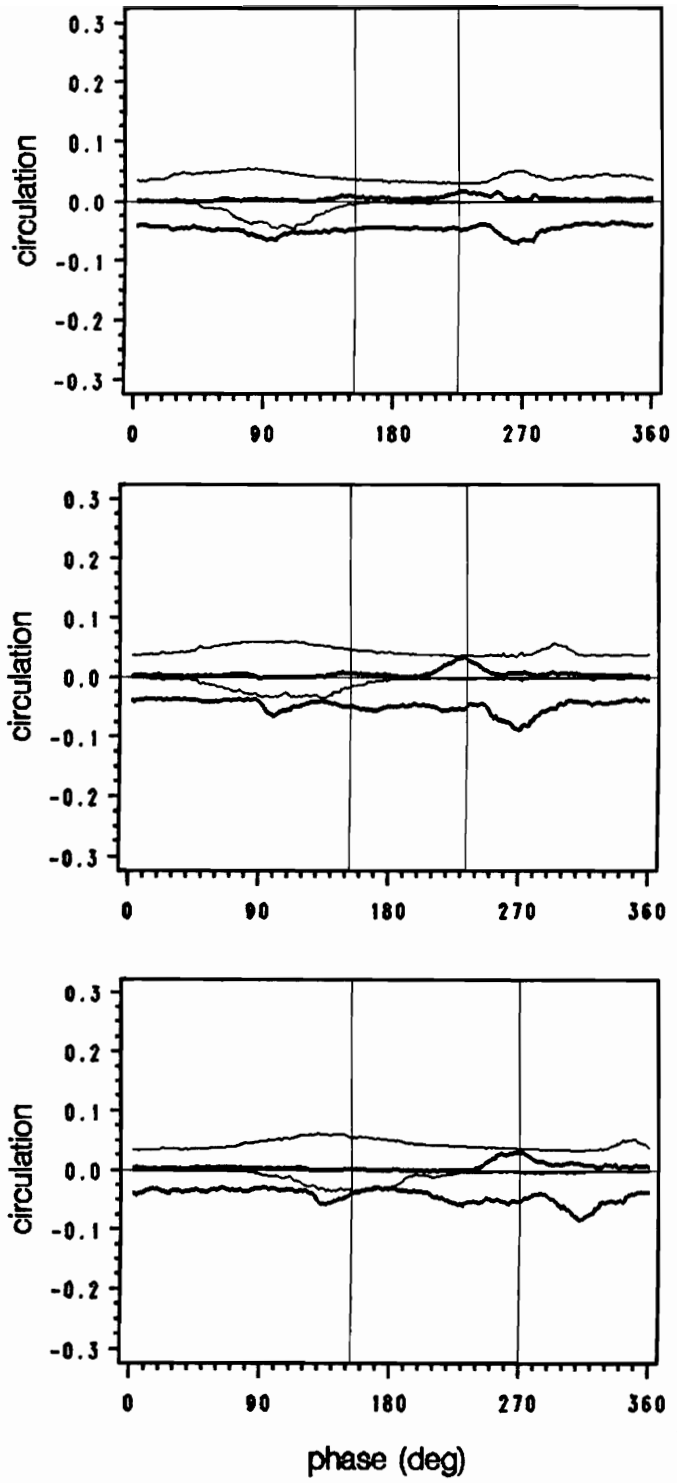

Figure 4.12. continued (case iii only): (a) x/c = 0.45 (b) x/c = 0.575 (c) x/c = 0.725

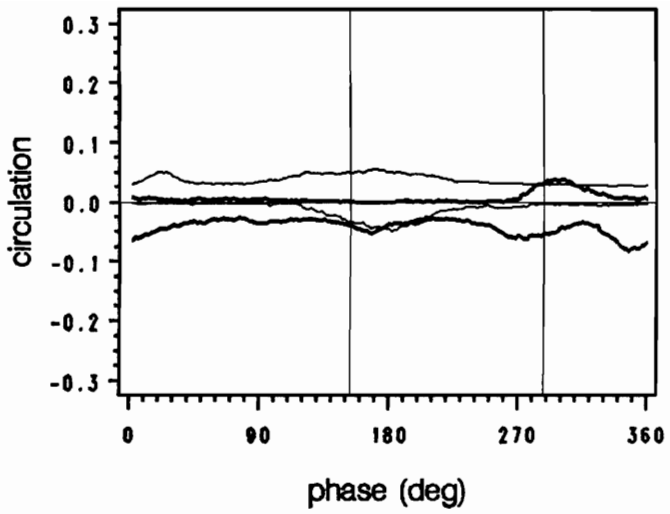

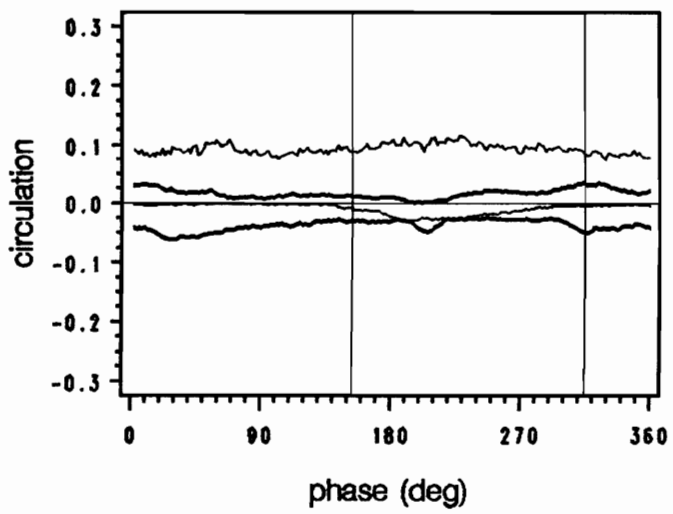

Figure 4.12. continued (case iii only): (a) x/c = 0.85 (b) x/c = 0.879 (t.e.)

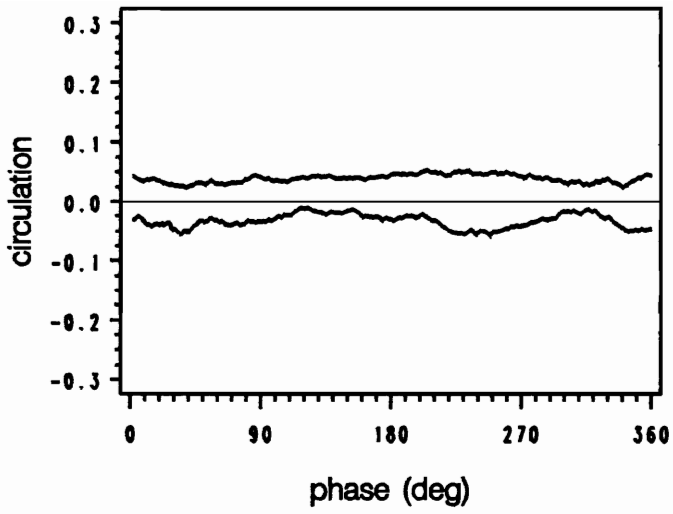

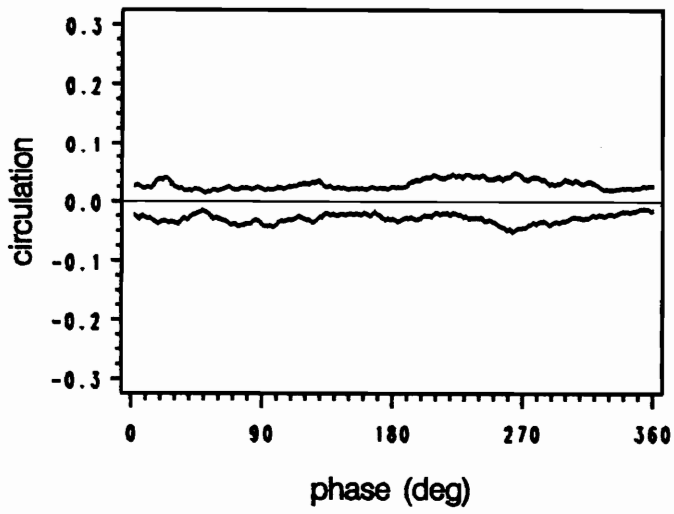

Figure 4.12. continued (case iii only): (a) x/c = 1.05 (b) x/c = 1.2

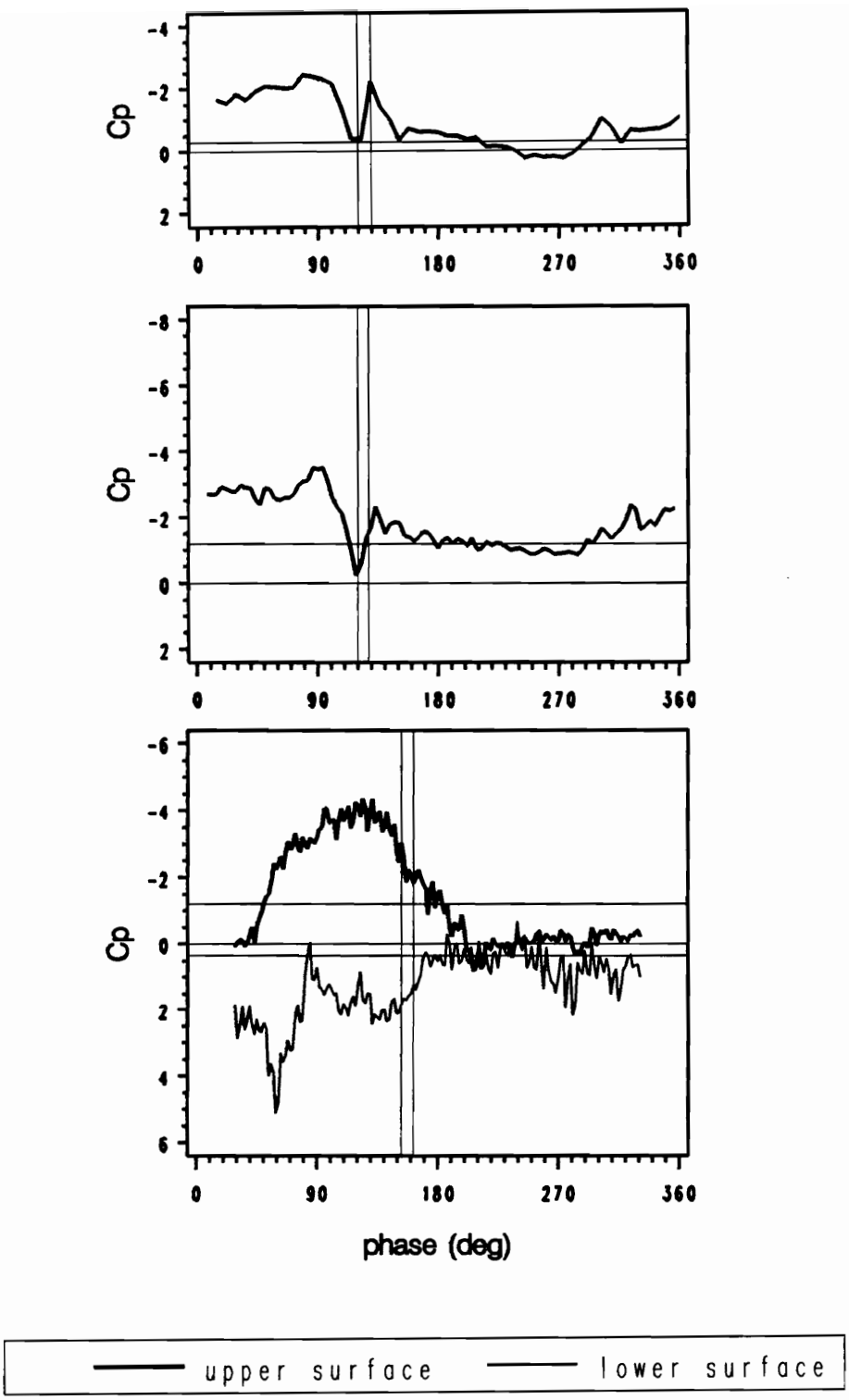

Figure 4.13. Surface pressure coefficients vs. phase: x/c = 0.05

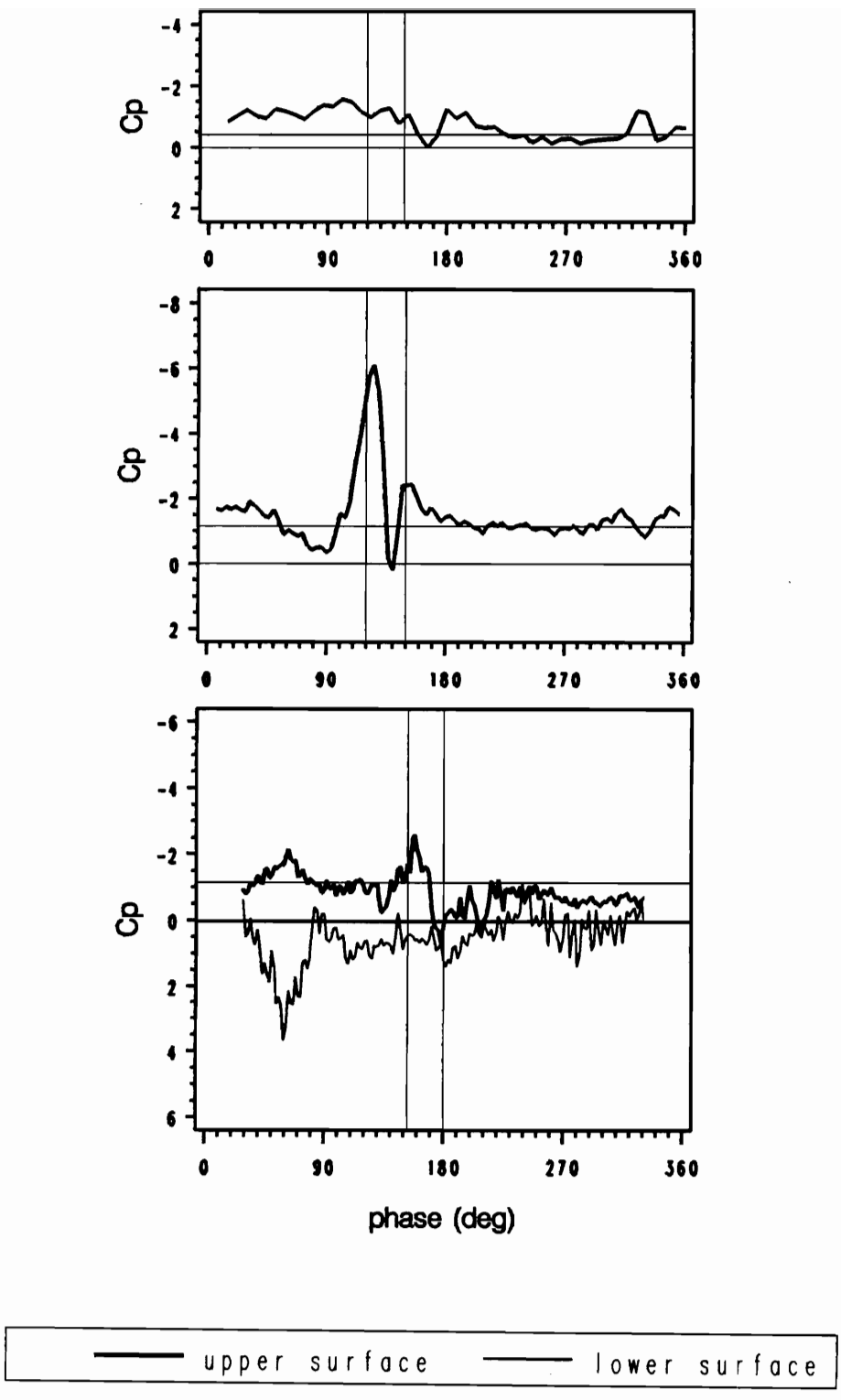

Figure 4.13. continued: x/c = 0.15

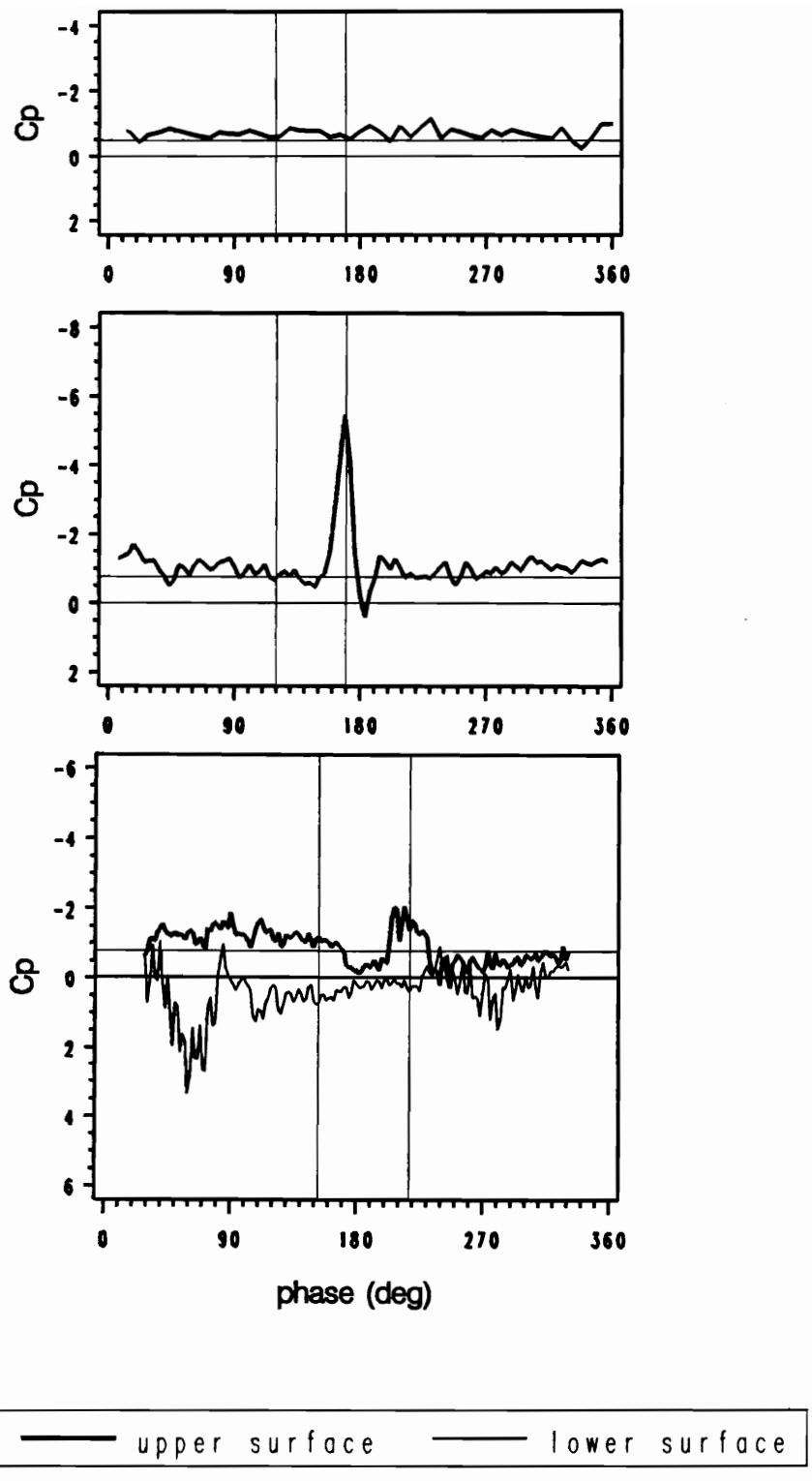

Figure 4.13. continued: x/c = 0.3

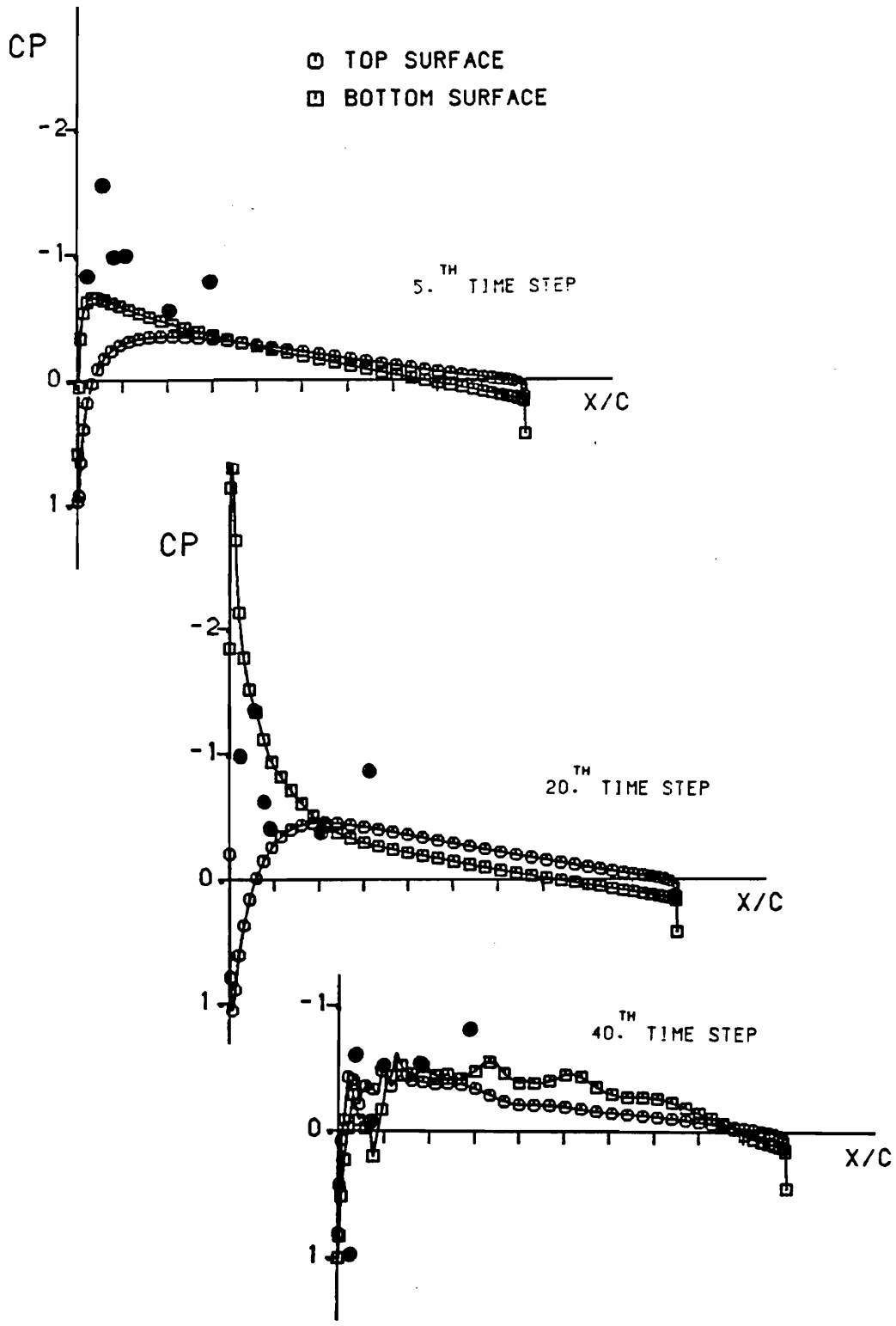

Figure 4.14. **Comparison of chordwise pressure distributions with theory: $\alpha = 0°$, source of theory: Poling et al., 1988.**

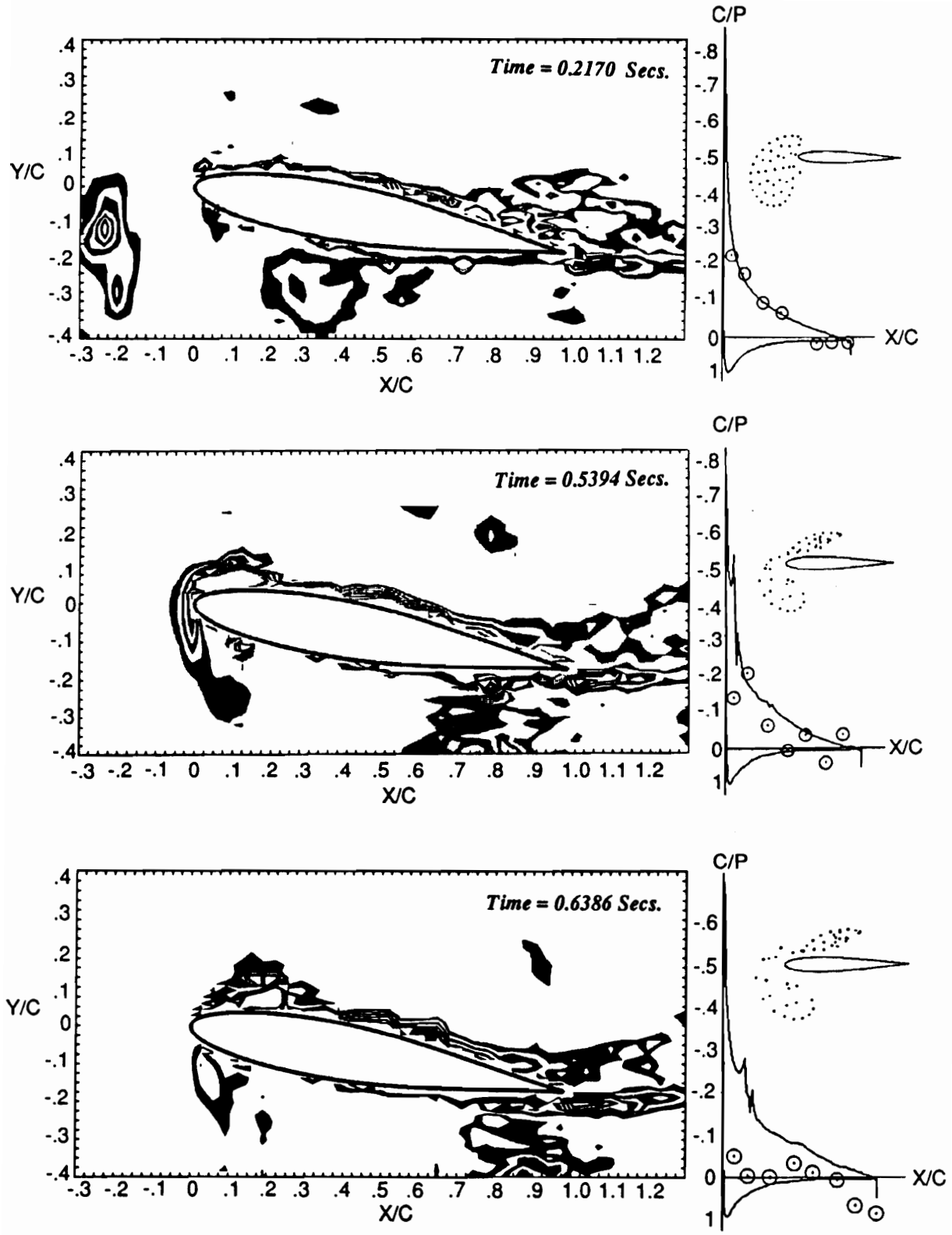

Figure 4.15. Comparison of chordwise pressure distributions with theory: $\alpha = 10°$, source of theory: Poling et al., 1991.

Chapter 5

Conclusions and Recommendations

Laser Doppler velociemetry, a non-intrusive velocity measurement technique, has been employed in a detailed investigation of the airfoil-vortex interaction phenomenon. Since the use of LDV allowed measurements very near the airfoil surface, as well as within the vortex core itself, the effect of the interaction, both on the vortex and on the vorticity of the airfoil's boundary layer could be quantitatively assessed.

Prior to investigating the interaction a detailed examination of the vortex disturbance was carried out. Vortices were generated by pitching a symmetrical NACA 0012 airfoil about its ¼-chord point. Sinusoidal oscillation at a high reduced frequency and about a zero-degree mean angle of attack resulted in the formation of a vortex street such that the top row of vortices rotated in the counterclockwise sence and the bottom row rotated in the clockwise sense. The focus of the investigation was placed on the upper row of counterclockwise rotating vortices (those with positive vorticity). A degree of control over the spacing and strength of the vortices was made possible by varying the reduced frequency or the pitching amplitude. Decreasing the reduced frequency increased the vortex spacing within the wake, but also decreased the strength of the vortices. Increasing the pitch amplitude while holding the reduced frequency constant

increased the vortex strength without altering the spacing, however, a larger vortex core diameter resulted. The interaction study required strong, widely spaced vortices in order to produce an isolated, energetic encounter. A large pitch amplitude, $\pm 10°$, and a reduced frequency of $k = 2$ were chosen. This combination of parameters is at the lower end of the roll-up wake region for an oscillating airfoil, and produced strong vortices ($\Gamma / U_\infty c_g \simeq 0.5$) with a relatively large spacing; we see in the vorticity contour maps that the spacing is about 0.7c with the target airfoil in the flow.

Two parameters controlling the nature of the interaction were varied in the experiments. First, the angle of attack of the airfoil, and second, the closeness of the encounter. A close encounter, with a counterclockwise rotating vortex skimming over the upper surface of the airfoil, was observed with the airfoil at an angle of attack of zero degrees and ten degrees. In both cases, the vortex was distorted but maintained its coherence during the encounter. In a third case, the vortex collided head-on with the airfoil at $\alpha = 10°$. The vortex was split in two, with one portion passing over the airfoil and the other passing beneath the airfoil.

Phase-averaged velocity measurements were obtained over the first forty percent of the airfoil's upper surface in the two close-encounter cases, and over the entire airfoil in the direct-encounter case. Vorticity, calculated from the velocities, was displayed as iso-level contour maps. The trajectory of the vortices as well as the distortions suffered by the vortices was discernible from these maps. Moreover, the formation of a secondary vortex at the leading edge was visible in the vorticity contour maps of the $\alpha = 10°$ cases. Area integrals of the vorticity were performed to determine the circulation strength of the vortex and of the vorticity at the boundary of the airfoil (which included the secondary vortex). It was shown that for the close encounter, the vortex was weakened during the encounter only when no strong secondary vortex was formed. Unsteady pressures were calculated by using the measurements to evaluate the velocity

derivatives of the Navier-Stokes equations. The resulting pressure gradients were integrated to give the pressure on the airfoil's surface. A pressure pulse at the leading edge was identified with the arrival of the vortex at this location. In the direct-encounter case this feature was very broad (not really a pulse), due to the deceleration of the vortex; the vortex lingered near the leading edge for a considerably longer time than in the close-encounter case. Fluctuations in the pressure were confined to the leading edge region in the $\alpha = 0°$ case, however, large pressure fluctuations due to the passage of the primary/secondary vortex pair occured all along the airfoil's chord in the two $\alpha = 10°$ cases. This confirms the belief that the airfoil-vortex interaction is a leading edge phenomenon.

A comparison of the experimental results was made with theoretical predictions. The vortex was modeled as a cluster of ideal vortices with a circulation distribution equivalent with the experimental vortex, and a comformal mapping approach was used to compute the flow about the airfoil. Chordwise pressure distributions compared well for the $\alpha = 0°$ encounter, but the ideal theory could not predict the secondary vortex formed in the $\alpha = 10°$ encounter.

Recently, the topic of altering a flow through the introduction of control vortices has received growing interest. When vorticity encounters a surface, vorticity of the opposite sense is generally induced. This has lead to attempts to reduce the drag on a body by altering the structure of the turbulent boundary layer. Small, thin plates (termed Large Eddy-BreakUp devices, or LEBU), inserted in the boundary layer, have been shown to markedly reduce the local skin friction drag (Anders et al., 1984; Bushnell, 1984; Wark et al., 1990). The influence of the LEBU extends several hundred boundary layer thicknesses downstream.

The results presented in chapter 4 of this text have shown that the surface pressure fluctuations on the airfoil and the strength of the secondary vorticity generated on the

airfoil surface were of a lower degree when the vortex was split by the airfoil. This fact has lead to the proposal of employing a large eddy-breakup device to "destroy" the vortex before the encounter with the airfoil. A small, thin plate mounted near the airfoil's leading edge may sufficiently alter the vorticity field to eliminate the undesirable effects of the encounter. Whether such an arrangment would be practical for application (on helicopter or turbine blades) is unclear. Preliminary work (Swirydczuk, Wilder, and Telionis, 1992) has been completed at the time of writting, and involved the interaction of vortices with flat plates of different length-to-thickness ratios and different leading/trailing edge shapes. The results were encouraging, and a continuation of the research including an airfoil and flat plate in tandem is recommended.

Bibliography

Abbott, I. H. and von Doenhoff, A. E., *Theory of Wing Sections*, Dover Publications, Inc., New York, 1959.

Anders, J. B., Hefner, J. N., and Bushnell, D. M., "Performance of Large-Eddy Breakup Devices at Post-Transitional Reynolds Numbers," AIAA Paper 84-0345, 1984.

Aref, H. and Siggia, E. D., "Vortex Dynamics of the Two-Dimensional Turbulent Shear Layer," *Journal of Fluid Mechanics*, Vol. 100, Part 4, 1980, pp. 705-737.

Betz, A., "Applied Airfoil Theory," *Aerodynamic Theory*, Vol. 4, edited by W. F. Durand, Durand Reprinting Committee, Califonia Institute of Technology, Pasadena, CA, 1943.

Booth, E. R., "Surface Pressure Measurements During Low Speed Two-Dimensional Blade-Vortex Interaction," AIAA Paper 86-1856, Seattle, Washington, July 1986.

Booth, E. R., "Experimental Observations of Two Dimensional Blade-Vortex Interaction," AIAA Paper 87-2745, Palo Alto, California, Oct. 1987.

Booth, E. R., "Measurements of Velocity and Vorticity Fields in the Wake of an Airfoil in Periodic Pitching Motion," NASA TP-2780, 1987.

Booth, E. R. and Yu, J. C., "Two-Dimensional Blade-Vortex Flow Visualization Investigation," *AIAA Journal*, Vol. 24, No. 9, Sep. 1986, pp. 1468-1473.

Bratt, J. B., "Flow Patterns in the Wake of an Oscillating Aerofoil," Aeronautical Research Council R&M 2773, 1953.

Brotherhood, P., "An Appraisal of Rotor Blade-tip Vortex Interaction and Wake Geometry from Flight Measurements," *Prediction of Aerodynamic Loads on Rotorcraft*, AGARD Conference Proceedings, No. 334, London, UK, May 1982.

Bushnell, D. M., "Body-Turbulence Interaction," AIAA Paper 84-1527, 1984.

Caradonna, F. X., Lautenschlager, J. L. and Silva, M. J., "An Experimental Study of Rotor-Vortex Interactions," AIAA Paper 88-0045, Reno, Nevada, January 1988.

De Ruyck, J. and Hirsch, C., "Instantaneous Turbulence Profiles in the Wake of an Oscillating Airfoil," *AIAA Journal*, Vol. 21, No. 5, May 1983, pp. 641-642.

Durst, F., Melling, A. and Whitelaw, J. H., *The Principles and Practice of Laser-Doppler Anemometry*, London, Academic Press, 1976.

Farassat, F. and Succi, G. P., "The Prediction of Helicopter Rotor Discrete Frequency Noise," *Vertica*, Vol. 7, No. 4, 1983, pp. 309-320.

Garrick, I. E., "Propulsion of a Flapping and Oscillating Airfoil," NACA TR 567, 1936.

Graf, H. R. and Durgin, W. W., "Measurement of the Nonsteady Flow Field in the Opening of a Resonating Cavity Excited by Grazing Flow," *International Symposium on Nonsteady Fluid Dynamics*, ASME, Toronto, Ontario, Canada, June 1990, pp. 409-416.

Gursul, I. and Rockwell, D., "Vortex Street Impinging upon an Elliptical Leading Edge," *Journal of Fluid Mechanics*, Vol. 211, 1990, pp. 211-242.

Hardin, J. C. and Lamkin, S. L., "Concepts for Reduction of Blade-Vortex Interaction Noise," AIAA Paper 86-1855, Seattle, Washington, July 1986.

Hardin, J. C. and Lamkin, S. L., "An Euler Code Calculation of Blade-Vortex Interaction Noise," *Journal of Vibration, Acoustics, Stress, and Reliability in Design*, Vol. 109, Jan. 1987, pp. 29-36.

Harvey, J. K. and Perry, F. J., "Flowfield Produced by Trailing Vortices in the Vicinity of the Ground," *AIAA Journal* Technical Notes, Vol. 9, No. 8, August 1971, pp. 1659-1660.

Ho, C. and Chen, S., "Unsteady Wake of a Plunging Airfoil," *AIAA Journal*, Vol. 19, No. 11, Nov. 1981, pp. 1492-1494.

Holman, J. P., *Experimental Methods for Engineers*, McGraw-Hill Book Company, New York, 1984.

Imaichi, K. and Ohmi, K., "Numerical Processing of Flow-visualization Pictures — Measurements of Two-dimensional Vortex Flow," *Journal of Fluid Mechanics*, Vol. 129, 1983, pp. 283-311.

Jones, W. P., "Vortex-Elliptic Wing Interaction," *AIAA Journal* Technical Notes, Vol. 10, No. 2, February 1972, pp. 225-227.

Karamcheti, K., *Principles of Ideal-Fluid Aerodynamics*, Robert E. Krieger Publishing Company, Malabar, Florida, 1980.

Katz, J. and Weihs, D., "Behavior of Vortex Wakes from Oscillating Airfoils," *Journal of Aircraft*, Vol. 15, No. 12, Dec. 1978, pp. 861-863.

Koochesfahani, M. M., "Vortical Patterns in the Wake of an Oscillating Airfoil," *AIAA Journal*, Vol. 27, No. 9, Sep. 1989, pp. 1200-1205.

Kurosaka, M. and Sundaram, P., "Illustrative Examples of Streaklines in Unsteady Vortices: Interpretational Difficulties Revisited," *Physics of Fluids*, Vol. 29, No. 10, October 1986, pp. 3474-3477.

Lee, D. J. and Roberts, L., "Interaction of a Turbulent Vortex with a Lifting Surface," AIAA Paper 85-0004, 1985.

Lee, D. J. and Smith, C. A., "Distortion of the Vortex Core During Blade-Vortex Interaction," AIAA Paper 87-1243, Honolulu, Hawaii, June 1987.

Lee, D. J., Kim, Y. N. and Park, J. H., "Numerical Study of Vortex-Wedge Interaction," AIAA Paper 90-3918, Tallahassee, Florida, October 1990.

Martin, R. M. and Splettstoesser, W. R., "Acoustic Results of the Blade-Vortex Interaction Acoustic Test of a 40-Percent Model Rotor in the DNW," AHS Specialists' Meeting on Aerodynamics and Acoustics, 1987.

Mathioulakis, D. S., Kim, M. J., Telionis, D. P. and Mook, D. T., "On the Wake of a Pitching Airfoil," AIAA Paper 85-1621, Cincinatti, Ohio, July 1985.

McCroskey, W. J., "Some Current Research in Unsteady Fluid Dynamics," *Journal of Fluids Engineering*, Vol. 99, 1977, pp. 8-38.

McCroskey, W. J., "The Phenomenom of Dynamic Stall," NASA TM-81264, Mar. 1981.

McCroskey, W. J., "Unsteady Airfoils," *Annual Review of Fluid Mechanics*, Vol. 4, 1982, pp. 285-311.

Meier, G. E. A. and Timm, R., "Unsteady Vortex Airfoil Interaction," AGARD CP-386, May 1985.

Milne-Thomson, L. M., *Theoretical Hydrodynamics*, Fifth Edition, Macmillan Press LTD, London, 1968.

Mook, D. T., Roy, S., Choksi, G. and Alexander, D. M., "On the Numerical Simulation of the Unsteady Wake Behind an Airfoil," AIAA Paper 87-0190, Reno, Nevada, January 1987.

Mook, D. T. and Dong, B., "Applications of Vortex Dynamics to Simulations of Two-Dimensional Wakes," *International Symposium on Nonsteady Fluid Dynamics*, ASME, Toronto, Ontario, Canada, June 1990, pp. 435-448.

Oshima, Y. and Oshima, K., "Vortical Flow Behind an Oscillating Airfoil," *Theoretical and Applied Mechanics*, IUTAM, Toronto, Canada, Aug. 1980, pp. 357-368.

Panaras, A. G., "Numerical Modeling of the Vortex/Airfoil Interaction," *AIAA Journal*, Vol. 25, Jan. 1987, pp. 5-11.

Pao, S. P., "The Role of Unsteady Aerodynamics in Aeroacoustics," First National Fluid Dynamics Congress, Cincinatti, Ohio, July, 1988.

Park, S. O., Kim, J. S. and Lee, B. I., "Hot-Wire Measurements of Near Wakes Behind an Oscillating Airfoil," AIAA Paper 88-3715, Cincinatti, Ohio, July, 1988.

Park, S. O. and Kim, J. S., "Wake Measurements of an Oscillating Airfoil," in *Turbulence Measurements and Flow Modeling*, edited by C. J. Chen, L.-D. Chen and F. M. Holly, Jr., Hemisphere Publishing Corporation, 1987, pp. 127-136.

Pesce, M. M., "Unsteady Pressure and Vorticity Fields in Blade-Vortex Interactions," M. S. Thesis, Viginia Polytechnic Institute & State University, Blacksburg, Va., September 1990.

Pesce, M. M., Wilder, M. C. and Telionis, D. P., "The Evolution of Pressure and Vorticity Fields During Blade-Vortex Interaction," Second World Conference on Experimental Heat Transfer, Fluid Mechanics and Thermodynamics, Dubrovnik, Yugoslavia, June 23-28, 1991.

Poling, D. R., "Airfoil Responce to Periodic Disturbances- The Unsteady Kutta Condition," Ph.D. Dissertation, Viginia Polytechnic Institute & State University, Blacksburg, Va., Aug. 1985.

Poling, D. R. and Telionis, D. P., "Airfoil Responce to Periodic Disturbances- The Unsteady Kutta Condition," *AIAA Journal*, Vol. 24, No. 2, Feb. 1986, pp. 193-199.

Poling, D. R., Dadone, L., Wilder, M. C. and Telionis, D. P., "Two-Dimensional Interaction of Vortices with a Blade," AIAA Paper 88-0044, Reno, Nevada, January 1988.

Poling D. R. and Dadone, L., "Blade-Vortex Interaction," AIAA Journal, Vol. 27, No. 6, June 1989, pp. 694-699.

Poling, D. R., Wilder, M. C. and Telionis, D. P., "Fundamental Research in Helicopter Rotor Blade-Vortex Interaction Modeling," 47th Annual Forum of the American Helicopter Society, Phoenix, Arizona, May 1991.

Rockwell, D., "Unsteady Loading of Leading-Edges in Unstable Flows: An Overview," AIAA Paper 84-2306, 1984.

Rockwell, D. and Knisely, C., "The Organized Nature of Flow Impingement upon a Corner," *Journal of Fluid Mechanics*, Vol. 93, part 3, 1979, pp. 413-432.

Satyanarayana, B., "Unsteady Wake Measurements of Airfoils and Cascades," *AIAA Journal*, Vol. 15, No. 5, May 1977, pp. 613-618.

Satyanarayana, B. and Davis, S., "Experimental Studies of Unsteady Trailing Edge Conditions," *AIAA Journal*, Vol. 16, No. 2, Feb. 1978, pp.125-129.

Splettstoesser, W. R., Schultz, K. J. and Martin, R. M., "Rotor Blade-Vortex Interaction Impulsive Noise Source Identification and Correlation with Rotor Wake Predictions," AIAA Paper 87-2744, 1987.

Straus, J., Renzoni, P. and Mayle, R. E., "Airfoil Pressure Measurements During a Blade Vortex Interaction and a Comparison with Theory," *AIAA Journal*, Vol. 28, No. 2, Feb. 1990, pp. 222-228.

Sundaram, P., Kurosaka, M. and Wu, J. M., "Vortex Dynamics Analysis of Unsteady Vortex Wakes," *AIAA Journal*, Vol. 29, No. 3, March 1991, pp. 321-326.

Swirydczuk, J., "A Visualization Study of the Interaction of a Free Vortex with the Wake Behind an Airfoil," in *Experiments in Fluids*, Springer-Verlag, 1990, pp.181-190.

Swirydczuk, J., Wilder, M. C., and Telionis, D. P., "The Interaction of Vortices with Thin Flat Plates," abstract accepted to the 2nd National Fluid Dynamics Congress, 1992.

Takagi, S., "The Structure of Turbulent Boundary Layer Controlled by the Plates," 15th Turbulence Symposium, Tokyo, July 1983.

Telionis, D. P., Mathioulakis, D. S., Kim, B. K. and Jones, G. S., "Calibration of the ESM Water Tunnel," VPI & SU Engineering Report No. VPI-E-86-23, Nov. 1986.

Telionis, D. P. and Wilder, M. C., "Progress Report on the Interaction of Vortices with a Fixed Blade," VPI & SU Engineering Report No. VPI-E-88-2, Feb. 1988.

Thompson, T. L., Kwon, O. J., Kemnitz, J. L., Komerath, N. M. and Gray, R. B., "Tip Vortex Core Measurements on a Hovering Model Rotor," AIAA Paper 87-0209, Reno, Nevada, Jan. 1987.

Walker, J. M. and Robinson, M. C., "Impingement of Orthogonal Unsteady Vortex Structures on Trailing Aerodynamic Surfaces," AIAA Paper 88-2580, 1988.

Wark, C. E, Naguib, A., M., and Nagib, H. M., "Effect of Plate Manipulaters on Coherent Structures in a Turbulent Boundary Layer," *AIAA Journal*, Vol. 20, 1990, pp. 1877-1884.

Widnall, S., "Helicopter Noise Due to Blade-Vortex Interaction," *J. Acous. Soc. America*, Vol. 50, No. 1, Pt. 2, July 1971, pp. 354-365.

Wilder. M. C., Pesce M. M. and Telionis, D. P., "Blade-Vortex Interaction Experiments - Velocity and Vorticity Fields," AIAA Paper 90-0030, Reno, Nevada, January 1990.

Williams, D. R. and Hama, F. R., "Streaklines in a Shear Layer Perturbed by Two Waves," *Physics of Fluids*, Vol. 23, No. 3, March 1980, pp. 442-447.

Wu, J. C., Sankar, N. L. and Hsu, T. M., "Unsteady Aerodynamics of an Airfoil Encountering a Passing Vortex," AIAA Paper 85-0203, 1985.

Wygnanski, I. J. and Petersen, R. A., "Coherent Motion in Excited Shear Flows," *AIAA Journal*, Vol. 25, No. 2, February 1987, pp. 201-213.

Yu, Y. H., Schmitz, F. H. and Morse, H. A., "Aeroacoustic Research Programs at the Army Aviation Research and Technology Activity," Technical Support Package, "Research in Helicopter Noise", NASA Tech Briefs ARC-12171.

Appendix A

Airfoil-vortex interaction, $\alpha = 0°$: close encounter

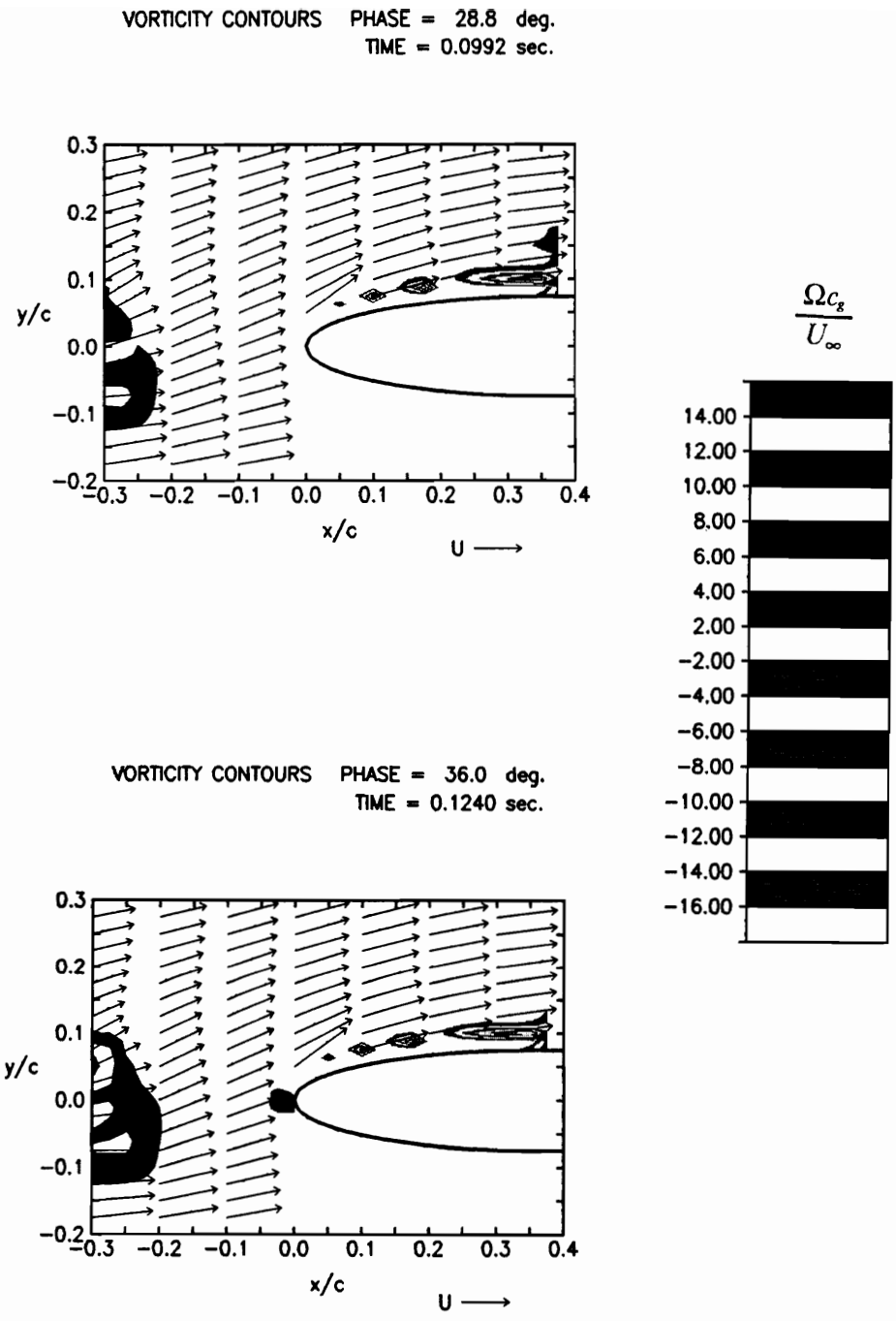

Figure A.1. Vorticity contour maps for the $\alpha = 0°$ close encounter: k = 2.05, H = 0.265, Re = 12600

VORTICITY CONTOURS PHASE = 43.2 deg.
TIME = 0.1488 sec.

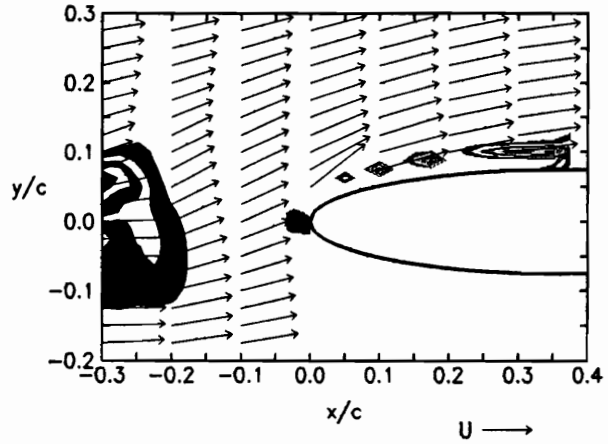

VORTICITY CONTOURS PHASE = 50.4 deg.
TIME = 0.1736 sec.

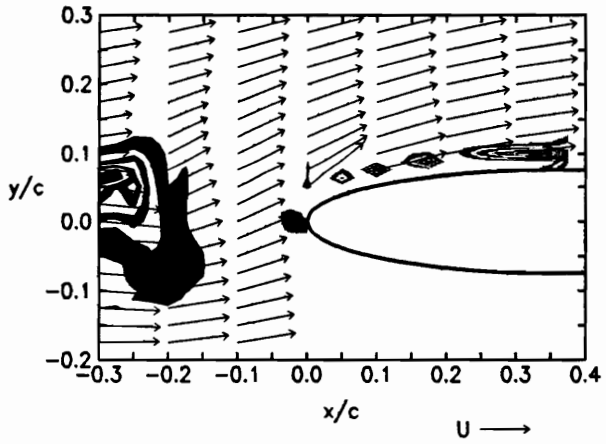

(continued) k = 2.05, H = 0.265, Re = 12600

VORTICITY CONTOURS PHASE = 57.6 deg.
TIME = 0.1984 sec.

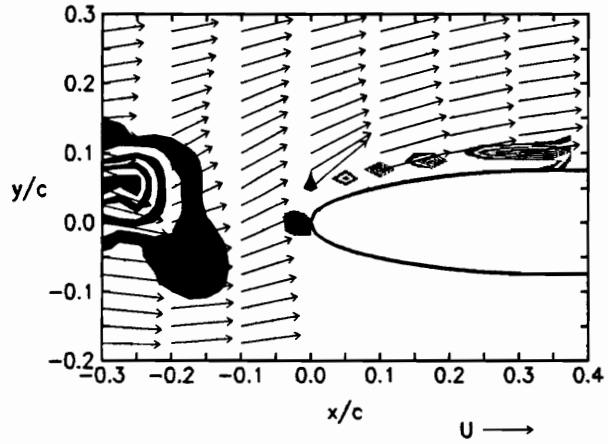

VORTICITY CONTOURS PHASE = 64.8 deg.
TIME = 0.2232 sec.

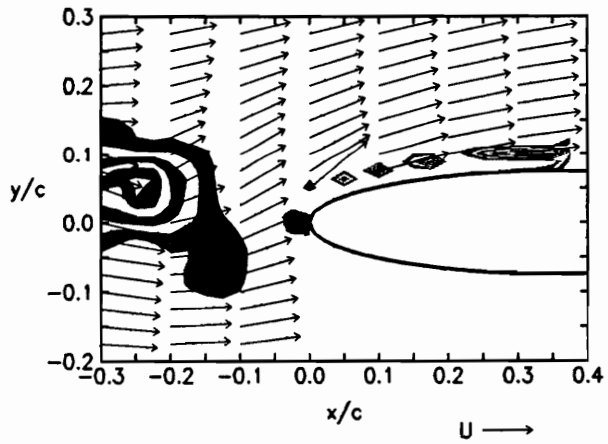

(continued) k = 2.05, H = 0.265, Re = 12600

VORTICITY CONTOURS PHASE = 72.0 deg.
TIME = 0.2480 sec.

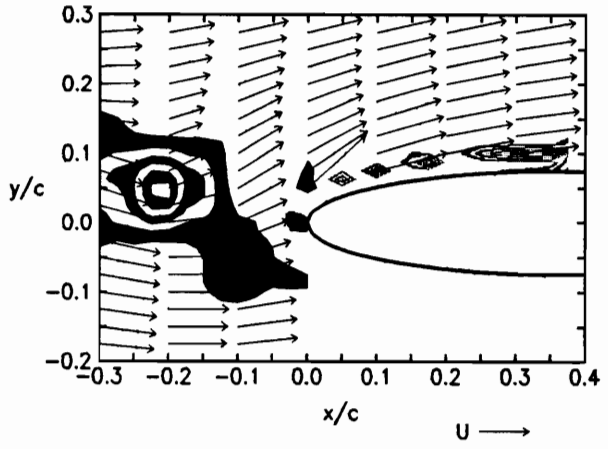

VORTICITY CONTOURS PHASE = 79.2 deg.
TIME = 0.2728 sec.

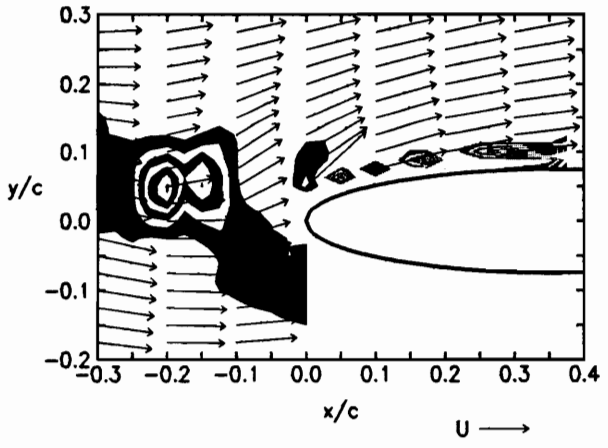

(continued) k = 2.05, H = 0.265, Re = 12600

VORTICITY CONTOURS PHASE = 86.4 deg.
TIME = 0.2976 sec.

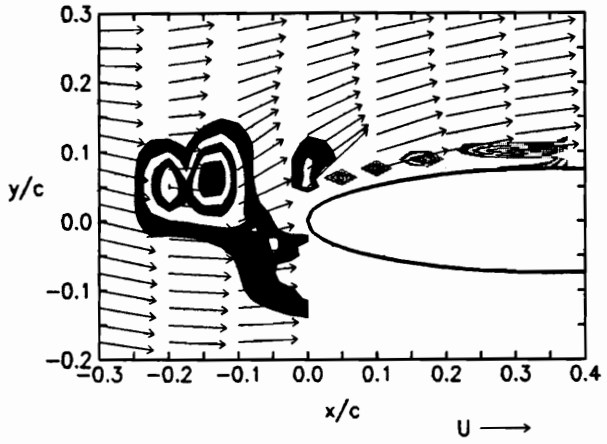

VORTICITY CONTOURS PHASE = 93.6 deg.
TIME = 0.3224 sec.

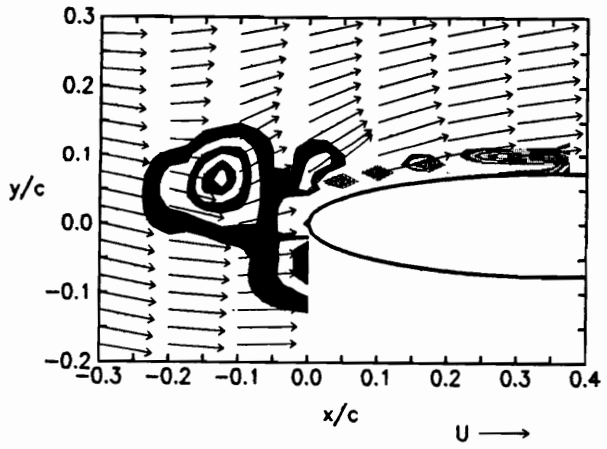

(continued) k = 2.05, H = 0.265, Re = 12600

VORTICITY CONTOURS PHASE = 100.8 deg.
TIME = 0.3472 sec.

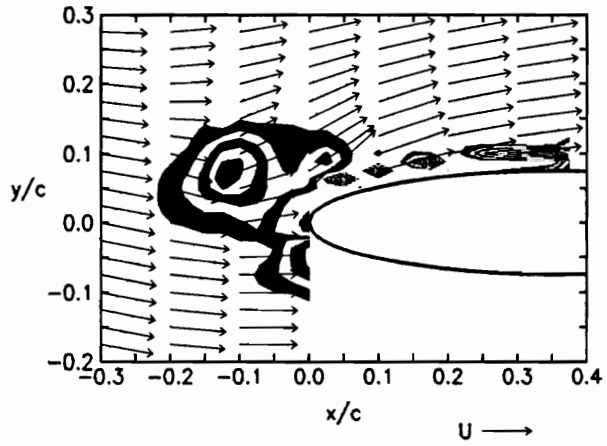

VORTICITY CONTOURS PHASE = 108.0 deg.
TIME = 0.3720 sec.

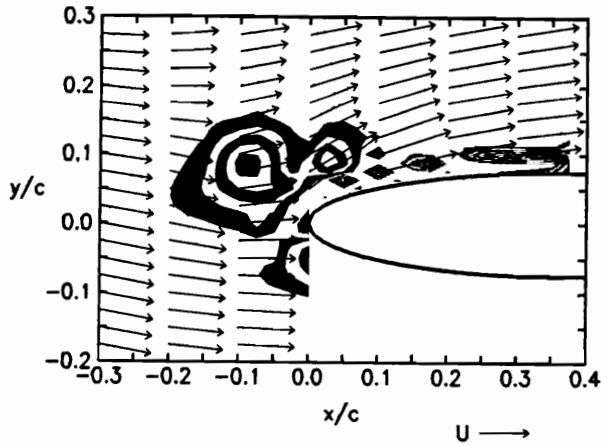

(continued) k = 2.05, H = 0.265, Re = 12600

VORTICITY CONTOURS PHASE = 115.2 deg.
TIME = 0.3968 sec.

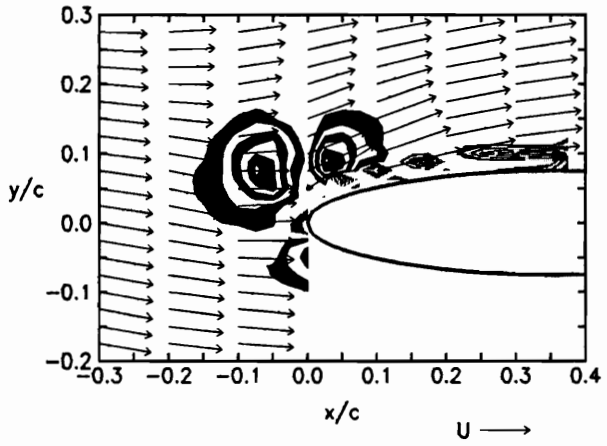

VORTICITY CONTOURS PHASE = 122.4 deg.
TIME = 0.4216 sec.

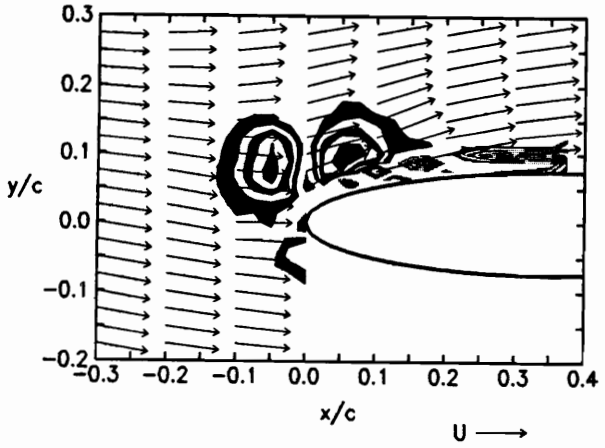

(continued) k = 2.05, H = 0.265, Re = 12600

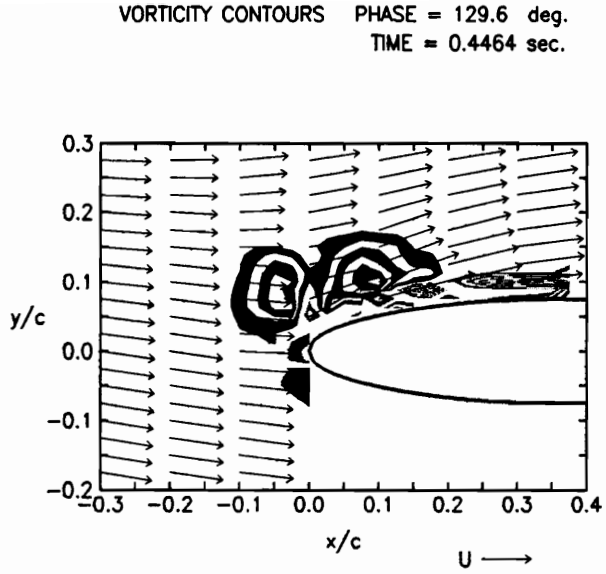

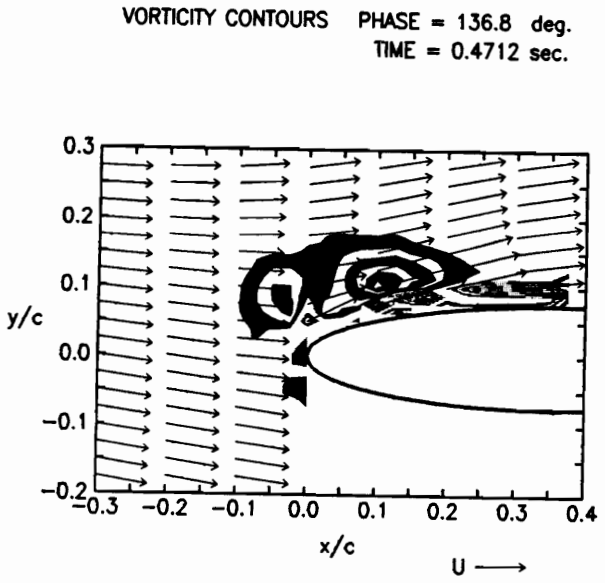

(continued) k = 2.05, H = 0.265, Re = 12600

VORTICITY CONTOURS PHASE = 144.0 deg.
TIME = 0.4960 sec.

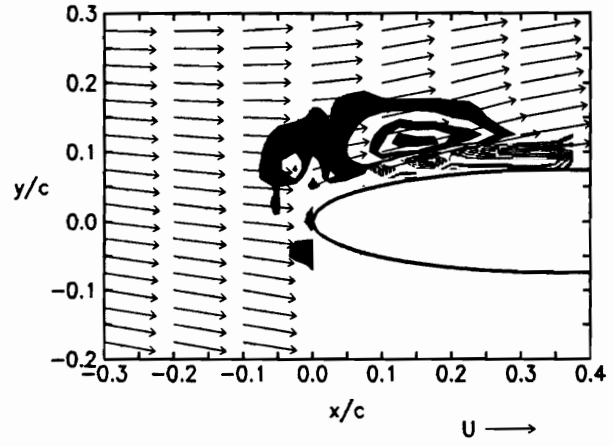

VORTICITY CONTOURS PHASE = 151.2 deg.
TIME = 0.5208 sec.

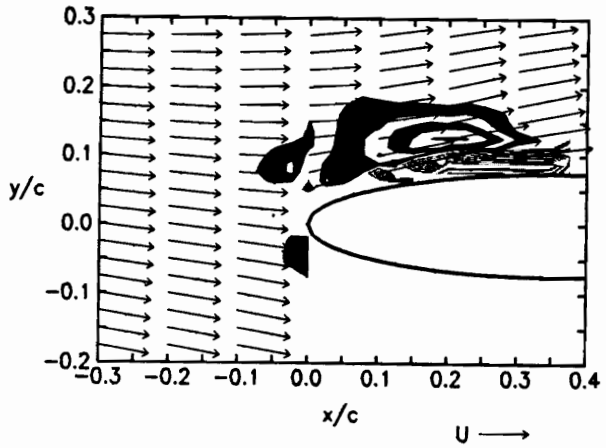

(continued) k = 2.05, H = 0.265, Re = 12600

VORTICITY CONTOURS PHASE = 158.4 deg.
TIME = 0.5456 sec.

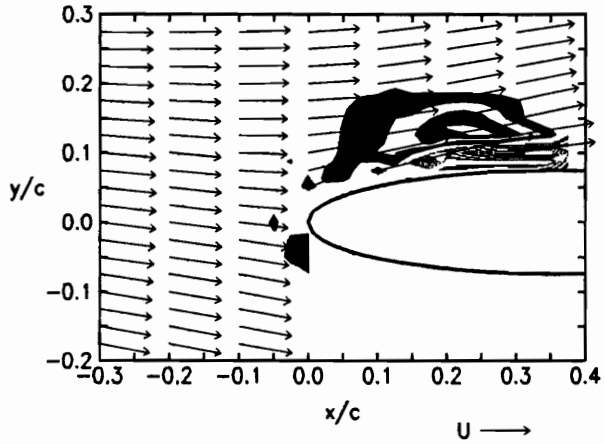

VORTICITY CONTOURS PHASE = 165.6 deg.
TIME = 0.5704 sec.

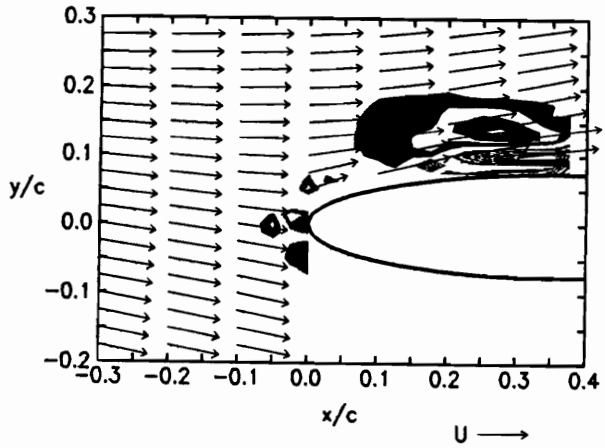

(continued) k = 2.05, H = 0.265, Re = 12600

VORTICITY CONTOURS PHASE = 172.8 deg.
TIME = 0.5952 sec.

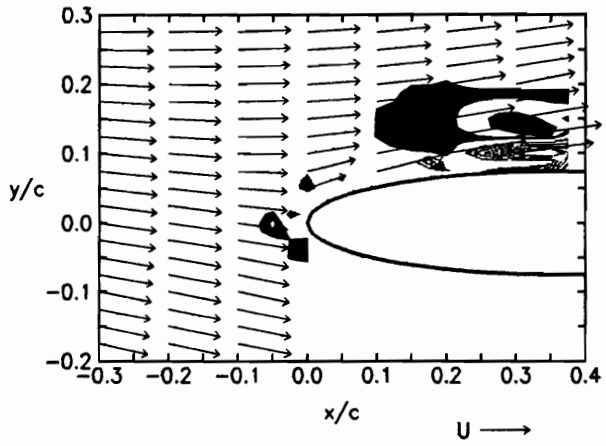

VORTICITY CONTOURS PHASE = 180.0 deg.
TIME = 0.6200 sec.

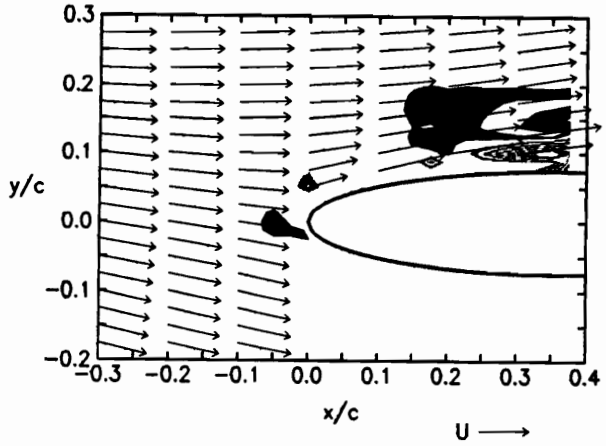

(continued) k = 2.05, H = 0.265, Re = 12600

VORTICITY CONTOURS PHASE = 187.2 deg.
TIME = 0.6448 sec.

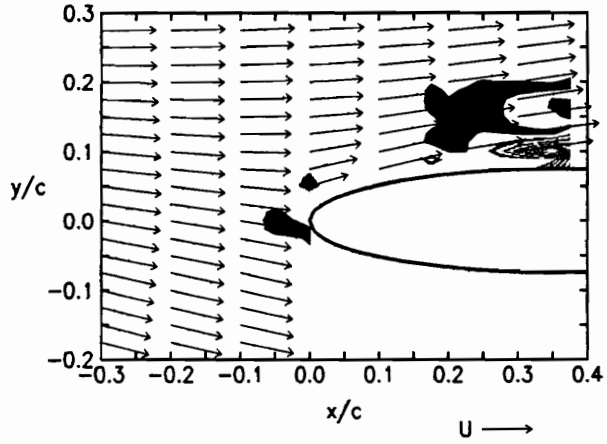

VORTICITY CONTOURS PHASE = 194.4 deg.
TIME = 0.6696 sec.

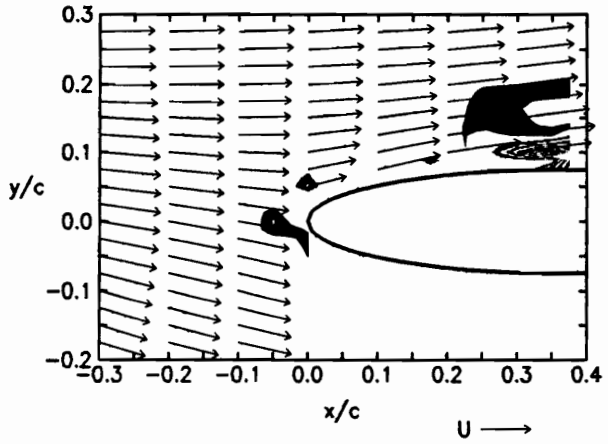

(continued) k = 2.05, H = 0.265, Re = 12600

VORTICITY CONTOURS PHASE = 201.6 deg.
TIME = 0.6944 sec.

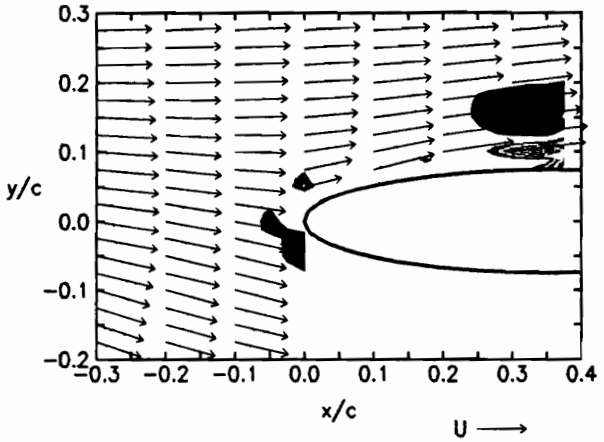

VORTICITY CONTOURS PHASE = 208.8 deg.
TIME = 0.7192 sec.

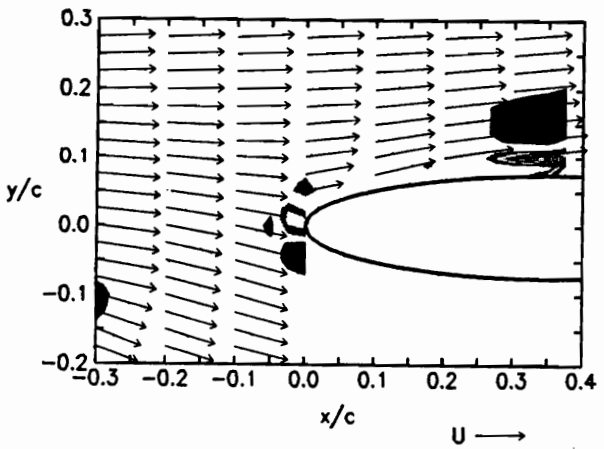

(continued) k = 2.05, H = 0.265, Re = 12600

VORTICITY CONTOURS PHASE = 216.0 deg.
TIME = 0.7440 sec.

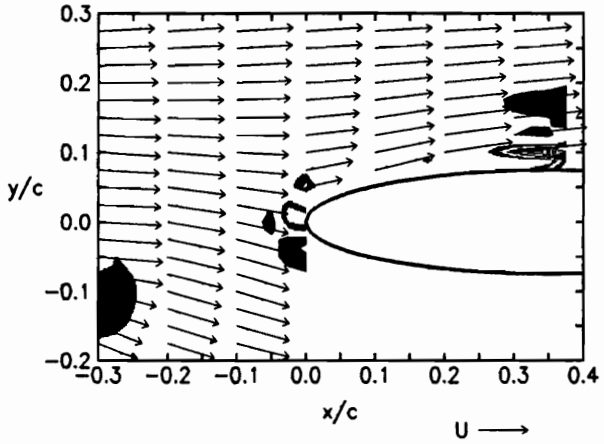

VORTICITY CONTOURS PHASE = 223.2 deg.
TIME = 0.7688 sec.

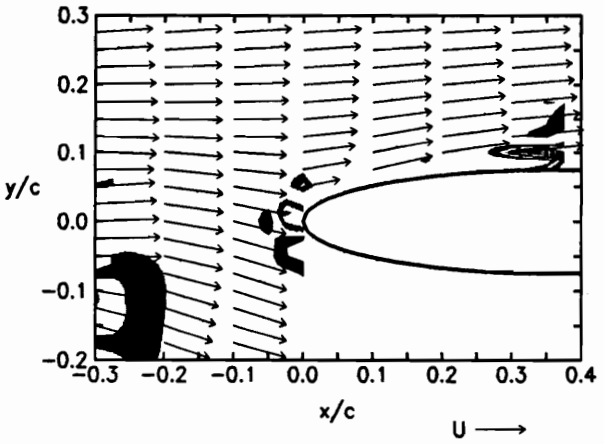

(continued) k = 2.05, H = 0.265, Re = 12600

VORTICITY CONTOURS PHASE = 237.6 deg.
TIME = 0.8184 sec.

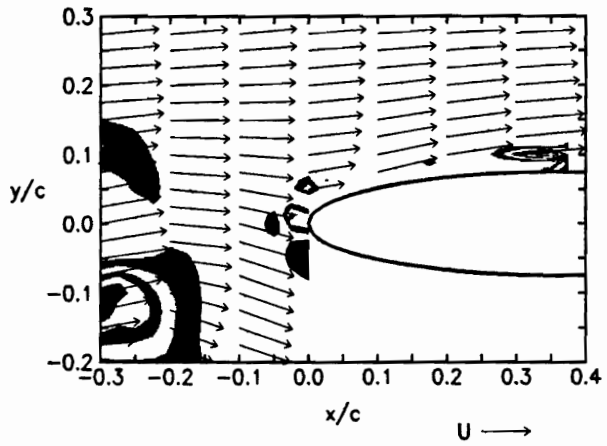

VORTICITY CONTOURS PHASE = 244.8 deg.
TIME = 0.8432 sec.

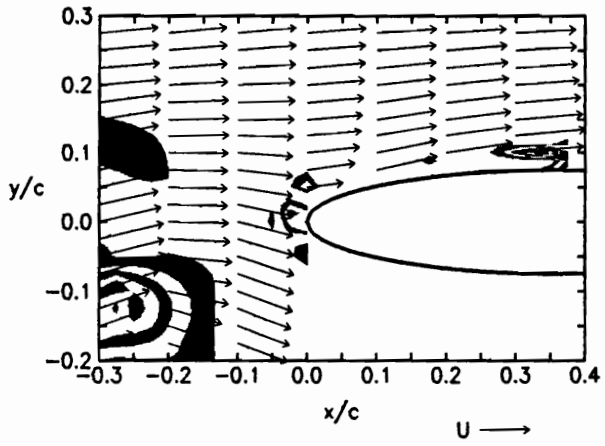

(continued) k = 2.05, H = 0.265, Re = 12600

VORTICITY CONTOURS PHASE = 252.0 deg.
TIME = 0.8680 sec.

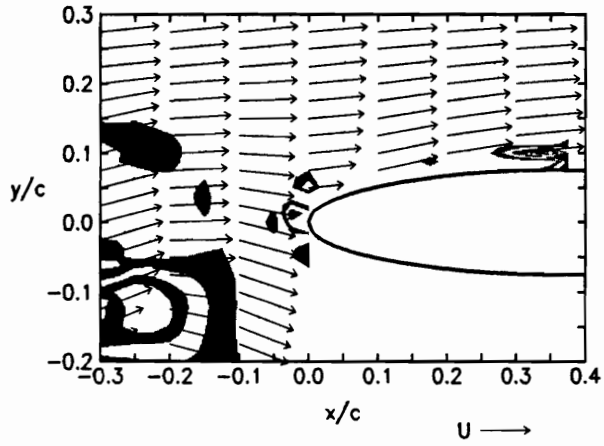

VORTICITY CONTOURS PHASE = 259.2 deg.
TIME = 0.8928 sec.

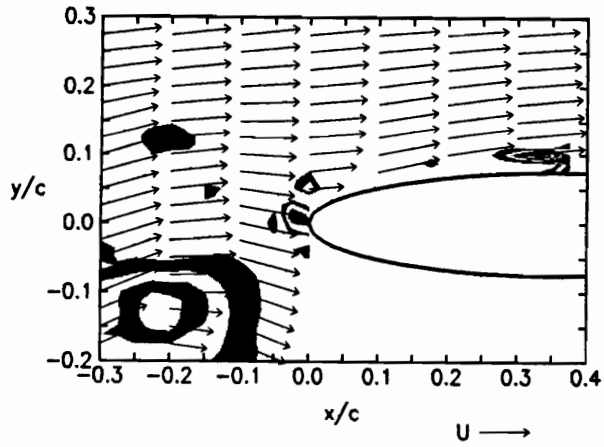

(continued) k = 2.05, H = 0.265, Re = 12600

VORTICITY CONTOURS PHASE = 266.4 deg.
TIME = 0.9176 sec.

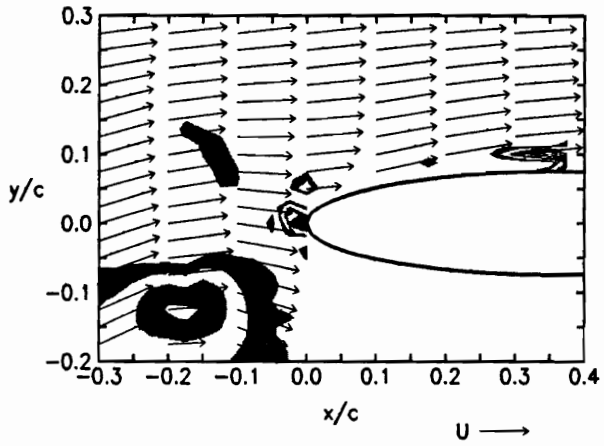

VORTICITY CONTOURS PHASE = 273.6 deg.
TIME = 0.9424 sec.

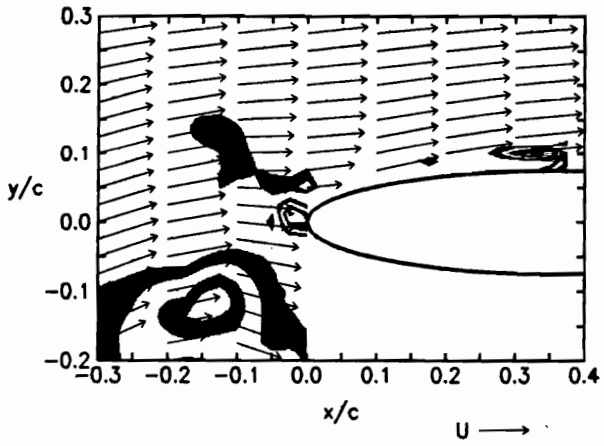

(continued) k = 2.05, H = 0.265, Re = 12600

VORTICITY CONTOURS PHASE = 280.8 deg.
TIME = 0.9672 sec.

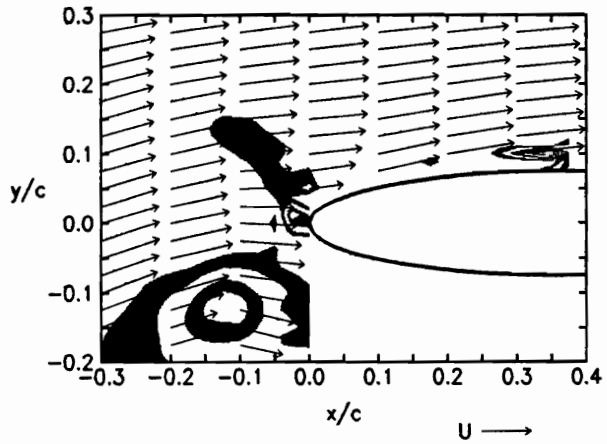

VORTICITY CONTOURS PHASE = 288.0 deg.
TIME = 0.9920 sec.

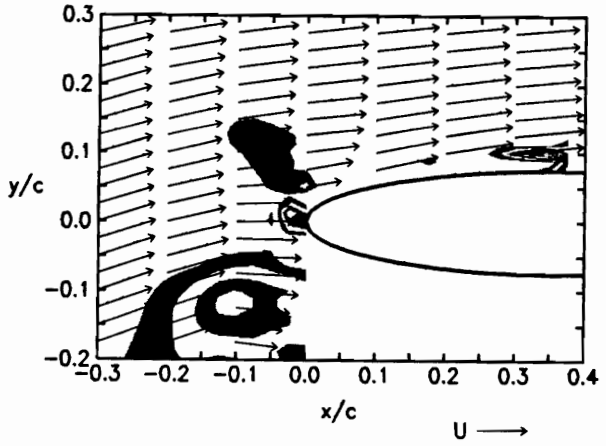

(continued) k = 2.05, H = 0.265, Re = 12600

VORTICITY CONTOURS PHASE = 295.2 deg.
TIME = 1.0168 sec.

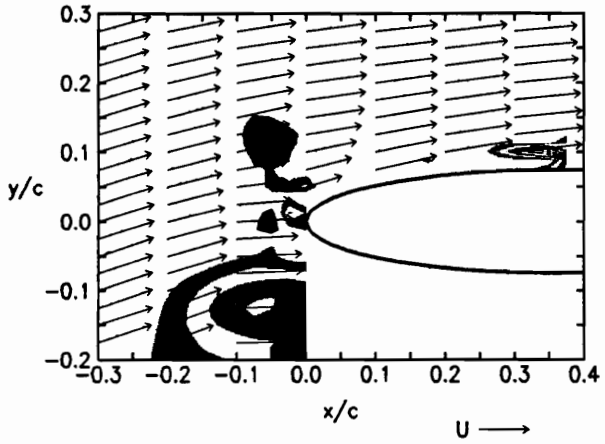

VORTICITY CONTOURS PHASE = 302.4 deg.
TIME = 1.0416 sec.

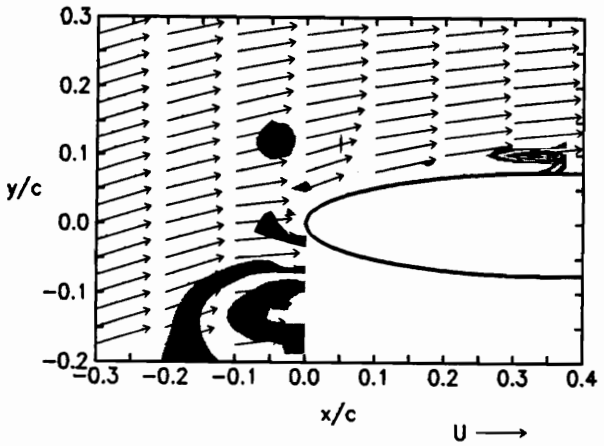

(continued) k = 2.05, H = 0.265, Re = 12600

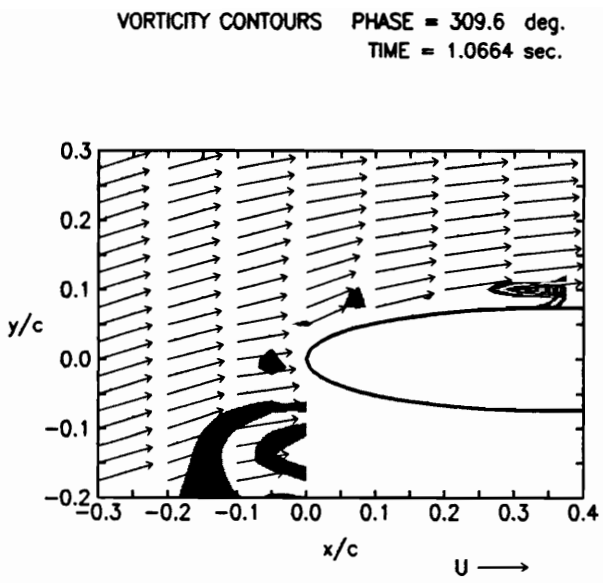

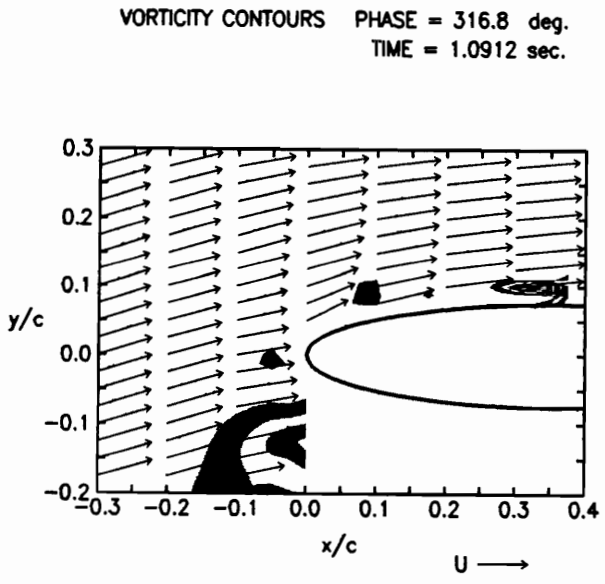

(continued) k = 2.05, H = 0.265, Re = 12600

Appendix B

Airfoil-vortex interaction, $\alpha = 10°$: close encounter

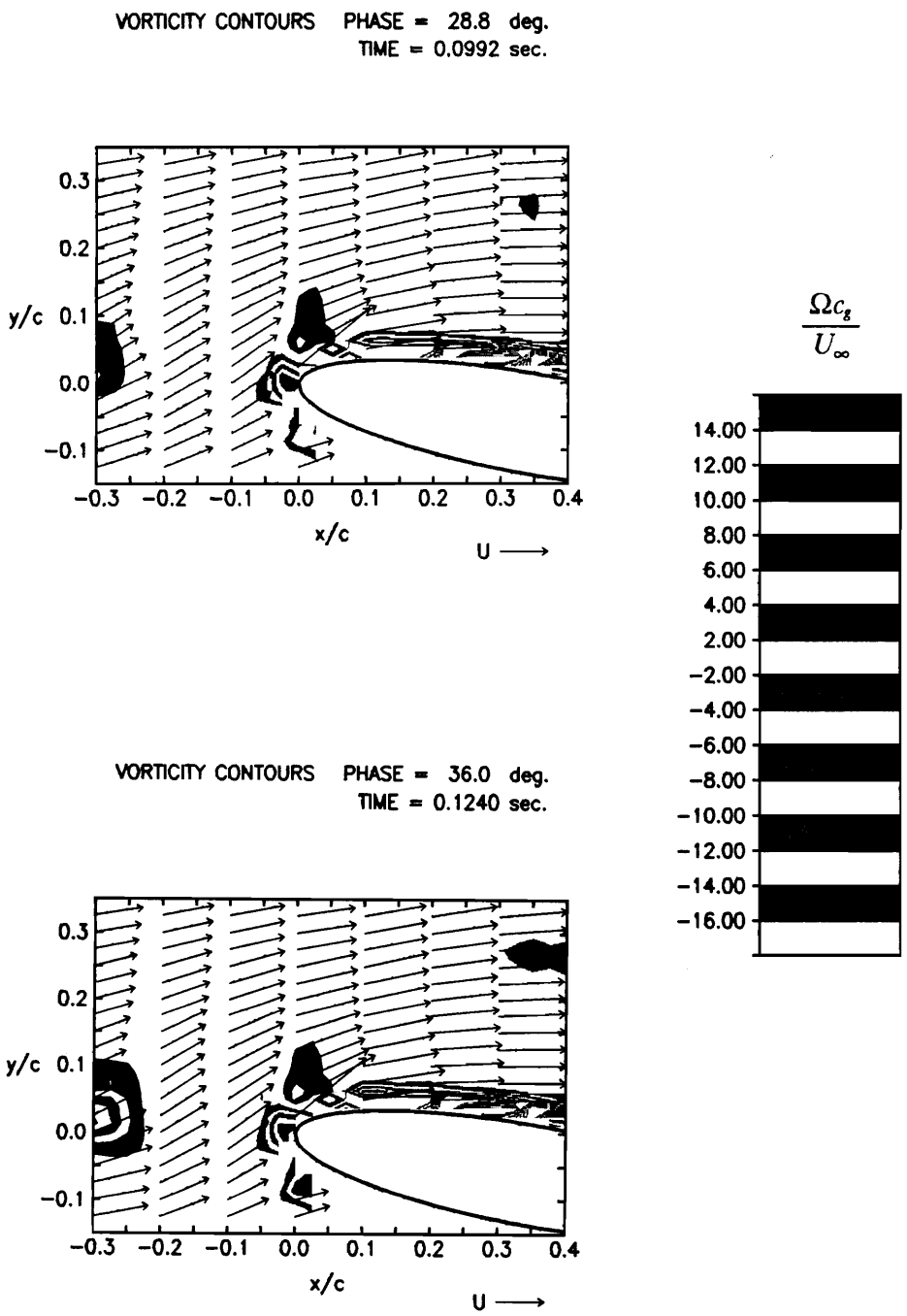

Figure B.1. Vorticity contour maps for the $\alpha = 10°$ close encounter: k = 2.05, H = 0.265, Re = 12600

VORTICITY CONTOURS PHASE = 43.2 deg.
TIME = 0.1488 sec.

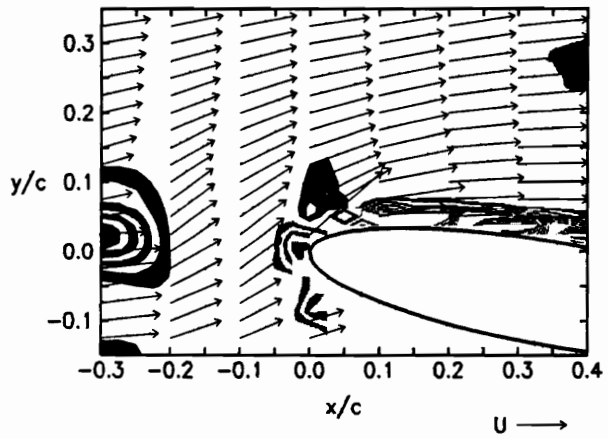

VORTICITY CONTOURS PHASE = 50.4 deg.
TIME = 0.1736 sec.

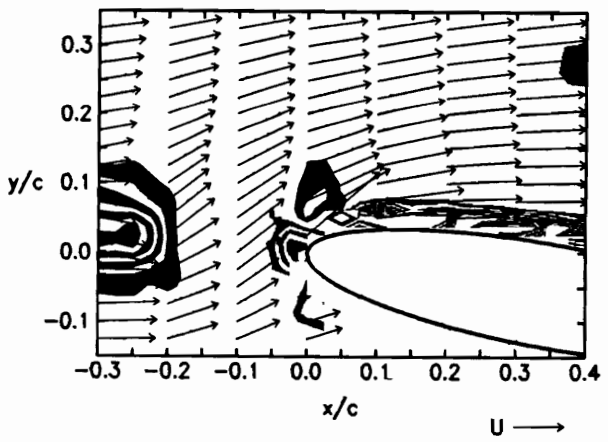

(continued) k = 2.05, H = 0.265, Re = 12600

VORTICITY CONTOURS PHASE = 57.6 deg.
TIME = 0.1984 sec.

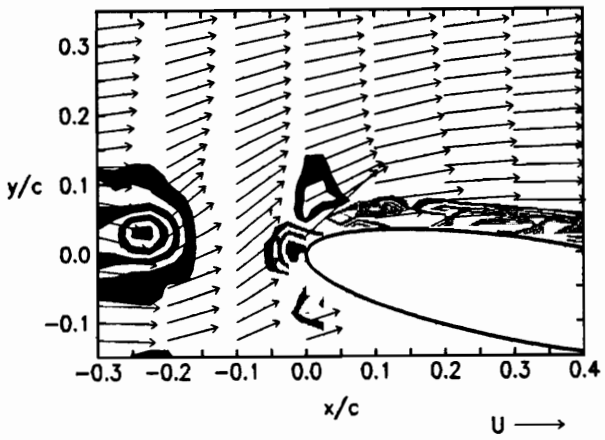

VORTICITY CONTOURS PHASE = 64.8 deg.
TIME = 0.2232 sec.

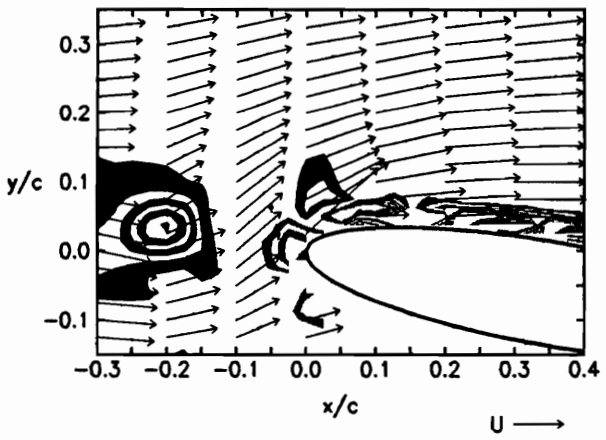

(continued) k = 2.05, H = 0.265, Re = 12600

VORTICITY CONTOURS PHASE = 79.2 deg.
TIME = 0.2728 sec.

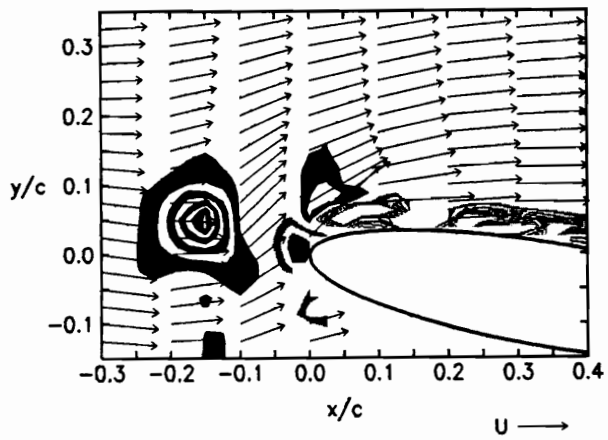

VORTICITY CONTOURS PHASE = 86.4 deg.
TIME = 0.2976 sec.

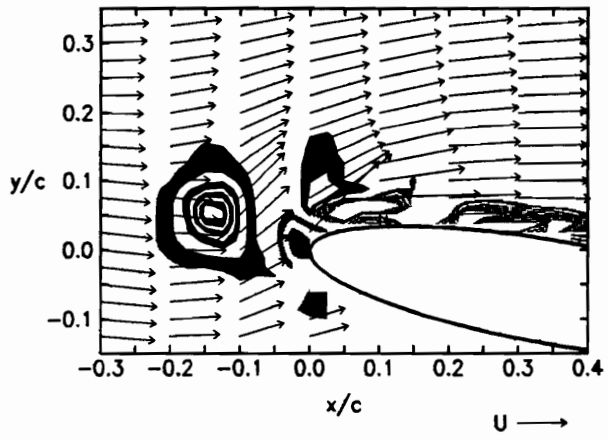

(continued) k = 2.05, H = 0.265, Re = 12600

VORTICITY CONTOURS PHASE = 93.6 deg.
TIME = 0.3224 sec.

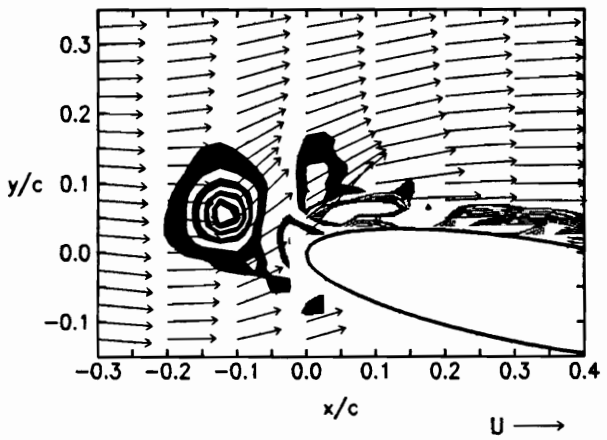

VORTICITY CONTOURS PHASE = 100.8 deg.
TIME = 0.3472 sec.

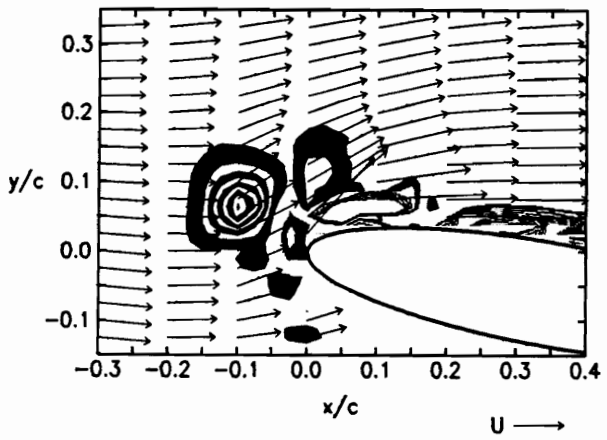

(continued) k = 2.05, H = 0.265, Re = 12600

VORTICITY CONTOURS PHASE = 108.0 deg.
TIME = 0.3720 sec.

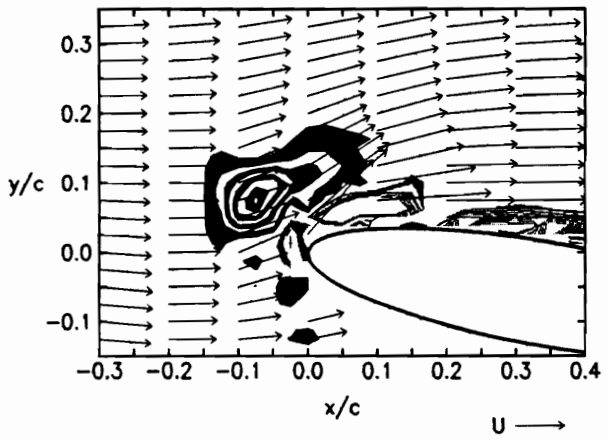

VORTICITY CONTOURS PHASE = 122.4 deg.
TIME = 0.4216 sec.

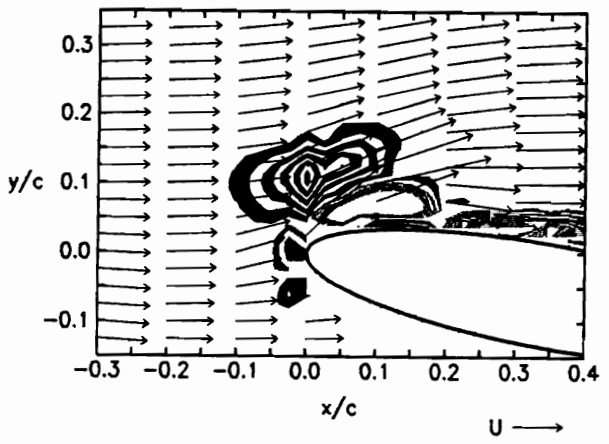

(continued) k = 2.05, H = 0.265, Re = 12600

VORTICITY CONTOURS PHASE = 136.8 deg.
TIME = 0.4712 sec.

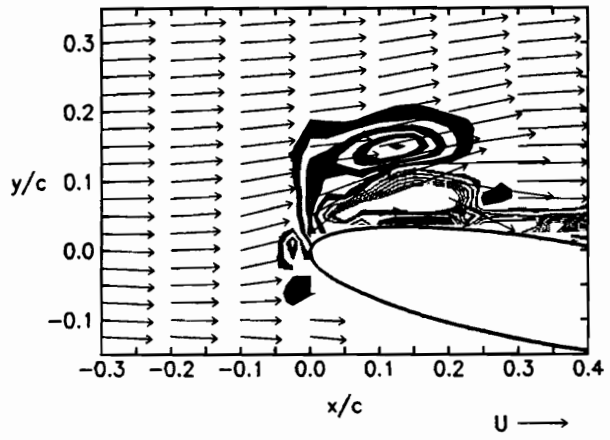

VORTICITY CONTOURS PHASE = 151.2 deg.
TIME = 0.5208 sec.

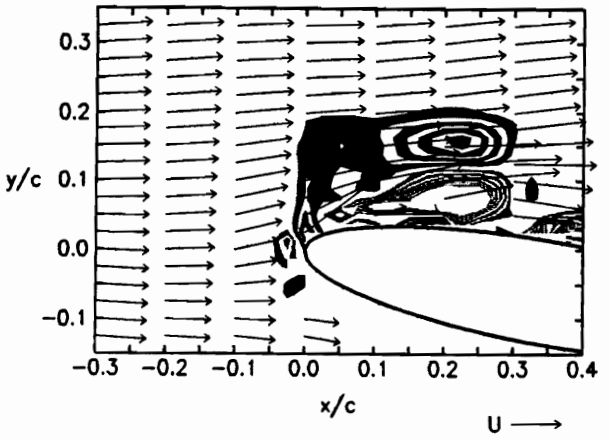

(continued) k = 2.05, H = 0.265, Re = 12600

VORTICITY CONTOURS PHASE = 158.4 deg.
TIME = 0.5456 sec.

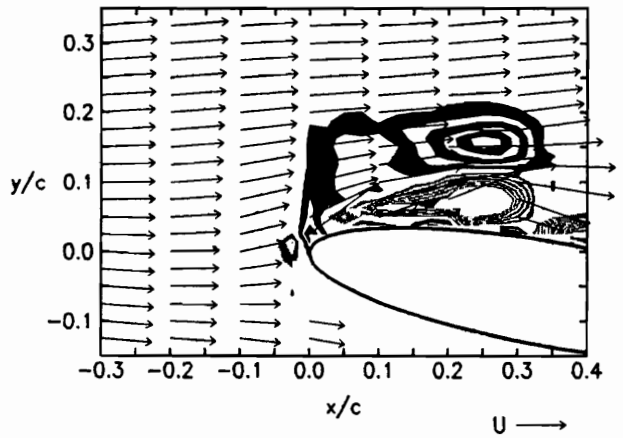

VORTICITY CONTOURS PHASE = 172.8 deg.
TIME = 0.5952 sec.

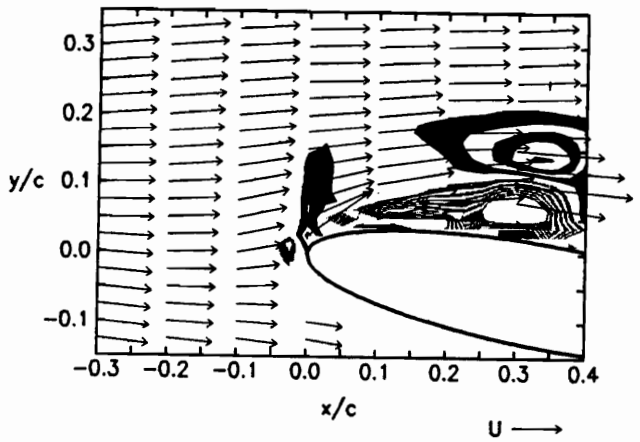

(continued) k = 2.05, H = 0.265, Re = 12600

VORTICITY CONTOURS PHASE = 180.0 deg.
TIME = 0.6200 sec.

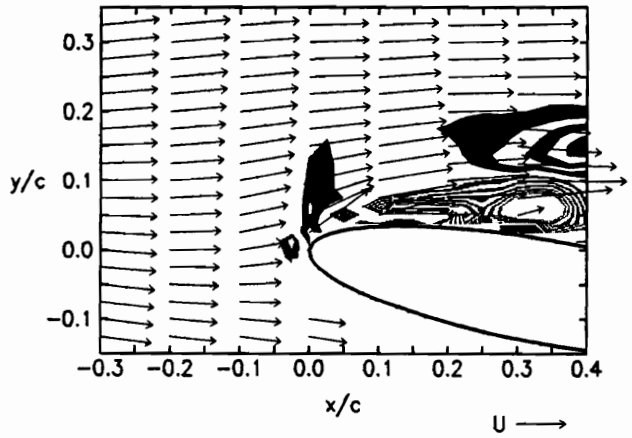

VORTICITY CONTOURS PHASE = 187.2 deg.
TIME = 0.6448 sec.

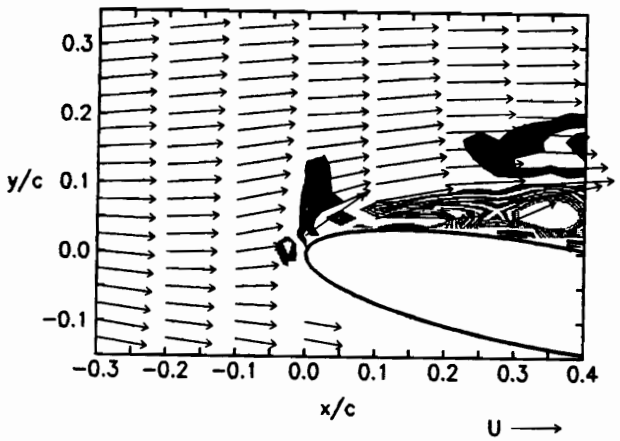

(continued) k = 2.05, H = 0.265, Re = 12600

VORTICITY CONTOURS PHASE = 194.4 deg.
TIME = 0.6696 sec.

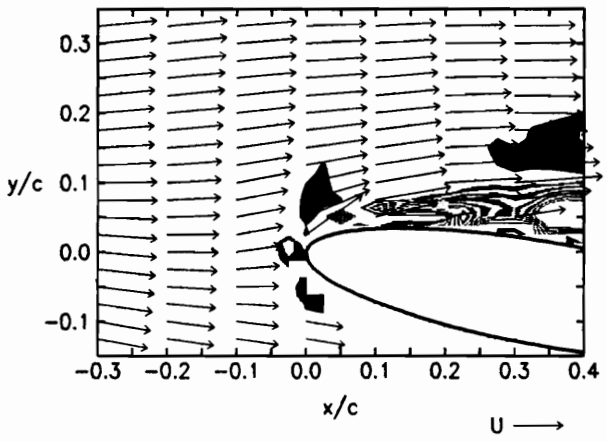

VORTICITY CONTOURS PHASE = 201.6 deg.
TIME = 0.6944 sec.

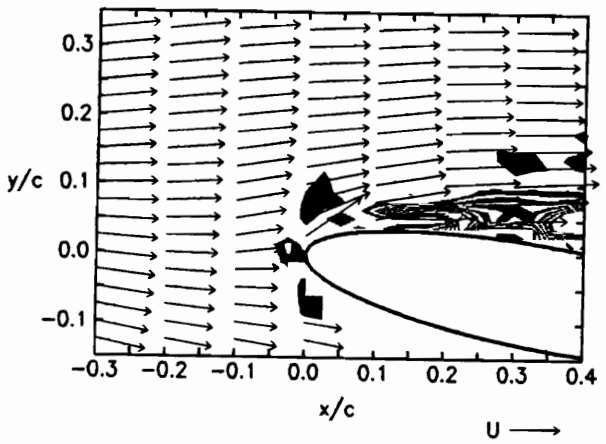

(continued) k = 2.05, H = 0.265, Re = 12600

VORTICITY CONTOURS PHASE = 208.8 deg.
TIME = 0.7192 sec.

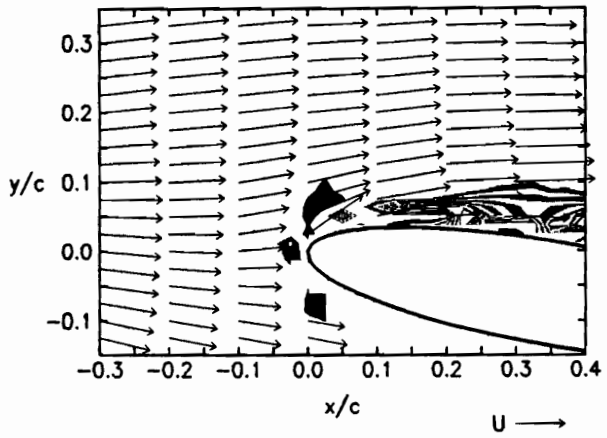

VORTICITY CONTOURS PHASE = 216.0 deg.
TIME = 0.7440 sec.

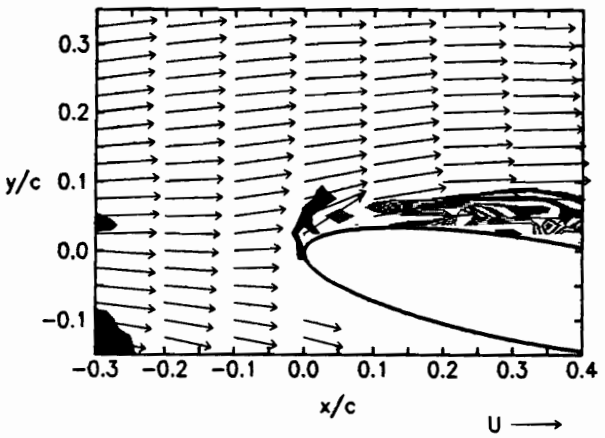

(continued) k = 2.05, H = 0.265, Re = 12600

VORTICITY CONTOURS PHASE = 223.2 deg.
TIME = 0.7688 sec.

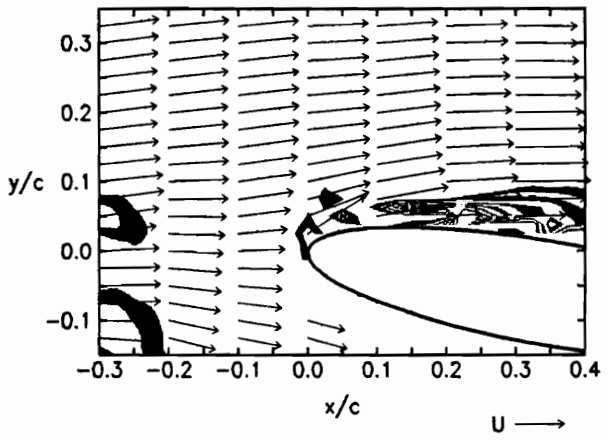

VORTICITY CONTOURS PHASE = 230.4 deg.
TIME = 0.7936 sec.

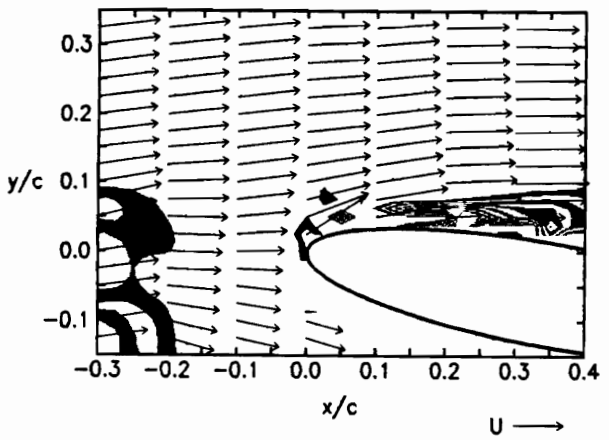

(continued) k = 2.05, H = 0.265, Re = 12600

VORTICITY CONTOURS PHASE = 237.6 deg.
TIME = 0.8184 sec.

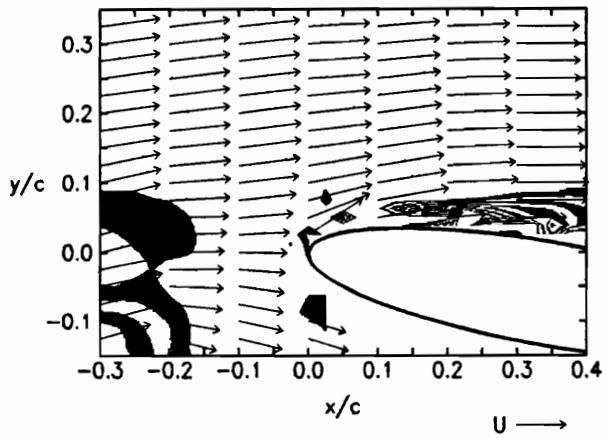

VORTICITY CONTOURS PHASE = 244.8 deg.
TIME = 0.8432 sec.

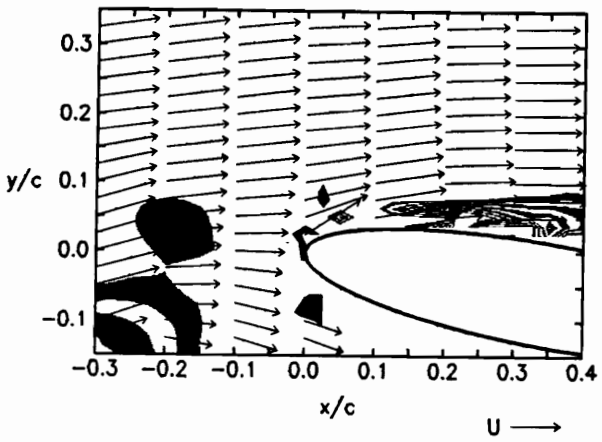

(continued) k = 2.05, H = 0.265, Re = 12600

VORTICITY CONTOURS PHASE = 252.0 deg.
TIME = 0.8680 sec.

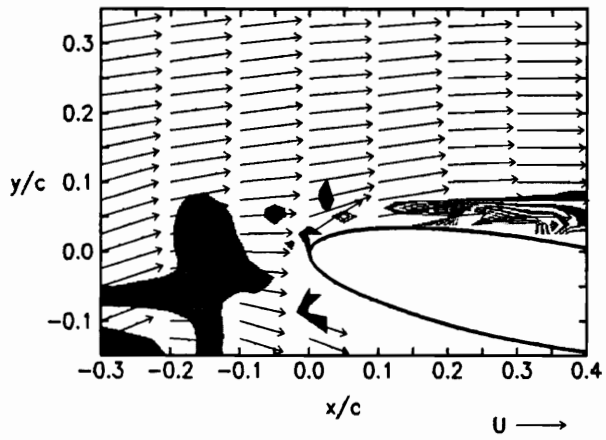

VORTICITY CONTOURS PHASE = 259.2 deg.
TIME = 0.8928 sec.

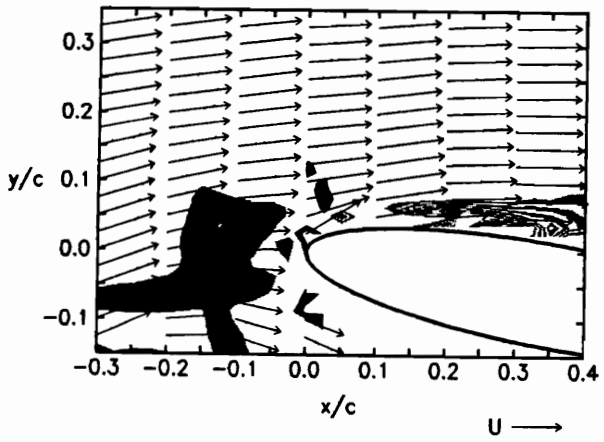

(continued) k = 2.05, H = 0.265, Re = 12600

VORTICITY CONTOURS PHASE = 266.4 deg.
TIME = 0.9176 sec.

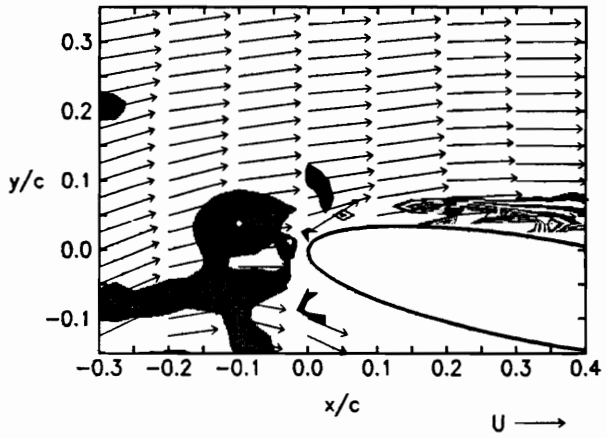

VORTICITY CONTOURS PHASE = 273.6 deg.
TIME = 0.9424 sec.

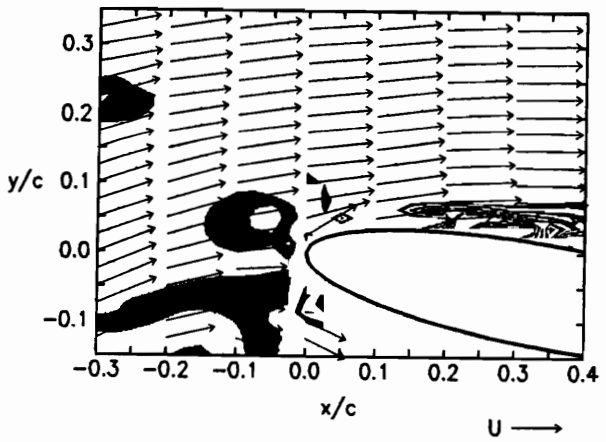

(continued) k = 2.05, H = 0.265, Re = 12600

VORTICITY CONTOURS PHASE = 280.8 deg.
TIME = 0.9672 sec.

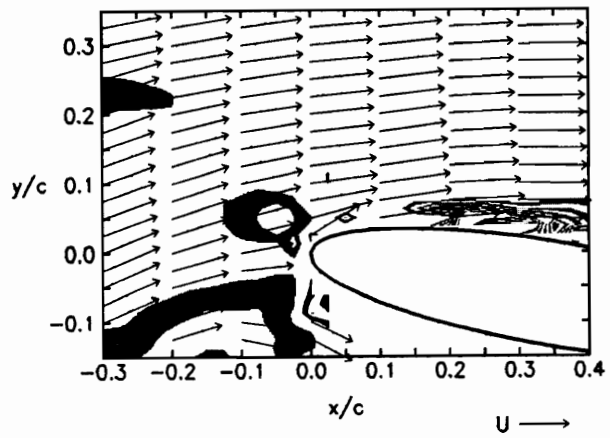

VORTICITY CONTOURS PHASE = 288.0 deg.
TIME = 0.9920 sec.

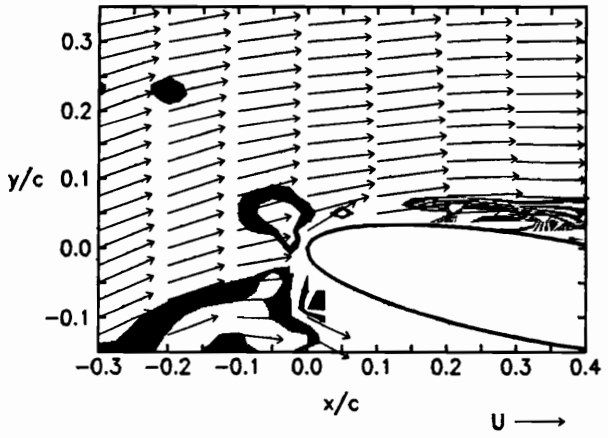

(continued) k = 2.05, H = 0.265, Re = 12600

VORTICITY CONTOURS PHASE = 295.2 deg.
TIME = 1.0168 sec.

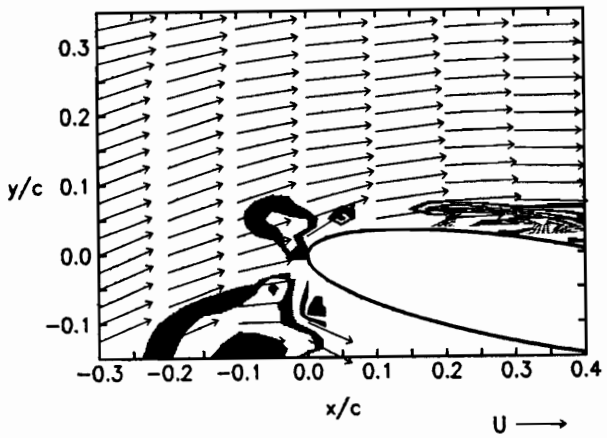

VORTICITY CONTOURS PHASE = 302.4 deg.
TIME = 1.0416 sec.

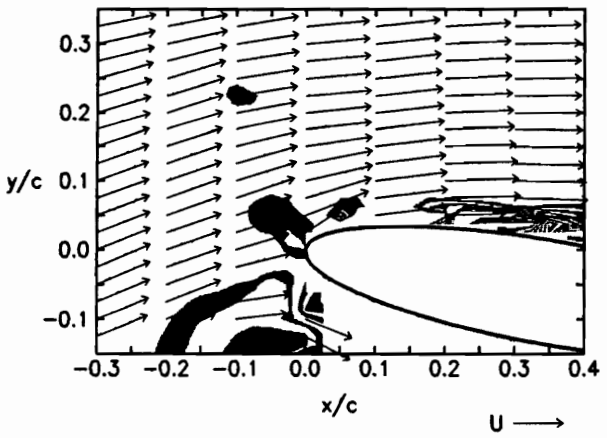

(continued) k = 2.05, H = 0.265, Re = 12600

VORTICITY CONTOURS PHASE = 309.6 deg.
TIME = 1.0664 sec.

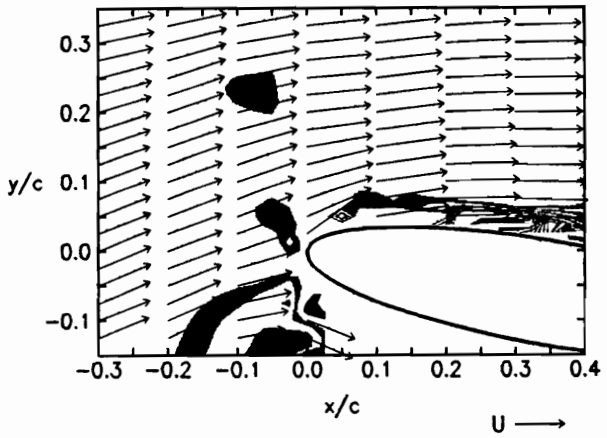

VORTICITY CONTOURS PHASE = 316.8 deg.
TIME = 1.0912 sec.

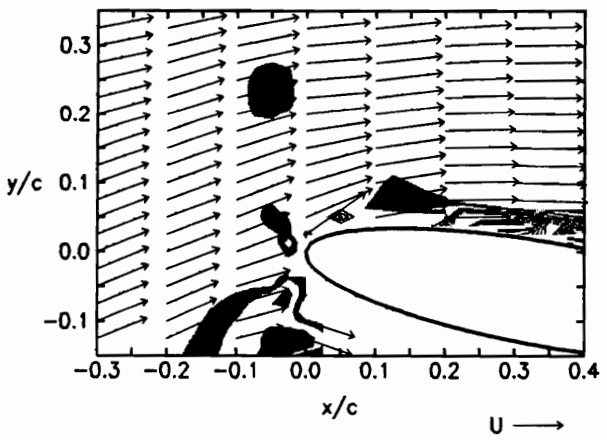

(continued) k = 2.05, H = 0.265, Re = 12600

VORTICITY CONTOURS PHASE = 324.0 deg.
TIME = 1.1160 sec.

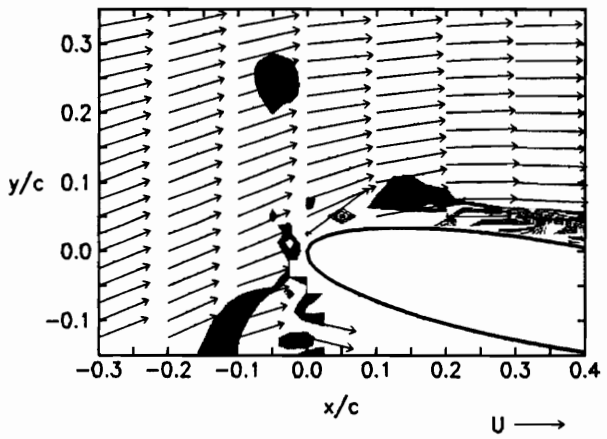

VORTICITY CONTOURS PHASE = 331.2 deg.
TIME = 1.1408 sec.

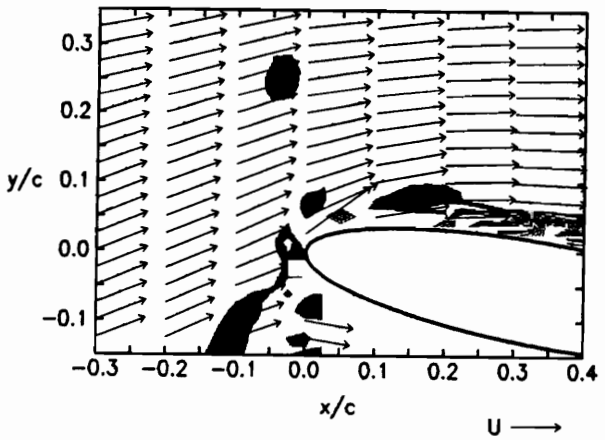

(continued) k = 2.05, H = 0.265, Re = 12600

VORTICITY CONTOURS PHASE = 338.4 deg.
TIME = 1.1656 sec.

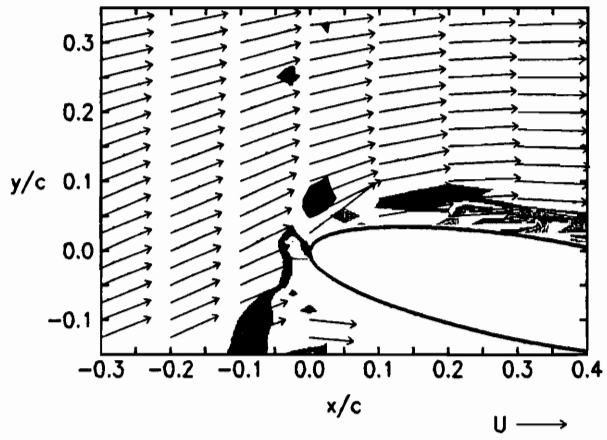

VORTICITY CONTOURS PHASE = 345.6 deg.
TIME = 1.1904 sec.

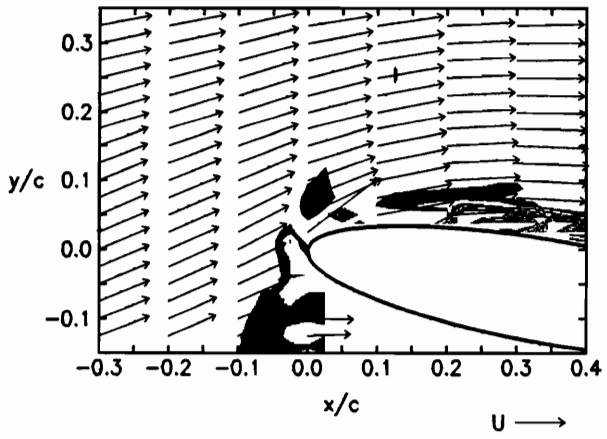

(continued) k = 2.05, H = 0.265, Re = 12600

Appendix C

Airfoil-vortex interaction, $\alpha = 10°$: direct encounter

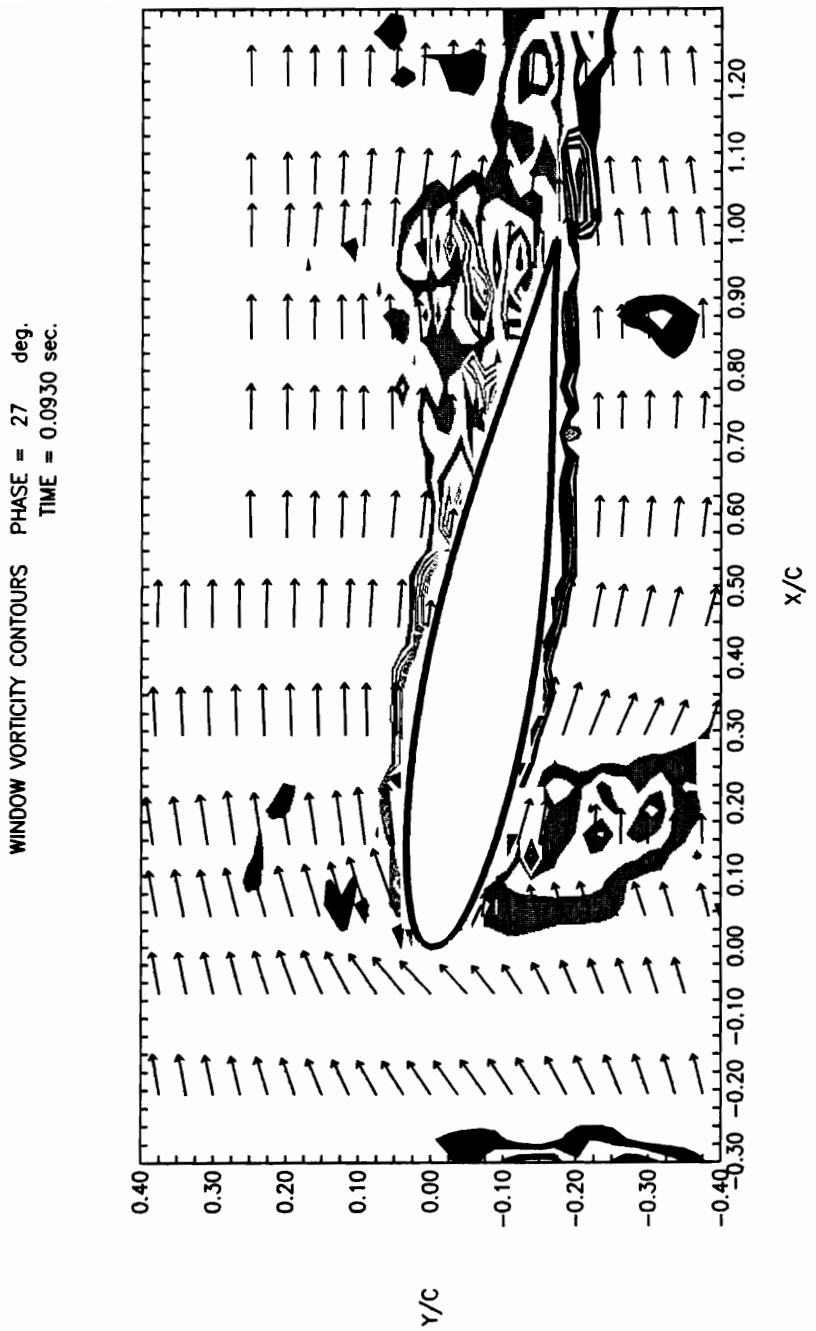

Figure C.1. Vorticity contour maps for the $\alpha = 10°$ direct encounter: $k = 2.05$, $H = 0.265$, $Re = 12600$

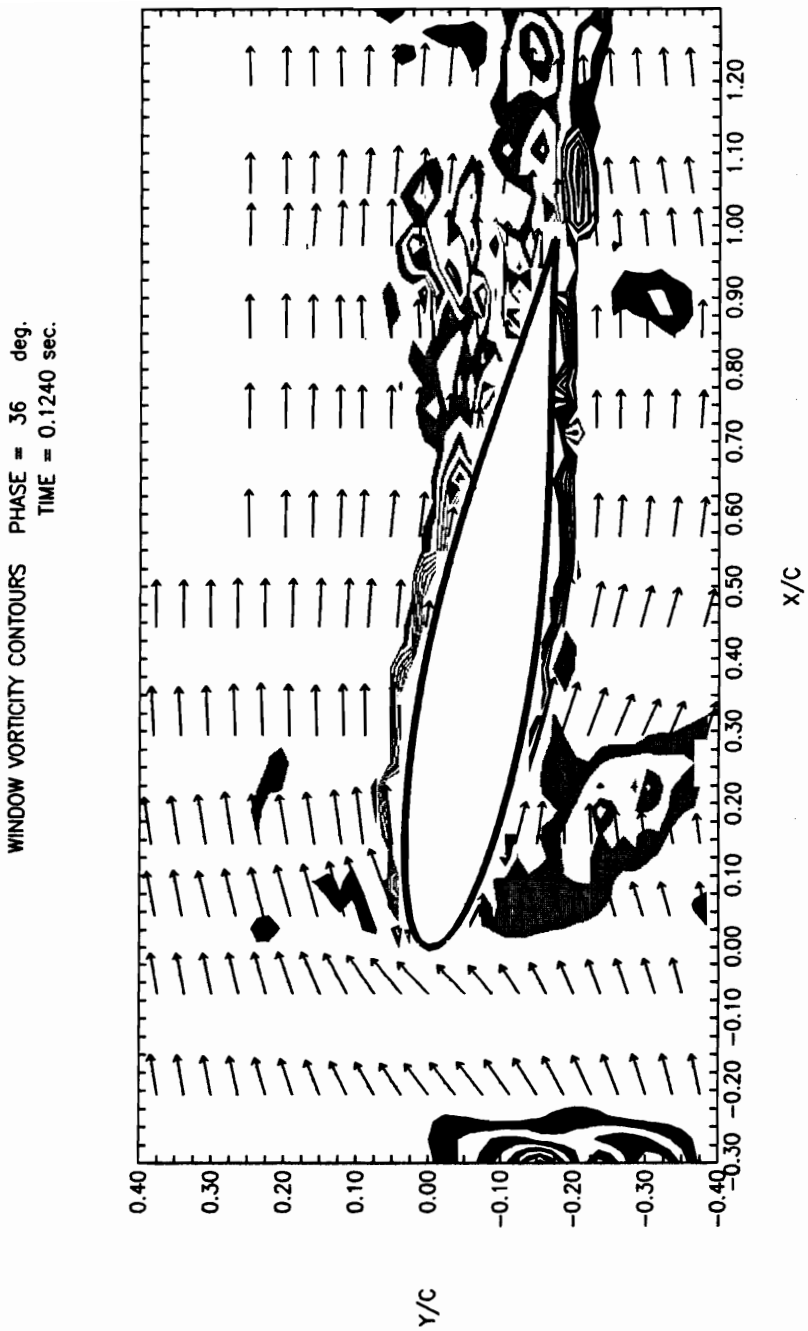

(continued) k = 2.05, H = 0.265, Re = 12600

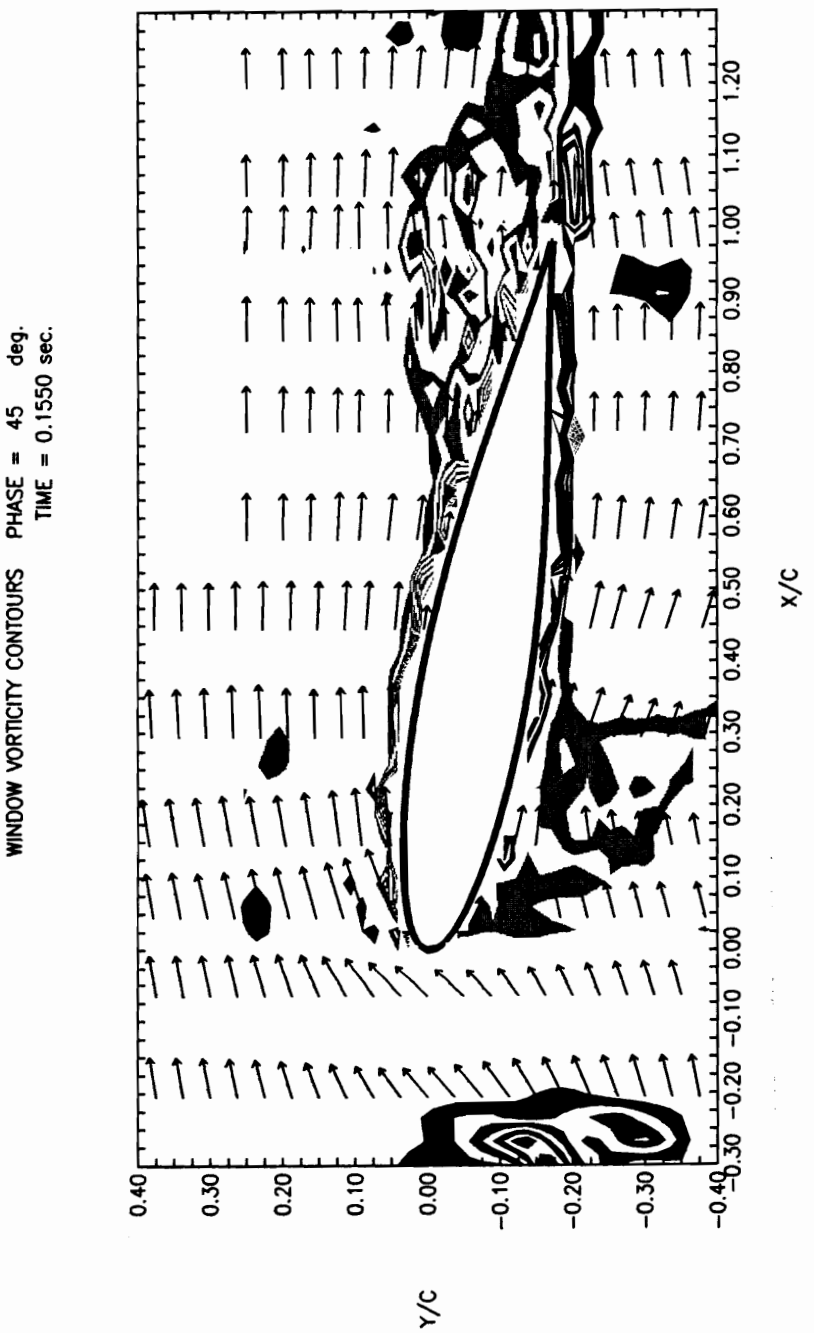

(continued) k = 2.05, H = 0.265, Re = 12600

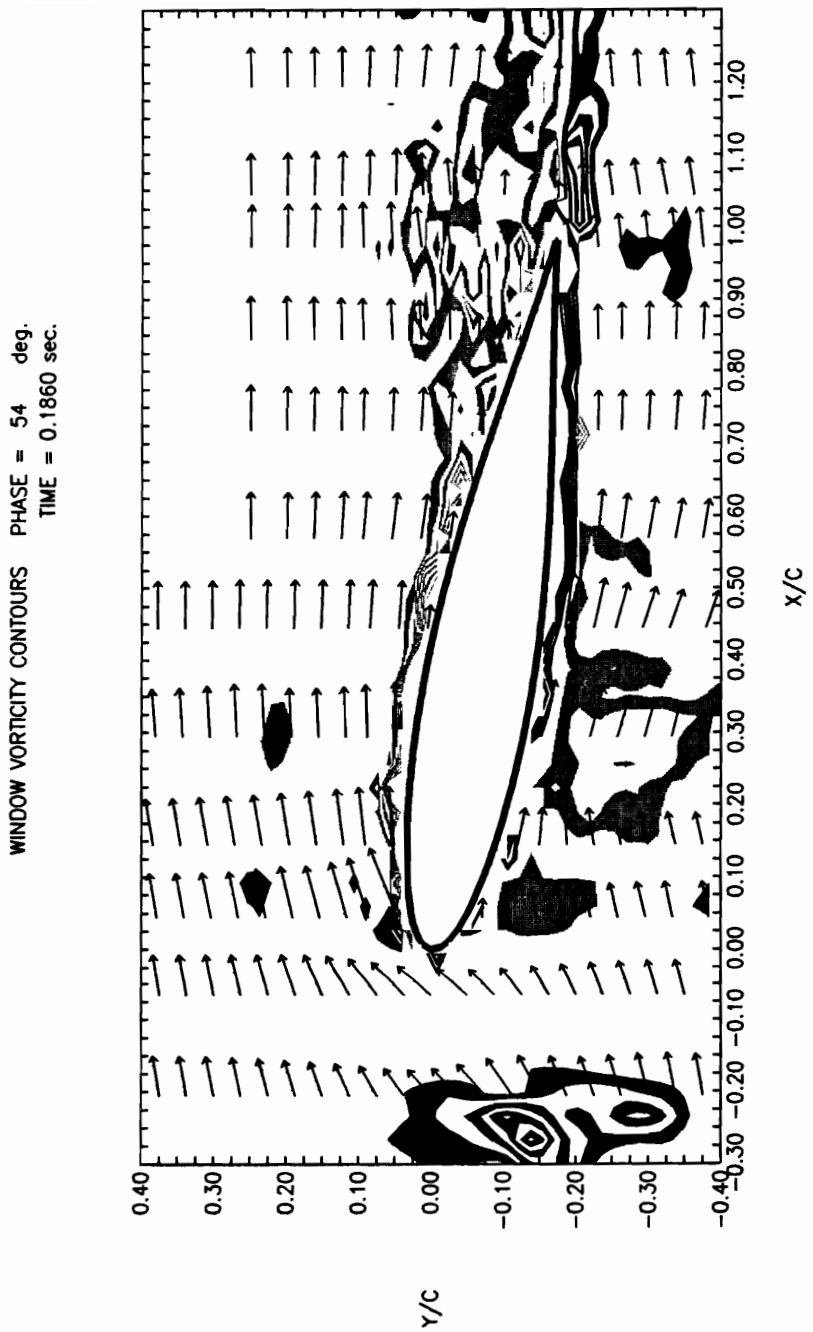

(continued) k = 2.05, H = 0.265, Re = 12600

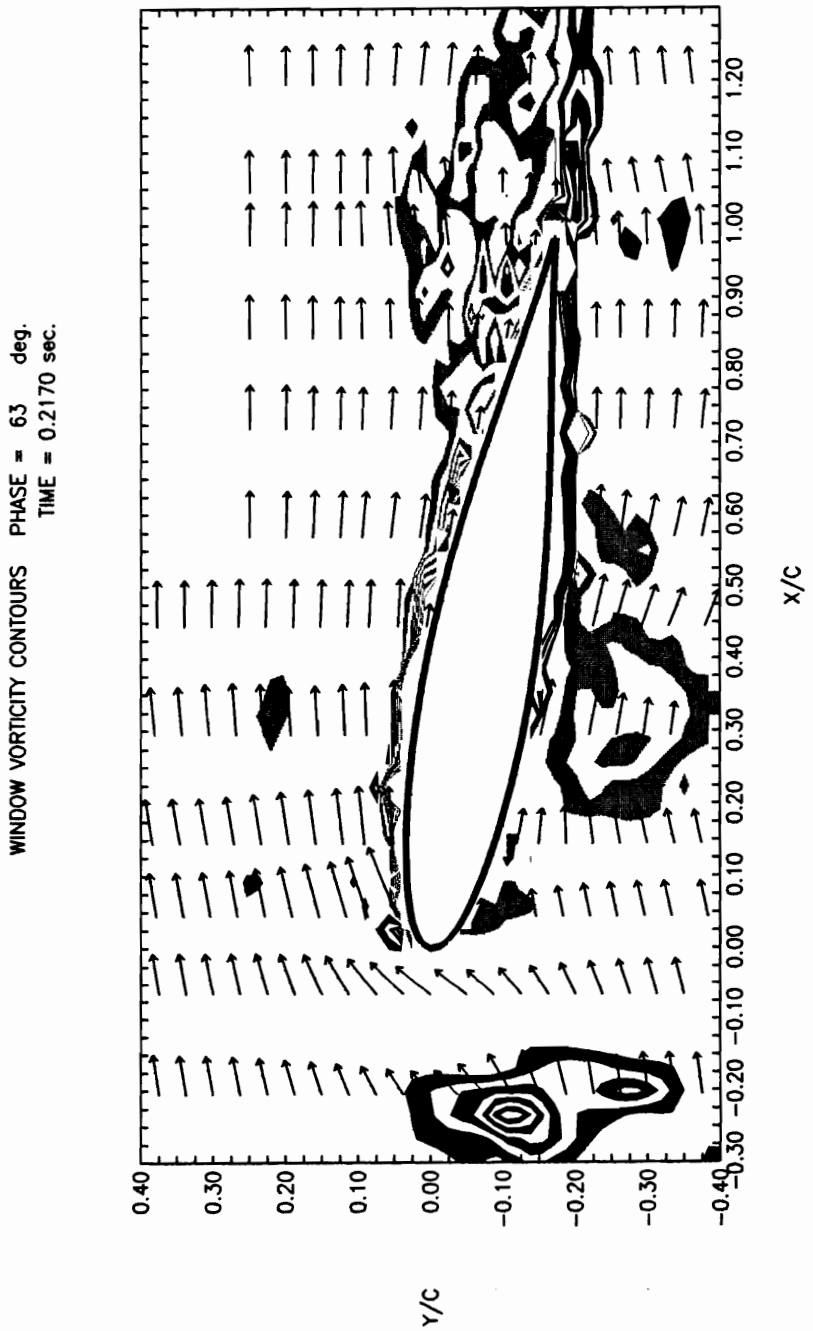

(continued) k = 2.05, H = 0.265, Re = 12600

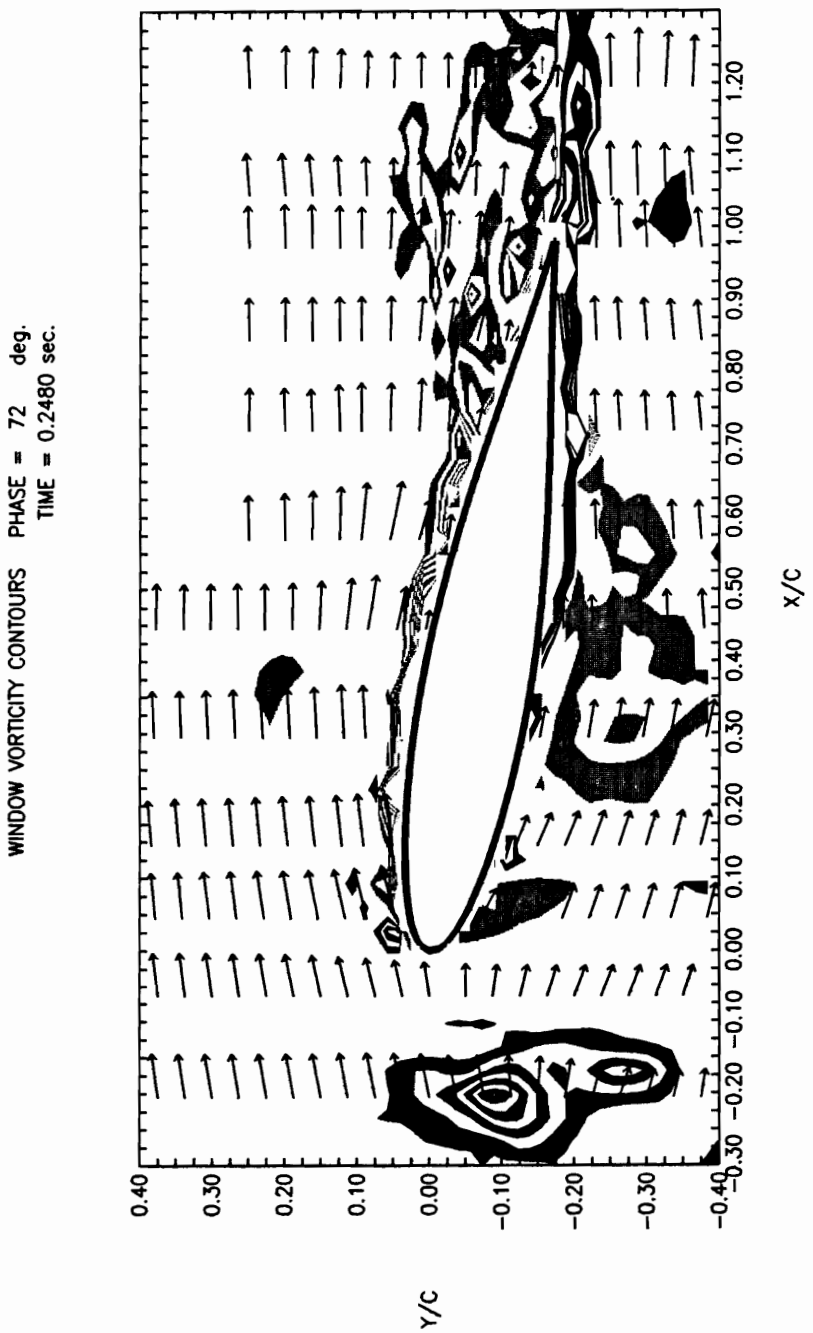

(continued) k = 2.05, H = 0.265, Re = 12600

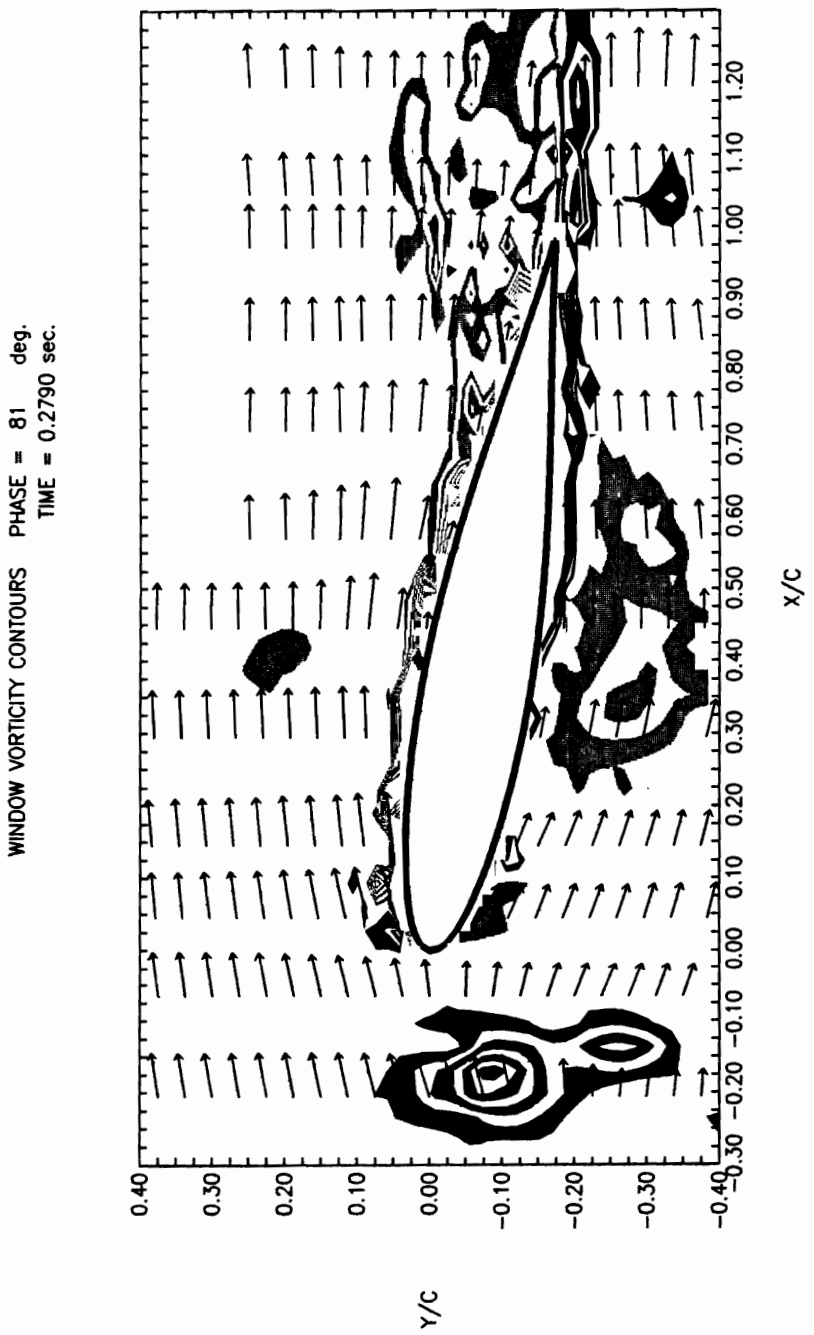

(continued) k = 2.05, H = 0.265, Re = 12600

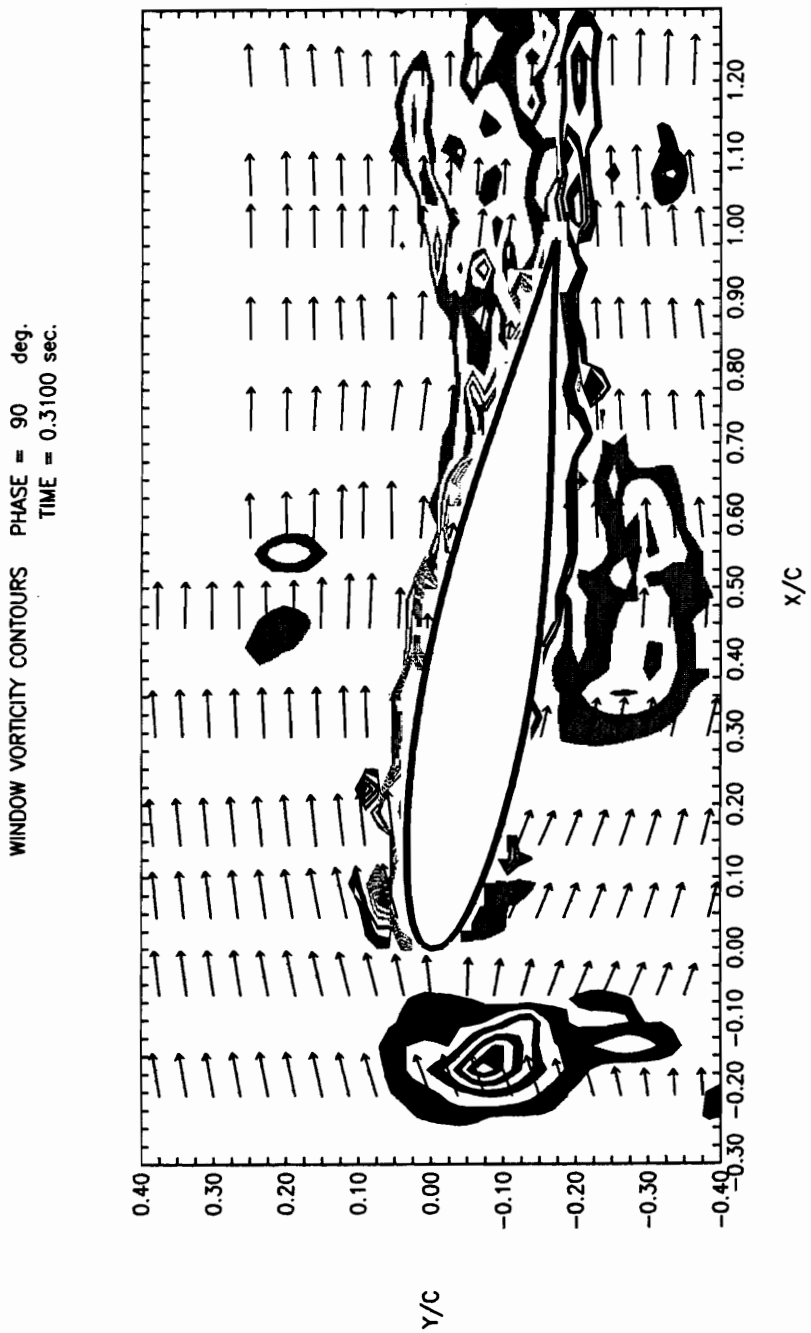

(continued) k = 2.05, H = 0.265, Re = 12600

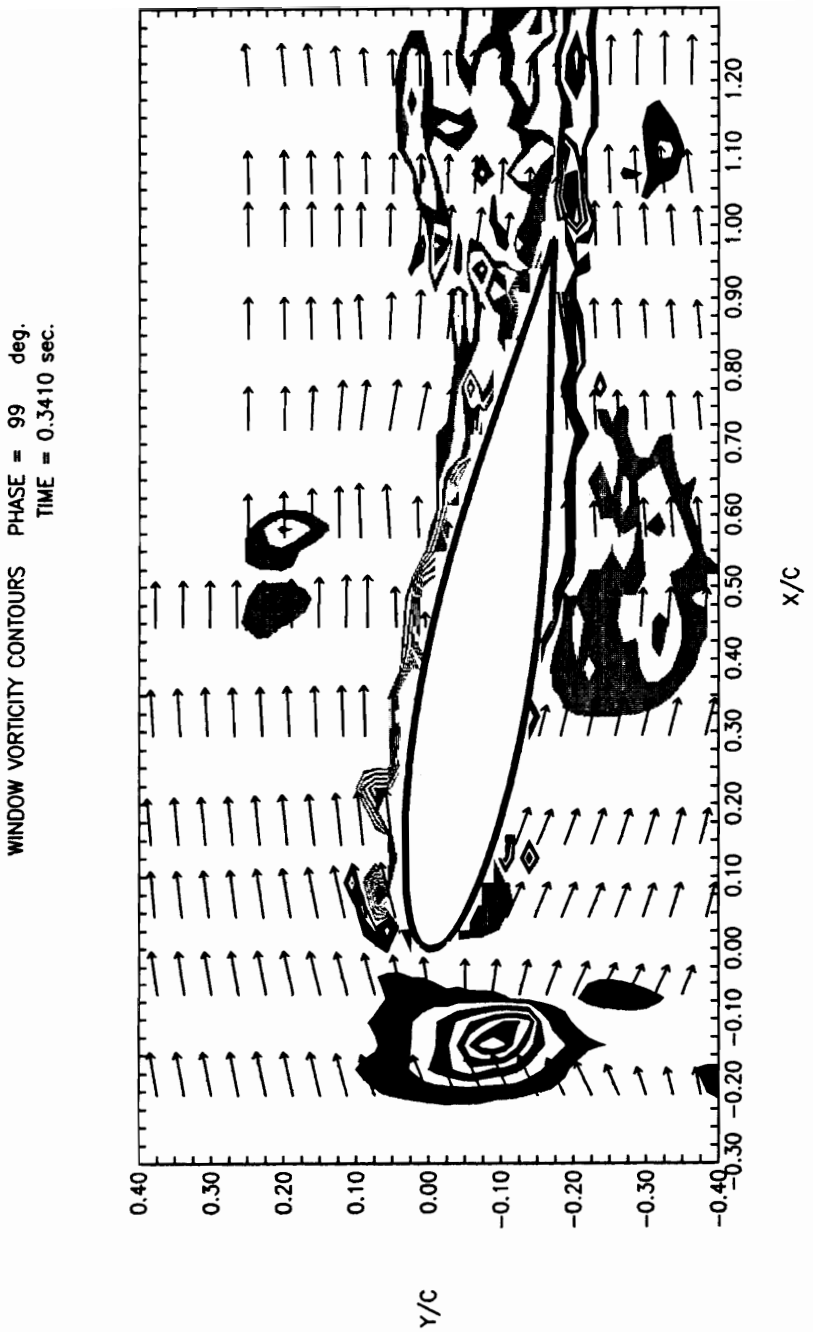

(continued) k = 2.05, H = 0.265, Re = 12600

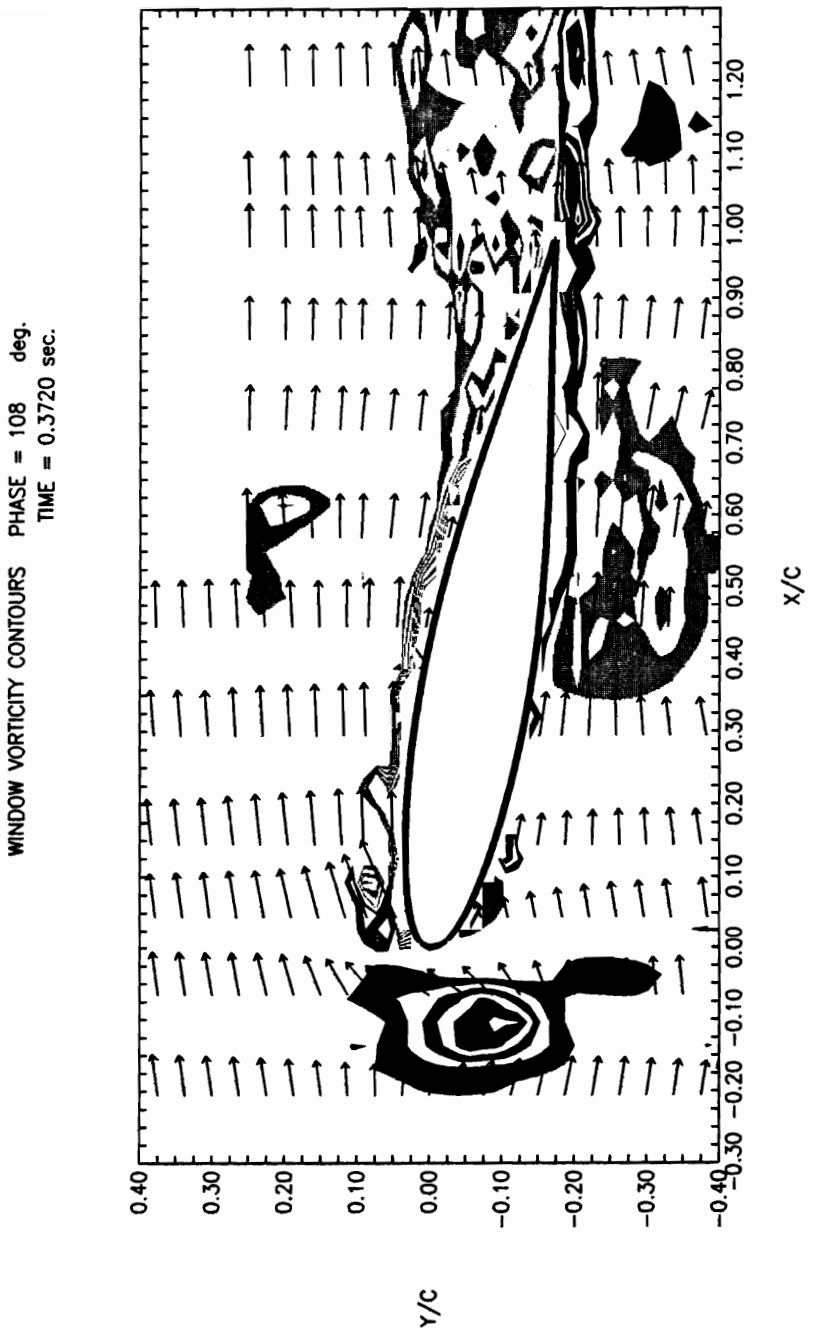

(continued) k = 2.05, H = 0.265, Re = 12600

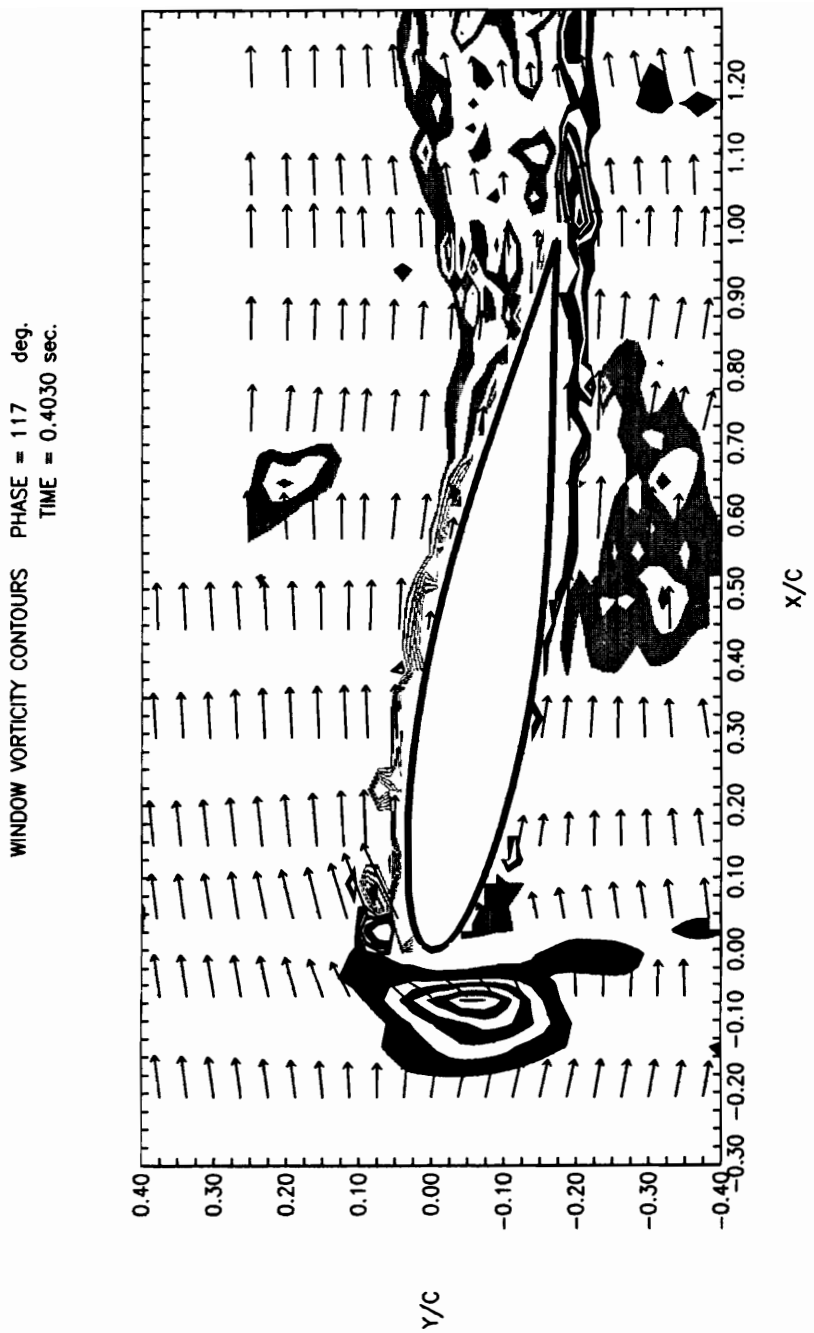

(continued) k = 2.05, H = 0.265, Re = 12600

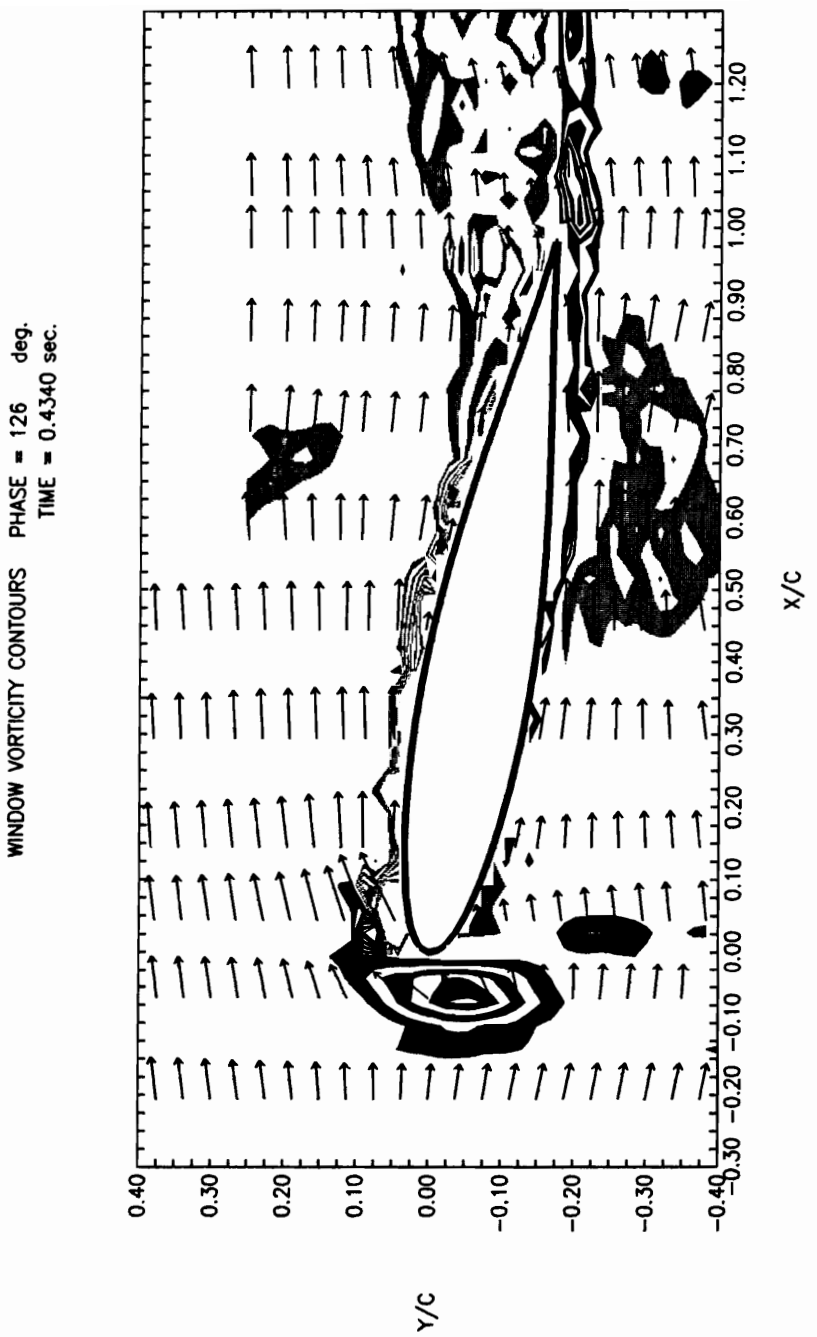

(continued) k = 2.05, H = 0.265, Re = 12600

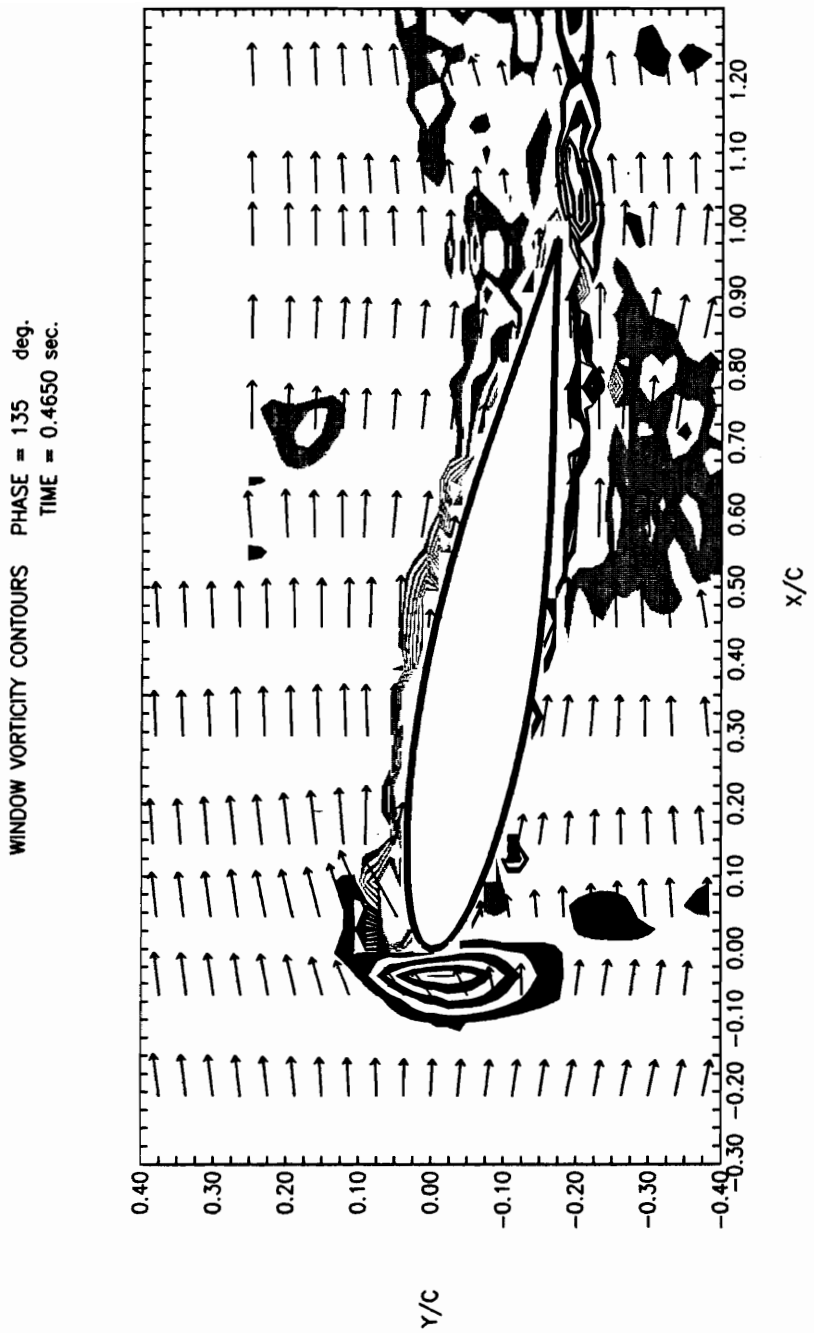

(continued) k = 2.05, H = 0.265, Re = 12600

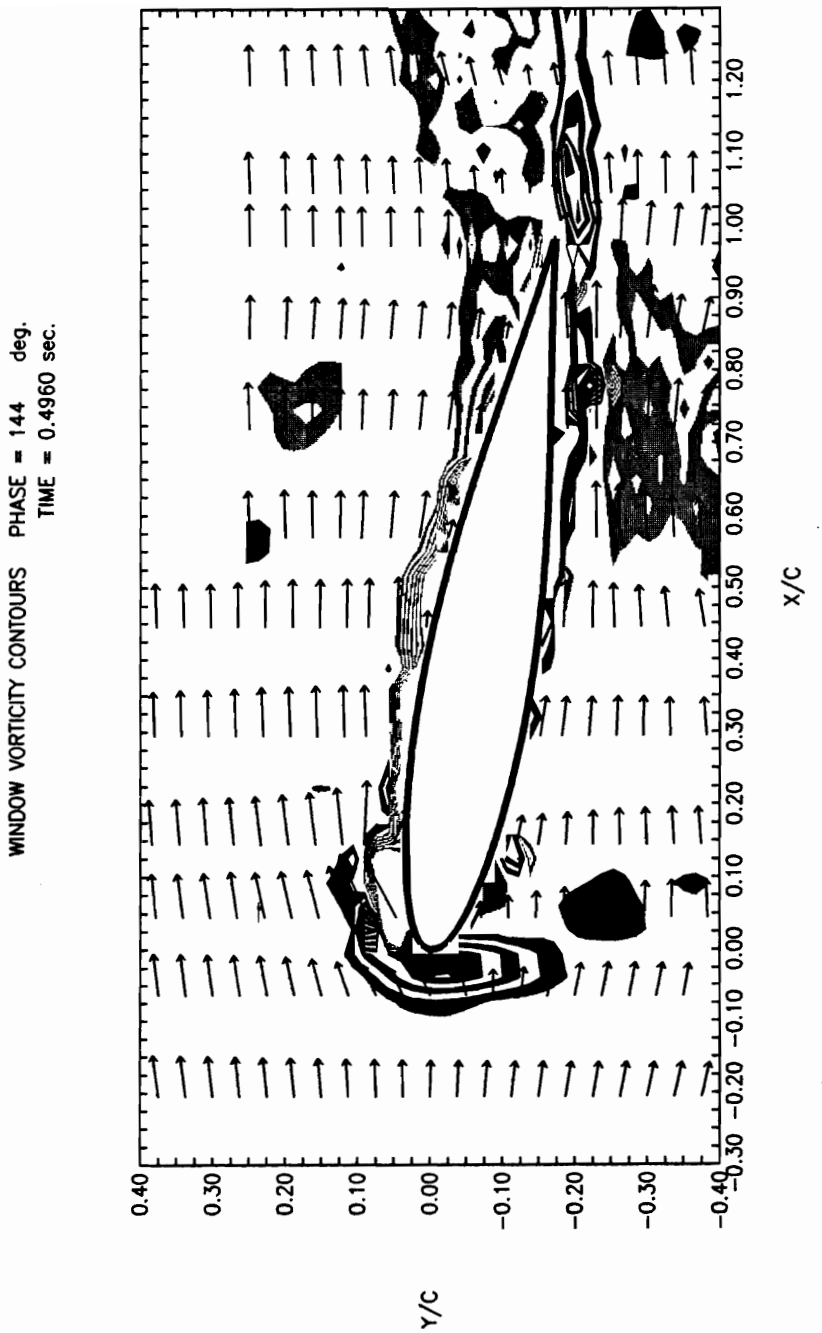

(continued) k = 2.05, H = 0.265, Re = 12600

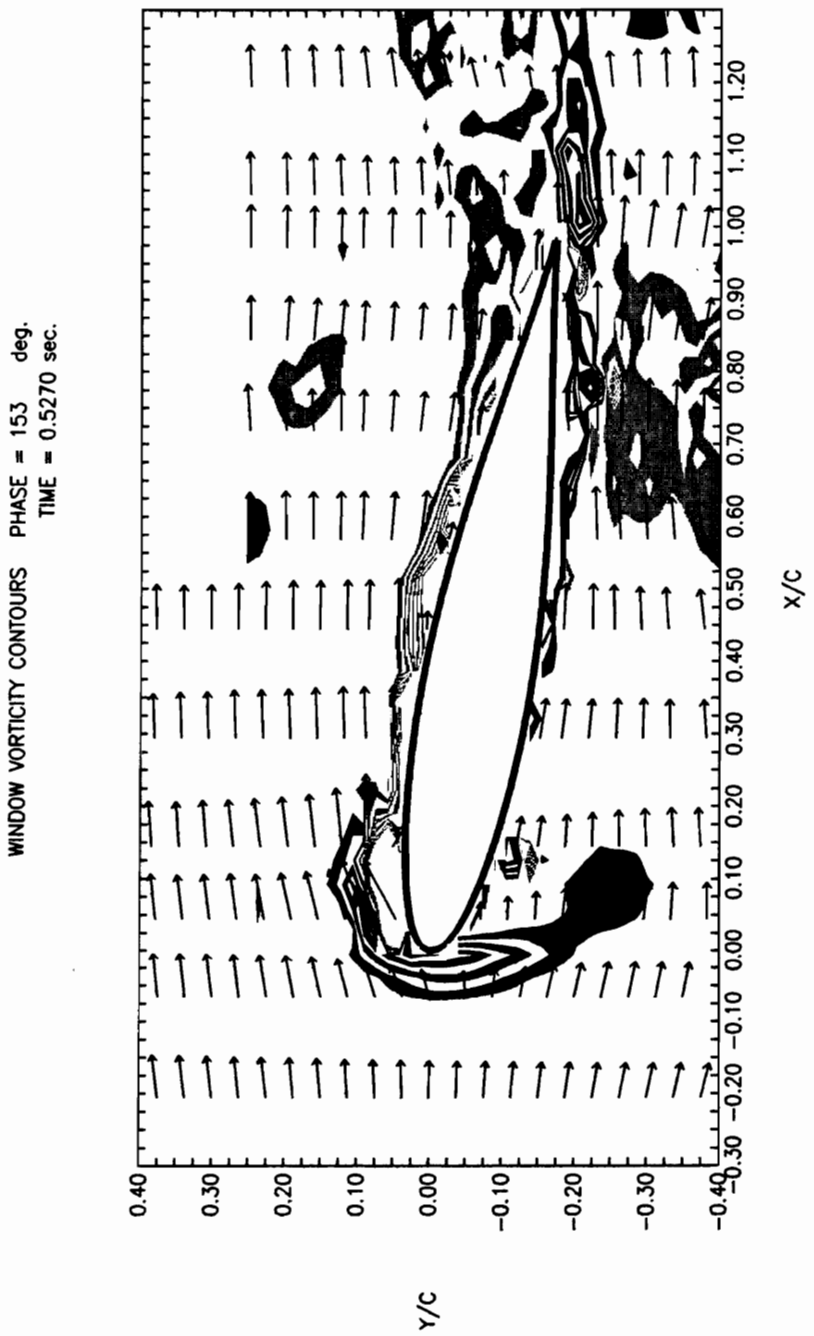

(continued) k = 2.05, H = 0.265, Re = 12600

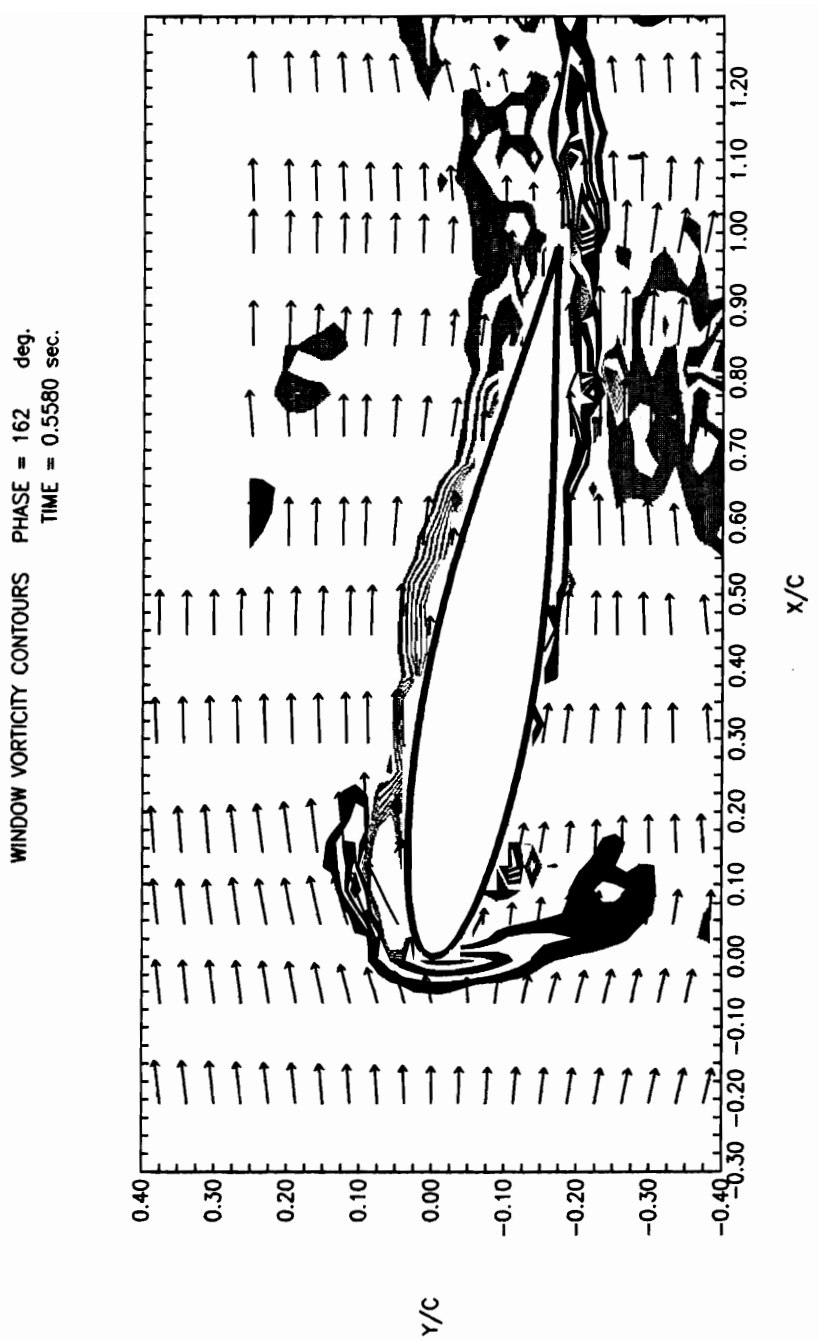

(continued) k = 2.05, H = 0.265, Re = 12600

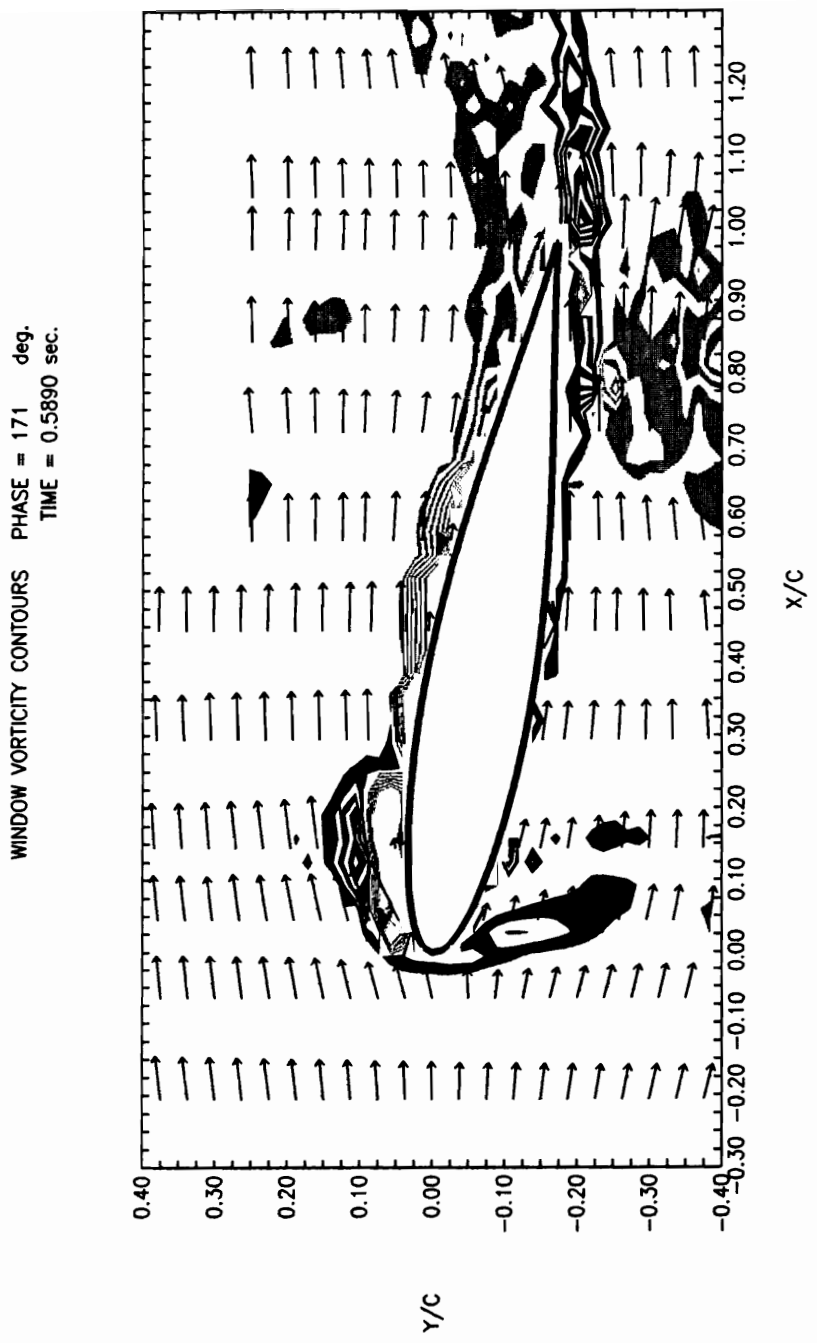

(continued) k = 2.05, H = 0.265, Re = 12600

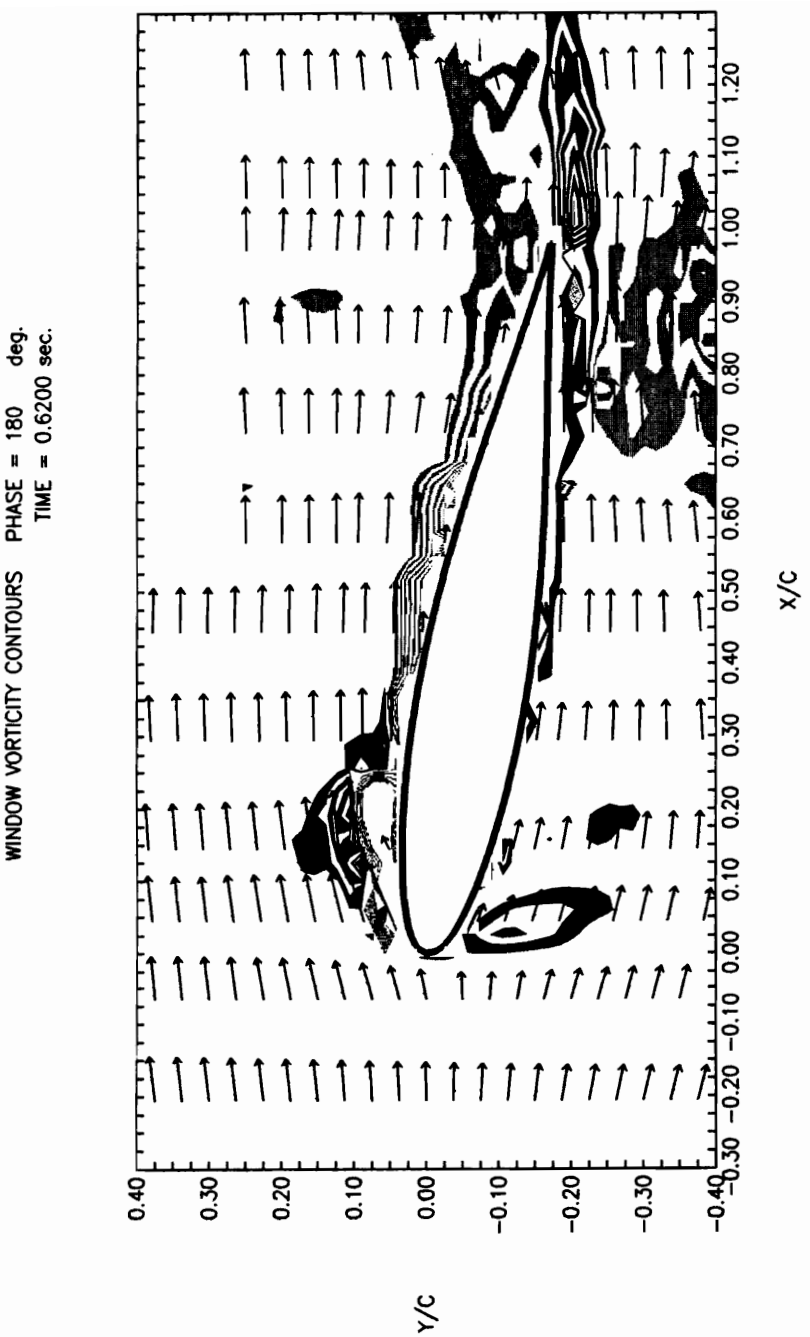

(continued) k = 2.05, H = 0.265, Re = 12600

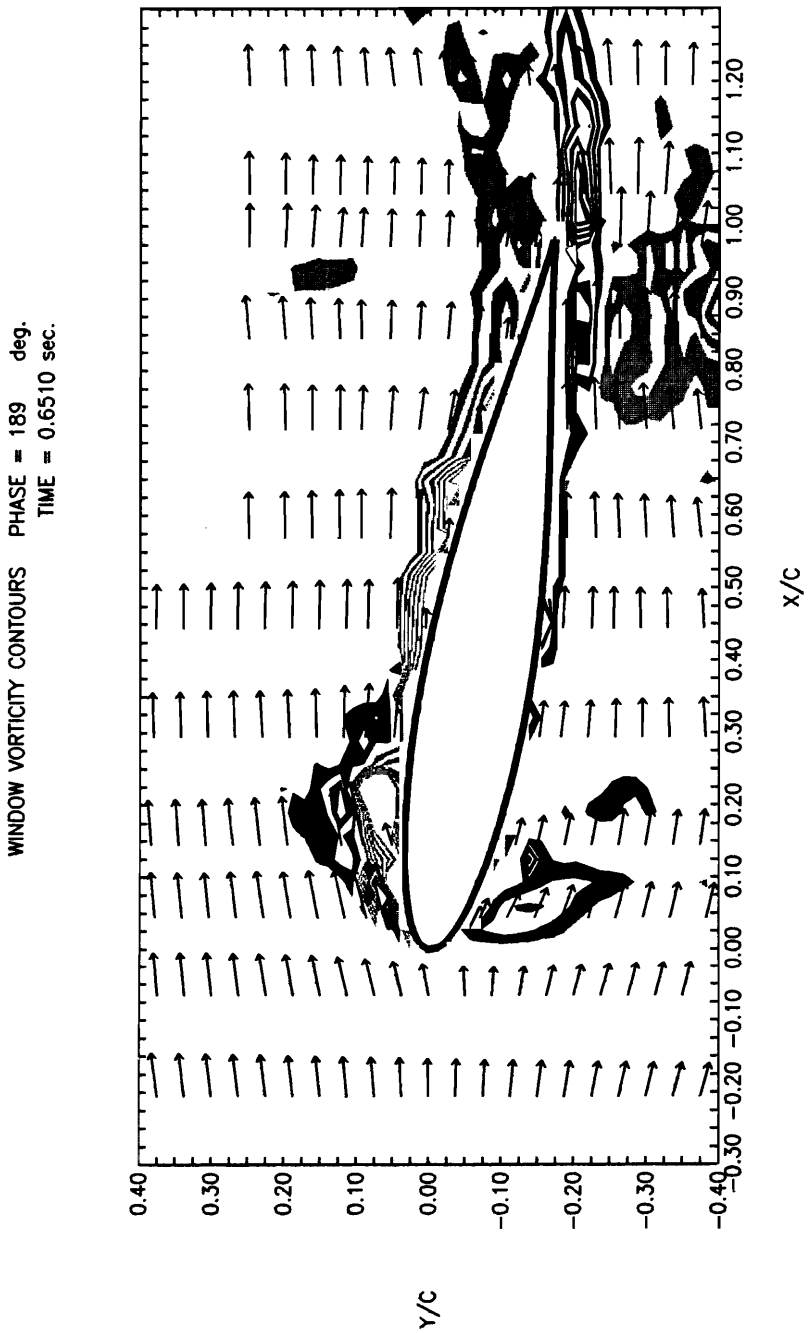

(continued) k = 2.05, H = 0.265, Re = 12600

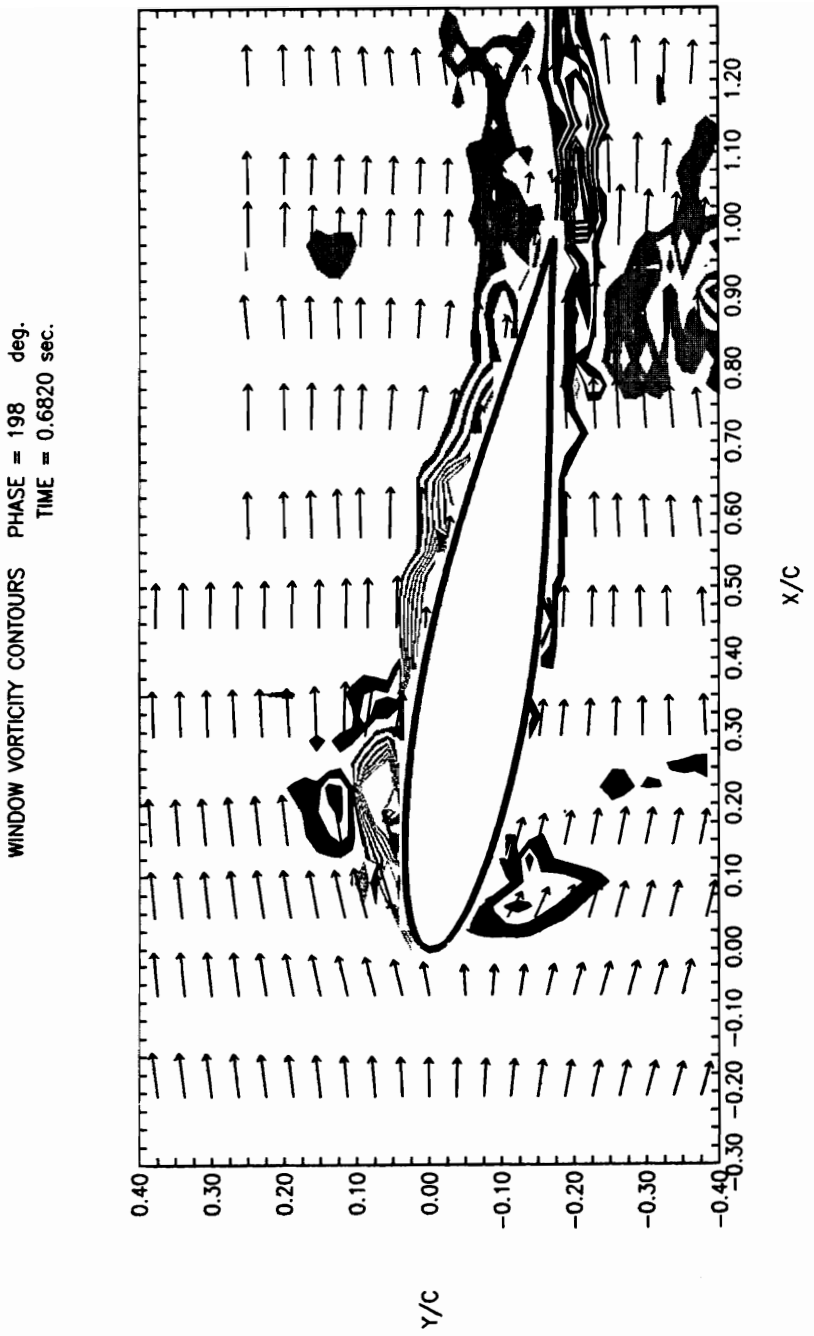

(continued) k = 2.05, H = 0.265, Re = 12600

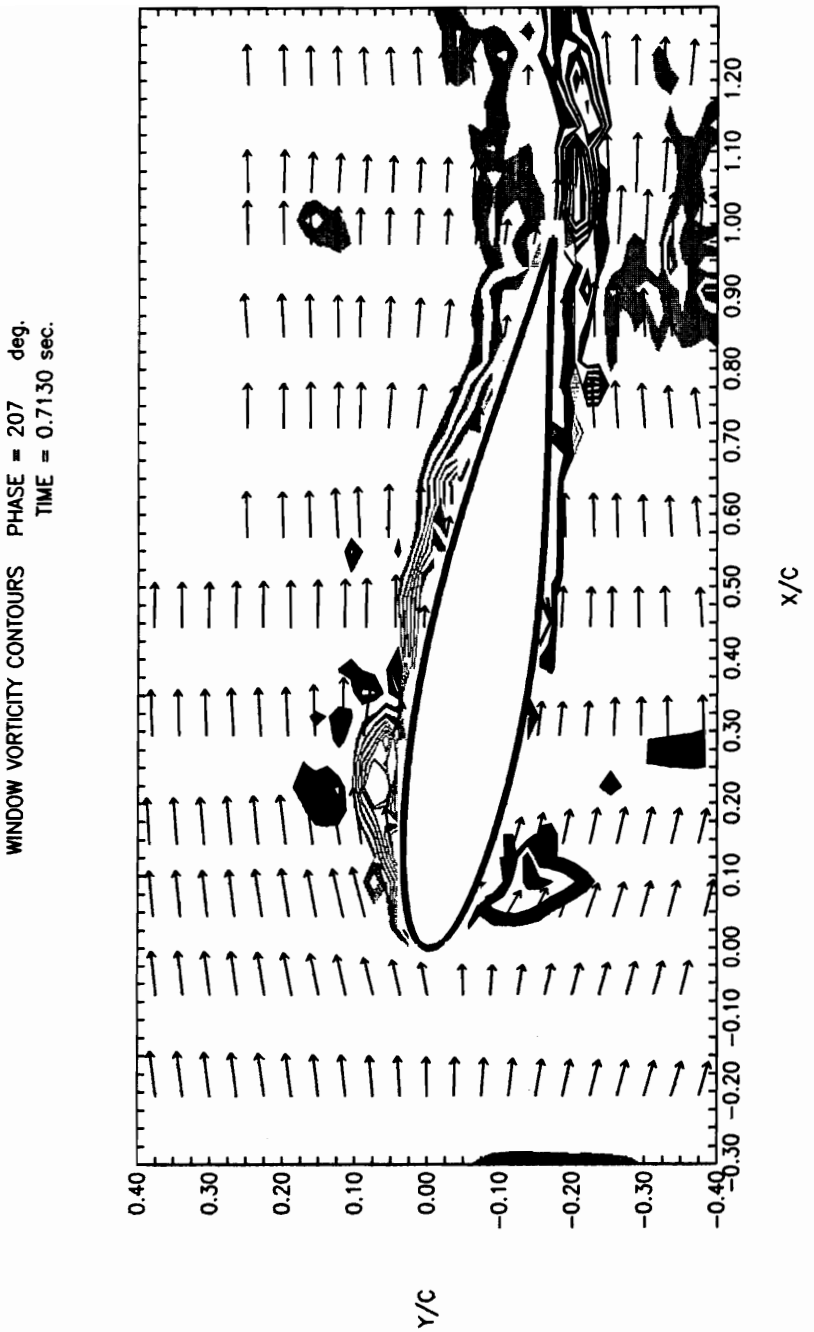

(continued) k = 2.05, H = 0.265, Re = 12600

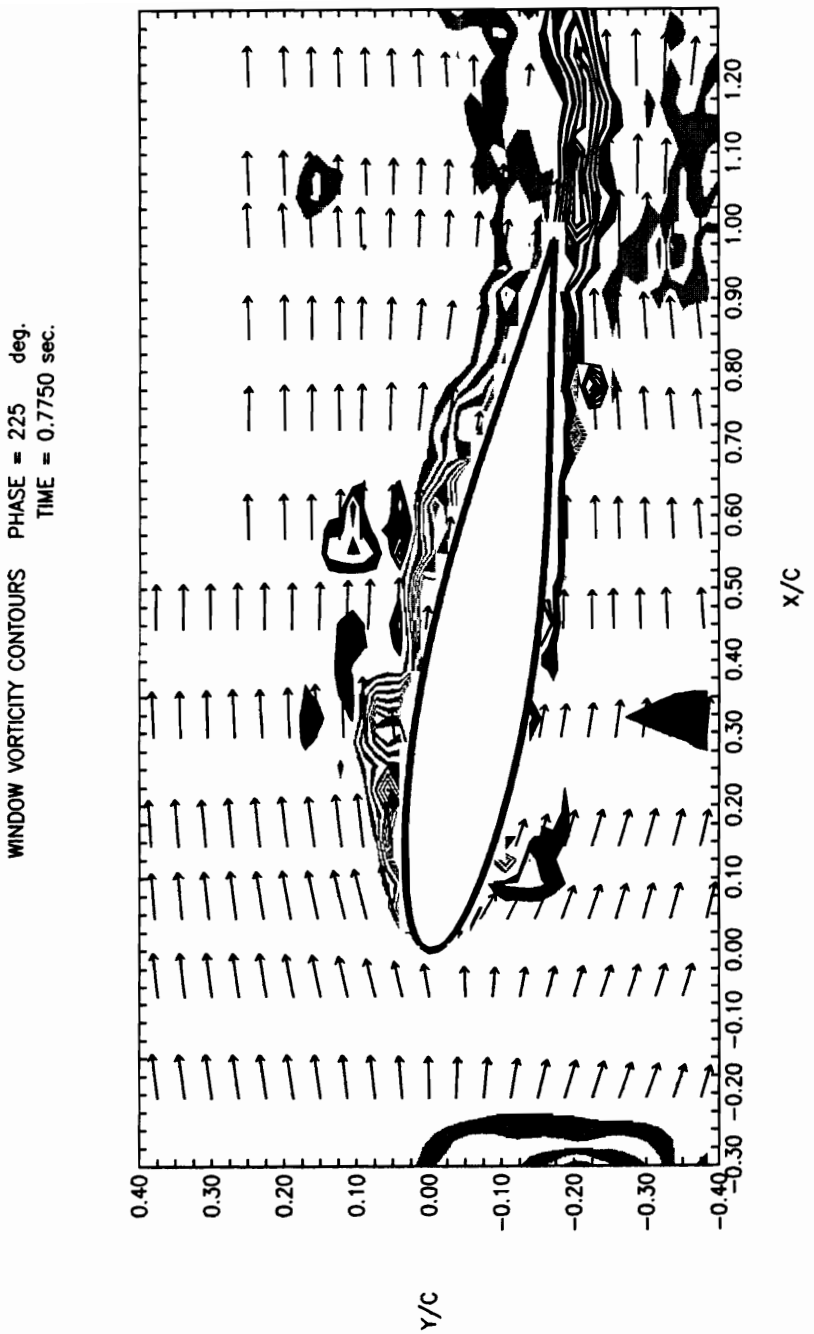

(continued) k = 2.05, H = 0.265, Re = 12600

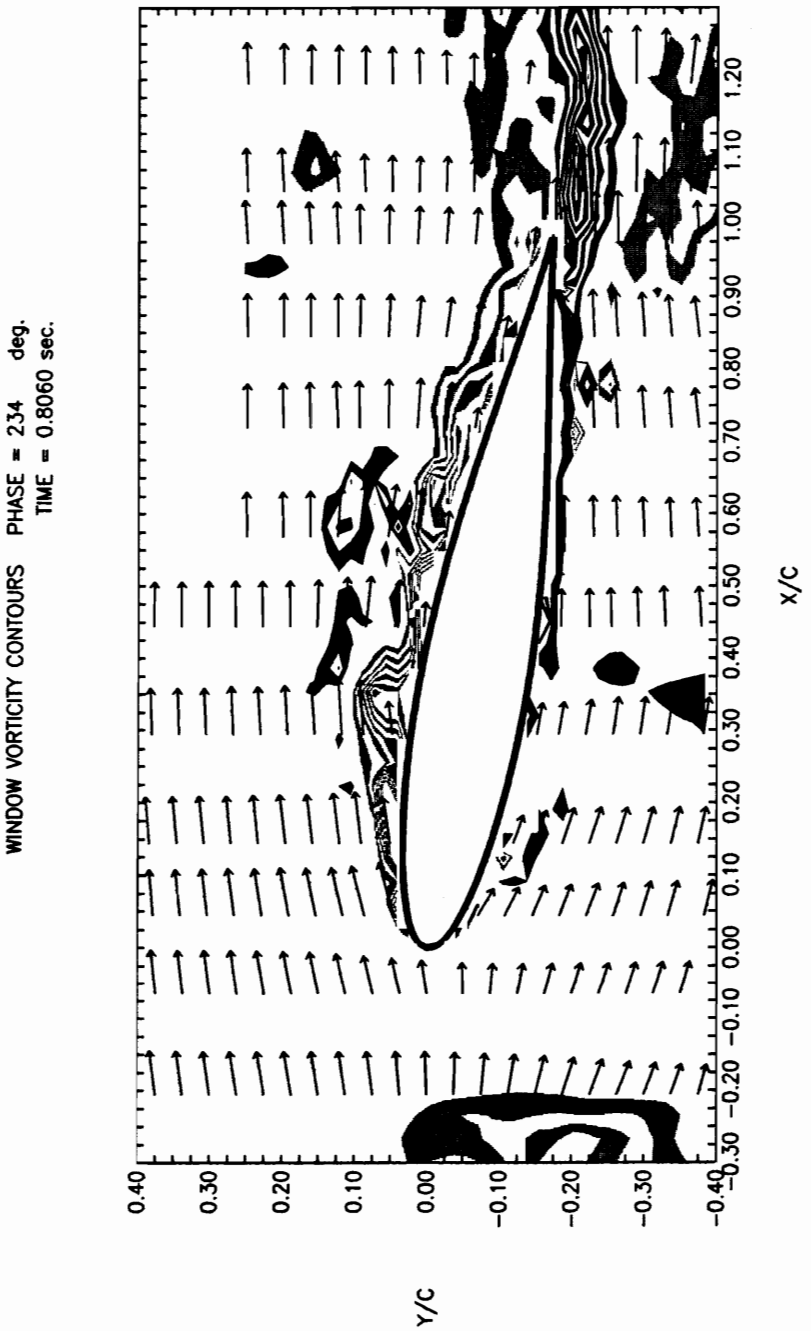

(continued) k = 2.05, H = 0.265, Re = 12600

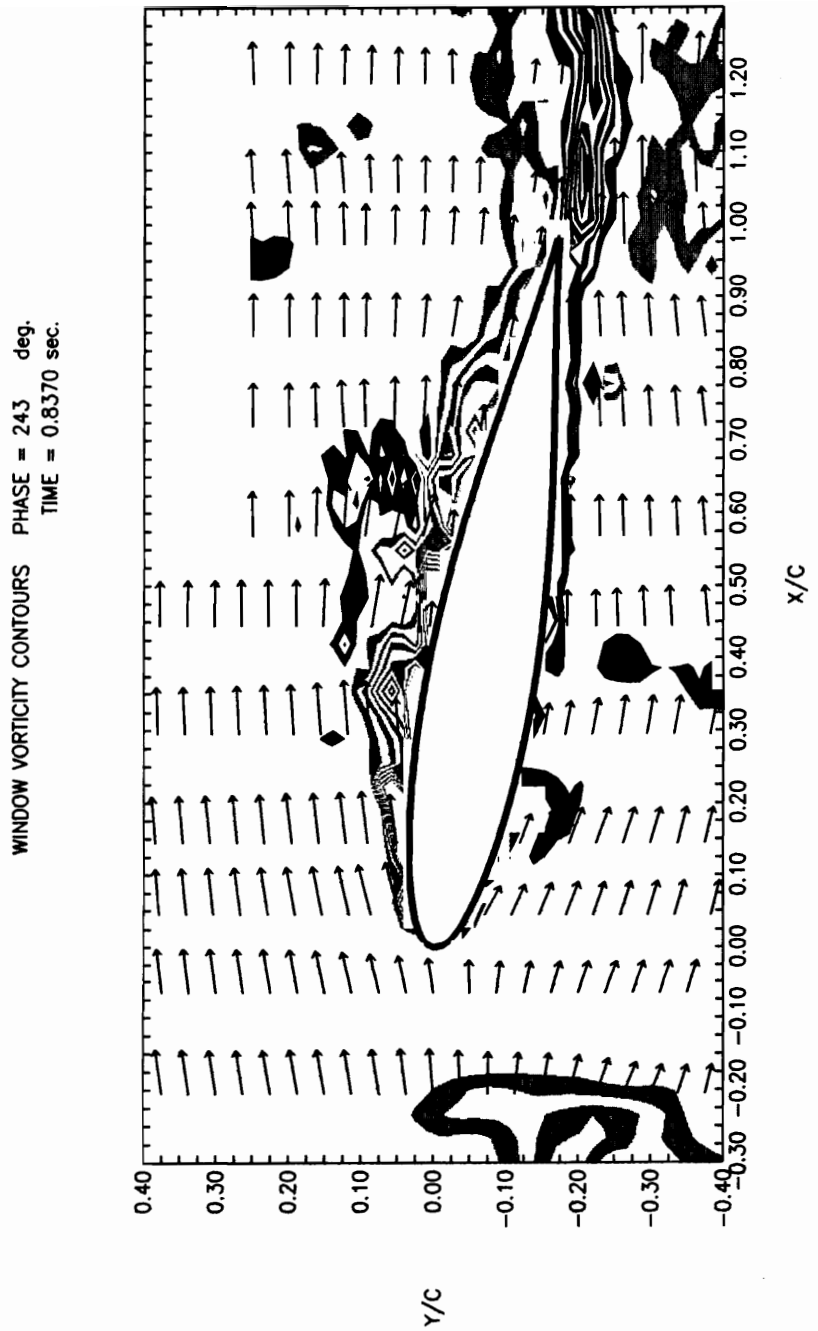

(continued) k = 2.05, H = 0.265, Re = 12600

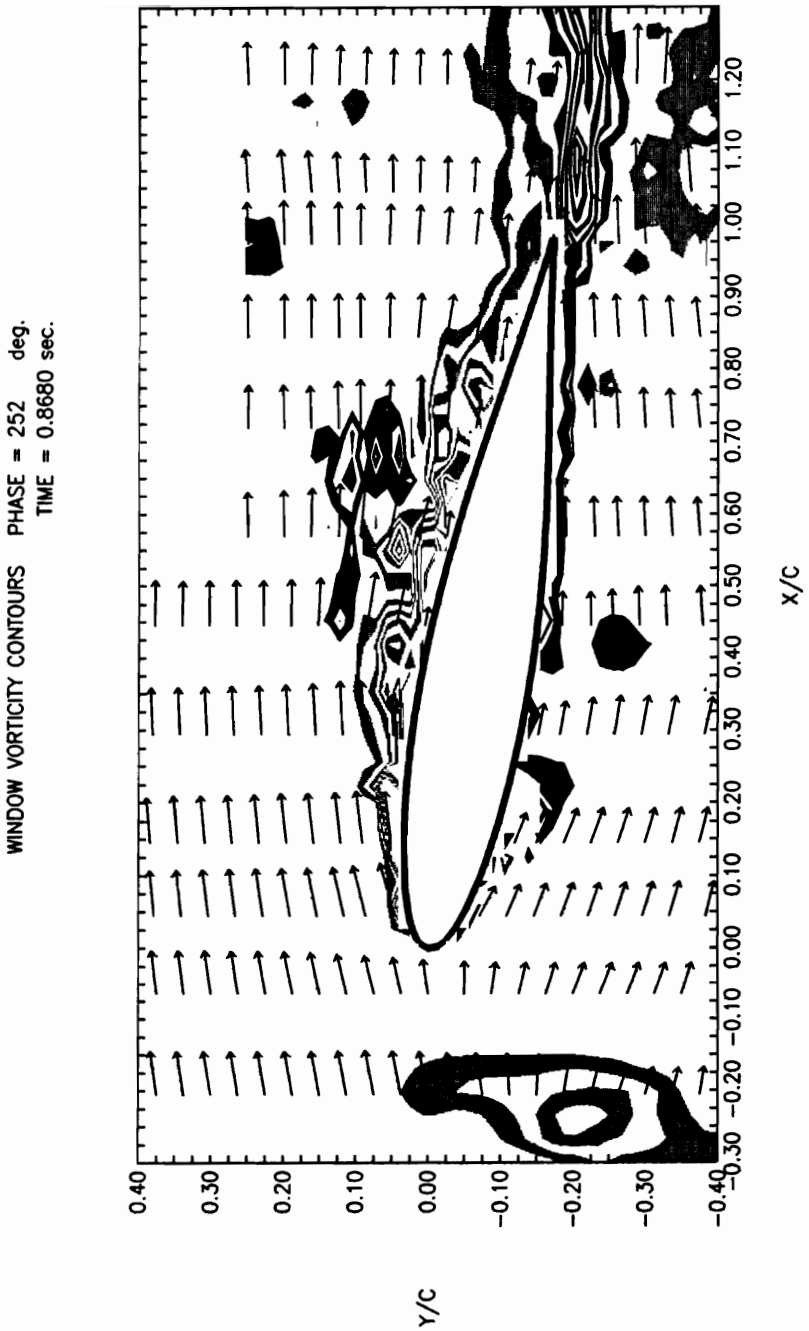

(continued) k = 2.05, H = 0.265, Re = 12600

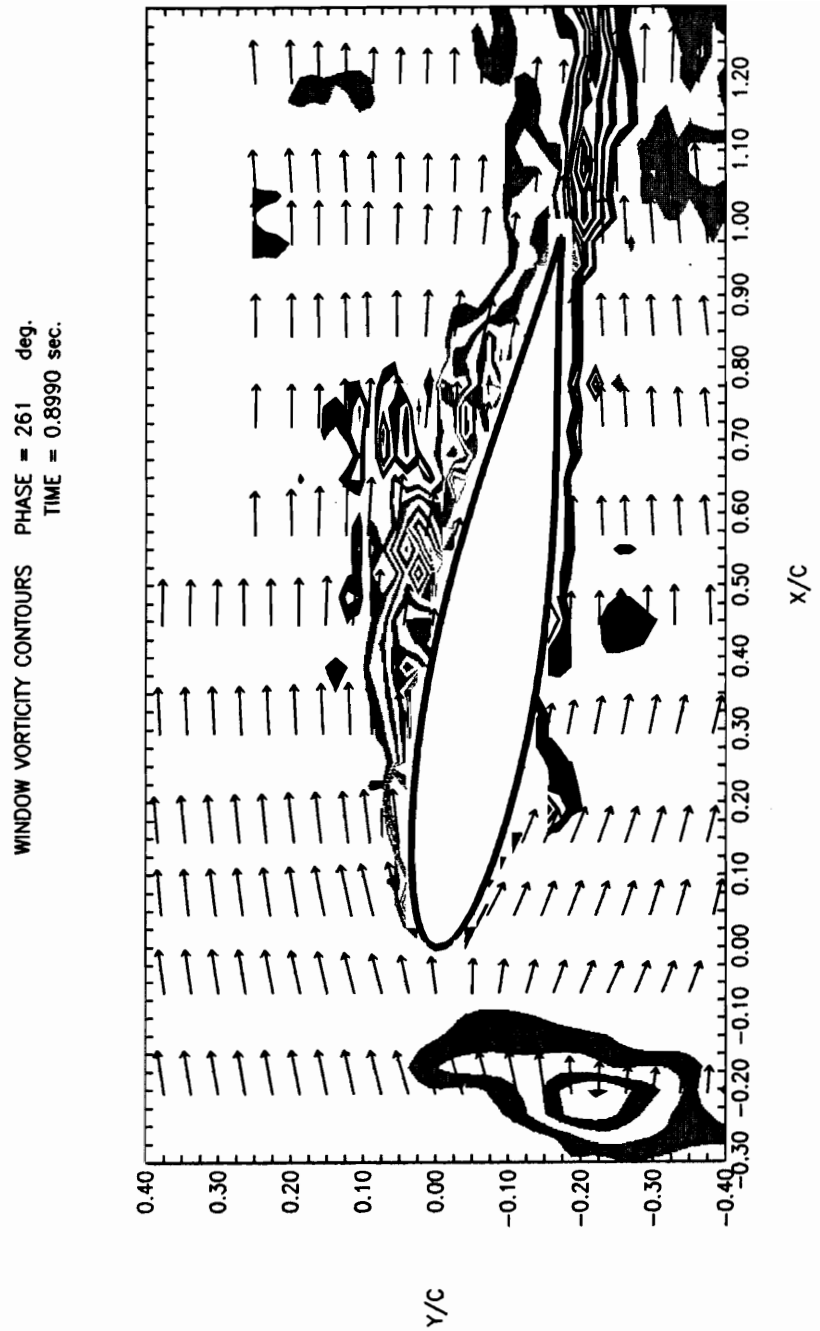

(continued) k = 2.05, H = 0.265, Re = 12600

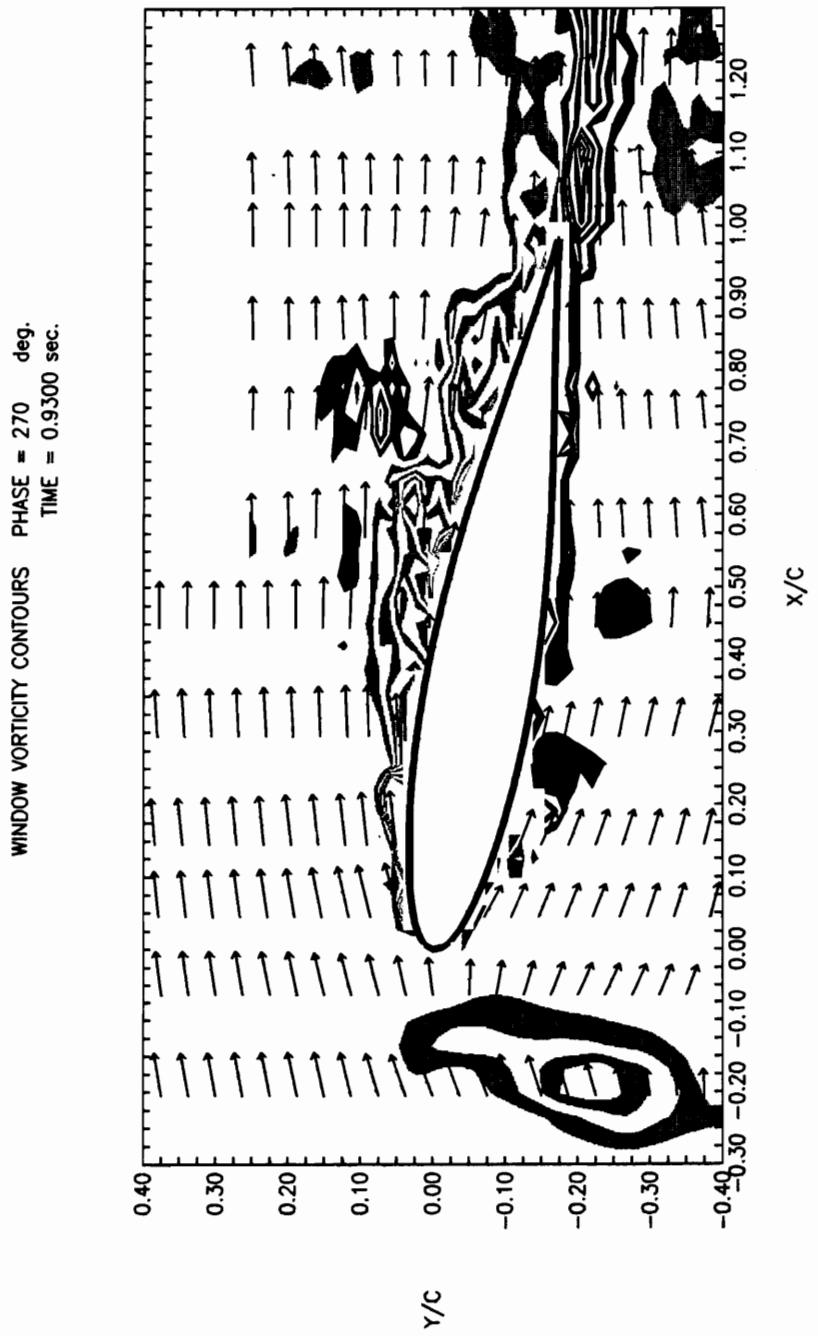

(continued) k = 2.05, H = 0.265, Re = 12600

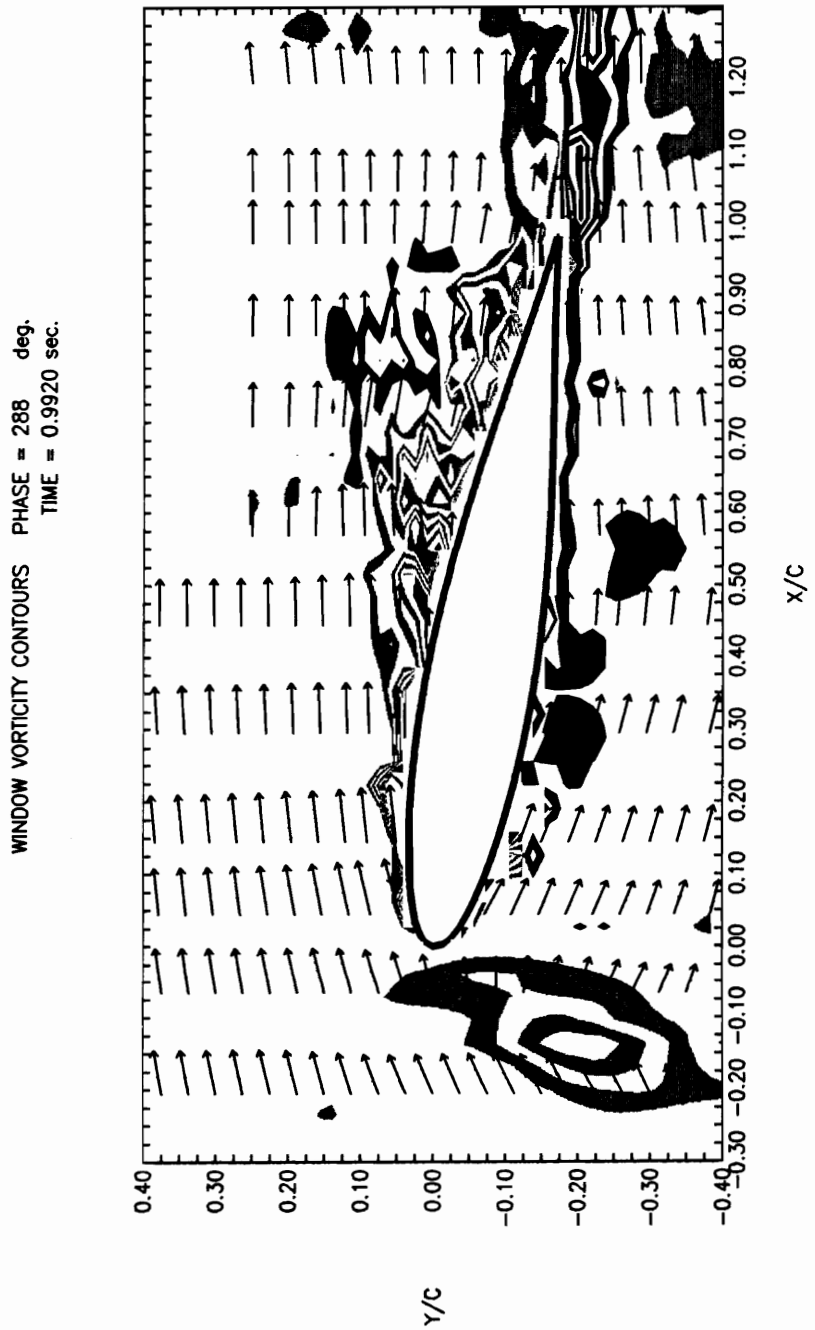

(continued) k = 2.05, H = 0.265, Re = 12600

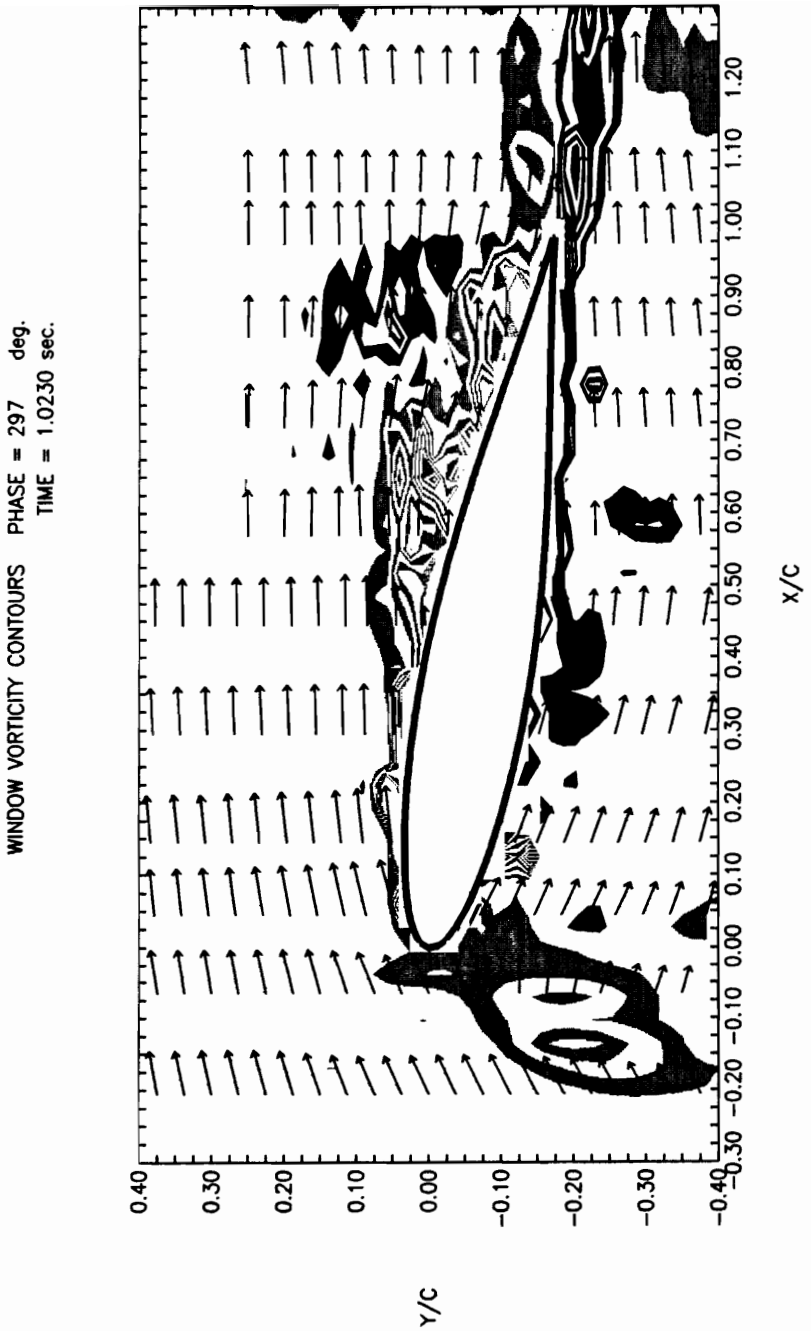

(continued) k = 2.05, H = 0.265, Re = 12600

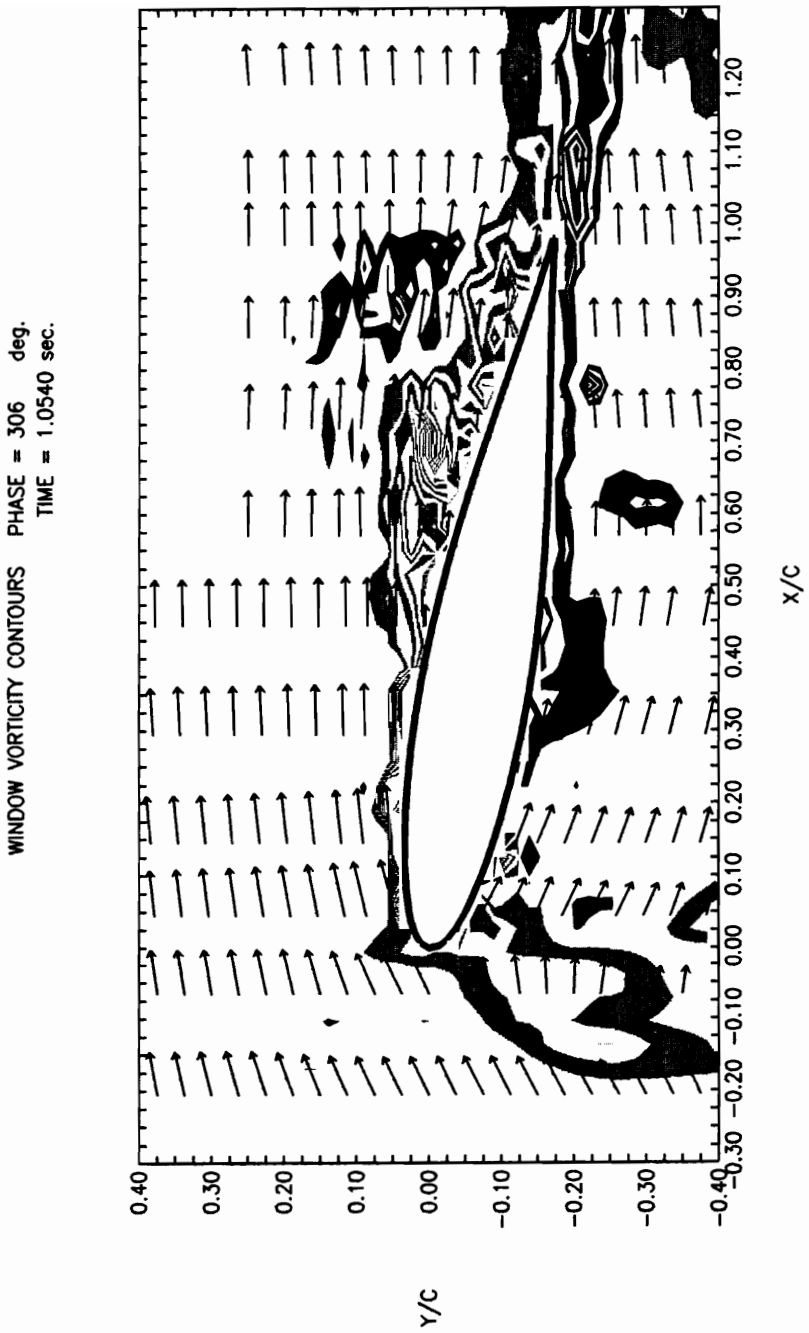

(continued) k = 2.05, H = 0.265, Re = 12600

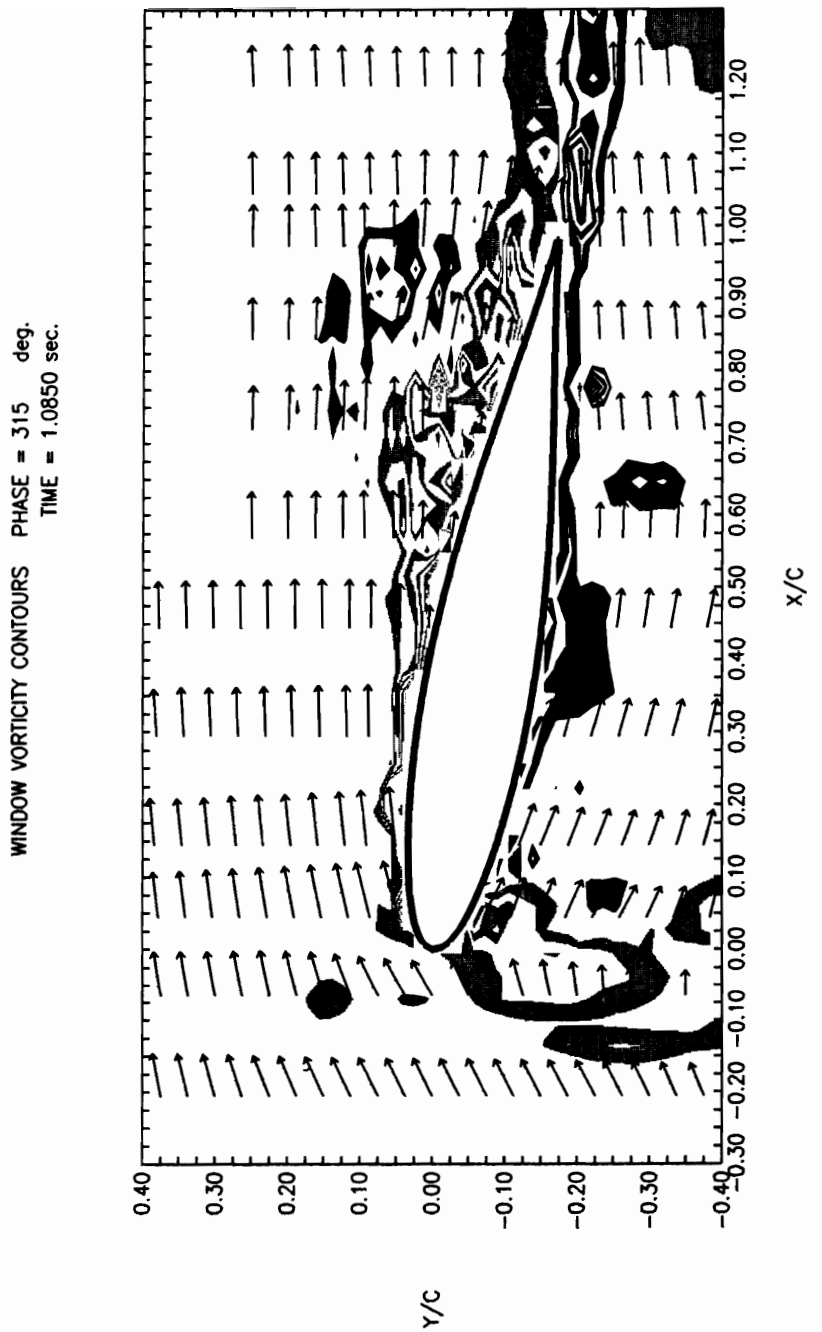

(continued) k = 2.05, H = 0.265, Re = 12600

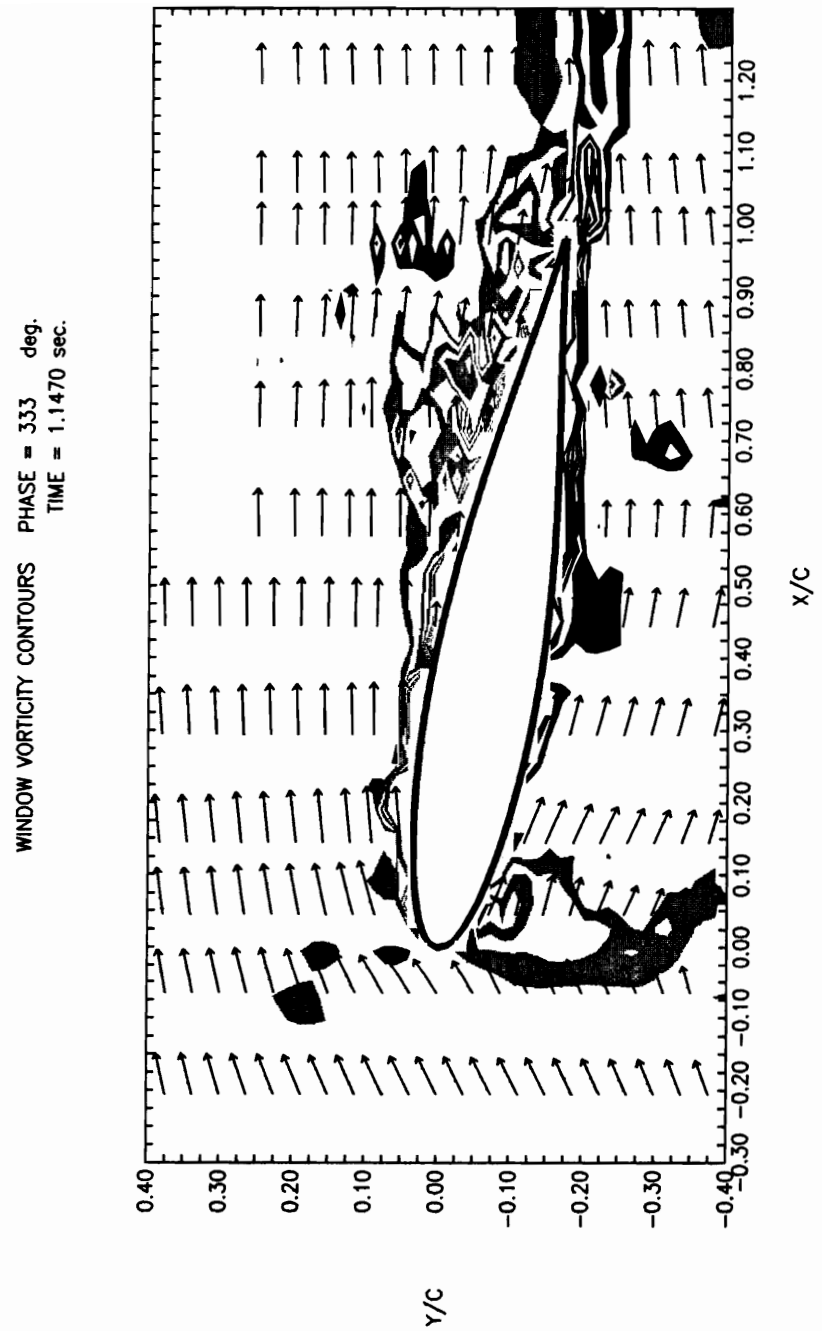

(continued) k = 2.05, H = 0.265, Re = 12600

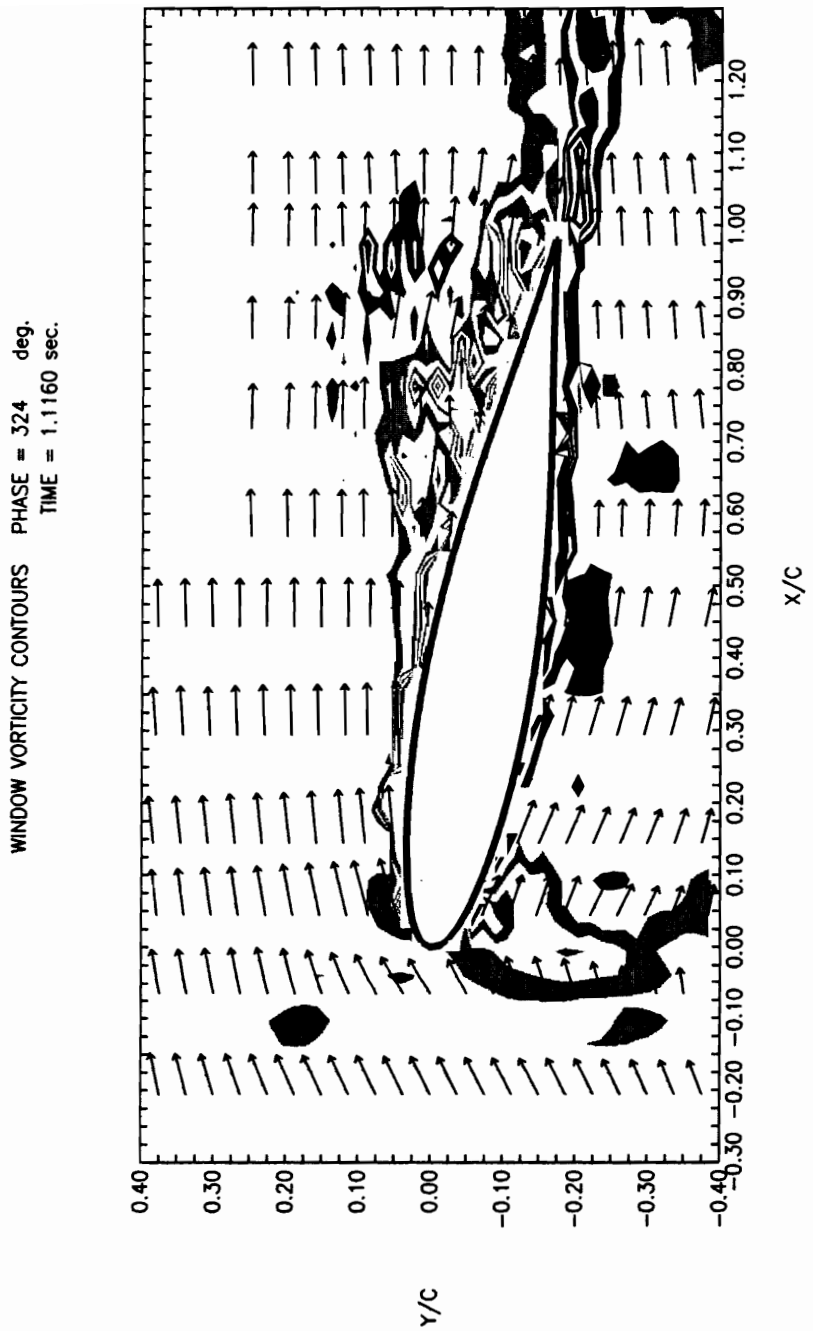

(continued) k = 2.05, H = 0.265, Re = 12600

Vita

Michael Curtis Wilder was born the third son of three to Zola and Martin Wilder in 1963 in Roanoke, Virginia. He attended William Fleming High School in Roanoke, and graduated with his B.A. in Physics/Astronomy from the University of Virginia in 1985. The next year was spent at the Mount Stromlo Observatory in Canderra, Australia, in the employment of the University of Virginia. In 1986 he matriculated at Virginia Tech and subsequently received an M.S. (1990) and Ph.D. (1992) in Engineering Mechanics.

Michael Curtis Wilder